




2019

Miniaturizing High Throughput Droplet Assays For Ultrasensitive Molecular Detection On A Portable Platform

Venkata Ravitheja Yelleswarapu
University of Pennsylvania, vraviy@gmail.com

Follow this and additional works at: <https://repository.upenn.edu/edissertations>

 Part of the [Biomedical Commons](#), [Electrical and Electronics Commons](#), and the [Molecular Biology Commons](#)

Recommended Citation

Yelleswarapu, Venkata Ravitheja, "Miniaturizing High Throughput Droplet Assays For Ultrasensitive Molecular Detection On A Portable Platform" (2019). *Publicly Accessible Penn Dissertations*. 3297.
<https://repository.upenn.edu/edissertations/3297>

This paper is posted at ScholarlyCommons. <https://repository.upenn.edu/edissertations/3297>
For more information, please contact repository@pobox.upenn.edu.

Miniaturizing High Throughput Droplet Assays For Ultrasensitive Molecular Detection On A Portable Platform

Abstract

Digital droplet assays – in which biological samples are compartmentalized into millions of femtoliter-volume droplets and interrogated individually – have generated enormous enthusiasm for their ability to detect biomarkers with single-molecule sensitivity. These assays have untapped potential for point-of-care diagnostics but are mainly confined to laboratory settings due to the instrumentation necessary to serially generate, control, and measure millions of compartments. To address this challenge, we developed an optofluidic platform that miniaturizes digital assays into a mobile format by parallelizing their operation. This technology has three key innovations: 1. the integration and parallel operation of hundred droplet generators onto a single chip that operates >100x faster than a single droplet generator. 2. the fluorescence detection of droplets at >100x faster than conventional in-flow detection using time-domain encoded mobile-phone imaging, and 3. the integration of on-chip delay lines and sample processing to allow serum-to-answer device operation. By using this time-domain modulation with cloud computing, we overcome the low framerate of digital imaging, and achieve throughputs of one million droplets per second. To demonstrate the power of this approach, we performed a duplex digital enzyme-linked immunosorbent assay (ELISA) in serum to show a 1000x improvement over standard ELISA and matching that of the existing laboratory-based gold standard digital ELISA system. This work has broad potential for ultrasensitive, highly multiplexed detection, in a mobile format. Building on our initial demonstration, we explored the following: (i) we demonstrated that the platform can be extended to >100x multiplexing by using time-domain encoded light sources to detect color-coded beads that each correspond to a unique assay, (ii) we demonstrated that the platform can be extended to the detection of nucleic acid by implementing polymerase chain reaction, and (iii) we demonstrated that sensitivity can be improved with a nanoparticle-enhanced ELISA. Clinical applications can be expanded to measure numerous biomarkers simultaneously such as surface markers, proteins, and nucleic acids. Ultimately, by building a robust device, suitable for low-cost implementation with ultrasensitive capabilities, this platform can be used as a tool to quantify numerous medical conditions and help physicians choose optimal treatment strategies to enable personalized medicine in a cost-effective manner.

Degree Type

Dissertation

Degree Name

Doctor of Philosophy (PhD)

Graduate Group

Bioengineering

First Advisor

David Issadore

Keywords

assays, digital, droplet, microfluidics, portable, ultrasensitive

Subject Categories

Biomedical | Electrical and Electronics | Molecular Biology

MINIATURIZING HIGH THROUGHPUT DROPLET ASSAYS FOR ULTRASENSITIVE
MOLECULAR DETECTION ON A PORTABLE PLATFORM

Venkata Ravitheja Yelleswarapu

A DISSERTATION

in

Bioengineering

Presented to the Faculties of the University of Pennsylvania

in

Partial Fulfillment of the Requirements for the

Degree of Doctor of Philosophy

2019

Supervisor of Dissertation

David Issadore

Associate Professor, Bioengineering

Graduate Group Chairperson, Ravi Radhakrishnan

Dissertation Committee

Christopher Fang-Yen, Associate Professor of Bioengineering and Neuroscience

Arjun Raj, Associate Professor, Penn Bioengineering

Daeyeon Lee, Professor of Chemical and Biomolecular Engineering

Ronald Collman, Professor of Medicine, University of Pennsylvania School of Medicine

MINIATURIZING HIGH THROUGHPUT DROPLET ASSAYS FOR ULTRASENSITIVE
MOLECULAR DETECTION ON A PORTABLE PLATFORM

COPYRIGHT

2019

Venkata Ravitheja Yelleswarapu

This work is licensed under the
Creative Commons Attribution-
NonCommercial-ShareAlike 3.0
License

To view a copy of this license, visit

<https://creativecommons.org/licenses/by-nc-sa/3.0/us/>

ACKNOWLEDGMENT

Grad school and getting the PhD was fun, despite many stressful valleys of death for experiments and research ideas! I want to thank Chris, Arjun, Daeyeon, and Ron for their advice during the proposal and committee meeting on how to steer the experiments. My grad school experience would not have been as amazing without Dave as my adviser. I am grateful Dave inspired me without ever forcing or stressing me out, but by setting an example to work hard even after his tenure. Though I was nervous sitting next to him in lab my first year, I liked the constant feedback and his interest in my research. Outside of academics, Dave was a part of building my non-academic interests such as running, creating a startup, debating politics, playing piano, cooking advice and overall having a work life balance that made grad school enjoyable.

I would like to thank Microsoft for giving me the confidence early on in my PhD by selecting me for their fellowship, and enabling me to attend several international conferences with their travel grant which was extremely useful in my development as a global citizen. Chip Diagnostics and IPGroup were instrumental in helping me understand research translation, and I am thankful to Dave/Nena/Josh for allowing to sit in on board meetings and learn commercialization strategies.

I would also like to thank the lab as a whole. I will miss sitting in my bay (napping at times), and chilling on weekends (Nishal/Jess/Zijian). I enjoyed our surprise birthday celebrations, going to conferences from Italy to Hawaii, to eating giant plates of dosas and nachos. Jozi lab meetings were certainly exciting. Outside of lab, I always felt I could talk/vent with my close college friends and Nishal/Meagan/Jess/Sonia/Mike, and am glad they put up with my awkwardness. I will miss our group lunches, and genuinely thank you for helping me grow as a person.

Finally, and most importantly, I would like to thank my family for supporting me every step of the way. My brother was my role model growing up, and my parents' sacrificed so much for an opportunity to succeed, which I can never repay them for. Despite all their sacrifice, they never forced me to study, and I got to play video games and relax, and choose to work hard when I wanted to learn and follow my passions. I feel lucky to have so much support from friends and family, who have made it possible for me to chase my ambitions.

ABSTRACT

MINIATURIZING HIGH THROUGHPUT DROPLET ASSAYS FOR ULTRASENSITIVE MOLECULAR DETECTION ON A PORTABLE PLATFORM

Venkata Yelleswarapu

David Issadore

Digital droplet assays – in which biological samples are compartmentalized into millions of femtoliter-volume droplets and interrogated individually – have generated enormous enthusiasm for their ability to detect biomarkers with single-molecule sensitivity. These assays have untapped potential for point-of-care diagnostics but are mainly confined to laboratory settings due to the instrumentation necessary to serially generate, control, and measure millions of compartments. To address this challenge, we developed an optofluidic platform that miniaturizes digital assays into a mobile format by parallelizing their operation. This technology has three key innovations: 1. the integration and parallel operation of hundred droplet generators onto a single chip that operates >100x faster than a single droplet generator. 2. the fluorescence detection of droplets at >100x faster than conventional in-flow detection using time-domain encoded mobile-phone imaging, and 3. the integration of on-chip delay lines and sample processing to allow serum-to-answer device operation. By using this time-domain modulation with cloud computing, we overcome the low framerate of digital imaging, and achieve throughputs of one million droplets per second. To demonstrate the power of this approach, we performed a duplex digital enzyme-linked immunosorbent assay (ELISA) in serum to show a 1000x improvement over standard ELISA and matching that of the existing laboratory-based gold standard digital ELISA system. This work has broad potential for ultrasensitive, highly multiplexed detection, in a mobile format. Building on our initial demonstration, we

explored the following: (i) we demonstrated that the platform can be extended to >100x multiplexing by using time-domain encoded light sources to detect color-coded beads that each correspond to a unique assay, (ii) we demonstrated that the platform can be extended to the detection of nucleic acid by implementing polymerase chain reaction, and (iii) we demonstrated that sensitivity can be improved with a nanoparticle-enhanced ELISA. Clinical applications can be expanded to measure numerous biomarkers simultaneously such as surface markers, proteins, and nucleic acids. Ultimately, by building a robust device, suitable for low-cost implementation with ultrasensitive capabilities, this platform can be used as a tool to quantify numerous medical conditions and help physicians choose optimal treatment strategies to enable personalized medicine in a cost-effective manner.

TABLE OF CONTENTS

ACKNOWLEDGMENT	iii
ABSTRACT	iv
LIST OF ILLUSTRATIONS	viii
CHAPTER 1: INTRODUCTION	1
1.1 Need for ultrasensitive, multiplexed assays in diagnostics	1
1.2 Current techniques for diagnostics	5
1.3 Digital Assays	7
1.4 Point of Care Diagnostics	20
1.5 Challenges with current systems	22
CHAPTER 2: Ultra-High Throughput Detection (1 Million Droplets / Second) of Fluorescent Droplets Using a Cell phone Camera and Time Domain Encoded Optofluidics.....	27
2.1 Abstract.....	27
2.2 Introduction	28
2.3 Methods.....	33
2.4 Discussion.....	51
2.5 Supplementary Information	54
2.6 Supplimentary Code.....	58
CHAPTER 3: Mobile Platform for Rapid Sub pg/mL, Multiplexed, Digital Droplet Detection of Proteins	86
3.1 Significance Statement	86
3.2 Abstract.....	86
3.3 Introduction	87
3.4 Results and Discussion	92

3.5 Conclusion	104
3.6 Methods and Materials	106
3.7 Supplementary Material	109
3.8 Supplementary Code	116
CHAPTER 4: Magnetic Nickel iron Electroformed Trap (MagNET): A master / replica fabrication strategy for ultra-high throughput (> 100 mL/hr) immunomagnetic sorting	136
4.1 Abstract	136
4.2 Introduction	137
4.3 Methods	142
4.4 Results	146
4.5 Discussion	157
4.6 Supplementary Information	160
CHAPTER 5: Multicolor Detection of Fluorescent Droplets on a Cell Phone using Time Domain Encoded Optofluidics	164
5.1 Introduction	164
5.2 Background	165
5.3 Methods	167
5.4 Results and Discussion	168
CHAPTER 6: Future work	176
6.1 Digital PCR	176
6.2 Higher order multiplexing for ddELISA	185
6.3 Washless ddELISA	190
6.4 Nanoparticle enhanced ddELISA	192
REFERENCES	195

LIST OF ILLUSTRATIONS

Figure 1.1 Traditional vs Digital Assays.

Figure 1.2: Miniaturizing bulky equipment into an integrated, portable platform.

Figure 2.1. (microdroplet Megascale Detector) μ MD Implementation

Figure 2.2. Signal Analysis Workflow.

Figure 2.3. μ MD Chip Design

Figure 2.4. Modeling and Simulating the μ MD.

Figure 2.5. Experimental Validation of the μ MD's Key Features.

Figure 2.6. Characterization of the μ MD's Performance.

Supplementary Figure 2.1: Software Image Correction.

Supplementary Figure 2.2: μ MD App for Cloud computing.

Supplementary Figure 2.3: Velocity Distribution.

Figure 3.1. Miniaturization and parallelization of droplet (digital enzyme-linked immunosorbent assay) dELISA.

Figure 3.2. Integrated μ MD workflow.

Figure 3.3. Software workflow for multi-color phase and velocity invariant optofluidic fluorescence droplet detection.

Figure 3.4. Flow rate invariant droplet generation using step emulsification generate droplets of the same diameter.

Figure 3.5. Benchmarking and characterization of ultrasensitive, duplex protein detection in complex media.

Figure 3.6. The measurement of endogenous protein in human serum.

Supplementary Figure 3.1. 3D design of chip.

Supplementary Figure 3.2. Design of μ MD mobile device.

Supplementary Figure 3.3. Mixing of aqueous phases.

Figure 4.1. High throughput immunomagnetic sorting with the Magnetic Nickel iron Electroformed Trap (MagNET).

Figure 4.2. Master / replica fabrication of MagNET.

Figure 4.3. Finite element simulations of MagNET.

Figure 4.4. Characterization of the MagNET using microbeads.

Figure 4.5. Characterizing MagNET's ability to sort tumor cells from leukocytes.

Figure 4.S1. Characterization of polyimide pillars on the master and during electroformation.

Figure 4.S2. Bead distribution capture rate on the top and bottom surface of each MagNET filter in stacked devices.

Figure 4.S3. MagNET Device Fabrication

Figure 5.1. Design Strategy of our Multiplexed (μ MD).

Figure 5.2. Components and dyes were selected to separate the excitation and emission spectra for each of the LED/dye combinations to prevent crosstalk.

Figure 5.3. Software Workflow for Phase and Velocity Invariant Detection of fluorescent droplets.

Figure 5.4. Simulation for Multicolor Detection.

Figure 5.5. Experimental Verification of μ MD.

Figure 6.1. Comparison of traditional and digital PCR.

Figure 6.2 Components and workflow for integrated digital PCR.

Figure 6.3 Heating component for on chip isothermal amplification.

Figure 6.4. Rapid on chip thermal cycling.

Figure 6.5 Higher order multiplexing strategy.

Figure 6.6 Color-coded beads resolved in μ MD.

Figure 6.7 Schematic of washless ELISA.

Figure 6.8 Enhancement from nanoparticle based digital ELISA.

CHAPTER 1: INTRODUCTION

1.1 Need for ultrasensitive, multiplexed assays in diagnostics

Effective healthcare relies on the ability to treat patients based on symptoms that differentiate healthy patients from those that are at risk for certain conditions or are in a state of disease. Since treatment can be expensive, and comes with side effects, it is paramount that diagnosis must be accurate. Diagnostic sensitivity measures the proportion of correctly classified patients with disease as having a disease, while specificity measures the proportion of healthy patients who receive a negative result. While these are binary measures, predictive values give probabilities that these classifications are truly accurate. Diagnosis can be done by checking physiological features such as heart rate; removing tissue and checking for any abnormalities; various forms of imaging; and liquid biopsies. Of these, liquid biopsy^{1,2} shows immense potential since measuring basic physiological features do not provide enough information to classify patients accurately, while techniques like needle biopsy can be expensive, painful, and time consuming³. In addition, tests that require lab-grade facilities require patients to travel, creating a burden on how frequently these tests can be administered.

Liquid biopsies focus on sampling body fluids and testing these for target biomarkers that may indicate the condition of the patient⁴⁻⁷. Liquid biopsies can be more practical than techniques like surgery, magnetic resonance imaging, CT scans, etc. since a blood draw can be administered routinely, is inexpensive, less painful, and time efficient. The convenience also makes it possible to track patients through multiple stages of screening and treatment to verify that treatment is working effectively. In

addition to blood, samples as saliva, sputum, urine, and cerebral spinal fluid also contain vast resources for biomarkers.

One technique that is employed is to search for the presence of target material that would only be present if a patient is infected. This strategy works in infectious diseases like HIV^{8,9}, where a single virus particle circulating in blood indicates infection; or cancers where rare tumor cells start to appear in the bloodstream that would otherwise not be there¹⁰. Conditions where the target concentration is extremely low – ~a few particles/mL of sample – require large patient sample volumes, since detecting rare molecules in a finger prick of blood would also mean that there is a high probability that the finger prick would not even contain the target. Therefore, it is crucial to collect volumes as large as 10mL and screen this entire sample for rare circulating tumor cells, or virus particles to catch them at early stages. In addition, drug treatments that may not have completely eradicated cancer or HIV can be monitored frequently, which is not practical via tissue biopsy or imaging.^{9,11,12} By monitoring frequently, any signs of remission can be addressed immediately before cancer cells can metastasize or infectious pathogens spread latently to other regions of the body.

While detecting rare targets that are only present in diseased conditions is ideal, this may not be practical due to specificity issues, or lack of knowledge of physiological conditions. Instead, biomarkers that are normally present in healthy individuals can either increase or decrease in response to changing physiology, which can also be measured to indicate disease^{13–15}. For example, in traumatic brain injury (TBI), biomarkers panels have not been fully established that link specific proteins or nucleic acids to conditions like concussion. Instead, if it is observed that cytokines or exosomes are responding to a TBI condition, it is useful to measure the concentrations of these

over several time points before classifying a patient for treatment⁴. Therefore, liquid biopsies also can be a strategy for drug discovery since large panels of biomarkers between known healthy and diseased patients can be studied to find biomarkers with the most fold change, and then use these in diagnosis.

In order to catch early onset of certain diseases, ultrasensitive detection is necessary¹⁶. miRNA and proteins previously thought to be of little importance can in fact have a lot of information in them¹⁷. Since traditional assays cannot measure these low concentrations accurately, the “right” biomarkers for disease may never be found without the proper tools. As ultrasensitive assays are being developed, proteins once thought to not provide any value in diagnostics such as PSA in prostate cancer, have shown promising diagnostic value when measured at lower limits of detections¹⁷. Furthermore, ultrasensitive detection enables trace molecules that could not be measured to now provide valuable information.

Ultrasensitive technology is driving development of biomarker panels as miRNA, mRNA, exosomes, and proteins are being mapped onto various conditions such as pancreatic cancer¹⁰, HIV¹⁸, Alzheimer’s¹⁹, cancers, TB, cytokines²⁰. In pancreatic cancer, a single base mutation in the KRAS gene could be detected in the background of ~200,000 copies of nonmutated genes, enabling incredible sensitivity to catch mutations early in blood¹⁰. In HIV, capsid protein p24 measurements showed similar limit of detection to nucleic acid amplification^{8,18}. With 2000 p24 molecules per HIV particle as opposed to two copies of RNA, ultrasensitive immunoassays could potentially replace the need for more equipment-dependent polymerase chain reaction (PCR). For Alzheimer’s, measurements of change in Neurofilament light chain (NfL) proteins over a ten year period showed predictive value compared to just the absolute quantity¹⁹. This

study highlights that while detecting concentrations is important, the rate of change is critical, which is only possible if inexpensive, convenient assays are available for use in the clinic. Blood tests for tuberculosis are currently in development that combine four host proteins measurements with machine learning with 80% sensitivity and 65% specificity when compared with TB-like diseases²¹, showing potential for blood-based diagnostics but also lots of room to improve. Lastly, measurement of multiple cytokines have implications in diseases ranging from brain injuries, cancers, and infection.²⁰

Clinical studies have also shown that one biomarker is not enough to classify patient groups. Complex diseases mean that heterogeneous patients will display different biomarker levels, which will also vary over time in the same individual. To make this even more complicated, cells are heterogeneous and using a single biomarker as a diagnostic often risks having low specificity²². Diagnosing cancer improves significantly when combining biomarkers that may not be related to each other or one's that may follow separate trends among patients²³. TBI measurements have shown that some biomarkers change immediately in response to an insult, while others respond later^{24,25}, indicating diagnosis can also indicate the progression of disease. While DNA and RNA changes are routinely measured with sequencing technologies, they might not paint entire picture without proteins and epigenetic information that can further illustrate what is happening on a physiological level²⁶.

Lastly, laboratory facilities are important for developing new technologies, but if these new powerful technologies can never be implemented in resource-poor areas or in the field, there will be less impact for the diagnostic value. In order to develop meaningful point-of-care technologies, the ASSURED (affordable, sensitive, specific, user-friendly, rapid and robust, equipment free, and deliverable to users) criteria lists out

several features that make technologies adaptable in the field²⁷. Therefore, an ideal device would follow these ASSURED criteria, offer ultrasensitive detection, contain sample prep on chip, and be able to detect a panel of biomarkers to maximize its impact.

1.2 Current techniques for diagnostics

Blood based diagnostics enables several advantages discussed above, but also has a unique opportunity for diseases where other techniques often find the symptoms too late^{4–7}. For example, in cases like Tuberculosis, while sputum and cell culture are known to be the widely adopted methods for clinical testing, a problem arises in getting access to sputum. For young children, it becomes difficult to force them to cough up large amounts of sputum and then grow these cultures out for over a week²⁸. Similarly, in cases like pancreatic cancer, imaging is often too late to find tumors before they have already metastasized, so the survival rate is ~5% despite major advances in imaging techniques²⁹.

Blood-based tests that have shown practical uses in the clinic, as well as point of care assays that can be purchased without the need for a medical expert. These range in complexity from laboratory facility limited equipment that can scan for many biomarkers but require a trained expert to run; to simple at home blood prick tests that change color to indicate the disease status. The simplest of blood based diagnostics are those based on paper, or later flow assays^{30–32 33}. These assays change color or create an easy to read qualitative mark in the presence of a biomarker – and are used widely in at home self-care tests for pregnancy and diabetes. Some come with portable readers that can somewhat quantify the color change or other properties by having optical or electrochemical biosensors. However, these types of devices require that a sample is concentrated, abundant in a small sample volume, and does not require precise

quantification of change in levels. Nonetheless, several companies have built commercial platforms such as Alere (HIV/AIDS), Claros Diagnostics (urological, infectious disease), Cepheid (respiratory infections), Daktari (HIV/AIDS), Abbott i-STAT (coagulation, blood chemistry, cardiac markers) to address these needs³⁴. While techniques have been developed to concentrate molecules in targets with paper or other materials, or even purify serum or plasma from the rest of the blood³⁵, these tests still do not have the sensitivity for ultrasensitive detection.

In order to achieve more quantitative measurements, techniques such as flow cytometry exist, where cells or beads that capture target biomarkers are then labeled with fluorescent tags and pass through multiple lasers, each then read out by photodetectors after emitted light passes through many optical elements^{36,37}. These types of systems have great precision since the lasers generate sharp excitation wavelengths, optical elements separate emission light into multiple wavelengths, which are then read out by sensitive photodetectors. Flow cytometers can thus cover a large dynamic range, measure multiple colors simultaneously and even detect the size and makeup of particles from the side and forward scatter. Recently, imaging flow cytometry combines images of particles and implements machine learning to combine what is fluorescently detected with image data, allowing more precise morphological measurements to be taken³⁸. Combined with sorting, these workflows offer flexibility, precision, and accuracy. However, flow cytometry suffers from low adoptability in resource-poor settings due to their size, cost, training required, and the low throughput nature since the particles are often filed one by one through a focused laser spot.

In order to address fluorescent readouts that require expensive equipment, several other approaches to biosensors have been built that are based on graphene³⁹,

plasmonic sensors⁴⁰, micro-Hall detectors⁴¹, and nanopore sequencing⁴². While these biosensors have shown great promise in multiple human samples for various diseases, the specialized nature of fabricating them makes them hard to scale up, manufacture, and replicate in various lab settings. Therefore, simplicity is also a requirement that ensures simple fabrication strategies, limited steps for protocols, and limited use of complex engineering techniques if a chip is to be manufactured en masse for portable environments.

1.3 Digital Assays

While the above assays have made enormous strides in liquid biopsies, many still lack the sensitivity for detecting single molecules in the background of billions of nontarget molecules. Trying to detect single molecules in bulk volumes is nearly impossible since nonspecificity and diffusion of fluorescent molecules will generate only a weak signal. Trying to detect one molecule in a 100 μL sample (as is often used for traditional assays) means that the target molecule can diffuse into the entire space. If any fluorescence is to be measured from the molecule, or any reaction that amplifies the reaction such as polymerase chain reaction (PCR) or enzyme-linked immunosorbent assay (ELISA), the product to be measured would diffuse in this vast space (**Fig 1.1a**). The concentration of a single molecule in that space would be 2×10^{-20} M, which would make it extremely difficult to distinguish between a true positive and a blank sample.⁴³ Additionally, what if there are billions of other off target molecules in the sample? Since typical K_d of antibodies are in the range of μM to nM range⁴⁴, this would mean that even with the specificity of a sandwich ELISA, the 2×10^{-20} M protein concentration would result in a false positives or false negatives even with the strongest binding affinities. This also does not improve significantly if there is amplification since the same amplified

molecules can diffuse freely, so the signal would not be concentrated. In addition, any generated signal would be hard to quantize into single molecules since the difference between zero, one, two, ten, so on in 100 μL would look nearly identical in most detection strategies (**Fig 1.1a**). The reason conventional assays such as qPCR and ELISA are unable distinguish between individual copy numbers is that the initial concentration is calculated by using calibrator curves. These calibrator curves are used as a reference, but the threshold settings used to compare the values are either empirically or subjectively determined, causing a major source for variation. In addition, in large samples low target copies are dominated by background signal that is much larger than the fluorescence of a single target copy⁴⁵ (**Fig 1.1a**).

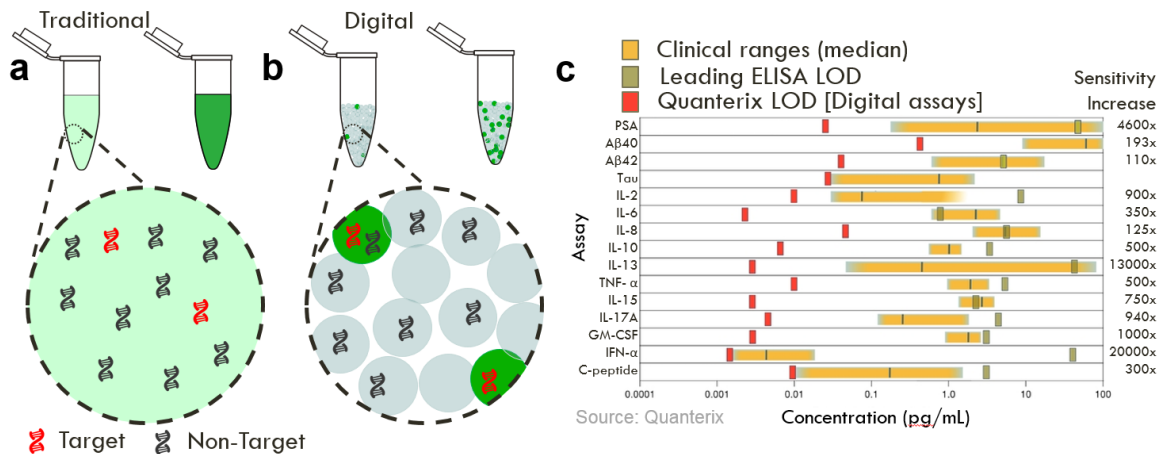


Figure 1.1 Conventional Analog vs Digital Assays. **a.** In conventional analog assays, the change between a negative sample and those with trace amounts of target molecules are hard to distinguish. **b.** When the sample is compartmentalized either into droplets or static arrays, the effective concentration increases by many orders of magnitude, and the fluorescent substrate is concentrated. In addition, these compartments contain a single target molecule or none, allowing them to be counted for absolute quantification as opposed to compared to standards. **c.** The limit of detection of

state-of-the-art ELISA assays can be above the clinical range needed, making it impossible to measure physiological concentrations of these relevant proteins. Quanterix's digital ELISA, has shown up to 10^4 increase in several proteins by using digital assays.

To overcome the challenges of conventional ELISA assays, digital approaches have been developed.. While different strategies have been employed for portioning a sample ("digitize"), the result is that the individual molecules are confined into solutions that are on the order of \sim fL in volume. Thus the same molecule that was in 100 μ L, when placed into fL volumes would be 2nM, or 10^{11} more concentrated. The resulting higher concentration means molecules are confined and more easily observed, with the additional benefit that by partitioning a volume into these tiny compartments, most will only contain either one or zero target molecules based on distribution based on Poisson statistics⁴⁶ (**Fig 1.1a**). In addition, the background competition is also significantly reduced, reducing signal from background molecules. Rather than relying on quantifying the change in fluorescence, digital assays measure endpoints. If a compartment is fluorescent, it signifies a single molecule. Counting the number of fluorescent compartments gives a count of total target molecules without the need for standards or an analog readout, making this technique robust. Digital assays have demonstrated enormous improvements in sensitivity with over 10^4 -fold improvements in several biomarkers (**Fig 1.1b**). There are three main methods to perform digital assays: static arrays, electrowetting on dielectric (EWOD) surfaces to manipulate droplets, and continuous flow droplets.

1.3.1 Static Arrays

Static array digital assays use compartments that are separated by physical barriers or by dispersing liquid into emulsions separated by a continuous phase of oil, and are often the simplest to build due to the lack of moving fluids. The sample is placed into these compartments through gravity, centrifuging sample into tiny wells, applying pressure on top of wells to force the sample into the thousands of wells, or using fluidic paths to seal wells and ducts after loading reagents. Several strategies use self compartmentalization⁴⁷ or reagent introduction into wells that are then sealed and observe such as the SlipChip⁴⁸. One particular strategy that has been developed into a commercial platform is the Quanterix's Single Molecule Array (Simoa) ⁴⁹, which began as with etched glass fiber wells and evolved to manufacturing using Bluray technology to create multiple 250k wells regions on a disc⁵⁰. This technique is used for bead-based protein capture, where beads that have captured single protein molecules and are labelled with enzyme will cause a well to fluorescence. A CCD camera measures fluorescence and calibrates for crosstalk into empty wells, and detect multiple colored beads simultaneously.

Other techniques create water in oil emulsions, which contain the sample and reagents which are then injected into a reservoir chip that acts as a viewing platform, where these emulsions spread out in a monolayer and can be observed for fluorescence over time⁵¹. The advantages of static arrays are that they are often image based, since the endpoint of the reaction is measured after the reagents are sealed into an array. This allows for long integration times that can be overlaid with several optical filters to generate images for multiple color, that can be used to identify multiple biomarkers. Image based detection can potentially enable lower grade cameras such as cell phone cameras if the number of compartments fit the pixel resolution of the camera – again

demonstrating the tradeoff between hardware complexity and dynamic range of a target biomarker to be measured. Static arrays are often simpler to build since the fluid sits inside wells without moving, and do not require precise pumps but still require machines like centrifuges, careful pipetting, etc. The main drawback of static arrays is that they are limited by the number of compartments that can be imaged to fit onto a chip. Therefore, the sample volume is limited since it must fit in the volume of the compartments, thus sacrificing dynamic range. To address this issue, techniques such as the Simoa can measure multiple targets in a single well by correcting for Poisson encapsulation probabilities to back calculate the initial concentration. In addition, once the wells become increasingly full, the overall fluorescence from the entire array can be measured and compared to a calibration curve to measure both digital and analog⁵².

1.3.2 Digital Microfluidics based on Electrowetting on Dielectrics (DMF on EWOD)

Certain reactions call for the complex steps that include introduction of reagents and wash steps that cannot be addressed if the compartments are isolated. While pico-injectors for continuous flow droplet systems and workflows exist for exchanging liquids between steps in arrays, these still do not allow the user to manipulate the volumes with much control. Digital Microfluidics (DMF)^{36,38,53} was developed to have precise control over how droplets move and have complex liquid handling protocols automated by addressing each droplet individually. The spatial position is controlled through electrowetting by having insulating layers on electrodes that separate them from the liquid on top. While electrowetting on dielectric surfaces is most common, approaches also exist that use acoustic waves, magnetic force, optical wetting, and thermal gradients. Furthermore, the droplets can be sandwiched on both sides, or be open so that color and fluorescent properties can be measured from the open side. Once

programmed, these multistep protocols obviate the need for human intervention since the spatial position can be controlled precisely. The advantages of this technique include monitoring droplets over time and keeping track of location of each droplet and mixing conditions. Applications where such precision are required include chemical synthesis,

However, the dynamic range again is limited since typical assays run up to tens of droplets in parallel, and the droplets tend to be larger in size (μL to 100 nL)⁵⁴. Since the force applied to move the droplets is on the order of seconds, operations on DMF are typically in the Hz range, which limit how quickly reactions occur⁵⁴. Additionally, fabrication often involves more complex steps compared to soft lithography of droplet microfluidics, or well based approaches for static arrays. Thus, the dynamic range is smaller, and multiplexing becomes more complicated to scale, making the system low throughput. This makes DMF more difficult as a diagnostic platform since a wide range of biomarkers and dynamic range from rare to concentration targets cannot be measured simultaneously.

1.3.3 Continuous flow high throughput droplet systems

Continuous flow high-throughput droplet systems use thousands to millions of droplets that are generated, incubated while a reaction takes place, and then observed after. These droplets can be manipulated through merging, sorting, splitting⁵⁵; or used to create complex particles such as two faced Janus particles or cured using several chemical approaches like UV to create nanoparticles^{54,56}. In diagnostics, the tiny volumes afford better heating, mixing, increasing the concentration of particles, encapsulating primarily one or zero target molecules for strong signal to background

separation, and allow lower reagent consumption for running millions of experiments in parallel.^{57–61}

Continuous flow droplets offer several advantages over arrays and DMF, in that millions of droplets can be measured – enabling large dynamic range and sensitivity with no limit on sample size. In addition, the liquid-liquid interface as opposed to walls also provides benefits. With the proper surfactants, these interfaces can reduce enzymes, nucleic acids, and targets from sticking to surfaces and thus reducing sensitivity⁶². Since these droplets are encapsulated in oil, they are at a lower risk of drying from exposed air, since static arrays in several oils have shown to exchange gases and evaporated out⁵¹. In addition, since the channels where droplets travel through after they are generated are not fouled, the risk of contamination also reduces since the dispersed liquid inside the compartment never makes contact with walls, which also allows chips to be reused^{63,64}.

1.3.4 Applications of Digital Assays

Diagnostic digital assays are primarily used to amplify nucleic acids through PCR, or proteins through ELISA. If droplets need to be analyzed further in cases such as single cell sequencing applications, or to process only droplets of interest to save reagent costs, the droplets can be sorted for further downstream analysis.

Table 1.1 – Digital PCR Technologies

Ref.	Throughput	Droplet Volume	Method of Thermal	Method of Detection
On Chip Heating				
Hatch ⁵¹	125 to 250 k/s based on 4-8s exposure	50 pL	Thermoelectric Cooler, Copper, Si wafer, PDMS	Wide field 21 MP DSLR camera

Schaerli⁶⁵	Flow rates ~ 160 ul/h; 4.7*10 ⁶ /mL	40um to 150um; 33.5 pL to 1.76nL	Peltier module with copper rod at center; spatial	Droplets were collected, opened for gel electrophoresis
Beer⁶⁶	Generate 1k/s and then stop while it cycles.	10 pL	Peltier temporal heating	Nikon microscope w/ 5k fps camera.
Kiss⁶⁷	500/s	65 pl; observed 14k droplets per cycle at 11 points	Spatial heating; two heaters at 95 and 65c zone; 55 s cycles/ 35 min	Droplets flash frozen and analyzed on gel and fluorescence microscope
Terazono⁶⁸	2.2k/3.5 min	20-30um droplets made with micro- pipetting 10- 30uL at a time	Single monolayer of droplets heated w/ IR laser; 3.5min for 50 cycles	Inverted microscope, laser,
Off Chip Heating				
Biorad	1.92 mL can be loaded on thermocycler at once	1 nL; 1 k/s	Off chip thermocycler	Dual laser
Raindance	400 µL sets	5 pL; 1 k/s		Dual laser
Isothermal				
Rane⁶⁹	1M/110 min; 10uL per 110min	8 pL; 1-2 ms/droplet	Peltier heater with water cooling	Custom built optical dual fluorescence
Li et al ⁷⁰	27,000	314 pL Static array	Peltier heater with copper chamber, PWA chip, and glass; 10 min... 30 min for entire procedure at 39C	Wide field image microscopy
SlipChip⁴⁸	1550 reaction wells	9 nL each; 1550 wells/hr	39C on flat metal adapter; plate reader with temperature controlled at 25°C. 1 hr at 39C, 30 min at 42C	Leica DMI 6000 B epi-fluorescence microscope (Leica Microsystems, Germany) with a 5X / 0.15 NA objective and L5 filter
Schuler⁷¹	Volume calculated from given dimensions: ~30000	0.9048 nL; volume of chamber where droplets form is	Labdisk player with built in heater; 30 min for entire thing	Stroboscopic setup for droplet dia only; fluorescence imaging with Lavion

	120um dia droplets;	27 μ L		bioanalyzer
Kang ⁷²	100 kHz	10 kHz	Red/Green colors;	Rotating cuvette with mini confocal detector for DNAzyme detection

Digital PCR: Digital PCR can quantify specific nucleic acid targets, including DNA, miRNA, and mRNA, by compartmentalizing large volumes into tiny droplets that are then thermocycled for the nucleic acids to amplify (**Table 1.1**). Several approaches exist for RNA amplification, where a heating step is dedicated to first creating cDNA^{73,74}. As the DNA amplifies in the droplets, dyes such as EvaGreen or quenched probes come apart in the presence of amplified DNA, causing a fluorescence readout^{75,76}. Studies have shown that when compared directly with qPCR, ddPCR results are more precise and reproducible. Digital PCR demonstrates much lower variance than qPCR when targets are at low abundance targets, in highly contaminated sample, or when the fold change difference between samples is 2-fold or lower (variance between 7%-30% for ddPCR compared to 60-87% for qPCR in replicates)^{77,11}. Endpoint reactions do not depend on primer efficiency if the final fluorescence is achieved in positive droplets, while in qPCR the fluorescence of the sample can vary significantly based on acceptable primer pairs (90 to 110%). Absolute quantification relies on counting positive droplets, and do not rely on standards for comparison, although most assays run them as quality check⁷⁸.

Digital PCR can also be multiplexed such that a single test volume can be tested for multiple nucleic acids simultaneously^{79 80}. Multiplexing can be achieved by adding additional dyes for each target, however, this becomes limited by the optics and hardware, making each addition more expensive and crosstalk among dyes a larger

issue as more colors are added. Therefore, commercial techniques often use “higher order multiplexing” where the endpoint fluorescence amplitude is used to differentiate target strands.^{79,80} In “amplitude based multiplex assay”, different concentrations of probes are used such that the end point fluorescence depends on this concentration and can identify which target strand is amplified. In order to expand this to multicolor, multiple dyes can increase the number of genes targeted. To scale up practically, each target also has different probe concentrations such that even within one dye, multiple levels of final endpoint fluorescence can be generated based on the probe concentration per specific target. Other techniques also use the fact that since longer strands can potentially bind more EvaGreen, they should be more fluorescent, so while probe concentration remains the same, the endpoint fluorescence will now depend on the target strand length. However, multiplexing comes with a host of issues including probe specificity, competition with other primers, and differential PCR efficiencies^{79,80}. Digital PCR has made its mark on the field for nucleic acid detection and has been adopted for ultrasensitive measurements on nucleic acids, generating \$318 million in 2017 and projected to reach \$1.2B by 2025 (Allied Market Research, 2019).

Table 1.2 – Digital ELISA Technologies

Ref.	LOD	Volume / compartment ments	Device material	Method
Guan ⁸¹	0.88 μ M	4.2 pL/ 200k	PDMS	-Single β -Gal in droplets -Measured rate of fluorescence production
Obayashi ⁸²	7.0 fM	44 fL/ 7600*120 chamber	CYTOP on glass coverslip	-Noted only 2.5% of the substrate was consumed in 20 min with ALP and β -Gal

Rissin ⁴⁴	6 fg/mL (200aM)	50 fL / 50k wells	Glass wells Silicone gasket/oil	Microarray with bead based dELISA
Chang ⁸³	100 vir/mL	50 fL / 50k wells	Simoa array	-Measured number of p24 proteins -Converted to virion count by dividing 2000 p24 proteins/virion Verified with RNA extracted
Shim ⁸⁴	1.2 pg/mL (43 fM)	32 fL / 20k drops	PDMS Glass	-Static array with around 20k droplets analyzed -Low dynamic range -No false positives reported
Leirs ⁸⁵	4 fM in buffer	38 fL / 62.5k wells	Patterned Teflon-Af on glass slides	-Detected nucleoprotein from flu virus in nasopharyngeal swabs to show dELISA in clinical sample
Wilson ⁸⁶	3.8 fg/mL	40 fL /216k wells	Cyclic Olefin Polymer	-Fully automated
McGuigan ⁴⁹	(200 aM)			commercial digital ELISA
Kan ⁸⁷	IL-10	25-50k beads	Bluray Printing	from Quanterix Simoa HD-1 Analyzer
Yelleswarapu ⁸⁸	3.7 fg/mL (300 aM) 7.0 fg/mL (350 aM)	22.5 pL / 10M droplets 1M beads	PDMS and Glass 3D stack	-Integrated mobile platform with parallelized droplet generation and detection with cloud computing

Digital ELISA: In addition to nucleic acids, proteins have enormous potential in measuring the physiological conditions, but traditional ELISA techniques cannot generate the single molecule sensitivity due to background fluorescence of blank samples. To overcome this obstacle, digital ELISA confines single molecules into partitions by first using a bead-based ELISA approach, where antibody-functionalized

beads capture a single protein from the sample by setting the concentration of beads higher than the number of proteins. The unbound sample is washed away, and the captured protein is then labelled with a detection antibody, washed to remove unbound detection antibodies, and then labeled with an enzyme^{43,89}. When these enzymes are present in a partition, the inactive substrate turns fluorescent, and the fluorescent dye and bead are measured together to count the total protein molecules (**Figure 1.1a, Table 1.2**). In PCR, specificity comes from the primers that can bind to very specific target sequences. In ELISA however, any enzyme that is not washed away properly and remains in a well not bound to a bead will cause a false positive. Therefore, there are two critical requirements for developing a successful digital ELISA assay: the sandwich assay between the protein and antibodies must be strong and not dissociate during subsequent wash steps, else it will result in false negatives. Second, excess labeling enzyme must be completely washed away, else it will result in false positives⁴⁴. In bulk, a single molecule in 100 μL is $2 \times 10^{-20}\text{M}$, thus even the best antibodies with low K_d in the nM range would be unable to compete with background protein molecules in serum or plasma that would create false positives from non-specificity issues. But when confined in fL volumes, the 10^{11} higher concentration now allows combinations of antibodies that are in the μM to nM range^{8578443,89}. The bead based approach of capturing a target molecule and labeling it an enzyme can also be accomplished with nucleic acids^{90,91}. A powerful advantage of ELISA comes from its simplicity without the need for thermocyclers – and if the same sensitivity of target molecules in a 100 μL sample can be matched – digital ELISA offers great potential for simpler ultrasensitive detection compared to digital PCR. In addition, multiplexing can be achieved by using color encoded beads with different combinations of dye that each capture a specific protein; creating a higher order multiplexing strategy similar to multiplex digital PCR²¹⁹².

Single Cell Sequencing: More complicated approaches with digital assays also exist that can identify large amounts of heterogeneity. Personalized medicine aims to find these differences in heterogeneity and optimize treatment options. Since droplets allows millions of experiments to be done simultaneously, digital assays with single cell sequencing has evolved to measure cells from large tissues in entire organisms to find variations in how genes are expressed. One popular technique termed “Drop-seq”⁵³ analyzes mRNA from individual cells by compartmentalizing a single cell, lysis buffer and primer barcoded beads into droplets. As cells are lysed, mRNA can bind to the primers. All the droplets are broken to release beads, which go through a reverse transcription process to generate cDNA. This DNA can be amplified and sequenced to measure a large panel of mRNA from single cells. *Tabula Muris* is an example of taking all of the resulting information that was generated from commercial platforms such as Biorad’s digital PCR, 10x Genomics, and sequencing⁹³. These types of parallel assays generate enormous amounts of biological data. The interpretation of this data is still in nascent stages as researchers are using data mining algorithms to eventually map out how genes, proteins, and physiology are all linked to classify patients in different states.

1.4 Point of Care Diagnostics

While digital assays have proven ultrasensitive detection has enormous advantages for early detection and in general understanding physiological conditions, most of these techniques rely on bulky, expensive equipment. Point of care devices eliminate equipment that cannot be used in the field and instead rely on simpler tests that often have a qualitative readout such as a color or turbidity change⁹⁴. The simplest of these are based on paper and use the wicking motion of liquid to flow liquid over a region where a reaction takes place⁹⁵. The most common are lateral flow assays, where antibodies are printed onto a region, and after the sample is introduced, can change color in the presence of a target biomarker. These have been successfully commercialized for pregnancy tests, while other electrochemical sensors are used for glucose measurements with a prick of blood⁹⁶. Point of care devices excel in conditions that have concentrated biomarkers in a small volume, allowing qualitative measurements to provide satisfactory information.

However, most point of care devices cannot provide the quantitative information and the ability to detect rare molecules necessary for many diagnostic applications. Diseases like HIV, cancer, and traumatic brain injury are hard to diagnose using PoC devices since the small fold changes or limit of detection required cannot be achieved through lateral flow assays^{97,98}. Several groups have used inexpensive CMOS cameras with LEDs, and 3d printed casing where a reaction on a microfluidic chip can be observed⁹⁹. A large subset of these have transitioned to the use of smartphone-based readouts, due to their powerful cameras, built in LEDs, computation power, and connection to the cloud to transmit data and results^{100,101}. In addition, smartphone-based

systems have been combined with brightfield, fluorescence imaging, spectroscopy, phase imaging, and multicolor techniques to demonstrate the power of a handheld device that is ubiquitous around the world¹⁰². By combining smartphone-based technology with techniques like machine learning, powerful image analysis and diagnostics have emerged¹⁰³.

Several groups, including our own, have combined the power of smartphone technology with digital assays to achieve ultrasensitive detection in a mobile platform¹⁰⁴. Most groups use static arrays where compartments are made on a simple chip and an LED excitation source is separated from the emission through optical filters. Slip Chip is an example of a microfluidic platform that uses arrays with isothermal amplification, and counts the total number of fluorescent compartments¹⁰⁵. Other readouts such as a rotating cuvette with a laser diode readout was also used for a smaller footprint device, termed the Integrated Comprehensive Droplet Digital Detection¹⁰⁶. While many portable techniques have been developed, they often lack the dynamic range, sensitivity, or integration required for a point of care device with ultrasensitive detection.

1.5 Challenges with current systems

Current digital systems often require that the input sample must be purified or diluted. If the sample is not processed or enriched, volumes required could be as large as 10mL to interrogate for sparse targets that would otherwise be missed if sampling only 100 μ L. For example, in the case of pancreatic cancer, there can be as few as one-three pancreatic cancer cells in the background of billions of other particles in 1 mL of blood^{107,108}. Therefore, to get a confident readout, it is best multiple mL of blood. However, most commercial techniques such as Biorad's digital PCR system, or Quanterix's Simoa often use 100uL of sample as an input for a test. If a large sample is broken up into 100uL aliquots, this would increase the reagent cost and time cost. This becomes an even larger issue in cases like single cell sequencing, where the library prep and costs for processing these large samples for extremely rare cells would be resource intensive. In addition, many of the technologies developed for digital assays took what was available in flow cytometry and applied the same principles to droplets¹⁰⁹. The inherently low throughput nature of generating droplets one by one for analysis for up to 10mL of sample is highly impractical since measuring this volume would take nearly 10h per sample, assuming a 10kHz processing time and 40 μ m diameter droplets. Therefore, parallelization from sample preparation, enrichment, droplet generation, incubation, detection and analysis is mandatory to make digital assays appealing for the most challenging, yet highest impact, applications.

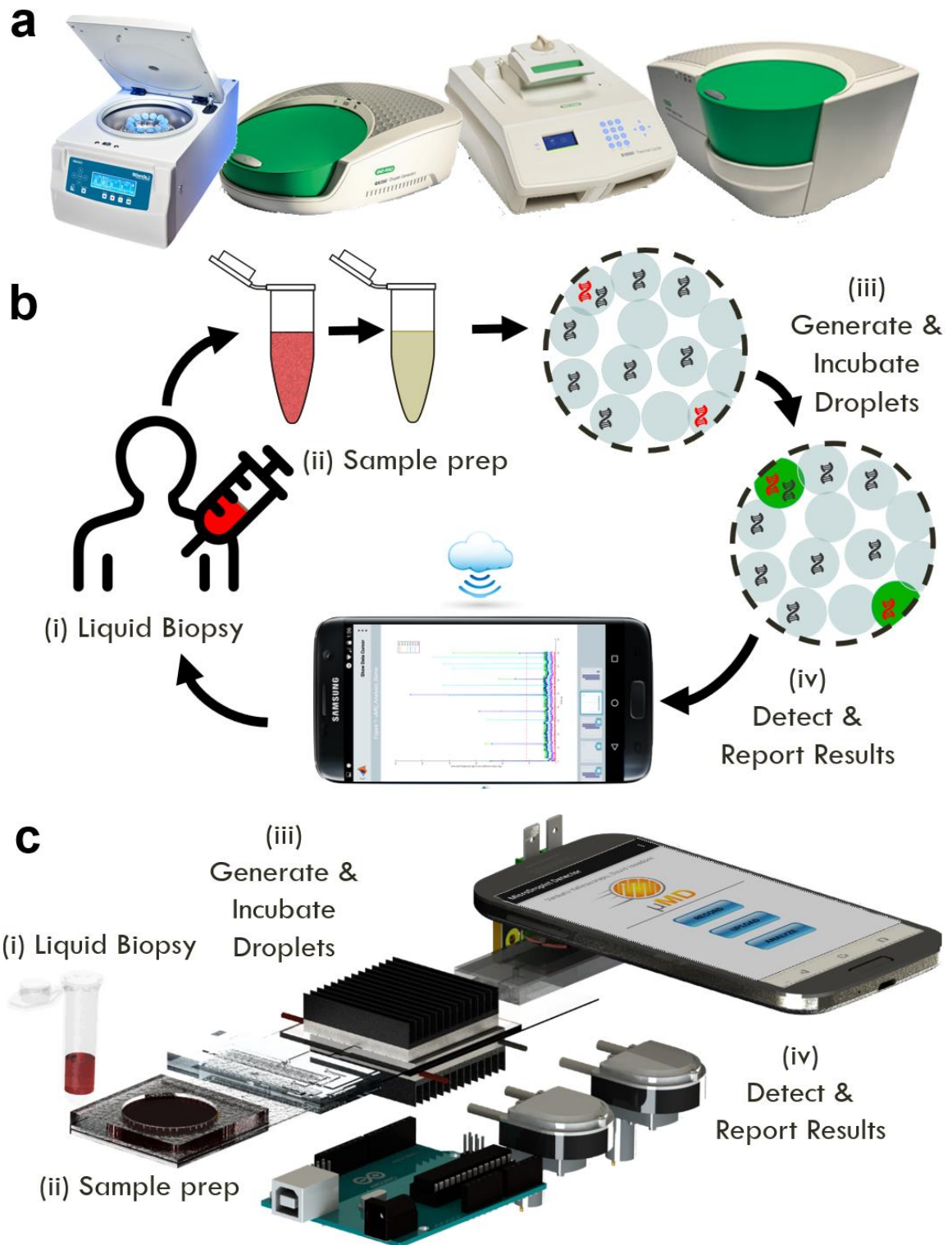


Figure 1.2: Miniaturizing bulky equipment into an integrated, portable platform. a.

The Biorad Digital PCR workflow requires first centrifuging sample to separate plasma or

serum. The sample is then used for the droplet generator, where it is transferred to a plate sealer, and then moved to a droplet detector that is connected to a computer. **b,c.** In order to compress the systems, we have envisioned an ideal device that has a membrane sample processor to first filter out molecules based on size or magnetic sorting. Downstream of the membrane is a 3D chip where droplets are generated, incubated, and detected in parallel. Using a smartphone-based readout with peristaltic pumps, equipment is inexpensive without sacrificing robustness or sensitivity. A true sample in to results out can be displayed on a cell phone with multiplexed, ultrasensitive measurements.

The ASSURED criteria sets the standards for an ideal point-of-care device, and the addition of ultra-sensitivity would be a feature that further extends what could be possible in a portable device. Assay sensitivity, reproducibility, specificity and dynamic range are criteria that can act as quantifiable measures for an ideal device. First, a limit of detection for nucleic acids have already been shown with up to 1:200,000 specificity for single mutated KRAS genes in the background of unmutated genes, showing the capability of digital PCR.¹⁰¹¹⁰ Similarly, zM concentrations of enzymes can accurately be detected through digital ELISA – making droplets ideal platforms due to their inherent robustness and endpoint measurements. Next, specificity in PCR comes from base pair bonding, while in ELISA comes from the binding events between the antibodies and the proteins. A major advantage of amplification inside droplets is that millions of dye molecules can be detected in a small volume – obviating the need for expensive lenses, optical setups, and lasers that are traditionally required for flow cytometry-based approaches.

One of the main tradeoffs in commercially available ultrasensitive assays and those that have been implemented in the field, is that dynamic range is often sacrificed for simplicity¹¹¹. This means that static arrays with a small number compartments can be implemented on simple devices in the field, making more complicated scenarios where multiple biomarkers are at varied concentrations over a 10^3 range becomes difficult to measure without serially diluting samples. However, diluting samples does not always produce a linear effect due to matrix effects¹¹², which can complicate the attempt to serially dilute and run multiple digital assays. If the same sample is broken up into 10^3 droplets as opposed to 10^6 , a positive partition will have a lower signal to background. In addition, lower number droplet assays often employ the use of the Most Probable Number (MPN) algorithm that back calculates the initial concentration based on empty droplets due to statistical filling of positive droplets¹¹³. This means that the absolute quantification of digital assays is lost with a limited number of partitions.

In addition, having the ability to process millions of droplets enables key applications in areas like copy number variation genotyping, detecting of sparse cell free DNA in large samples of blood, low-level viral load and pathogens, and preparing for next generation sequencing libraries.¹¹³ Applications that require multiplexing are also highly limited if the 10k droplets in an assay workflow have to be split by 10 biomarkers and then back calculated, which loses the strengths of digital assays. Furthermore, next gen sequencing and techniques that employ barcoding mechanisms for cells or DNA-tagged antibodies require millions of droplets to cast a wide net for the inherent variability in biological systems¹¹⁴. Since current workflows that can process such large quantities are too expensive and bulky, an ideal device would also be able to process droplets at ultra high-throughput.

Sample prep would have to be integrated such that machines such as centrifuges that require lab facilities are not needed. Next, while many microfluidic chips are small, they often rely on expensive syringe pumps to control flow, or a computer to analyze the results – making them not truly portable. In other scenarios, these microfluidic chips also rely on microscopes, lasers, and optical components that must be fixed precisely, or the imaging becomes impaired. Therefore, another feature of an ideal device is that it is robust to the precision needed for many microfluidic platforms, without requiring expensive pumps or detection platforms. Integration is also critical, since having users transfer samples, collect droplets, and reinject them results in loss and variability between runs. Therefore, a sample to readout device with ultrasensitive detection while being portable can unlock the potential of digital assay from lab facilities to a wider group of researchers and clinicians.

CHAPTER 2: ULTRA-HIGH THROUGHPUT DETECTION (1 MILLION DROPLETS / SECOND) OF FLUORESCENT DROPLETS USING A CELL PHONE CAMERA AND TIME DOMAIN ENCODED OPTOFLUIDICS

This chapter is a slightly modified version of a manuscript published in *Lab on a Chip*:

VR. Yelleswarapu, H. Jeon, S. Yadavali, D. Issadore, Ultra-High Throughput Detection (1 Million Droplets / Second) of Fluorescent Droplets Using a Cell Phone Camera and Time Domain Encoded Optofluidics, *Lab on a Chip*, DOI: 10.1039/C6LC01489E, 2017.

V. Y. conceived and performed all experiments in this study, coded the Matlab software, created the Android app, as well as prepared the manuscript and figures.

2.1 Abstract

Droplet-based assays — in which ultra-sensitive molecular measurements are made by performing millions of parallel experiments in picoliter droplets — have generated enormous enthusiasm due to their single molecule resolution and robustness to reaction conditions. These assays have enormous untapped potential for point of care diagnostics but are currently confined to laboratory settings due to the instrumentation necessary to serially generate, control, and measure tens of millions of droplets. To address this challenge, we have developed the microdroplet Megascale Detector (μ MD) that can generate and detect the fluorescence of millions of droplets per second (1000x faster than conventional approaches) using only a conventional cell phone camera. The key innovation of our approach is borrowed from the telecommunications industry, wherein we modulate the excitation light with a pseudorandom sequence that enables individual droplets to be resolved that would otherwise overlap due to the limited frame rate of digital cameras. Using this approach, the μ MD measures droplets at a rate of 10^6 droplets/sec ($\phi = 166$ mL/hr) in 120 parallel microfluidic channels and achieves a limit of detection LOD = 1 μ M Rhodamine dye, sufficient for typical droplet based assays. We

incorporate this new droplet detection technology with our previously reported parallelized droplet production strategy, incorporating 120 parallel droplet makers and only one set of continuous and droplet phase inputs and one output line. By miniaturizing and integrating droplet based diagnostics into a handheld format, the μ MD platform can translate ultra-sensitive droplet based assays into a self-contained platform for practical use in clinical and industrial settings.

2.2 Introduction

Droplet-based assays, in which microscale emulsions are used as isolated compartments to run many independent chemical reactions, have demonstrated enormous utility in recent years as a platform for the ultrasensitive detection of small molecules, proteins, and nucleic acids^{115–122}. The sensitivity of droplet-based assays arises from the $10^6\times$ reduction in volume from conventional assays ($>\mu\text{L}$) to the volume of individual microscale droplets (pL). However, the enormous increase in sensitivity comes at the expense of cumbersome instrumentation and time-consuming, not fully automated processing ($T \gg 1$ hour for current commercial systems¹²³) to generate, incubate, and measure millions of droplets — including pumps, optics, thermal cyclers, and multiple microfluidic chips. Primarily, this processing time is currently limited by the inherently low throughput rate ($<10^4$ droplets/sec) in which microscale droplets are serially generated and fluorescently detected^{69,124–126}. **(Fig. 1a)**

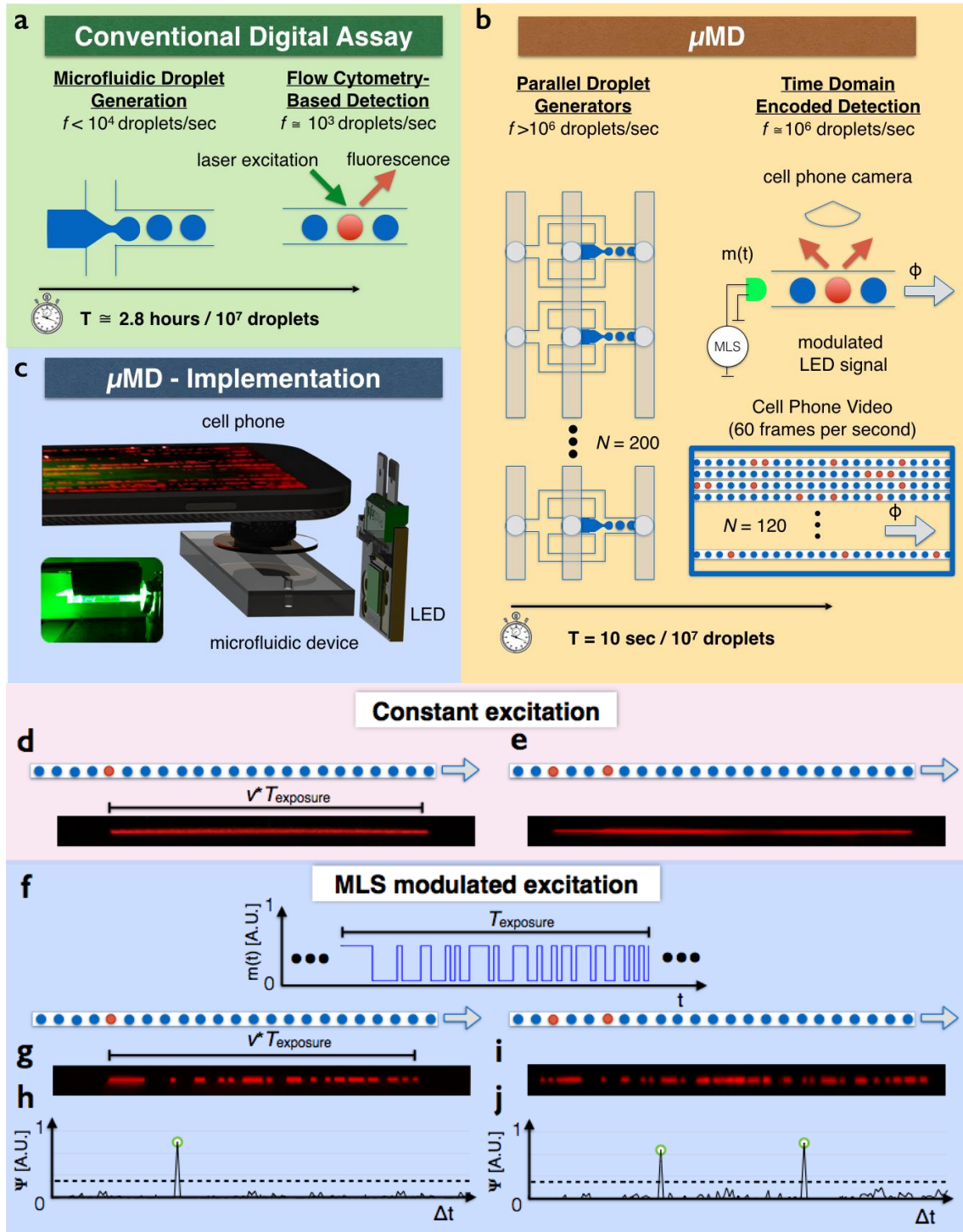


Figure 2.1. μ MD Implementation. a. Conventional digital assays are currently confined to laboratory settings due to the instrumentation necessary to

serially generate, control, and measure tens of millions of droplets, with typical droplet throughput limited to $f \cong 1$ kHz. For a 10^7 droplet experiment, the experiment time is $T \sim 2.8$ hours. **b.** Our μ MD can generate and detect the fluorescence of millions of droplets per second, by parallelizing both the generation of droplets and the detection of droplets to achieve $f = 1$ MHz, resulting in $T = 10$ seconds for a 10^7 droplet experiment. **c.** The μ MD consists of a cell phone, a custom 3D printed piece that contains inexpensive optics, an LED, and a disposable microfluidic chip. **d.** Using conventional excitation that is constant in time, as a droplet travels through a microfluidic channel, it is imaged as a streak that has a length $L_{\text{streak}} = v \cdot T_{\text{exp}}$, where v is the droplet's velocity and T_{exp} is the camera's exposure time, that sets the minimum distance between droplets. **e.** Neighboring droplets closer than L_{streak} have streaks that overlap and cannot be resolved. **f.** The μ MD breaks the tradeoff relationship between droplet spacing and flow velocity v . The LED excitation is modulated

One promising direction to scale-up droplet production and detection has been the development of platforms that make it possible to operate many microfluidic droplet generators and detectors in parallel^{127–131}. Many promising technologies have been proposed in this area^{132–135}. **(Table 1)** Imaging platforms have been designed that can measure as many as 1 million droplets simultaneously¹⁹. In-flow detection systems, in which droplets pass one-by-one through an optical detector can measure a far greater number of droplets than is possible using static imaging, and have the advantage that droplets can be sorted downstream of the detector^{55,136–138}. In recent years, microfluidic-based techniques have been proposed to detect droplets without the need for expensive

lenses, cameras, and lasers, which were conventionally necessary for in-flow detection. In one particularly promising approach, hybrid CMOS/microfluidic chips have been reported that can detect droplets flowing in parallel channels, achieving high throughput detection (254×10^3 droplets/sec) using no lenses¹³⁹. However, these hybrid CMOS/microfluidic approaches are limited by the expense of incorporating centimeter sized post-processed CMOS chips ($> \$10/\text{chip}$)²⁷ into a disposable microfluidic component. Alternatively, devices have been developed in which the light coming from a fluorescent droplet is modulated using microfabricated apertures, enabling parallel streams of micro-scale droplets or cells to be detected using only a single photodetector^{129,140–143}. (Table 1) These approaches, however, are limited to a throughput $< 5\text{k}$ droplets/sec, resulting in > 30 minutes to read out each 10 million droplet-based assay, and require specialized optics, electronics, and micro-lithographically defined apertures on the microfluidic chip.

Table 1 - Technologies to Perform Digital Assays

Ref.	Throughput (Droplets/s)	Dynamic Range (Max Positive Droplets/s)	Sensitivity	Multiplex Capability	Droplet Volume	Method of Detection
This	1 MHz	32 kHz	1 μM Rhodamine	120 ch	22.5 pL	Cell phone Camera
19	125 to 250 kHz at 4-8s exposure	250 kHz	NA	-	50 pL	Wide field 21 MP DSLR camera for digital PCR
20	50 kHz	50 kHz	2.5 μM Fluorescein	25 ch	100 pL	Micro-optical lens array
22	100 kHz	10 kHz	NA	Red/Green colors	8 pL	Rotating cuvette with mini confocal detector for DNAzyme detection
23	200 kHz @ 2mM 6.3 kHz @ 1 μM	200 kHz	1 μM Resorufin	25 ch	4 pL	High speed camera with Fresnel lens
27	254 kHz	12.7 kHz	5 μM Fluorescein	16 ch	40 pL	CMOS sensor with PDMS channels directly on top
30	1.7 kHz	1.7 kHz	10 nM Rhodamine	4 ch	113 pL	Lens free photodetector
Biorad	1 kHz	1 kHz	NA	FAM/VIC or HEX colors	1 nL	Dual laser for digital PCR
Raindance	~1 kHz	1 kHz	NA	FAM/VIC colors	5 pL	Dual laser for digital PCR
Cytometry						
36	1 $\mu\text{L}/\text{min}$	8000 cells/ μL	NA		-	Cell phone imaging at 7 fps to detect SYTO17 stained WBCs
37	20 mL/min	≥ 1 cell/10mL	NA		-	Webcam at 4 fps to detect SYTO-9 labelled monocytes

Building on this previous work, we have developed a new approach to miniaturizing droplet based assays that can achieve a throughput of 10^6 droplets/sec, 1000x faster than conventional methods, using a conventional smartphone camera and inexpensive disposable chips. **(Fig. 1b)** By harnessing ultra-bright LEDs with the sensitivity and computing power of smartphone based imaging and cloud computing^{134,144}, we were able to implement our platform as a self-contained mobile device. **(Fig. 1c)** The key innovation of our approach is modulation of the excitation light in time with a pseudorandom sequence that enables individual droplets to be resolved that would otherwise overlap due to the limited frame rate of digital cameras. Using conventional excitation that is constant in time, as a droplet travels through a microfluidic channel and moves across the camera's field of view, it is imaged as a streak¹⁴⁵ whose length $L_{\text{streak}} = v \cdot T_{\text{exp}}$ is a function of the droplet's velocity v and the camera's exposure time T_{exp} . **(Fig. 1d)** This streak length L_{streak} sets the minimum distance that must be maintained between droplets for them to be resolved. To illustrate this point, for droplets that have a diameter $d_{\text{drop}} = 35 \mu\text{m}$ that are traveling through a typical microfluidic channel (40 μm wide and 35 μm tall) at $\phi = 5 \text{ mL/hr}$, using a typical camera with $1/T_{\text{exp}} = 60$ frames per second (FPS), the minimum separation is $L_{\text{streak}} = 472 \cdot d_{\text{drop}}$. Droplets that are separated by less than L_{streak} are imaged as overlapping streaks that cannot be resolved. **(Fig. 1e)**

The key innovation of our approach breaks the tradeoff relationship between droplet spacing and flow velocity v , allowing the throughput and dynamic range to be dramatically increased. To this end, we modulate the LED excitation with a pseudorandom sequence at a rate $>10\times$ faster than the exposure time of the camera, encoding the droplet streak with a pattern that allows it to be resolved using correlation-

based detection amongst neighboring droplets with a separation as small as $3.5 \cdot d_{\text{drop}}$. **(Fig. 1f)** Moreover, we use the entire field of view of the camera to include 120 parallel channels, enhancing the throughput by a further 120x relative to a single channel. In contrast to previous approaches, which used lithographically patterned apertures to modulate the fluorescent droplet in the time-domain¹²⁹, we can achieve 100x improved throughput and obviate the need for lithographically defined apertures, enabling extremely low-cost implementation that requires no lithography (<10¢/chip)¹⁴⁶. Furthermore, our use of conventional cell phone cameras offers an opportunity for droplet microfluidics to be harnessed for point of care applications due to the ubiquitous availability of smartphones^{144,147,148}. To demonstrate the utility of our platform, we demonstrated extremely high throughput (1M droplets/sec, $\phi = 166$ mL/hr), sensitivity comparable to conventional laser-based techniques (1 μ M resorufin dye)¹³⁶, and a dynamic range of fluorescent droplets:non fluorescent droplets (1:10⁷ to 1:40) that matches the typical dynamic ranges for ultrasensitive digital assays^{149,150}. **(Table 1)**

2.3 Methods

Microdroplet Megascale Detector (μ MD) Design

The key innovation of our μ MD technology is the modulation of the excitation light with a pseudorandom maximum length sequence (MLS). **(Fig. 1f)** This modulation of the excitation light in time translates into a modulation of the image streak in space, **(Fig. 1g)** which allows fluorescent droplets to be detected even amongst other densely packed fluorescent droplets. **(Fig. 1i)** The modulated image is analyzed by correlating the image with the expected modulation pattern m , creating a signal $\Psi(X) = \int S_n(x)m(x+X)dx = S_n \otimes m$, wherein droplets can be resolved with far greater resolution than in the unprocessed image. **(Fig. 1h,j)** We have chosen as our modulation pattern

the MLS sequence because its autocorrelation function approximates a Kronecker delta, thereby allowing the best possible resolution of droplets in the processed signal Ψ . MLS sequences were originally developed for applications in radar and telecommunications,¹⁵¹ and have previously been used in droplet based detection schemes¹²⁹.

To design the optimal MLS sequence for our detection platform, there are two main considerations. First, it is advantageous to include as many bits in the MLS sequence as is possible to minimize the width of its autocorrelation peak. The number of bits is constrained by several key parameters of our smartphone based implementation. The maximum number of bits in the MLS sequence $|m|_{max} = L_{streak}/\Delta x = v \cdot T_{exp}/\Delta x$ is set by the spatial resolution of the camera Δx , the droplet velocity v , and the exposure time of the camera T_{exp} . This value is further constrained by the length of our imaging field of view $L_{FOV} = 12$ mm, which sets the length of the droplet streak L_{streak} that can be imaged. We chose to set $L_{streak} \approx 1/3 \cdot L_{FOV}$, such that each droplet's modulated streak is measured fully in at least one frame. The length of the MLS sequence that we used was $|m| = 63$ bits. One further consideration for our technique is droplet diameter d . If the droplets have a diameter d larger than the resolution of our camera Δx , it sets the minimum bit size in the MLS pattern. In this implementation, we set the droplet diameter to $d = 35$ μm . For the $|m| = 63$ bit MLS pattern that we use, where each bit is ~ 60 μm , the droplet diameter must follow the condition $d < 60$ μm to avoid blurring the MLS pattern.

Signal Extraction

The μMD 's signal analysis workflow is as follows: *i.* the video stream from the cell phone camera is partitioned into individual frames. (**Fig. 2a**) *ii.* The image is digitally filtered, such that only the red component from the RGB image representation remains

and spherical aberrations, which arise from our inexpensive smartphone based optics, are digitally corrected. (**Fig. S1**). iii. Each of the individual 120 microfluidic channels in the image is partitioned, (**Fig. 2b**) and for each channel, the fluorescence intensity is measured along the length of the channel using a line average. Thus, each video frame is converted into 120 one-dimensional vectors $S_{n=1:120}$ of length 1080. iv. For each of these vectors S_n , droplets are identified by correlating the fluorescence intensity in the channel S_n with the expected MLS signal m , $\Psi = S_n \otimes m$. (**Fig. 2c**) v. Indexed by the video frame k and the channel n , a matrix $[x_{k,n}, v_{k,n}]$ is generated that reports the droplets detected.

A major challenge of our detection technique is that it requires knowledge of each droplet signal's velocity v and its phase shift θ relative to the MLS pattern m used to excite the droplets. Rather than add additional cost to our platform by phase locking the excitation of our LED to the cell phone camera or controlling velocity using a more expensive pump, we instead use a cloud computing implemented algorithm to optimally detect each droplet with unknown velocity v and phase θ . To this end, we correlate each $S_{n,k}$ with the MLS pattern $m(x, v, \theta)$, a three dimensional matrix that contains all possible phases θ and velocities v , (**Fig. 2d**) and search within the resultant 3D matrix $\Psi(x, v, \theta)$ (**Fig. 2f**) for peaks with an amplitude greater than a defined threshold, and record the position and velocity $[x_{k,n}, v_{k,n}]$ of every droplet. This analysis allows the correct phase θ_c (**Fig. 2g**) and velocity v_c (**Fig. 2h**) to be determined for each individual droplet.

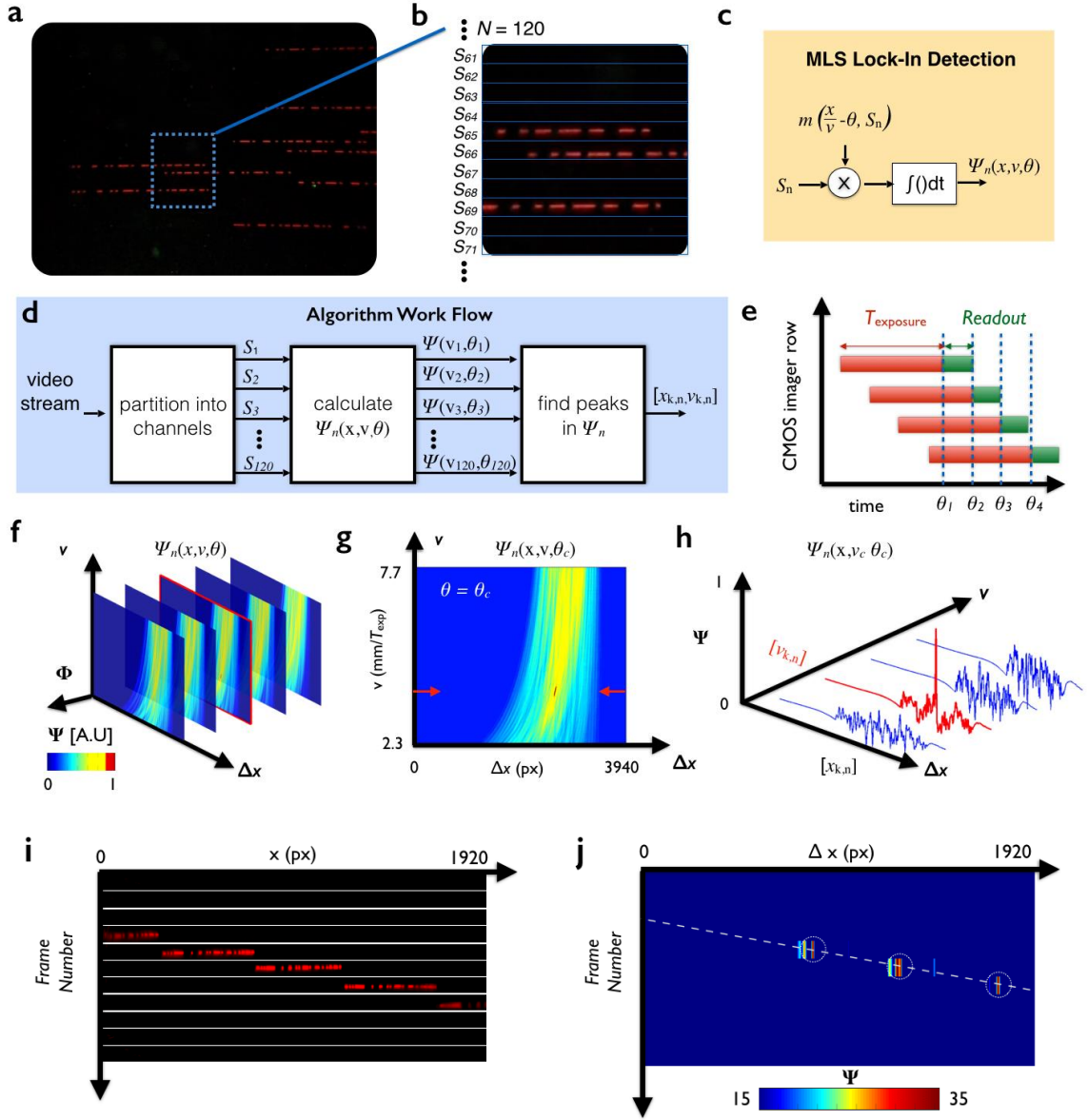


Figure 2.2. Signal Analysis Workflow. **a.** Each video frame from the cell phone camera is first partitioned into 120 one dimensional vectors S_n (**b**), corresponding to the fluorescence intensity along the length of each microfluidic channel. **c.** Each vector S_n is analyzed by correlating it with the expected signal $m(x/v - \theta)$, where v is the expected droplet velocity and θ is the expected droplet phase. **d.** A flow chart of the μ MD's algorithm to detect droplets with unknown velocity v and phase θ . **e.** A timing diagram of our cell phone's rolling shutter readout, which complicates our measurement by giving

each vector S_n a different phase θ . **f.** Each S_n is correlated with $m(x,v,\theta)$, a three dimensional matrix that contains all possible phases θ and velocities v , resulting in a 3D matrix $\Psi(x,v,\theta)$. Within this 3D vector $\Psi(x,v,\theta)$, peaks are identified that allow droplets to be detected at their correct phase θ_c (**g**) and velocity v_c (**h**). **i.** A single microfluidic channel is shown at various frames k , showing that individual droplets are detected in multiple frames. **j.** We perform correlation analysis on Ψ between subsequent frames to further improve accuracy. with a pseudorandom sequence, modulating the streak (**g**) such that it can be resolved using correlation based detection (**h**), even amongst close by neighboring droplets (**i,j**).

There are several considerations, based on our hardware implementation, that inform the design of our algorithm. The computation time for our algorithm is approximately proportional to the number of velocities v that our algorithm searches. To determine the appropriate number of velocities, we measured the coefficient of variation of droplet velocity $CV = 4.4\%$ at $\phi = 100$ mL/hr by imaging the streak lengths of sparse non-overlapping droplets. (**Fig. S3**) Based on this measurement, we calculate $\Psi(x,v,\theta)$ over a domain that covers $\pm 20\%$ of the mean velocity, with 34 increments. Matching the phase θ for each signal S_n to the phase of the MLS pattern m is complicated by our cell phone camera's (Samsung Galaxy S7 Edge) use of rolling shutter. In a digital camera that uses rolling shutter, which includes most currently available cell phone cameras, each row of the imaging sensor is sequentially readout over the period defined by the frame rate. (**Fig. 2e**) Thus, the exposure time for each row T_{exp} is sampled at an offset window in time, resulting in a phase shift between each S_n . Because of this readout

technique, we choose to orient our microfluidic channels to align with the rows of the CMOS sensor in the digital camera, such that within each vector S_n the phase θ is constant.

In addition to the analysis performed on each individual frame k in the video, we also perform correlation analysis between subsequent frames to further improve accuracy. Detected droplets in a given frame k are cross referenced with droplets detected in subsequent frames (**Fig. 2i**) by comparing the droplet's expected position $x_{k+1,n}^* = x_{k,n} + v_{k,n} T_{exp}$, based on its measured velocity and position $[x_{k,n}, v_{k,n}]$, (**Fig. 2j**) with its measured position in the subsequent frame $x_{k+1,n}$. The algorithm described above is implemented in Matlab (**source code provided in SI**). Due to the required computational power, this program is not performed directly on the cell phone. Using a Windows 7 PC with an Intel Core i7-4700 @ 3.4 GHz and 16 GB RAM, we can locally process the data at a rate of 10^6 droplets/30 min. In addition, we take advantage of ubiquitous wireless networks, and perform the computation either on a local server or using Matlab's Cloud service, to greatly speed up processing, both of which interface with a mobile app installed on the cell phone based device that we created. (**Fig. S2**)

μ MD Implementation

The μ MD consists of a disposable microfluidic chip, a cell phone, and a 3D printed piece that we designed. The 3D printed piece contains an LED, a low-cost commercial plastic lens (<\$4), and a slot to automatically align and focus the microfluidic chip. (**Fig. 3a**) The disposable microfluidic chip is constructed of only PDMS and glass, and is prototyped using soft lithography at The University of Pennsylvania's Singh Center. A hobbyist-grade, clip-on plastic macro lens (15x magnification, Carson HookUpz, ML-515) is used to magnify the microfluidic chip to a field of view FOV = 7x12

mm². Mounted in-line with this lens is a longpass filter ($\lambda_c = 605$ nm, Edmund Optics, #52-528) to diminish background scattered excitation light in the image. (**Fig 3b**) An ultra-bright green LED ($\lambda_{ex} = 530$ nm, Luminus, CBT-90-G-C11-JK201) is used with a bandpass filter ($\lambda_{cuton} = 535$, $\lambda_{cutoff} = 585$ nm, Omega Optical, 560AF50-X), to further diminish the excitation light that reaches the cell phone's camera. The LED is driven using external electronics consisting of an LED driver circuit (Luminus Development Kit, DK-114N-3) and a microcontroller (Arduino Mega2560). To illuminate the droplets in the microfluidic channels we make use of anti-resonant side coupling¹⁵² which ensures uniform illumination. The MLS sequence that we use is stored in our microcontroller, and is used to modulate our LED. The non-disposable cost, excluding the cell phone, of the μ MD prototype is < \$500.

schematic of the μ MD chip, showing the droplet generation module, the droplet distribution module, and the detection module. Micrographs of each of these modules are shown. Scale bars are 100 μ m.

The disposable microfluidic chip consists of three modules, *i.* a module to rapidly generate monodispersed droplets^{130,131}; *ii.* a module to distribute these droplets to parallel detection channels⁴⁴, and which in future implementations can include delay lines for chemical reactions to take place within the droplets⁴⁵; and *iii.* the μ MD's ultra-high throughput cell phone based fluorescence droplet detection. These modules are integrated into a low-cost all-polymer (PDMS) and glass chip, for point of care implementation. To rapidly generate droplets, we make use of an architecture previously published by our group¹⁷, which enables $N = 200$ droplet generators to be incorporated onto a single chip with only one input for the droplet phase, one input for the continuous phase, and one output line.^{16,17} (**Fig. 3c**) Droplets were generated with droplet diameter $d = 35 \mu\text{m}$, using a ladder geometry that can achieve high throughput $>10^6$ droplets/sec with only small variation in droplet diameter ($\text{CV} < 7\%$)¹⁷. Droplet diameter was validated using fluorescence microscopy (**Fig. 3c**). Downstream of the droplet generator, the droplets are evenly distributed over the 120 channels using an array of pillars, which are 60 μm in diameter and are spaced by 180 μm in a hexagonal array. (**Vid. S1**, CAD schematic provided in SI)¹⁵³. The $N = 120$ flow channels where μ MD detection is carried out have a height of 40 μm and a width of 35 μm to accommodate $d = 35 \mu\text{m}$ diameter water droplets suspended in 0.65 cSt Silicone Oil (Consolidated Chemical) with 5% v/v Span80 (Sigma). We fabricate the chip using

traditional soft lithography¹⁵⁴ and use oxygen plasma surface activation to permanently bond the PDMS to a glass slide (Corning® Glass Slides, ID: 26005).

Simulations to Parameterize Device Performance

To characterize and to aid in the design of our platform, we created a numerical model to simulate the performance of the μ MD. The model was carried out using Matlab and all source code is included in the Supplementary Information. In this model, a simulated signal from the passing droplet was created using an MLS sequence $m(x/v - t_p)$, scaled by a droplet velocity v and placed into a particular channel's signal S_n at time point t_p . N droplets are iteratively placed into S_n with randomly generated t_p , and Gaussian noise is added to the signal to obtain the intended signal to noise ratio (SNR). The model was verified by comparing it directly to our experimental data. Using this model, we were able to determine the limits of our detection strategy, and answer the following questions: *i.* how does our platform's sensitivity scale with the number of bits in the MLS sequence? and *ii.* what design parameters define the throughput of our platform? For these simulations, we set velocity $v = 4 \text{ mm}/T_{\text{exp}}$, which corresponds to a volumetric flow rate $\phi = 145 \text{ mL/hr}$, for 120 channels with dimensions that match our prototype device and a frame rate of 60 FPS.

To quantify the scaling of our platform's performance with the number of bits in the MLS sequence, we measured the SNR in our model system using MLS sequences that ranged from 10 bits to 100 bits. The output signal from our platform Ψ is expected to have a greater SNR_ψ than the raw data SNR_{raw} , as correlation of the raw image with the expected MLS pattern acts as an ideal filter, diminishing the majority of the noise because it does not correlate with the expected pattern. To determine the SNR_ψ of our platform, we calculate the ratio of the energy of the signal from a passing droplet $\int \Psi_{\text{sig}}^2 dx$

to the energy of a background signal, where there is only noise and no signal $\int \Psi_{bg}^2 dx$, over the length of the signal. To test each condition, we ran the simulation for 500 independently simulated droplets. We found that as the number of bits in the MLS sequence increased, so did the SNR_ψ (**Fig 4a- top inset**). Moreover, as we increased the number of bits in the MLS sequence, we could detect droplets with diminishing values of SNR_{raw} (**Fig 4a- bottom inset**). For example, for a droplet with an $SNR_{raw} = 1$ (0 dB), the SNR_ψ of the output of our platform, for an $|m| = 63$ bit MLS, increased to $SNR_\psi = 100$ (20dB).

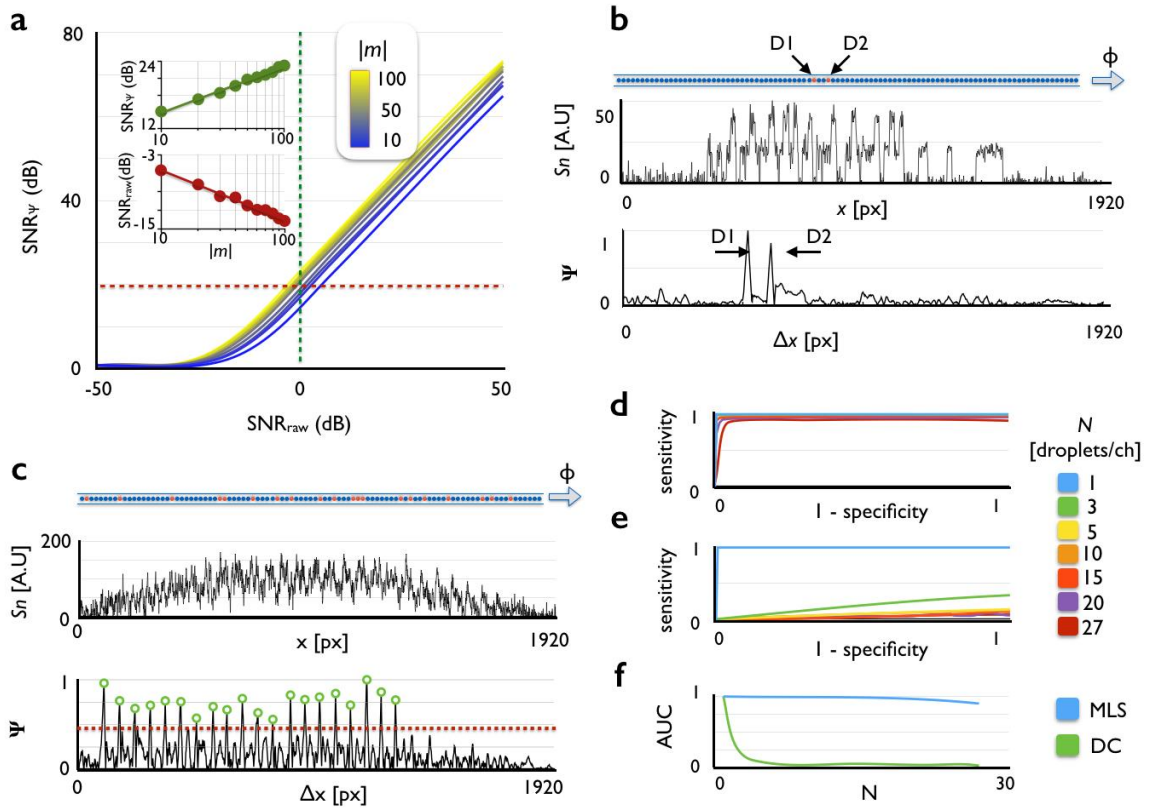


Figure 2.4. Modeling and Simulating the μ MD. **a.** To determine the number of bits in the MLS sequence $|m|$, we compared the signal to noise ratio SNR_ψ of the droplet in ψ to the droplet in the unprocessed signal SNR_{raw} . *Inset Top:* At $SNR_{raw} = 0$ dB, as the number of bits $|m|$ increased, SNR increased. *Inset Bottom:* As the number of bits $|m|$

increased at $\text{SNR}_\psi = 20$ dB decreased, we could detect droplets with diminishing values of SNR_{raw} . **b.** Droplets D1 and D2, not resolvable in the raw signal S_n , could be resolved in Ψ . **c.** Twenty droplets, not resolvable in the raw signal S_n , could be resolved in Ψ with perfect fidelity. **d.** Receiver Operator Characteristic (ROC) curves for increasing number of droplets per channel, demonstrate excellent performance Area Under the Curve (AUC) ~ 1 up to $N = 20$ droplets in a channel. **e.** In comparison, using conventional constant excitation, performance degraded with more than one droplet in the channel. **f.** For the MLS patterned droplets, the $\text{AUC} > 0.95$ for as many as $N = 20$ droplets in a channel, but the AUC degrades severely for $N > 1$ droplets using constant (DC) excitation.

To determine the design parameters that control the μMD 's throughput, we performed a simulation to determine how many positive droplets could be simultaneously detected in a single channel. For these simulations we used an MLS sequence containing $|m| = 63$ bits. We created a set of simulated data consisting of signals S_n that have N droplets pass through the μMD at random time points t_p , within a single exposure time T_{exp} . To illustrate the μMD 's performance at high droplet densities N , we first successfully demonstrated detection of individual droplets with $N = 2$ droplets (**Fig. 4b**) and $N = 20$ (**Fig. 4c**) droplets per channel, which could not be detected using non-modulated detection due to droplet overlap. The signal from passing droplets in Ψ was found to have a full width half maximum of 10 pixels, allowing droplets to be resolved as long as the spacing between droplets was > 20 pixels ($3.5 \cdot d_{\text{drop}}$). To quantify the tradeoff of sensitivity, specificity, and throughput, we calculated the sensitivity = TP/P and specificity = $(P - \text{FP})/P$ at various numbers N of positive droplets per channel, where

true positives (TP) are instances where the detected droplet matched the true locations of the droplets that were randomly spaced, positives (P) were the total number of droplets that were randomly placed, and false positives (FP) were detected droplets that did not co-register with a true droplet. We quantified the device's performance by sweeping the droplet detection threshold in Ψ , to create a Receiver Operator Characteristic curve (ROC) and calculate the corresponding Area Under the Curve (AUC). We tested the device using a density of positively fluorescent droplets with densities ranging from $N = 1$ to $N = 27$ droplets per channel in a given frame. **(Fig. 4d)** To test each condition, we ran the simulation 100 times to average over the effect of random droplet placement t_p . We demonstrated that device performance was near perfect ($AUC \sim 1$) for $N < 19$ droplets per channel per frame, above which the AUC began to drop off. **(Fig. 4d,f)** We compared this performance to non-modulated detection, and found that without modulation, at only $N = 2$ droplets per channel per frame, the performance ($AUC = 0.43$) was already extremely degraded. **(Fig. 4e,f)**

Design Validation

We performed a series of experiments to validate our prototype μ MD's capability to detect droplets across a wide range of velocities v , phase shifts θ , droplet density N , and fluorophore concentrations C . We first demonstrated that neighboring channels in the μ MD's detection region can be partitioned automatically into channels S_n , allowing passing droplets to be detected without cross-talk between channels. **(Fig. 5a)** Next, to demonstrate that droplets can be detected that have a signal comparable to the noise level, we measure a droplet with $C = 1 \mu\text{M}$ Rhodamine. In the raw image, the signal from this passing droplet is barely detectable ($\text{SNR}_{\text{raw}} \sim 1$). However, in the correlation output Ψ , the signal from the passing droplet is easily detected versus the background

($\text{SNR}_\psi \sim 100$). (**Fig. 5b**) Next, we demonstrate that nearby droplets can be detected, which would otherwise overlap due to the exposure time of the cell phone camera. In **Fig. 5c**, two droplets are shown in the raw data, which are not resolvable in S_n , but become easily resolvable in the correlation output Ψ . We next demonstrate the μMD 's capability to detect droplets across a range of droplet velocities v . In **Fig. 5d**, two droplets from separate flow rate experiments, one with a velocity of $v = 2.5 \text{ mm}/T_{\text{exp}}$ and another with a velocity of $v = 6.25 \text{ mm}/T_{\text{exp}}$, were simultaneously detected using our velocity and phase scanning algorithm. We demonstrated the μMD 's capability to detect droplets across a range of droplet phase shifts θ , which arise from the lack of phase locking and the rolling shutter of modern cell phone cameras. **Fig. 5e** shows three separate channels with different phase shifts θ , which were correctly detected using our detection algorithm. For these experiments, we generated $d = 35 \text{ }\mu\text{m}$ diameter droplets containing Dextran Rhodamine B 10,000 MW with 0.15 M MgSO_4 (Thermo, D1824). These droplets were dispersed in a continuous phase consisting of 0.65 cSt Silicone Oil (Consolidated Chemical) with 5% v/v Span80. We chose Silicone oil due to its low viscosity and cost, and found that the known PDMS swelling effects to the oil were minimal given the short time frame droplets were driven through the device¹⁵⁵. These experiments were conducted at a volumetric flow rate $\phi = 80 \text{ mL/hr}$ and 30 FPS.

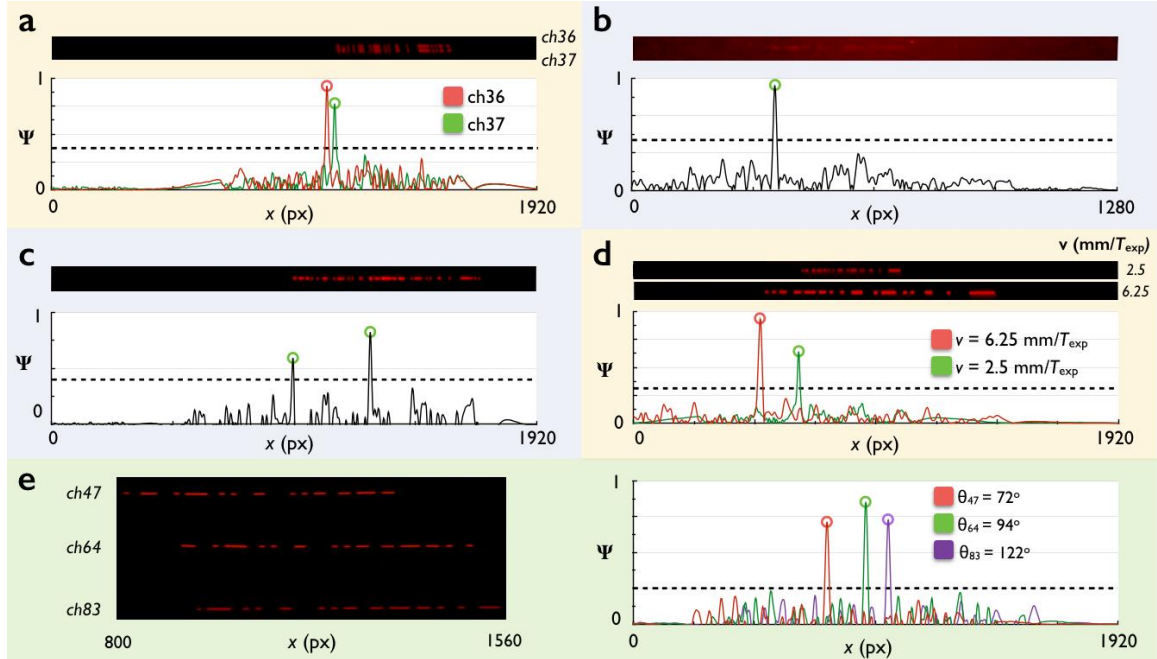


Figure 2.5. Experimental Validation of the μ MD's Key Features. **a.** Droplets in neighboring channels can be detected, and their correct channel identified. **b.** Droplets with low signal to noise ratio in the raw signal $\text{SNR}_{\text{raw}} \sim 1$ could be resolved with high SNR in Ψ . **c.** Two droplets that overlap and cannot be resolved in the raw data are easily resolved in Ψ . **d.** Two droplets traveling at different velocities v are both detected accurately due to our velocity invariant detection method. **e.** Three droplets, in three different channels $n = 47, 64$, and 83 , with different phases θ , are detected accurately due to our phase θ invariant detection method.

Quantification of Device Sensitivity and Dynamic Range

To quantify the limit of detection (LOD) of the μ MD, we performed a serial dilution with Rhodamine dye and demonstrated an $\text{LOD} = 1 \mu\text{M}$, sufficient for performing biological assays such as digital PCR¹³², enzyme assays¹³³, and ELISA¹⁵⁶. In these experiments, we diluted the dye at various concentrations and measured the SNR of passing droplets in our μ MD. The SNR_{Ψ} of a passing droplet in Ψ was calculated by

integrating the energy of the signal $\int \Psi_{\text{sig}}^2 dx$ over its length, 20 pixels, and compared it to the case when there is no droplet passing. The μMD 's camera frame rate, which modifies T_{exp} and thus the SNR, controls the tradeoff between throughput and sensitivity. In the raw images, the SNR_{raw} can be seen to decrease with concentration C of dye. The droplets became difficult to observe relative to the noise at concentrations below $C = 10 \mu\text{M}$ Rhodamine at 30 FPS (**Fig. 6a**) and $50 \mu\text{M}$ Rhodamine at 60 FPS. (**Fig. 6b**) After running the raw video data through our algorithm, the SNR_{ψ} for both the 30 FPS (**Fig. 6c**) and 60 FPS (**Fig. 6d**) data increased by 100x compared to SNR_{raw} . The measured limit of detection was $C_{\text{LOD}} = 1 \mu\text{M}$ Rhodamine at 30 FPS and $C_{\text{LOD}} \cong 5 \mu\text{M}$ Rhodamine at 60 FPS, and was ultimately not defined by SNR_{ψ} but by the digitization error of the digital camera. Thus, sensitivity can be further improved by using a camera with higher gain or by increasing the intensity of the LED. For these experiments, the throughput was $\phi = 80 \text{ mL/hr}$ for the 30 FPS measurements and $\phi = 166 \text{ mL/hr}$ for the 60 FPS experiments.

Quantification of Dynamic Range and Throughput

To quantify the μMD 's dynamic range for counting droplets and its throughput, we performed experiments where we spiked a known number of fluorescent droplets into a suspension of non-fluorescent droplets and evaluated the accuracy of the device's response. The positive fluorescent droplets contained $100 \mu\text{M}$ Rhodamine and the negative droplets contained only water. These positive and negative droplets were generated on two separate flow-focusing droplet generating chips and collected separately. Droplets in the collection tubes were concentrated based on buoyancy, as the aqueous phase ($\rho_{\text{aq}} = 1.00 \text{ g/mL}$) had a higher density than the oil phase ($\rho_{\text{oil}} = 0.75 \text{ g/mL}$) and sank to the bottom. Positive fluorescent droplets were then spiked into negative droplets and thoroughly mixed by pipetting to generate a concentration of 1:40

positive:negative droplets. This suspension was then serially diluted into lower concentrations of positive:negative droplets, and each concentrations was independently measured using microscopy. These suspensions were reinjected into the detection module of our chip for evaluation. These emulsions had a volumetric fraction of 53% of $d = 35 \mu\text{m}$ droplets suspended in 0.65 cSt Silicone Oil with 5% v/v Span80.

As the concentration of positively fluorescent droplets increases, passing droplets begin to overlap in the raw video such that they are not detectable without processing. (**Fig. 6e,f**) For numbers of spiked droplets ranging from 3 to 6×10^5 per mL, the droplets could be quantified on the μMD with extremely high fidelity ($R^2 = 0.985$). (**Fig 6g**) In **Fig. 6g**, we demonstrate that the μMD can detect as few as $1:10^7$ to $1:40$ positive: negative droplets using the same settings. The upper limit of the dynamic range was experimentally validated at concentrations as high as $1:40$ positive:negative droplets, beyond which overlapping signals within a single channel begin to limit device performance. We demonstrated this effect in simulations (**Fig. 4f**), wherein the performance began to drop ($\text{AUC} < 0.95$), as the number of overlapping droplets increased beyond $N > 19$ droplets in a single channel at any given time, which corresponds to a concentration of $\sim 1:18$ positive:negative droplets. The limit of detection of $1:10^7$ could be improved even further by analyzing more droplets, at the expense of increased assay time. These experiments were carried out at $\phi = 166 \text{ ml/hr}$, corresponding to an $f = 1 \text{ MHz}$ detection rate (Calculations provided in SI) for ratios of positive:negative droplets of 10^{-7} to 2.5×10^{-2} , a value consistent with typical digital assays¹⁵⁷.

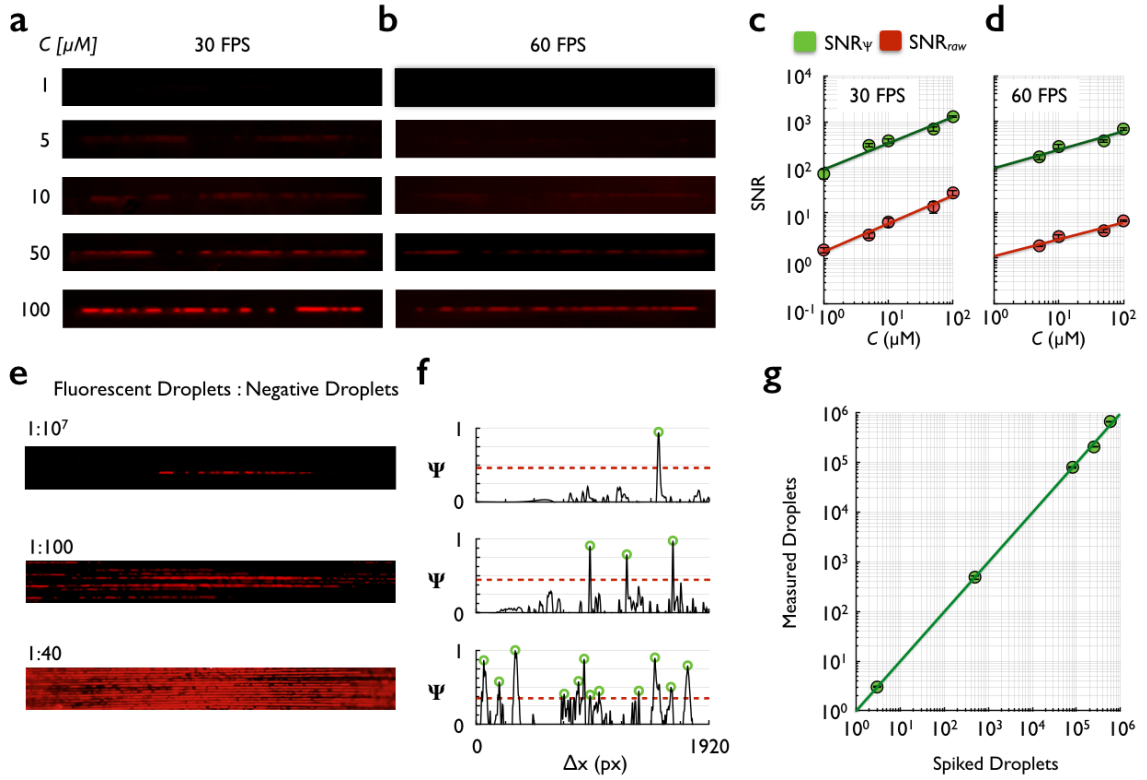


Figure 6. Characterization of the μ MD's Performance. **a.** Raw cell phone images of a passing droplet at different concentration of Rhodamine dye, at a frame rate of **(a)** 30 FPS and **(b)** 60 FPS. The μ MD could detect droplet with $SNR_{\psi} > 100$ for dye concentrations as low as $C = 1 \mu M$, where the $SNR_{raw} \sim 1$ at both **(c)** 30 FPS and **(d)** 60 FPS. **e.** The ratio of positively fluorescent droplets to the negative number of droplets was titrated from 1:10⁷ to 1:40, to evaluate the devices dynamic range for detecting positive droplets. **f.** As the density of positive droplets increased to 1:40, many of the droplets were not resolvable in the raw data due to droplet overlap, but could be resolved with high fidelity in Ψ . **g.** A serial dilution of fluorescent droplets: negative droplets was performed, and a dynamic range from 3 positive droplets /mL to 6*10⁵ positive droplets /mL was demonstrated ($R^2 = 0.985$).

2.4 Discussion

Our μ MD platform, with its very large scale integrated parallelized droplet production and detection, allows digital assays containing 10 million droplets to be performed in as little as three minutes on a mobile cell phone based platform. By automating, speeding up, and miniaturizing digital assays, the μ MD can translate digital diagnostics from a laboratory research tool to a point of care diagnostic. Building on this work, temperature control and delay lines can be additionally incorporated into the μ MD¹⁵⁸, to move this work beyond a proof of concept and to molecular sensing. In addition to making existing digital assays more accessible, due to the μ MD's ultra-high throughput rate, it can detect sparse molecules in large volume samples ($V > 10$ mL) that are impractical to measure using conventional hardware, for applications such as detecting mutant KRAS genes in the blood of pancreatic cancer patients⁵ or for evaluating cures for HIV by detecting sparse copies of latent HIV in the blood of patients¹⁵⁹. While in this paper each of the device's channels were used to measure droplets from the same suspension, individual channels, or sets of channels, can be used to measure independent assays simultaneously, allowing for facile multiplexed biomarker detection. Because our detection method is invariant to droplet velocity, it is possible to use the detection scheme with low cost portable pumps for point of care applications. While the droplet generation module demonstrated in this paper^{130,131} would suffer from increased droplet polydispersity with a low cost pump, recent strategies for droplet generation that have greater flow rate invariance could potentially solve this issue¹⁸. Additionally, though this platform was designed for detecting droplets, due to the high sensitivity of its correlations based detection, it can also be applied to the detection of fluorescently labeled cells or microbeads^{145,147}. Moreover, this high throughput droplet-

based chip can be combined with sample processing modules to sort out rare cells, bacteria, virus, or exosomes for integrated downstream analysis^{160–162}.

To further expand the μ MD's functionality, there are several additional features that can be incorporated onto the μ MD's monolithic, microchip-based format. For example, we postulate that this technique can be extended to the detection of multiple fluorescent colors by including multiple LEDs with different colors, each uniquely identified by its modulation with a distinct MLS pattern. In addition to measuring the fluorescence signal from each droplet, dielectric sensors¹⁵⁸ could also be added to count the non-fluorescent droplets as well. The counting of negative droplets is not necessary for quantifying the number of molecular targets in a digital assay, in the case when the total number of droplets is much greater than the number of molecular targets. By adding dielectric sensing to quantify the number of negative droplets, the dynamic range can be extended to the regime when the number of molecular targets approaches the total number of droplets. In this paper, we demonstrated cloud computing using a local server or Matlab's cloud computing service. Achieving the real time data processing required for droplet sorting will be challenging and cannot feasibly be done at this time with cloud computing. Alternatively, local digital signal processing (DSP) based processing techniques have the potential to solve this problem¹⁶³. However, resources such as Amazon Cloud services that allow access to larger numbers of computing cores could be used to dramatically increase the rate at which the signal is analyzed. Alternatively, the processing can be carried out using parallel computing on a Graphical Processing Unit (GPU) for improved computing times.

Author Contributions

V.Y. conceived and performed all experiments in this study, coded the Matlab software, created the Android app, as well as prepared the manuscript and figures. H.J. and S.Y. helped design and fabricate the droplet generators, and select the proper continuous phase for high-throughput operation. D.I. conceived and oversaw all aspects of this study, and prepared the manuscript.

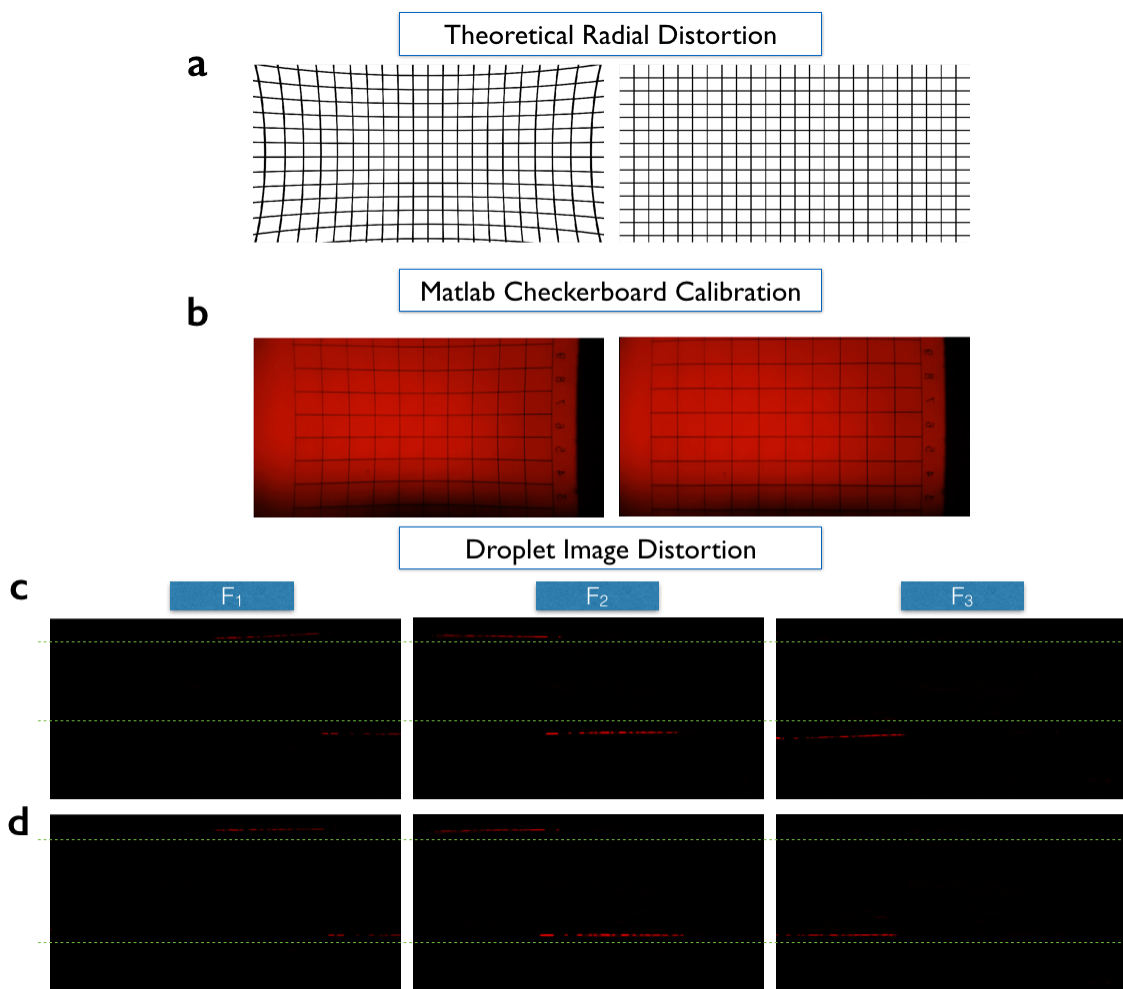
Acknowledgements

This work was supported by the Department of Bioengineering, University of Pennsylvania. Funding was provided by the National Institute of Health: 1R21CA182336-01A1. David Issadore, PhD was supported by an American Cancer Society - CEOs Against Cancer - CA Division Research Scholar Grant, (RSG-15-227-01-CSM). Venkata Yelleswarapu is generously supported by the Microsoft Graduate Fellowship. We would also like to thank Gershon Buchsbaum for discussions on choosing sequences with minimal correlation.

Conflict of Interest

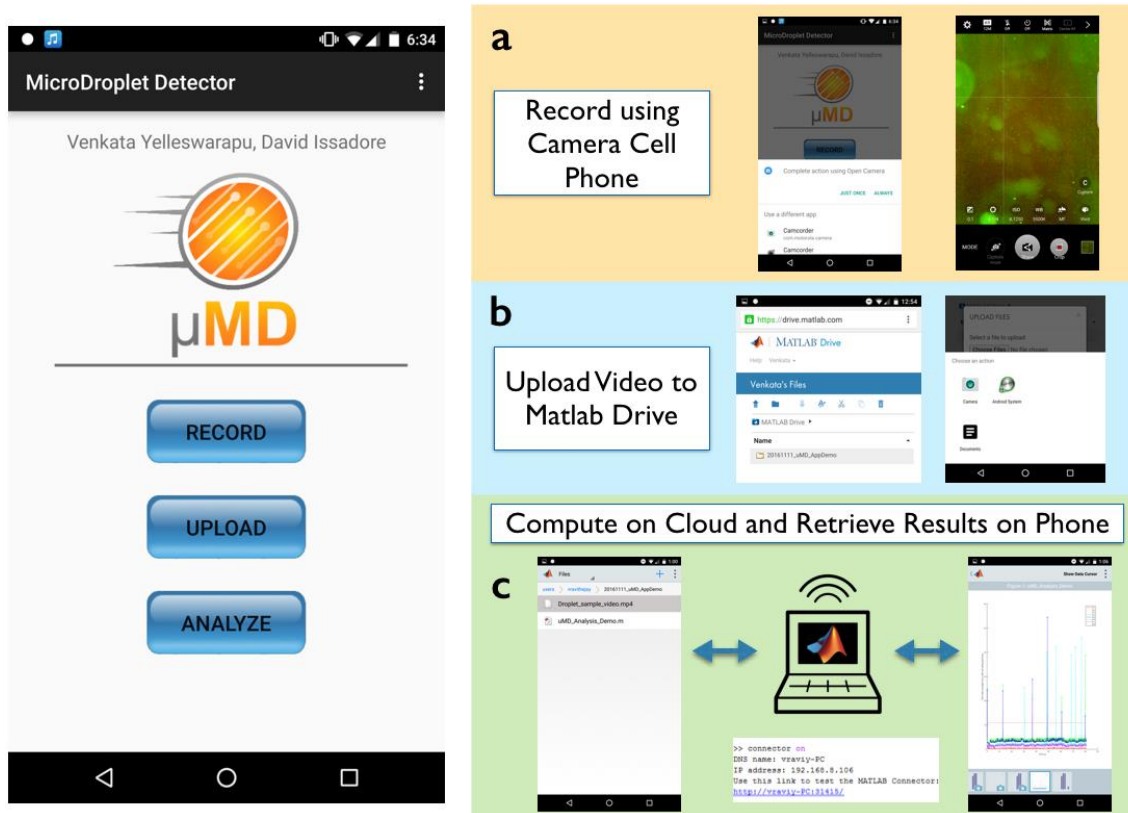
David Issadore is the founder and currently holds equity in Chip Diagnostics.

2.5 Supplementary Information

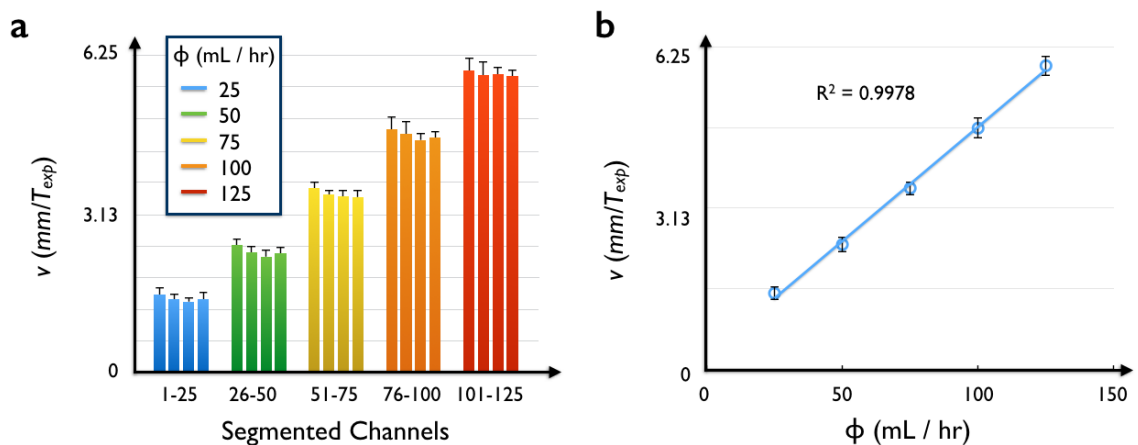


Supplementary Figure 2.1: Software Image Correction. **a.** The low cost macro lens used in our μ MD caused a pincushion distortion (left) on the acquired images that could be corrected using Matlab's computer vision toolbox (right). The theoretical distortion was generated by creating a grid and running the image correction parameters in reverse to demonstrate how distortion from the lens can be corrected using software rather than resorting to expensive hardware solutions. **b.** To calculate the camera parameters for the image distortion, we used MATLAB's `cameraParameters` function to

find how the coordinates of the checkerboard were distorted due to the lens (left). These coordinates were used to correct the distortion (right), and these parameters were also saved for the microfluidic device **c.** We then implemented this transform for our microfluidic device, where corrections from translation vectors due to misalignment were adapted. We show three sequential frames (F_1 , F_2 , F_3) where initially the distortion does not allow for proper segmentation as the curvature bends the channels. **d.** We show that after image correction, the channels can be properly segmented and the droplet can be followed through the frames for correlation and further analysis.



Supplementary Figure 2.2: μ MD App for Cloud computing. A custom built app allows users to record droplet video, upload the video to the Matlab drive, and retrieve results after running the code online **a**. The record button opens the Camera app on the phone. **b**. The upload button connects to the Matlab drive via a browser, where the files sync to the cloud. **c**. The analyze button opens the Matlab Mobile app, which connects to the Matlab drive and allows users to run the analysis code remotely. The app is provided in the SI as an .apk file that can be installed on Android phones.



Supplementary Figure 2.3: Velocity Distribution. To determine the dispersion of droplet velocity v in the μ MD, we measured velocity of droplets in multiple channels at multiple flow rates ϕ . **a.** At a given flow rate ϕ , the channels were binned to determine if the droplet velocity varied as a function of the row position in the device. There was no significant change in velocity moving across the chip. The error bars represent the standard deviation. **b.** Droplet velocity scales linearly with the flow rate ($R^2 = 0.9978$). Error bars show the standard deviation at each of the given data points.

Supplementary Video 1: Animation of device setup and workflow, along with how the app interfaces with the cell phone to record and analyze the data.

Cell Phone Parameters:

Unlike a traditional scientific CMOS camera where the user is in control of most image acquisition parameters³⁵, a cell phone camera has only a handful of features that can to be optimized prior to recording. Using the S7 Edge's Camera "Pro" Mode, the following settings were used to record: *i.* the focus was manually fixed so the chip could slide in to an acrylic casing without having to align the chip; *ii.* the ISO was set to 3200 and

Exposure to +2 maximize light input unless specified otherwise; *iii.* aperture was set to 1/30; *iv.* metering mode was set to Matrix; and (*v*) the color correction was set to Auto. All videos were recorded 1920x1080p size at 60 fps or 30 fps using the OpenCamera App, since this setting captured all 120 channels properly without extremely large file sizes, and with a field of view of ~12mm by 7mm. While higher resolution videos could be captured, this would create file sizes that would take much longer to analyze without significantly increasing the field of view.

Calculation of Droplet Throughput:

To calculate the droplet throughput, we first measured the droplet diameter to be $d = 35 \mu\text{m}$ and the volume fraction of dispersed phase to continuous phase to be $\chi = 53\%$. For the volumetric throughput $\phi = 166 \text{ ml/hr}$, the droplet throughput $f = \phi / (V_d * \chi) = 1.1 \text{ MHz}$ was calculated. To create a suspension with a filling factor of $\chi = 53\%$, we generated the droplets using a separate chip and concentrated the droplets based on buoyancy before re-injecting them into the detection region of our chip.

2.6 Supplementary Code:

The supplementary zip file contains: (i) Matlab code for simulations, (ii) Matlab code for video analysis, (iii) Arduino code to modulate the LED, (iv) CAD schematic of detection chip, and (v) an apk to install the app on an Android phone. Each folder contains a readme on how to run the code and parameters to change.

20161111_Clean_matlab_code_COMPLETE

~~~~~ Simulation_Spacing_Distance_two_beads_ONLY

Simulation_Spacing_Distance_two_beads_ONLY.m

```
clear all
close all

num_bits = 63; %number of bits in the MLS to use
logbase2pow = ceil(log2(num_bits)); %get base power of 2 for number of
bits desired

MLS_seq = mseq(2,logbase2pow,0,0); %generates an MLS
MLS_seq = MLS_seq(1:num_bits); %truncates only the first bits of the
MLS desired

%Stretch the MLS such that each bit = 10 points, or that each bit = 10
%pixels in in the CMOS frame
x = 1:length(MLS_seq);
v = MLS_seq;
xq = 1:.1:length(MLS_seq);
vq2 = 10*(interp1(x,v,xq,'nearest')+1);

%Store a signal matrix
Signal_Mat = zeros(27,1920);

%Create several signals that are spaced apart
Signal_Mat(1,1:length(vq2)) = vq2;
for i = 2:27
    Signal_Mat(i,1+floor((i-1)*length(vq2)/13):length(vq2)+floor((i-
1)*length(vq2)/13)) = vq2;
end

%Add white noise to the signal
snr = -10;
for i = 1:27
    Signal_Mat(i,:) = awgn(Signal_Mat(i,:),snr);
end

%Plot the first, middle, and last pattern in the matrix
figure
stairs(Signal_Mat(1,:), 'Color',[1 0 0])
hold on
stairs(Signal_Mat(13,:), 'Color',[0 1 0])
hold on
stairs(Signal_Mat(27,:), 'Color',[0 0 1])

Signal = zeros(1,length(Signal_Mat(1,:)));
```



```

%Add two signals that are next to each other
for i = 13:14
    Signal = Signal + Signal_Mat(i,:);
end

%Find correlatoin between the expected and summed signals
corr_vector = xcorr(vq2,Signal);
figure
subplot(2,1,1)
plot(Signal)
title('Summed Signal of 2 64-bit patterns spaced 23 px apart')
subplot(2,1,2)
plot(corr_vector)
title('Correlation of expected signal with Summed Signal')

figure
stairs(Signal, 'LineWidth',1)
title('Summed signal')
axis([0 1920 0 300])

%Filter out DC and low frequencies from the correlation
figure
Fs = 1920;
half_freq = Fs/2;
notch_freq_filter =1;
low_freq_filt = 2;
smoothing_factor = 2;
w0=notch_freq_filter/half_freq;
[num,den]=iirnotch(w0,w0/35,-45);
[a,b]=butter(2,low_freq_filt/half_freq,'high');

y=filter(num,den,corr_vector);
yfil=filtfilt(a,b,y);
ysm=smooth(yfil,smoothing_factor);
figure
plot(abs(ysm))

figure

%Due to the shift in the correlation, only a segment of it is relevant
to
%when the expected and signal of interest overlap
actual_vector_that_matters = abs(ysm(640:1920+640));
actual_vector_that_matters=actual_vector_that_matters/max(actual_vector_
_that_matters);
plot(actual_vector_that_matters, 'LineWidth',2)
%select a threshold
threshold2 = max(actual_vector_that_matters)*.4;
%Find peaks based on a minimal peak distance

```

```

[pks,locs] =
findpeaks(actual_vector_that_matters,'MinPeakDistance',20,'MinPeakHeigh
t',threshold2);

%Plot the information
threshold_line_x = 1:20:length(actual_vector_that_matters);
threshold_line_y = zeros(1,length(threshold_line_x))+threshold2;

hold on
plot(locs,pks,'ro','MarkerSize',6,'LineWidth',2)
hold on
plot(threshold_line_x,threshold_line_y,':','Color',[1 0
0], 'LineWidth',4)
axis([0 1920 0 1.2])
xlabel('Frame Pixel')
ylabel('Signal Correlation')
title('Max beads that can be packed into a frame')

%Plot all the relevant information onto one figure
figure
subplot(4,1,1)
stairs(Signal_Mat(13,:), 'LineWidth',1)
axis([400 1400 0 50])
title('Signal 1')
grid off
box off
subplot(4,1,2)
title('Signal 2')
stairs(Signal_Mat(14,:), 'LineWidth',1)
axis([400 1400 0 50])
grid off
box off
subplot(4,1,3)
stairs(Signal_Mat(14,:)+Signal_Mat(13,:), 'LineWidth',1)
title('Signals Overlap')
axis([400 1400 0 50])
grid off
box off
subplot(4,1,4)
plot(actual_vector_that_matters, 'LineWidth',2)
hold on
plot(locs,pks,'ro','MarkerSize',6,'LineWidth',2)
title('Correlation peaks')
plot(threshold_line_x,threshold_line_y,':','Color',[1 0
0], 'LineWidth',4)
axis([400 1400 0 1.2])

grid off
box off
% set(gca,'visible','off');

```

~~~~~ Simulation\_packing\_dense\_droplets\_COMPLETE

## SpacingProximity\_vs\_ROC

### Function\_to\_call\_noplotsV3.m

```
%pick number of bits for MLS and generate signal
num_bits = 63;
logbase2pow = ceil(log2(num_bits));%get base power of 2 for number of
bits desired
MLS_seq = mseq(2,logbase2pow,0,0);
MLS_seq = MLS_seq(1:num_bits);
x = 1:length(MLS_seq);
v = MLS_seq;
close all
xq = 1:.1:length(MLS_seq);
vq2 = 10*(interp1(x,v,xq,'nearest')+1);

%preallocate a signal matrix
Signal_Mat = zeros(27,1920);

%add droplets randomly into segments that are atleast two droplet
diameters
%apart; some code was borrowed from the following:

Signal_Mat(1,401:400+length(vq2)) = vq2;
Signal_Mat(2,401+distnace:400+distnace+length(vq2)) = vq2;
real_locations_droplets = [401 401+distnace];

%place the droplets at different starting points
% for i = 1:num_droplets
%     number_toshift = Pshuffled(i);
%     Signal_Mat(i,1+number_toshift:number_toshift+length(vq2)) = vq2;
%     real_locations_droplets(i) =1+number_toshift;
% end

%add noise to the signal
snr = -10;
for i = 1:2
    Signal_Mat(i,:) = awgn(Signal_Mat(i,:),snr);
end

%start adding the droplets such that they overlap
Signal = zeros(1,length(Signal_Mat(1,:)));
for i = 1:2
    Signal = Signal + Signal_Mat(i,:);
end
%take a correlation from the expected to the signal that contains all
the
%droplet summations
corr_vector = xcorr(vq2,Signal);

%filter out DC components
Fs = 1920;
```

```

half_freq = Fs/2;
notch_freq_filter = 1;
low_freq_filt = 2;
smoothing_factor = 2;
w0=notch_freq_filter/half_freq;
[num,den]=iirnotch(w0,w0/35,-45);
[a,b]=butter(2,low_freq_filt/half_freq,'high');

y=filter(num,den,corr_vector);
yfil=filtfilt(a,b,y);
ysm=smooth(yfil,smoothing_factor);

%plot a portion where the vectors overlap completely
actual_vector_that_matters = abs(ysm(640:1920+640));
actual_vector_that_matters = flipud(ysm(1:1920));

%normalize the vector
actual_vector_that_matters=actual_vector_that_matters/max(actual_vector_
_that_matters);
%the threshold is set from earlier. the threshold value can be changed
to
%get differnet amounts of counted droplets
[pks,locs] =
findpeaks(actual_vector_that_matters,'MinPeakDistance',6,'MinPeakHeight
',threshold2);

threshold_line_x = 1:20:length(actual_vector_that_matters);
threshold_line_y = zeros(1,length(threshold_line_x))+threshold2;

%true positives are where locs match the locs of where droplets are
placed
%false positives are when locs show up that are no in the original list
%false negatives are when a peak is supposed to be there but nothing
shows
%up

%we already know where the droplets were initially placed; so find
those
%locations first and sort
locs2 = locs;
real_locations_droplets2
=sort(real_locations_droplets(real_locations_droplets~=0));

%this is the known number of droplets we placed randomly
positives = 2;

%preallocate
true_pos = 0;
locs =locs(locs~=0);
real_locations_droplets
=real_locations_droplets(real_locations_droplets~=0);

```

```

%another way to measure this is to look at the differences between
where
%droplets were placed and the distances between peaks incase the
%correlation is off from the exact location; both can be used to affirm
%positive droplets
diff_locs = diff(locs2);
diff_reals = diff(real_locations_droplets2);

diff_locs2 = diff_locs;
diff_reals2 = diff_reals;

%for each of the locations found in correlation, compare it to the
list of
%locations where droplets were randomly placed in simulation. If a
droplet
%location matches that of where it was placed, add a true positive.
for i = 1:length(locs)
    for j = 1:length(real_locations_droplets)
        if locs(i) == real_locations_droplets(j)
            true_pos = true_pos + 1;
            real_locations_droplets(j) = 5000;
            locs(i) = 0;
        end
    end
end

for i = 1:length(real_locations_droplets)
    if real_locations_droplets(i) == 5000;
        real_locations_droplets(i) = 0;
    end
end

true_pos2 = 0;
for i = 1:length(diff_locs)
    for j = 1:length(diff_reals)

        if diff_locs(i) == diff_reals(j)
            true_pos2 = true_pos2 + 1;
            diff_reals(j) = 5000;
            diff_locs(i) = 0;
        end
    end
end

for i = 1:length(diff_reals)
    if diff_reals(i) == 5000;
        diff_reals(i) = 0;
    end
end

```

```

%false positives are locations that were found in correlation but were
not
%locations where droplets were placed
true_pos ;
false_neg = nnz(real_locations_droplets);
false_pos = nnz(locs);

    true_pos2 ;
false_neg2 = nnz(diff_reals);
false_pos2 = nnz(diff_locs);

```

## **Packing\_MLS\_droplets\_simulation\_MAIN.m**

```

% clear all
% close all

%pick the number of droplets you want to pack
dropletspacing = [6:40];
distances_analyzed = length(dropletspacing);

%set a threshold that you can change to manually sweep different levels
of
%the ROC curve to find the tradeoff between sensitivity and
specificity.

%after inputting a threshold value, the resulting values from the
matrices
%need to be transferred to generate the roc plots
% threshold2 = .5;

%the first matrix set keeps track of the number of droplets
%the second
total_stat_matrix = zeros(distances_analyzed,2);
total_stat_matrix2 = zeros(distances_analyzed,6);
total_stat_matrix3 = zeros(distances_analyzed,6);

%for each number of droplets to look at...
for distance_iteration= 1:distances_analyzed
    distnace = dropletspacing(distance_iteration);

    %loop through and simulate the total number of false and true
    positives
    %that occur
    %   for repeatingtrialnumber = 1:1
        repeatingtrialnumber=1;
        Function_to_call_noplotsV3
        true_pos_total(distnace) = true_pos;

```

```

%         false_neg_total(repeatingtrialnumber) = false_neg;
%         false_pos_total(distnace) =false_pos;
%         true_pos_total2(repeatingtrialnumber) = true_pos2;
%         false_neg_total2(repeatingtrialnumber) = false_neg2;
%         false_pos_total2(repeatingtrialnumber) =false_pos2;
%         locs2_length(repeatingtrialnumber) = length(locs2);
% %     end
%     total_stat_matrix(distnace,1:3) = [distnace mean(locs2_length)
std(locs2_length)] ;
%     total_stat_matrix2(distnace,1:6) = [mean(true_pos_total)
std(true_pos_total) mean(false_neg_total) std(false_neg_total)
mean(false_pos_total) std(false_pos_total) ];
%     total_stat_matrix3(distnace,1:6) = [mean(true_pos_total2)
std(true_pos_total2) mean(false_neg_total2) std(false_neg_total2)
mean(false_pos_total2) std(false_pos_total2) ];
%     clearvars -except threshold2 numberofdropletstocall
rangeofdroplets total_stat_matrix total_stat_matrix2 total_stat_matrix3
rangeofdroplets
end

```

```

% total_stat_matrix;
% total_stat_matrix2;
% total_stat_matrix3;
%
%
%
sens = true_pos_total/2;
one_minspec = false_pos_total/2;

```

### **Packing\_thresholdvalue\_change.m**

```

% Change threshold value and change
close all
clear all

%several threshold values to sweep for the ROC
threshold_vec = [0:.05:1];
Sensitivity_vector = zeros(40,length(threshold_vec));
Specificity_vector = zeros(40,length(threshold_vec));

%Select a threshold and start running the relevant code
for threshold_iterator = 1:length(threshold_vec)
    threshold2 = threshold_vec(threshold_iterator);
    Packing_MLS_droplets_simulation_MAIN
    fprintf('%i',threshold_iterator)

    %The matrices here are the sensitivity and 1-specificity of the
    %resulting analysis
    Sensitivity_vector(:,threshold_iterator) = sens;

    Specificity_vector(:,threshold_iterator) = one_minspec;
end

```

```
%create ROCs curves
% close all
% clear all
```

67



```

1 1 1 1 1 1 1 1 1 1 1 1 1 1 1 1 1 1
0.5 0.5 0
1 1 1 1 1 1 1 1 1 1 1 1 1 1 1 1 1 1
0.5 0.5 0
1 1 1 1 1 1 1 1 1 1 1 1 1 1 1 1 1 0.5
0.5 0.5 0
1 1 1 1 1 1 1 1 1 1 1 1 1 1 1 1 1 0.5
0.5 0.5 0
1 1 1 1 1 1 1 1 1 1 1 1 1 1 1 1 1 1
0.5 0.5 0
1 1 1 1 1 1 1 1 1 1 1 1 1 1 1 1 1 0.5
0.5 0.5 0
1 1 1 1 1 1 1 1 1 1 1 1 1 1 1 1 1 0.5
0.5 0.5 0
1 1 1 1 1 1 1 1 1 1 1 1 1 1 1 1 0.5 0.5
0.5 0.5 0
1 1 1 1 1 1 1 1 1 1 1 1 1 1 1 1 1 0.5
0.5 0.5 0
1 1 1 1 1 1 1 1 1 1 1 1 1 1 1 1 1 0.5
0.5 0.5 0
1 1 1 1 1 1 1 1 1 1 1 1 1 1 1 1 1 0.5
0.5 0.5 0
1 1 1 1 1 1 1 1 1 1 1 1 1 1 1 1 1 0.5
0.5 0.5 0
1 1 1 1 1 1 1 1 1 1 1 1 1 1 1 1 1 0.5
0.5 0.5 0
];

```

```

%oneminusspec

```

```

one_min_spec = [49.5 10 3.5 1 0 0 0 0 0 0 0 0 0 0 0 0 0
0 0 0 0 0 0 0 0
46.5 10.5 4.5 1 0 0 0 0 0 0 0 0 0 0 0 0 0
0 0 0 0 0
49.5 12 5.5 1 0 0 0 0 0 0 0 0 0 0 0 0 0
0 0 0 0
45 12.5 3.5 1.5 0.5 0 0 0 0 0 0 0 0 0.5 0 0.5 0
0 0 0 0
47.5 11 4.5 1.5 1 0 0 0.5 0 0 0 0 0 0.5 0 0 0
0 0 0 0
49.5 13 5 2.5 0.5 0 0 0 0 0 0 0 0 0 0 0 0
0 0 0 0
51 12.5 6.5 1.5 0 0 0 0 0 0 0 0 0 0 0 0 0
0 0 0 0
54 15 6.5 2.5 1 0 0 0 0 0 0 0 0 0 0 0 0
0 0 0
52.5 13 4 3 0.5 0 0 0 0 0 0 0 0 0 0 0 0
0 0 0 0
51 13.5 5 2.5 1 0 0 0 0 0 0 0 0 0 0 0 0
0 0 0 0

```

```

51.5    13    5    2.5 1    0.5 0    0    0    0    0    0    0    0    0    0    0    0
0    0    0    0
50    14.5    6    1.5 1.5 0.5 0    0    0    0    0    0    0    0    0    0    0    0
0    0    0    0
51.5    13    4    1    1    0    0    0    0    0    0    0    0    0    0    0    0
0    0    0    0
52    13.5    5.5 1    0.5 0    0    0    0    0    0    0    0    0    0    0    0    0
0    0    0    0
44.5    12.5    7.5 1    1    0.5 0    0    0    0    0    0    0    0    0    0    0
0    0    0    0
51    12.5    6    1    1    0    0    0    0    0    0    0    0    0    0    0    0    0
0    0    0    0
46.5    12.5    8.5 2.5 0.5 0    0    0    0    0    0    0    0    0    0    0    0
0    0    0    0
47.5    13    5    2    0.5 0    0    0    0    0    0    0    0    0    0    0    0    0
0    0    0    0
50    10.5    5    1.5 0    0    0    0    0    0    0    0    0    0    0    0    0    0
0    0    0    0
47.5    13    4.5 1.5 0    0    0    0    0    0    0    0    0    0    0    0    0    0
0    0    0    0
47    13    5.5 0.5 0    0    0    0    0    0    0    0    0    0    0    0    0    0
0    0    0
52.5    13.5    5    1    0    0    0    0    0    0    0    0    0    0    0    0    0
0    0    0    0
46.5    14    6    1.5 0    0    0    0    0    0    0    0    0    0    0    0    0    0
0    0    0    0
50    15.5    5.5 1    0    0    0    0    0    0    0    0    0    0    0    0    0    0
0    0    0    0
50    13    5.5 1.5 0    0    0    0    0    0    0    0    0    0    0    0    0    0
0    0    0
50    13.5    7    1.5 0    0    0    0    0    0    0    0    0    0    0    0    0    0
0    0    0    0
51    12    6    1    0    0    0    0    0    0    0    0    0    0    0    0    0    0
0    0    0
46    13    6    1.5 0    0    0    0    0    0    0    0    0    0    0    0    0    0
0    0    0
47    12.5    5    2    0    0    0    0    0    0    0    0    0    0    0    0    0    0
0    0    0    0
52.5    13    6.5 2    0    0    0    0    0    0    0    0    0    0    0    0    0    0
0    0    0    0
51.5    12.5    5.5 1.5 0    0    0    0    0    0    0    0    0    0    0    0    0    0
0    0    0    0
46.5    14    4.5 2    0    0    0    0    0    0    0    0    0    0    0    0    0    0
0    0    0    0
45    13.5    5.5 1.5 0    0    0    0    0    0    0    0    0    0    0    0    0    0
0    0    0    0
47    12.5    5.5 1    0    0    0    0    0    0    0    0    0    0    0    0    0    0
0    0    0    0
52.5    13    6.5 0.5 0    0    0    0    0    0    0    0    0    0    0    0    0    0
0    0    0    0
];

% one_min_spec=one_min_spec';
% sens=sens';

```

```

figure
[ m n ] = size(sens);

%since we cannot interpolate with the same set of values, we add a tiny
%amount just to separate overlapping datapoints so that the
interpolation
%algorithm can work.
for i =1:m
    for j = 1:n
        one_min_spec(i,j) = one_min_spec(i,j) + .0001*j;
    end
end

figure
plot(one_min_spec(1,:),sens(1,:), 'LineWidth',2)
hold on
plot(one_min_spec(3,:),sens(3,:), 'LineWidth',2)
plot(one_min_spec(5,:),sens(5,:), 'LineWidth',2)
plot(one_min_spec(10,:),smooth(sens(10,:),3), 'LineWidth',2)
plot(one_min_spec(15,:),smooth(sens(15,:),3), 'LineWidth',2)
plot(one_min_spec(20,:),smooth(sens(20,:),3), 'LineWidth',2)
legend(' 1',' 3',' 5',' 10',' 15',' 20')
axis([-0.05 1.05 -0.05 1.05])

xq = 0:.01:1;
for i = 1:m
    x = one_min_spec(i,:);
    v = sens(i,:);
    vq1 = interp1(x,v,xq,'pchip');
    interp_plots(i,1:length(vq1)) = vq1;
end
[o p ] = size(interp_plots);

figure
for i = 1:m
    AUC(i) = sum(interp_plots(i,2:end))/(p-1);
end
AUC = smooth(AUC,4);
plot(AUC, 'LineWidth',2)

title('AUC v droplets in DC')
xlabel('Droplets overlapping')
axis([0 30 0 1])

figure
plot(xq,interp_plots(1,:), 'LineWidth',2)
hold on
plot(xq,interp_plots(3,:), 'LineWidth',2)
plot(xq,interp_plots(5,:), 'LineWidth',2)
plot(xq,interp_plots(10,:), 'LineWidth',2)
plot(xq,interp_plots(15,:), 'LineWidth',2)
plot(xq,interp_plots(20,:), 'LineWidth',2)

```

```

legend(' 1',' 3',' 5',' 10',' 15',' 20')
axis([-0.05 1.05 -0.05 1.05])

```

```

interp_plots = interp_plots';
xq = xq';

```

```

%the following loads the data from an example set and plots the
resulting
% AUCS
% figure
% load('AUC_AC.mat')
% load('AUC_DC.mat')
% figure
% plot(AUC_DC, 'LineWidth', 2)
% hold on
% plot(AUC_AC, 'LineWidth', 2)

```

~~~~~ uMD\_Video\_Analysis-code

The following files carry out the functions described:

The files follow the workflow described in Figure 2:

```

uMD_Initialize_Code.m
%initializes all variables such as expected signals, camera parameters,
etc.
%sets the frames to view within the video to start analysis
%calls Frame_Undistortion to start a chain to .m files that creates a
matrix where correlations are stored
%once the vector is saved into a .mat file that can also be accessed
later as done typically...
%calls Corr_Hough_matrix_script to begin a chain for peak finding
analysis

```

```

Frame_Undistortion.m
%uses camera parameters to undistort spherical aberrations and rotates
any offsets
%calls Frame_segmentation

```

```

Frame_segmentation.mat
%segments the frame into N channels and stores the vector into a 1d
line vector
%sends 1d line vector to Segmented_1D_CrossCorr_PhaseVel

```

```

Segmented_1D_CrossCorr_PhaseVel.m
%loops through phase and for each phase, begins proper correlation
initiation
%after calling Cross_Corr_no_graphs.m, it finds the optimal phase and
velocity

```

```

Cross_Corr_no_graphs.m

```

```
%begins a 2d correlation for the input signal and the selected expected
signal based on the phase
%finds the best matching velocity for the given phase after searching
through the 2d map
```

```
Corr_Hough_matrix_script.m
%loads the correlation matrix and begins to search for each segmented
channel, how droplets travel through sequentially
%calls detect_real_droplets
```

```
detect_real_droplets.m
%searches through the passed 2d matrix for a given segmented channel if
droplets appear more than 2+ frame in series
%based on expected velocity to designate as a true positive
```

uMD_Initialize_Code.m

```
%initializes all variables such as expected signals, camera parameters,
etc.
%sets the frames to view within the video to start analysis
%calls Frame_Undistortion to start a chain to .m files that creates a
matrix where correlations are stored
%once the vector is saved into a .mat file that can also be accessed
later as done typically...
%calls Corr_Hough_matrix_script to begin a chain for peak finding
analysis
```

```
close all force
clear all
% parpool
%uncommenting the above can start the parallel computing toolbox if
%available in matlab. Doing so increases computational speed
significantly
```

```
%initialize variables
```

```
x1 = 0 ;
x2 = 0;
y1 = 0;
y2 = 0;
inc = 0;
```

```
%load the MLS that was used in the Arduino Code
```

```
MLS_seq = [-1, 1, -1, 1, -1, 1, 1, -1, -1, 1, 1, -1, 1, 1, 1, -1,
1, 1, -1, 1, -1, -1, 1, -1, -1, 1, 1, 1, -1, -1, -1, 1, -1, 1,
1, 1, 1, -1, -1, 1, -1, 1, -1, -1, -1, 1, 1, -1, -1, -1, -1,
1, -1, -1, -1, -1, -1, 1, 1, 1, 1, 1, 1];
```

```
%load camera params once to fix image distortion
```

```
%The main variables that affect spherical distortion is
```

```
'RadialDistortion'
```

```
load('cameraParams1.mat')
```

```
cameraParams2 = cameraParameters('IntrinsicMatrix',
[716,0,0;0,716,0;1920/2,1080/2,1],...
```

```
    'RadialDistortion',[.06,0.0,.00],...
```

```
    'TangentialDistortion',[0,0],...
```

```

    'RotationVectors',[0 0 0],...
    'TranslationVectors',[0 0 0],...
    'ReprojectionErrors',[0 0],...
    'WorldPoints',cameraParams1.WorldPoints,...
    'WorldUnits',cameraParams1.WorldUnits,...
    'EstimateSkew',cameraParams1.EstimateSkew,...

    'NumRadialDistortionCoefficients',cameraParams1.NumRadialDistortionCoefficients,...

    'EstimateTangentialDistortion',cameraParams1.EstimateTangentialDistortion);

%select amount of channels and segment based on the pixels per channel
segmented_ch_num = 120;
pixels_per_ch = floor(1080/segmented_ch_num);

%load the interpolated masks. these represent the expected signal
%NOTE: the interpolated masks can change to fit the velocity range
required
%and can be increased or shortened to improve computation. In this
%particular case, the range was chosen to match the data, and
obviously,
%larger ranges with finer resolution will always work but the tradeoff
is
%computation time.
load('All_Interpolated_Masks.mat')

%the table below has several values, but the main ones that are
relevant
%are the first entry which is the filename of a video to be analyzed,
and
%the last term (flip) which represents the direction the droplets are
going
%in.

%Droplets can either go left to right or right to left based on how the
%chpi is attached; the flip vector properly selects the option

%The remaining variables can be ignored for this code.
data_table = {'20160927_165111.mp4' 27 7 624 800 1142 800 0 624
392 1142 377 624 1142 1};
load('cmap2.mat')

filename = data_table{1}; frame = data_table{2};
flip = data_table{15}; inc = data_table{8};
x1 = data_table{4}; y1 = data_table{5}-inc; x2 = data_table{6}; y2 =
data_table{7} -inc;
%bead two start and end
x3 = data_table{9}; y3 = data_table{10}; x4 = data_table{11}; y4 =
data_table{12};
dropletstart = data_table{13}; dropletend = data_table{14};

```

```

startframe = 450; endframe = 650; %select frames in video to analyze
%a portion of the video is analyzed since there may be a lag time for
%droplets to reach the proper velocity initially, saving computation
time.

%select the background frame to subtract out background signal in the
%algorithm
background_frame = 1;
v_file = VideoReader(filename);
video_frame = read(v_file,background_frame);
R_channel = video_frame(:,:,1);
R_background = R_channel;

%begin loop through each frame
for framestoprocess = 1:endframe-startframe+1
    framenum=framestoprocess ;
    frame = startframe+framestoprocess-1;
    fprintf(num2str(framestoprocess))
    %%%%%%%%%%%%% Workflow Chain Begins
    %%%%%%%%%%%%%
    Frame_Undistortion

end

%save the correlation results in a matrix for analysis later if
necessary
save('Frames450to650.mat','-v7.3','corr_matrix_final')
%begin analysis on the correlation matrix
Corr_Hough_matrix_script

```

Frame_Undistortion.m

```

%uses camera parameters to undistort spherical aberrations and rotates
any offsets
%calls Frame_segmentation

close all

%load frame and subtract background
video_frame = read(v_file,frame);
img = video_frame;
red = img(:,:,1)-R_background; % Red channel

%undistort with camera parameters chosen
[J1] = undistortImage(red, cameraParams2);

%define angle to rotate image
x_ang_1 = 607; y_ang_1 = 669;
x_ang_2 = 1435; y_ang_2 = 655 ;

```

```

J1 = imrotate(J1,rad2deg(atan((y_ang_2-y_ang_1)/(x_ang_2-x_ang_1))));
%resize properly. during this portion, we lose several channels that
can be
%imaged but are too distorted at the edges on the top and bottom.
J1 = J1(57:1026,119:1835,:);
red = imresize(J1,[1080 1920]);

%begin segmenting each channel to create 1D line vectors
Frame_segmentation

Segmented_1D_CrossCorr_PhaseVel.m
%loops through phase and for each phase, begins proper correlation
initiation
%after calling Cross_Corr_no_graphs.m, it finds the optimal phase and
velocity

%store the 1d vector in a variable
Patterned_droplet = droplet_line;
whatbead = 1;

sig = Patterned_droplet;

%if droplets flow in reverse direction, we can flip the 1d line vector
for
%correlation here
if flip ==1
    sig = fliplr(sig);
end

%begin looping through phase. phase is defined as when the MLS starts,
so
%since the MLS is cyclical, we simply begin at the next cycle of the
MLS to
%loop through the phase
for phase = 1:4:length(MLS_seq)
    %for each phase, store the output into a 2d matrix
    Cross_Corr_no_graphs
    Final_vec_before_phase(phase,1:mat_b) = FINAL_CORR_VECTOR;
end

%find the optimal fit for all the phases
[I,J] = find(Final_vec_before_phase==max(max(Final_vec_before_phase)));
max_corr_Vec_phase = fliplr(Final_vec_before_phase(I(1),:));

Cross_Corr_no_graphs.m
%begins a 2d correlation for the input signal and the selected expected
signal based on the phase
%finds the best matching velocity for the given phase after searching
through the 2d map

```



```

%To vary the range of velocities to scan, this variable can be altered.
%Preallocating the expected signal improves computational time.
Signal_Mat(:, :) = All_Interpolated_Masks(phase, :, :);
ma = Signal_Mat;
out8=xcorr2(sig,ma);
[mat_a mat_b] = size(out8);
%store the length of each MLS for different velocities to normalize
later
flipped_vec = fliplr(lengths_vector);
out8_new = zeros(mat_a,mat_b);

%take correlatoins and normalize by length of the mask
for i = 1:mat_a
    out8_new(i,1:mat_b) = out8(i,:)/flipped_vec(i);
end

%select the velocity that generates the largest peak.
[M,N] = find(out8_new==max(max(out8_new)));
Max_out = out8_new(M(1),:);

%Filter to get rid of DC effects
Fs = 1920;
half_freq = Fs/2;
notch_freq_filter = 1;
low_freq_filt = 1;
smoothing_factor = 1;
w0=notch_freq_filter/half_freq;
[num,den]=iirnotch(w0,w0/35,-45);
[a,b]=butter(2,low_freq_filt/half_freq,'high'); %remove low frequency
components

y=filter(num,den,Max_out);
yfil=filtfilt(a,b,y);
ysm=smooth(yfil,smoothing_factor);

FINAL_CORR_VECTOR = (ysm);

```

Corr_Hough_matrix_script.m

```

%loads the correlation matrix and begins to search for each segmented
channel, how droplets travel through sequentially
%calls detect_real_droplets
clear all
load('Frames450to650.mat')
clear loc_info_all
load('cmap2.mat')
%it may be useful to segment the vector into smaller pieces to analyze
% corr_matrix_final = corr_matrix_final(1+50*3:51+50*3, :, :);
[frames_total, numberofchannels ,framelengtha] =
size(corr_matrix_final);

```

```

%if the droplet was going in the reverse direction, the direction the
%droplet peaks move can be reversed if the proper flip variable was not
%set; rearranging the correlations can correct this
% for i = 1:numberofchannels-1
%     corr_matrix_final(:,i,:) = flipud(corr_matrix_final(:,i,:));
% end

%plot everything frame by frame
warning('off','all')
%convert the 3d matrix into a 1d for each channel

%count all the peaks in a certain channel
max_entire_vector = max(max(max(corr_matrix_final)));
numberofdroplets = zeros(numberofchannels);
allchannelsvectors =
zeros(numberofchannels,frames_total*framelengtha);
threshold2 = max_entire_vector*.4; %set threshold

%for each channel, loop through all the frames and begin counting
for chan_loop_2 = 1:numberofchannels
    for chan_loop_2_2 = 1:frames_total
        corr_matrix_per_channel(chan_loop_2_2,1:framelengtha) =
corr_matrix_final(chan_loop_2_2,chan_loop_2,:);
    end
    %for a particular channel, send the data to analyze to:
    detect_real_droplets
    %store detected droplets into a matrix for each channel
    n_matrix(chan_loop_2) = num_totalpeaks_final;
    nonzero_perchannel_matrix(chan_loop_2,:) = nonzeros_per_channel;
end

%calculates the total number of droplets in the matrix
sum(n_matrix)

```

detect_real_droplets.m

```

%detect peaks in array
%searches through the passed 2d matrix for a given segmented channel if
droplets appear more than 2+ frame in series
%based on expected velocity to designate as a true positive

%initialize variables and input data
hough_array = corr_matrix_per_channel';
[hough_array_a, hough_array_b] = size(hough_array);
loc_info_all = zeros(hough_array_b+3,20);
full_matrix_pks_locs = zeros(hough_array_b,100,100);

for i = 1:hough_array_b
    %find peaks in the data based on the threshold set and the expected
    %minimum distance between droplets

```

```

[pks,locs] =
findpeaks(hough_array(:,i), 'MinPeakDistance',20, 'MinPeakHeight',thresho
ld2);
%store the pk values and the locations in a matrix
full_matrix_pks_locs(i,1:length(locs),1:2) = [pks locs];
loc_info_all(i,1:length(locs)) = locs;
end

%find the total number of peaks that were found in the matrix by
%counting all entires that are nonzero as peaks that passed the
%thresholding step
num_totalpeaks_initial = nnz(loc_info_all);

%we now loop through and find repeating peaks.
%if peaks are within the expected velocity range, and occur at least
twice
%we count them as real droplets. If a peak only occurs once with no
%followup, this can be attributed to noise.
expected_velocity = 540;
range = 50;
for i = 1:hough_array_b
    set_of_locs = loc_info_all(i,:);
    for j = 1:length(set_of_locs)
        if set_of_locs(j) ~=0
            repeatcount = 0; %this variable checks if a droplet was
able to be seen two or three times successfully.
            locationvalue = set_of_locs(j);
            nextlocationvalue = locationvalue+expected_velocity; %this
finds the next location value based on the ranges selected
            set_of_locs2 = loc_info_all(i+1,:);
            for k=1:length(set_of_locs2)
                if set_of_locs2(k)>nextlocationvalue-range &&
set_of_locs2(k)<nextlocationvalue+range
                    repeatcount = 1; %if a droplet is within the range,
this means a peak was successfully found in the given range of
prediction
                    if repeatcount==1
                        nextlocationvalue2 = nextlocationvalue
+expected_velocity; %look for a third peak
                        set_of_locs3 = loc_info_all(i+2,:);
                        for l=1:length(set_of_locs2)
                            if
set_of_locs3(l)>nextlocationvalue2-range &&
set_of_locs3(l)<nextlocationvalue2+range
                                repeatcount = 2;
                                if repeatcount==2
                                    loc_info_all(i+2,l) = 0;
break %set repeat peaks to 0 so droples are not overcounted (three
peaks case)
                                end
                                end
                                end
                                loc_info_all(i+1,k) = 0; %set repeat peaks to 0 so
droples are not overcounted (two peaks case)

```

```

                                break
                                %in cases of repeat peaks, the original location
still
                                %remains, so this is the peak that gets counted as
a
                                %true positive
                                end
                                end
                                end
                                if repeatcount==0
                                    loc_info_all(i,j) = 0; %if a droplet was only detected
one time, then discard it. This peak corresponds to a false positive
                                end
                                end
                                end
end

%find all the remaining peaks that correspond to true droplets rather
than
%repeat peaks or single peaks from noise.
num_totalpeaks_final = nnz(loc_info_all);
nonzeros_per_channel= sum(loc_info_all~=0,2);
~~~~~ 2016111_uMD_App_Final_Package_COMPLETE

```

MainActivity.java

```

package vraviy.exosomedetection;

import android.app.Notification;
import android.app.NotificationManager;
import android.app.PendingIntent;
import android.content.ComponentName;
import android.content.Context;
import android.content.pm.PackageManager;
import android.graphics.Bitmap;
import android.media.MediaMetadataRetriever;
import android.support.v4.app.NotificationCompat;
import android.support.v7.app.AppCompatActivity;
import android.os.Bundle;
import android.view.Menu;
import android.view.MenuItem;
import java.io.File;
import java.io.FilenameFilter;
import java.util.Arrays;
import android.app.Activity;
import android.app.AlertDialog;
import android.app.AlertDialog.Builder;
import android.app.Dialog;
import android.content.DialogInterface;
import android.content.Intent;
import android.content.SharedPreferences;
import android.database.Cursor;
import android.graphics.Color;

```

```

import android.net.Uri;
import android.os.Bundle;
import android.os.Environment;
import android.preference.PreferenceManager;
import android.provider.MediaStore;
import android.provider.MediaStore.MediaColumns;
import android.util.Log;
import android.view.Menu;
import android.view.MenuInflater;
import android.view.MenuItem;
import android.view.MotionEvent;
import android.view.View;
import android.view.View.OnClickListener;
import android.widget.Button;
import android.widget.ImageView;
import android.widget.TextView;
import android.widget.Toast;
import android.widget.VideoView;
import java.util.HashMap;
import java.lang.Object;

public class MainActivity extends AppCompatActivity implements
OnClickListener{

    private static final int SELECT_VIDEO = 1;
    private static final int RECORD_VIDEO = 2;
    // private static final int SELECT_GIF = 3;
    private static final String TAG = "MainActivity";
    private NotificationManager notificationManager;
    MediaMetadataRetriever retriever = new MediaMetadataRetriever();
    //FFmpegMediaMetadataRetriever retriever = new
    FFmpegMediaMetadataRetriever();

    private VideoView selected_video;

    //Getting video dimensions for pixels
    private int vid_width = 0;
    private int vid_height = 0;

    //Frames from video

    ImageView img, img2, img3, img4, img5, img6, img7, img8, img9,
    img10;
    ImageView imageView;
    TextView textview_ratio, t0,t1,time0_text,time5_text,time10_text;
    TextView rotatedYLabel;
    @Override
    protected void onCreate(Bundle savedInstanceState) {
        super.onCreate(savedInstanceState);
        if(savedInstanceState != null){
            Log.d("STATE",savedInstanceState.toString());

```

```

    }

    setContentView(R.layout.activity_main);

    setupButtonClickListeners();

    notificationManager = (NotificationManager)
        getSystemService(Context.NOTIFICATION_SERVICE);

    CharSequence tickerText = "Hello";
    long when = System.currentTimeMillis();
    NotificationCompat.Builder mBuilder = new
NotificationCompat.Builder(this)
        .setSmallIcon(R.mipmap.ic_launcher)
        .setContentTitle("Microdroplet Detector");
    Intent resultIntent = new Intent(this, MainActivity.class);
    PendingIntent resultPendingIntent = PendingIntent.getActivity(
        this,
        0,
        resultIntent,
        PendingIntent.FLAG_UPDATE_CURRENT);
    mBuilder.setContentIntent(resultPendingIntent);
    Notification notification = mBuilder.build();
    notification.flags |= Notification.FLAG_NO_CLEAR |
Notification.FLAG_ONGOING_EVENT;

    NotificationManager mNotifyMgr = (NotificationManager)
getSystemService(NOTIFICATION_SERVICE);
    mNotifyMgr.notify(1, notification);

}

private void setupButtonClickListeners()
{
    //Button exitButton = (Button)findViewById(R.id.exit);
    //exitButton.setOnClickListener(this);

    ((Button)findViewById(R.id.GalleryButton)).setOnTouchListener(this);

    ((Button)findViewById(R.id.RecordButton)).setOnTouchListener(this);

    ((Button)findViewById(R.id.Matlabbutton)).setOnTouchListener(this);

}

@Override
public void onActivityResult(int requestCode, int resultCode,
Intent data)
{
    Log.d("CREATION", "Clicked button");
}

```

```

//      Intent browserIntent = new Intent(Intent.ACTION_VIEW,
Uri.parse("https://drive.matlab.com"));
//      startActivity(browserIntent);

}

private void VideoAnalysis(String path) {

    retriever.setDataSource(path);

    imageView.setImageBitmap(retriever.getFrameAtTime(1000000,
MediaMetadataRetriever.OPTION_CLOSEST));

}

private String getPath(Uri uri)
{
    //file:///mnt/sdcard/DCIM/Camera/VID_20111217_233451.mp4

    if(uri.toString().contains("content"))
    {
        try
        {
            String[] projection = {MediaColumns.DATA};
            Cursor cursor =
managedQuery(uri,projection,null,null,null);
            int column_index =
cursor.getColumnIndex(MediaColumns.DATA);
            cursor.moveToFirst();
            return cursor.getString(column_index);
        }
        catch(Exception ex)
        {
            return null;
        }
    }
    else
    {
        return uri.toString();
    }
}

private void handleClickEvent(View v)
{
    switch(v.getId())
    {
        case R.id.GalleryButton:
            Intent browserIntent = new Intent(Intent.ACTION_VIEW,
Uri.parse("https://drive.matlab.com"));
            startActivity(browserIntent);

```

```

//          Intent intent = new Intent();
//          intent.setType("video/*");
//          intent.setAction(Intent.ACTION_GET_CONTENT);
//
startActivityForResult(Intent.createChooser(intent, "Select
Video"), SELECT_VIDEO);
        //image/*
        break;
    case R.id.RecordButton:
        Intent recordIntent = new Intent();

recordIntent.setAction(MediaStore.ACTION_VIDEO_CAPTURE);
        recordIntent.putExtra(MediaStore.EXTRA_VIDEO_QUALITY,
1);
        //recordIntent.putExtra(MediaStore.EXTRA_OUTPUT,
Uri.fromFile(file));
        startActivity(recordIntent, RECORD_VIDEO);
        break;
    case R.id.Matlabbutton:
//          Intent intent = new Intent(Intent.ACTION_MAIN);
//
intent.setComponent(ComponentName.unflattenFromString("com.mathworks.ma
tlabmobile"));
//          intent.addCategory(Intent.CATEGORY_LAUNCHER);
//          startActivity(intent);

        PackageManager pm = this.getPackageManager();
        Intent appStartIntent =
pm.getLaunchIntentForPackage("com.mathworks.matlabmobile");
        if (null != appStartIntent)
        {
            this.startActivity(appStartIntent);
        }

        break;
    }
}

// #FFA500
@Override
public boolean onTouch(View v, MotionEvent event) {
    switch(event.getAction())
    {
        case MotionEvent.ACTION_DOWN:
            switch(v.getId())
            {
                case R.id.GalleryButton:

// ((Button) findViewById(R.id.GalleryButton)).setBackgroundColor(0xFFFFFA
500);

                break;
                case R.id.RecordButton:

```



```

//
((Button)findViewById(R.id.RecordButton)).setBackgroundColor(0xFFFFA500);

        break;

    }
    return true;
case MotionEvent.ACTION_UP:
    switch(v.getId())
    {
        case R.id.GalleryButton:
            //
            ((Button)findViewById(R.id.GalleryButton)).setBackgroundColor(Color.BLACK);

            handleClickEvent(v);
            break;
        case R.id.RecordButton:
            //
            ((Button)findViewById(R.id.RecordButton)).setBackgroundColor(Color.BLACK);

            handleClickEvent(v);
            break;
        case R.id.Matlabbutton:
            //
            ((Button)findViewById(R.id.RecordButton)).setBackgroundColor(Color.BLACK);

            handleClickEvent(v);
            break;
    }

    default:
        return true;
}

}

//In an Activity
private String[] mFileList;
private File mPath;
private String mChosenFile;
private static final String FTYPE = ".gif";
private static final int DIALOG_LOAD_FILE = 1000;

private void loadFileList(){

    try
    {
        mPath = new
File(getApplicationContext().getExternalFilesDir(null).getAbsolutePath()
) + "/" );
        Log.i(TAG,"loadFileList() path: " + mPath.getAbsolutePath()
+ "/" );
    }
    catch(Exception ex)
    {

```

```

        mPath = null;
        return;
    }
    try{
        mPath.mkdirs();
    }
    catch(SecurityException e){
        Log.e(TAG, "unable to write on the sd card " +
e.toString());
    }
    if(mPath.exists()){
        FilenameFilter filter = new FilenameFilter(){
            @Override
            public boolean accept(File dir, String filename){
                File sel = new File(dir, filename);
                return filename.contains(FTYPE) ||
sel.isDirectory();
            }
        };
        mFileList = mPath.list(filter);
    }
    else{
        mFileList= new String[0];
    }
}

@Override
public boolean onCreateOptionsMenu(Menu menu) {
    // Inflate the menu; this adds items to the action bar if it is
present.
    getMenuInflater().inflate(R.menu.menu_main, menu);
    return true;
}

@Override
public boolean onOptionsItemSelected(MenuItem item) {
    // Handle action bar item clicks here. The action bar will
    // automatically handle clicks on the Home/Up button, so long
    // as you specify a parent activity in AndroidManifest.xml.
    int id = item.getItemId();

    //noinspection SimplifiableIfStatement
    if (id == R.id.action_settings) {
        return true;
    }

    return super.onOptionsItemSelected(item);
}
}

```

CHAPTER 3: MOBILE PLATFORM FOR RAPID SUB PG/ML, MULTIPLEXED, DIGITAL DROPLET DETECTION OF PROTEINS

This chapter is a slightly modified version of a manuscript published in PNAS:

V Yelleswarapu, J Buser, M Haber, J Baron, E Inapuri, D Issadore. Mobile platform for rapid sub-picogram-per-milliliter, multiplexed, digital droplet detection of proteins. *PNAS*, 116, 4489–4495 (2019).

V.Y., J.R.B., and D.I. designed research; V.Y., M.H., J.B., and E.I. performed research; V.Y. contributed new reagents/analytic tools; V.Y. analyzed data; and V.Y. and D.I. wrote the paper.

3.1 Significance statement

Digital assays have enormous untapped potential for diagnostics, environmental surveillance, and biosafety monitoring, but are currently confined to laboratory settings due to the instrumentation necessary to generate, control, and measure millions of droplets. We instead use a mobile phone-based imaging technique that is >100x faster than conventional microfluidic droplet detection, does not require expensive optics, is invariant to flow-rate, and can simultaneously measure multiple fluorescent dyes in droplets. By using this time-domain modulation with cloud computing, we overcome the low frame rate of digital imaging, and achieve throughputs as high as one million droplets per second. We integrate on-chip delay lines and a microbead processing unit, resulting in a robust device, suitable for a low-cost implementation, with ultra-sensitive measurement capabilities.

3.2 Abstract

Digital droplet assays - in which biological samples are compartmentalized into millions of femtoliter-volume droplets and interrogated individually - have generated enormous enthusiasm for their ability to detect biomarkers with single-molecule sensitivity. These assays have untapped potential for point-of-care diagnostics but are currently mainly confined to laboratory settings due to the instrumentation necessary to serially generate,

control, and measure tens of millions of droplets / compartments. To address this challenge, we developed an optofluidic platform that miniaturizes digital assays into a mobile format by parallelizing their operation. This technology is based on three key innovations: 1. the integration and parallel operation of a hundred droplet generators onto a single chip that operates >100x faster than a single droplet generator. 2. the fluorescence detection of droplets at >100x faster than conventional in-flow detection using time-domain encoded mobile phone imaging, and 3. the integration of on-chip delay lines and sample processing to allow serum-to-answer device operation. To demonstrate the power of this approach, we performed a duplex digital ELISA. We characterized the performance of this assay by first using spiked recombinant proteins into a complex media (fetal bovine serum) and measured a limit of detection 0.004 pg/mL (300 aM), a 1,000x improvement over standard ELISA and matching that of the existing laboratory-based gold standard digital ELISA system. We additionally measured endogenous GM-CSF and IL6 in human serum from N = 14 human subjects using our mobile duplex assay, and showed excellent agreement with the gold standard system ($R^2 = 0.96$).

3.3 Introduction

Digital droplet-based assays achieve 1000x improved sensitivity over conventional assays by performing millions of assays in parallel within femtoliter volume droplets. This parallelization converts the traditionally analog problem of quantifying biomarkers into a digital one, where each droplet contains either one copy or zero copies of the target molecule. Digital assays have demonstrated enormous utility as a platform for the ultrasensitive detection of nucleic acids^{164–167} and proteins,^{84,85,168–172} as well as the analysis of single cells^{173–176} and single exosomes.¹⁷⁷ Digital enzyme-linked

immunosorbent assays (dELISA)^{86,170,178,179} and digital polymerase chain reaction (dPCR)¹⁸⁰ have found broad utility and have been successful achieving (attogram per mL) sensitivity and high levels of multiplexing for a broad range of targets.¹⁸⁰ In a particularly exciting demonstration, digital assays were recently used to measure both protein and mRNA simultaneously from single cells.¹⁸¹ The improvement in sensitivity of digital assays over conventional assays has allowed measurement of previously undetectable concentrations of clinical biomarkers, opening new opportunities for improved diagnostics and prognostics for applications such as traumatic brain injury, HIV, and early cancer detection.^{119,178,182–185}

Due to digital assays' high sensitivity, their capability for absolute quantification without calibration, and the robustness of digital detections to reaction conditions, they are particularly well-suited for point-of-care diagnostics. However, the instrumentation currently required to generate, process, and detect the many independent reaction vessels for ultrasensitive digital assays has proven cumbersome to implement. The gold standard commercial implementation of dELISA is Quanterix's Simoa^{49,86}, which uses a microfabricated array of 200,000 wells that are each 40 fL. The Simoa HD-1 Analyzer provides a fully automated sample-to-answer readout, capable of being loaded with up to four 96-well ELISA plates. The machine has automated the entire digital ELISA assay, minimizing the time required to process multiple samples through their workflow, resulting in a throughput of 66 samples per hour.⁸⁶ Furthermore, the Simoa HD-1 can perform a multiplexed 10-plex assay on each sample. While the Simoa system has demonstrated the value of ultrasensitive protein detection in a laboratory setting, it requires bulky optics and bulky fluid handling, resulting in a technology not suitable for portable use and that has an instrumentation cost of more than a hundred thousand

dollars. Point-of-care systems have been developed that typically use smaller numbers (< 10,000) of nanoliter wells, much larger than the femtoliter wells used in the ultrasensitive systems,¹⁸⁶ and as a result do not achieve the same sensitivity, dynamic range, or capability for multiplexing.^{132,187,188}

Compared to static arrays, continuous flow microfluidic droplet systems allow much greater numbers of partitions to be analyzed (> 1 million), allowing increased multiplexing, sensitivity, and the capability for downstream sorting of the droplets.^{55,84,171,175,176} However, droplet microfluidic systems are currently hindered by both **1.** the throughput (<10⁴ droplets per sec) at which droplets can be serially generated in microfluidic systems and be monodisperse^{131,189} and **2.** the throughput (<10⁴ droplets per sec) at which the fluorescence of droplets can be detected by flowing them one-by-one through a micrometer-scale laser spot. (**Fig. 1a**) (**SI Appendix, Table S1**)^{55,175,176} An emerging approach to overcome these limitations has been to incorporate many replica generators or detectors that can operate on the same chip in parallel to increase throughput.^{129,131,139,141,190,191} However, it has not yet been possible to fully implement ultrasensitive digital assays into a mobile format due to the required instrumentation to generate the highly controlled flows required for conventional droplet microfluidics,¹⁹² the difficulty of parallelizing the optics necessary for multi-color fluorescence detection, and the challenge of integrating sample preparation.

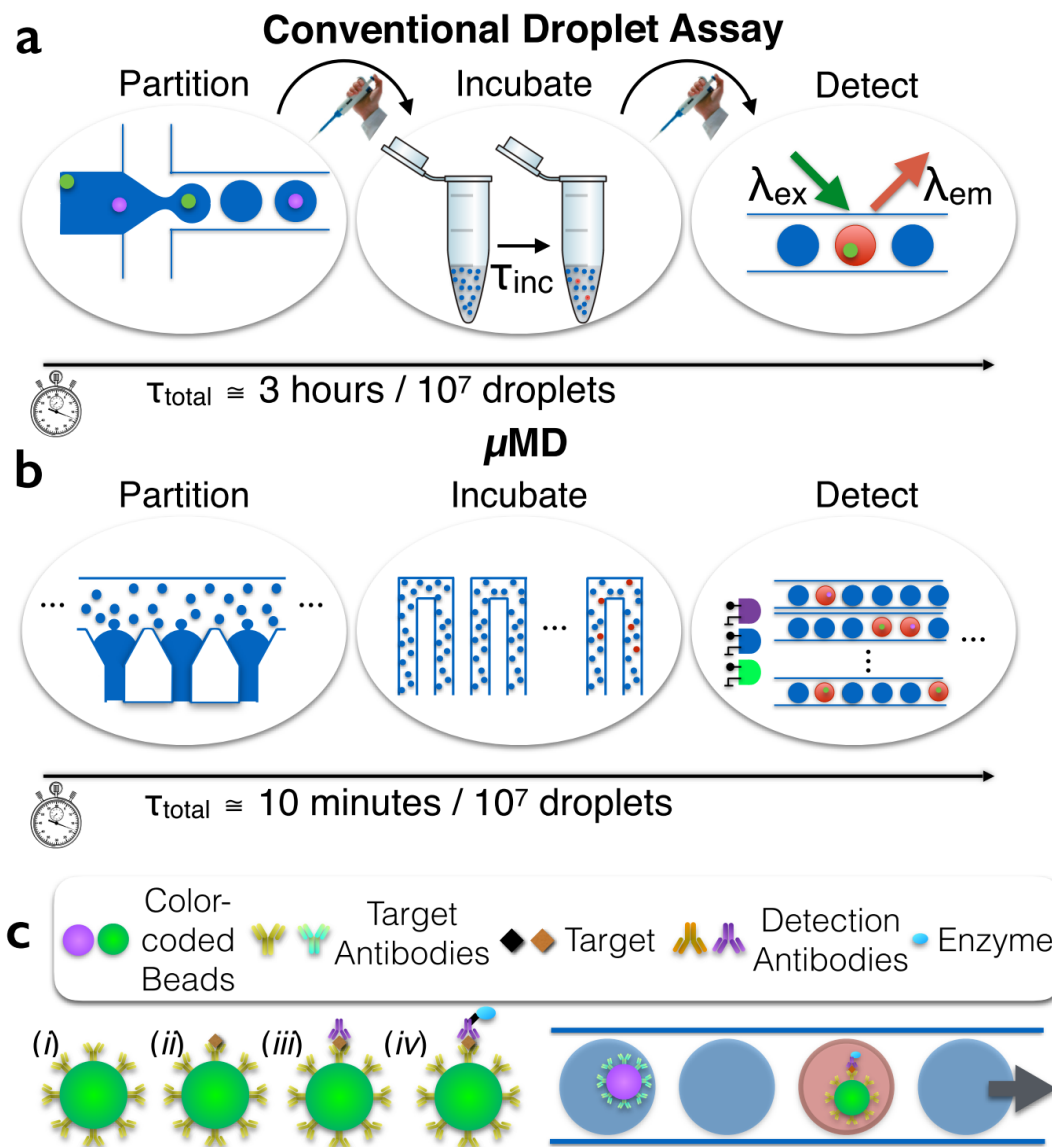


Figure 1. Miniaturization and parallelization of droplet dELISA. **a.** A schematic of the conventional workflow for dELISA, which requires multiple hands-on steps and is rate-limited by the serial partitioning of the sample into droplets and the serial detection of the fluorescence of each individual droplet. **b.** μ MD parallelizes droplet generation, incubation, and detection to miniaturize dELISA fully onto a mobile platform and increase its throughput by 100x. **c.** Antibody-functionalized, color-coded beads are used in a

duplex dELISA assay, wherein individual beads are encapsulated into droplets and read out if they have captured a single target protein.

To address this challenge, we have developed an optofluidic platform, the microdroplet Megascale Detector (μ MD), that miniaturizes digital droplet assays into a mobile device, while matching the limit of detection of the current laboratory-scale gold-standard technology. To achieve this limit of detection in a robust, mobile device, the μ MD is built on three key innovations. (**Fig. 1b**) **1.** Rather than generate droplets one at a time, we instead incorporate a parallelized microfluidic droplet generator that operates $>100\times$ faster than a single droplet generator. Moreover, by making use of the recently published Millipede geometry,¹³¹ the monodispersity of the generated droplets are invariant to flow rate, which allows use of inexpensive peristaltic pumps that can be incorporated into a mobile device. **2.** To rapidly read-out the fluorescence of the droplets ($>10^5$ drops/sec), we use a mobile-phone based imaging technique that is $>100\times$ faster than conventional detection, wherein droplets are detected one-by-one.^{55,176} Our approach does not require expensive optics and is invariant to flow-rate, making it well suited for a mobile implementation¹⁹⁰. The key innovation of this approach is that it overcomes the low frame rate of digital imaging, and can achieve multicolor fluorescence detection, by modulating multiple, differently colored LED/laser diode excitation sources with unique non-periodic signals. The video feed can be decoded to accurately measure each droplet's fluorescent signals at throughputs far exceeding that of the frame rate of the camera, as high as 1 million droplets per second. This work builds on a previously published proof-of-concept device that demonstrated the measurement of only a fluorescent dye in passing droplets,¹⁹⁰ and is here extended to measure three fluorescent channels in each droplet to implement dELISA. **3.** We

integrate a microbead processing unit, droplet generators, on-chip delay lines for droplet incubation, and droplet fluorescence detection, resulting in a robust device, suitable for a low-cost implementation, that allows raw serum to be input and for molecular data to be output.

To demonstrate the power of this approach, we implement multiplexed dELISA using microbeads color-coded with different fluorescent dyes, where the color code corresponds to the protein targeted by its antibody.(**Fig. 1c**) We performed a duplex cytokine assay (GM-CSF, IL6) in serum using UV and green fluorescent beads, where droplets containing a bead with a complete immunocomplex fluoresce red. We accurately measured IL6 and GM-CSF simultaneously in complex media (bovine serum) over four orders of magnitude with a limit of detection as low as 0.004 pg/mL (~300aM) – a thousand-fold improvement over standard ELISA and matching that of the current gold standard digital platform.^{168,169} Our chip is designed for minimal user interaction (**SI Appendix, Vid S1**), has a total droplet processing time of 10 minutes for 10 million droplets, where the workflow encompasses droplet generation, droplet incubation, and fluorescence droplet detection for each sample, and has a prototype instrumentation cost of \$500 and a disposable cost \$5.

3.4 Results and Discussion

μMD Design

The complete workflow of dELISA is incorporated onto our chip,(**Fig. 2a**) and consists of: **1.** A microbead processor where microbeads capture their target proteins from serum, are tagged with enzyme labeled immunocomplexes for downstream amplification within droplets, and are iteratively washed between each labeling step, **2.** a droplet generator, where the microbeads are mixed with the enzyme's substrate and

encapsulated into water-in-oil droplets. **3.** A three-dimensional microfluidic channel that takes 3.2 minutes for the droplets to pass, allowing time for the enzymatic amplification of the fluorescence signal. **4.** A mobile phone based detector, where the droplets' fluorescence are rapidly detected using time-domain encoded optofluidics.

The microbead processor unit consists of a semi-permeable membrane to immobilize the beads. Multiple reagents and washing buffers are sequentially delivered to the immobilized beads, after which the beads are released for downstream analysis. (**Fig. 2b**) One of the populations of color-coded microbeads (Spherotech, $d = 5.4 \mu\text{m}$, $\lambda_{\text{ex}}/\lambda_{\text{em}} = 470/490 \text{ nm}$) is functionalized with antibody for GM-CSF (R&D MAB2172). The other population of beads (Spherotech, $d = 4.5 \mu\text{m}$, $\lambda_{\text{ex}}/\lambda_{\text{em}} = 370/410\text{nm}$) is functionalized with antibody for IL6(MAB206). The beads are first incubated with the sample for 60 minutes, and then immobilized on the membrane. Subsequently, the beads are washed with 1 mL of T20 Buffer at 10 mL/hr, incubated with 0.1 mL of 0.7 nM detection antibody (R&D BAF206, BAM215) in T20 buffer for 30 minutes, washed in 1 mL of T20 Buffer at 10 mL/hr, and subsequently released from the membrane by reversing the flow at 6 mL/hr. The semi-permeable membrane is an $A = 300 \text{ mm}^2$ track etched polycarbonate membrane with $d = 3 \mu\text{m}$ pores. (**Fig. 2a**) The membrane is incorporated into the microfluidic chip using laser cut mylar membrane microfluidics.^{193,194} (**SI Appendix, Fig. S1, S2**) For testing, a syringe pump (Harvard Apparatus) or a low cost peristaltic (Intllab, <\$10) were used.

Downstream of the microbead processor, the released microbeads are mixed with the ELISA substrate (QuantaRed™ Enhanced Chemifluorescent HRP Substrate, Thermo) (**Fig. 2c,d**) and encapsulated into $d = 40 \mu\text{m}$ droplets suspended in QX200™ Droplet Generation Oil (Biorad, 1864006). (**Fig. 2d**) A channel length of 14 mm with a

staggered herringbone design is used to ensure proper mixing of the beads and the substrate, while minimizing background signal that comes from enzymes generating fluorescence signal before they are encapsulated into droplets^{195,196}. (**SI Appendix, Fig. S3**). To generate monodisperse droplets that are robust to flow rate, we used the Millipede geometry described by Amstad et al (Amstad2016). In brief, the millipede uses step emulsification, where the droplet diameter depends only on the channel geometry and not the flow rates of the dispersed or continuous phase over a large range of flow rates. Our device consists of 100 droplet generators to achieve a throughput of 100k droplets/sec. The droplet generator layer has a height $h = 10\text{ }\mu\text{m}$ and the continuous phase layer has a height $h = 120\text{ }\mu\text{m}$. (**SI Appendix, Fig. S2**) Each droplet encapsulates one or zero beads (**Fig. 2d**) by setting the concentration of beads such that there are 10x more droplets than beads, resulting in a 0.5% probability of a droplet containing two beads based on Poisson statistics.

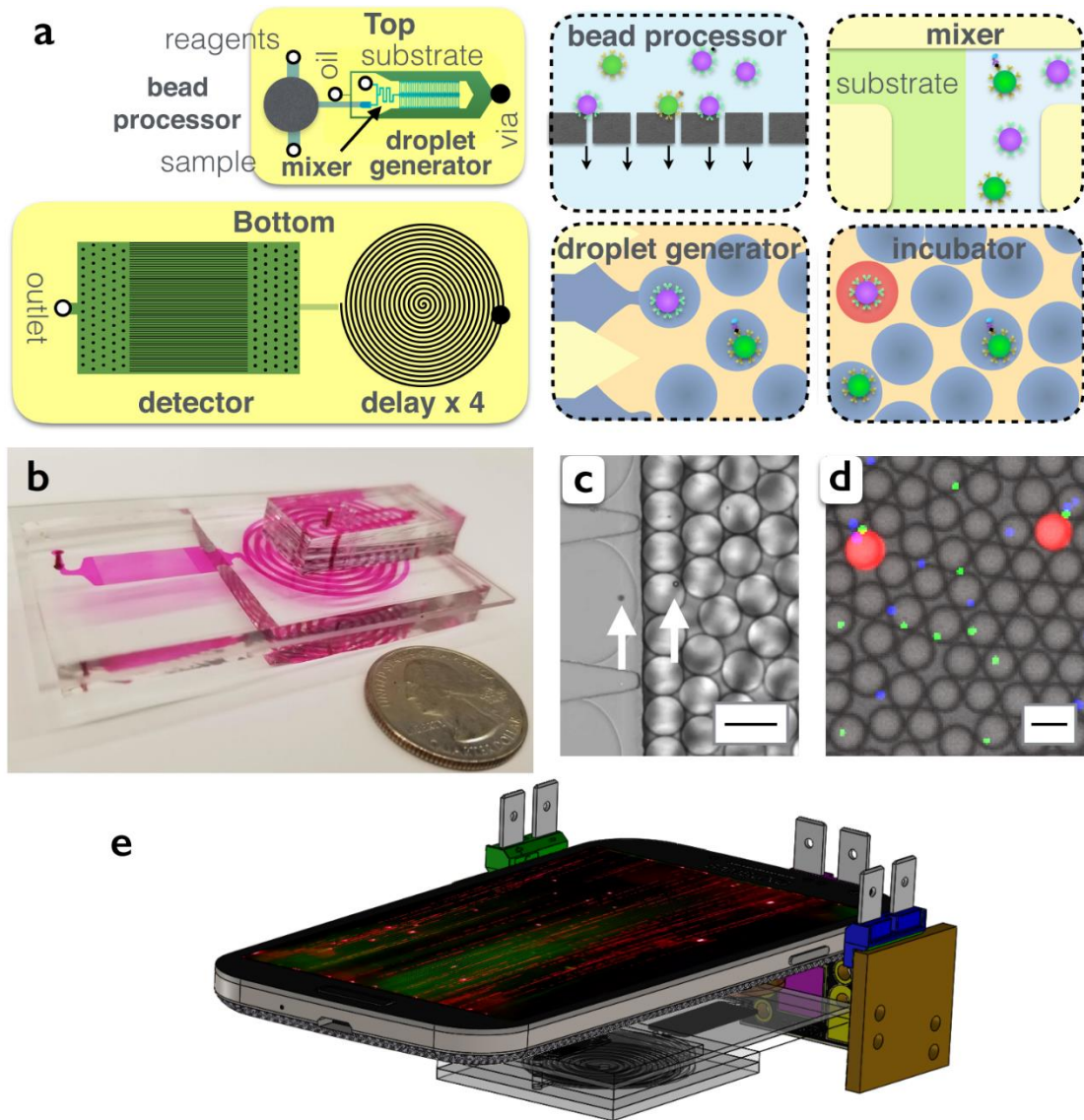


Figure 2. Integrated μ MD workflow. **a.** A schematic of the μ MD chip, showing both a top view and a bottom view. Each inset shows a schematic cartoon of the modules that are incorporated onto the μ MD. **b.** A photograph of the disposable μ MD chip, with the channels filled with dye to make them visible. **c.** A micrograph showing the droplet generator encapsulate microbeads into $d = 40 \mu\text{m}$ droplets. The arrows highlight the microbeads. (Scale bar = $50 \mu\text{m}$) **d.** A fluorescence micrograph of the droplets after the

delay line. (Scale bar = 50 μm) **e.** A schematic of the μMD platform, consisting of a mobile phone, three light sources, and the disposable μMD chip.

Downstream of the droplet generator, the droplets pass through a delay line, (**Fig. 2a**) which we have designed to hold droplets for a precise minutes-scale duration in continuous flow, without the need for active valves. To achieve a precise minute-scale delay, a channel is required that has both a large cross-sectional area, to reduce velocity, and a long length. To achieve a large cross-sectional area, we mold the PDMS microfluidics using a laser-cut acrylic mold rather than conventional SU-8 to achieve channels with width $w = 1.8 \text{ mm}$ and height $h = 1.5 \text{ mm}$. To achieve a large channel length, without leading to an overly large device footprint, we stack $N = 4$ spiral channels vertically by plasma bonding multiple PDMS pieces with punched hole vias. (**SI Appendix, Fig. S1**) Using a flow rate of $\Phi_d = 67 \text{ mL/hr}$, it takes droplets 3.2 minutes to traverse the entire channel, allowing the enzymes time to generate a measurable fluorescence signal. (**Fig. 2d**)

Time-domain encoded optofluidic fluorescence detection

To achieve high throughput, multicolor, fluorescence droplet detection on a mobile platform, we modulate the excitation light in time with a pseudorandom sequence that allows individual droplets to be resolved that would otherwise overlap due to the limited frame rate of digital cameras. Using conventional excitation that is constant in time, a droplet moving across a camera's field of view is imaged as a streak ($L_{\text{streak}} = v \cdot T_{\text{exp}}$, where v is the droplet velocity and T_{exp} the exposure time of the camera). This streak length L sets the minimum distance between droplets, and thus severely limits throughput. We overcome this limitation by modulating the excitation light source with a

pseudorandom sequence at a rate $>10\times$ faster than the exposure time of the camera, modulating the streak so that it can be resolved amongst neighboring droplets as close as three droplet diameters via correlation detection, and do so in 120 parallel channels in the camera's field of view. In our previous work in this area,^{129,190} we only interrogated a single fluorescent dye in each droplet, which is not sufficient to readout the multiplexed dELISA assays carried out in this paper. We had previously presented a proof-of-concept demonstrating that two distinct dyes could be detected.³⁶ Here, we expand this approach by using three light sources, each of which emits a wavelength tuned to excite a different dye and that is modulated in time with a unique maximum length sequence (MLS) that can be decoded independently to readout each fluorescence channel. A band-pass filter is placed on the camera to diminish the effects of scattered excitation light. (Edmund Optics, #87-241) We implemented a three-color system using two LEDs (blue, green) and one diode laser (UV). This μ MD platform is invariant to flow rate, has a maximum throughput of 160 mL/hr (10^6 droplets/sec), and a dynamic range of 1: 10^7 to 1: 40 fluorescent: non-fluorescent droplets.

To decode the videos taken by our cell phone camera we perform a correlation detection for the three expected modulation patterns m , corresponding to each of the three light sources. By doing so, we generate the correlation vectors $\Psi_{k,n}^{r,g,b} = \int S_{k,n}^{R,G,B}(x) m^{r,g,b}(x) dx = S_{k,n}^{R,G,B} \otimes m^{r,g,b}$, where the indices k are the video frames, n are the $n = 1:120$ channels in the device, (R,G,B) correspond to the color channels of the digital camera, and (r,g,b) correspond to each of the three unique excitation sources. (**Fig. 3a**) We chose to pattern the droplets using MLS with $|m| = 63$ bits, where each bit corresponds to 10 pixels in the digital image. Thus, 63 bits would correspond to 630px, or 1/3 of a 1920px wide video frame. To create a set of MLS with minimal auto-

correlation and cross correlation from each other, we followed the process in MacWilliams and Sloane ¹⁵¹ to create a pseudorandom vector with $(2^{12}-1=4095)$ elements, that we folded into a 63×65 matrix, and chose the first three rows to select the three MLS patterns.

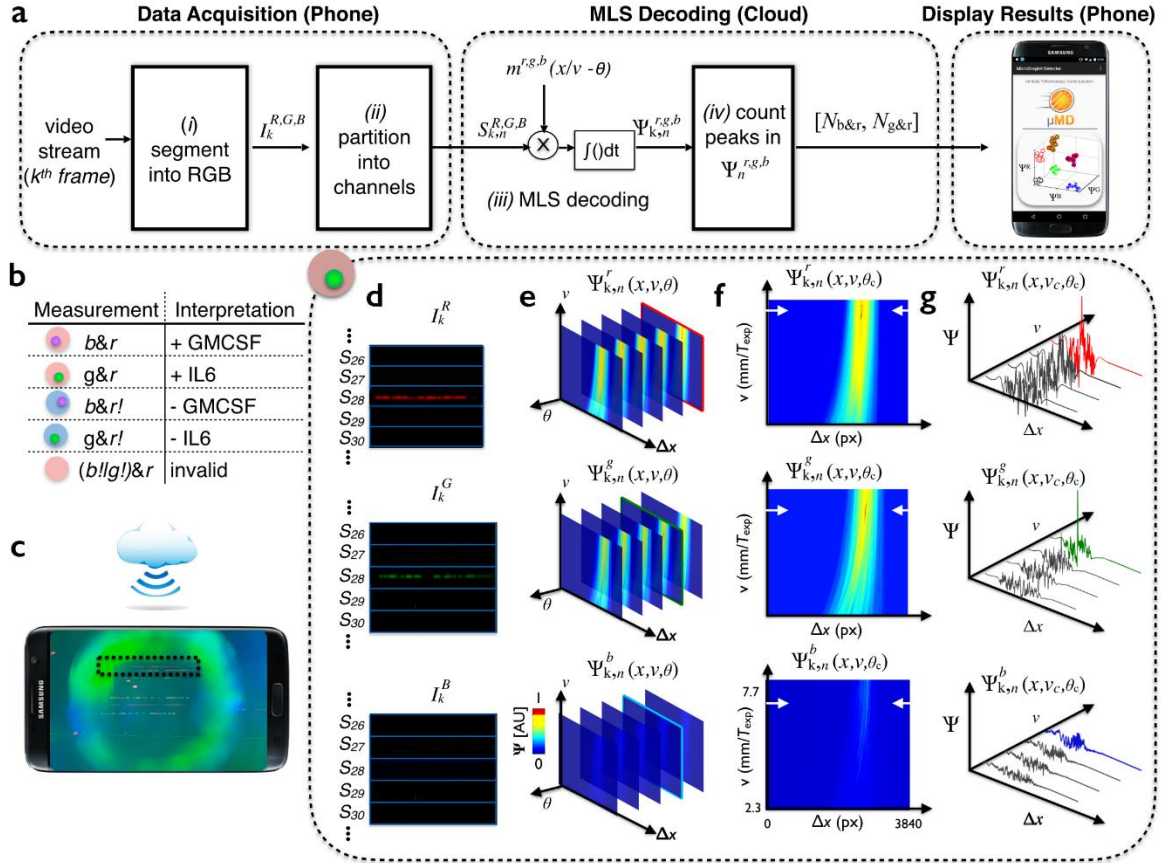


Figure 3. Software workflow for multi-color phase and velocity invariant optofluidic fluorescence droplet detection. **a.** The algorithm for detecting droplets. **b.** Truth table for interpreting the readout of the μ MD's three-color (r: red ELISA signal, g: green beads, b: blue beads) fluorescence measurement. **c.** Schematic showing the μ MD platform collecting data, which is sent to the cloud to be processed, and then returned to the mobile phone to report the results of the assay to the user. **d.** A sample workflow for

a droplet that contains a green bead and that is positive for its target. The video's image frames are segmented into 1d vectors. **e.** A 3D correlation results in a data matrix where the phase is first identified (**f**). From this 2D "slice" of the data matrix, the velocity of the droplet is found and the position is recorded for each peak in the correlation space (**g**).

The goal of the fluorescence detector is to inspect each droplet and determine 1. if the droplet contains a microbead, and if so determine its color (UV or green) which indicates the protein target the droplet is measuring (GM-CSF, IL6 respectively). (**Fig. 3b**), 2. if the droplet fluoresces red, which indicates whether the droplet has detected one molecule of its target. The workflow to extract this information from each droplet is as follows: (i) The k_{th} frame of the video is separated into its red, green, and blue components $I_k^{R,G,B}$ based on the camera's red, green, and blue sensors. (**Fig. 3d**) (ii) A line-average is taken along the direction of each of the $n = 120$ microchannels $S_{k,n}^{R,G,B}(x)$. (iii) To simplify the hardware of the system, rather than control the droplet velocity v or phase θ , relative to the MLS excitation, of the passing droplets we instead use cloud computing to computationally detect droplets with unknown phase and velocity. (**Fig. 3c**) We generate a 3d matrix by correlating each of the modulated signals with expected emission patterns that scans the range of velocities and phase at which the LED strobes $m_{r,g,b}(x/v-\theta) \otimes S_n^{R,G,B}$, corresponding to the three excitation sources (r,g,b) respectively. (**Fig. 3e**) (iv) By selecting the optimal phase (θ_c) and velocity (v_c) of every droplet, we can identify peaks in the correlation space $\Psi_{k,n}^{r,g,b}(x, v_c, \theta_c)$. (**Fig. 3f,g**) These detected signals are tabulated $[N_{b\&r}, N_{g\&r}]$, where $N_{b\&r}$ corresponds to droplets that contain a UV bead and fluoresce red and thus contain a molecule of GM-CSF and $N_{b\&r}$ corresponds to droplets that contain a green bead and fluoresce red and thus contain a molecule of IL6. The data is collected using our custom Android app, sent into the cloud,

processed using MATLAB in a remote server, and then sent back to the smartphone and reported to the user in an easy-to-interpret format. For each target molecule, the active enzymes per bead ¹⁶⁸ (AEB) is calculated by quantifying the number droplets that contained a bead and that fluoresced red, normalized to the total number of beads. The values that we report are calculated by subtracting the AEB measured when we ran a blank sample, which does not contain the target protein, and corrected for the pre-calculated loss factor, obtained in the measurements of spiked proteins into PBS, multiplied by the molecular weight of the target protein.

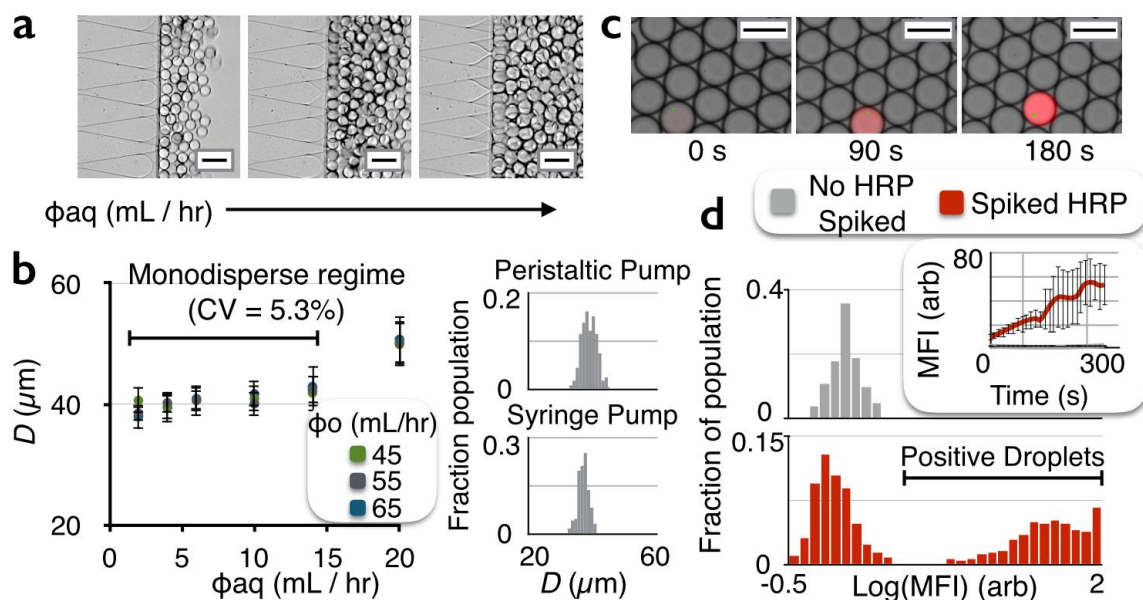


Figure 4. Flow rate invariant droplet generation using step emulsification generate droplets of the same diameter. a. By using the Millipede geometry, droplet size is invariant to dispersed phase flow rate. **b.** For a range of continuous flow rates (45-65 mL/hr) and dispersed flow rates (2-14 mL /hr), the generated droplets remained monodispersed with syringe pumps (CV = 5.3%) and with inexpensive peristaltic pumps (CV = 6.0%). **c.** To evaluate the enzymatic amplification of captured protein in the

droplets, we inspected the droplets after the delay line with fluorescence microscopy. **d.** After a 3.2 minute delay, the distribution of droplets positive and negative for enzyme were measured. (Scale Bar = 50 μm)

Droplet generation and integrated incubation line

Droplet uniformity is critical for digital assays, because variance in droplet diameter leads to variance in fluorescence after the delay line, confounding the ability to discriminate positive and negative droplets. To evaluate the droplet generator's capability to generate monodispersed droplets in a mobile setting, we scanned the continuous phase over flow rates $\Phi_c = 45\text{-}65 \text{ mL/hr}$ and we scanned the dispersed phase over flow rates $\Phi_o = 2\text{-}14 \text{ mL/hr}$. (**Fig. 4a**) We generated droplets with a diameter $d = 40 \text{ }\mu\text{m}$ and a coefficient of variation $CV < 6\%$ with both syringe pumps and inexpensive peristaltic pumps. (**Fig. 4b**) The greater the ratio of the aqueous flow rate to the continuous flow rate, the larger the volume fraction of droplets was, allowing increased throughput.

To evaluate and optimize the delay line and the enzymatic amplification of captured protein in the droplets, we inspected the droplets after the delay line with fluorescence microscopy (Leica DM4200). (**Fig. 4c**) We calculated the distribution of fluorescence intensities of droplets with and without an enzyme to identify the delay time that minimized their overlap. For a 3.2 minute delay, the ratio of the average droplet with an enzyme had a $> 30\times$ greater mean fluorescence intensity (MFI) than a droplet without an enzyme. (**Fig. 4d**)

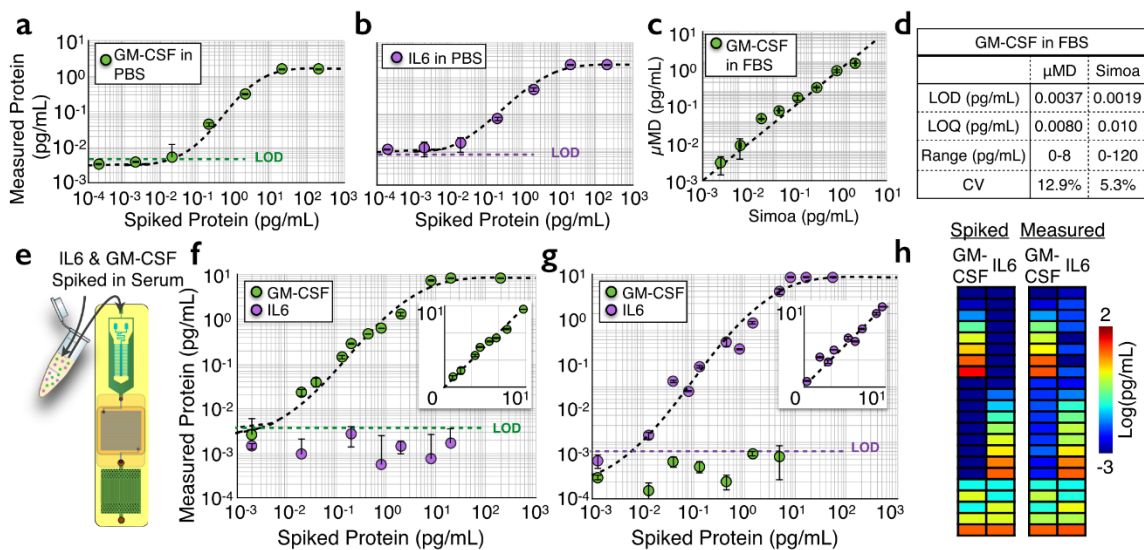


Figure 5. Benchmarking and characterization of ultrasensitive, duplex protein detection in complex media. **a.** Single-plex detection of GM-CSF spiked into PBS. The limit of detection LOD = 0.0045 pg/mL (320 aM). **b.** Single-plex detection of IL6 spiked into PBS. LOD = 0.0070 pg/mL. **c.** The same samples of fetal bovine serum (FBS) spiked with varying concentrations of GM-CSF were measured using the μ MD and Quanterix's Simoa. Good agreement was found between the two measurements (R^2)= 0.95. **d.** The limit of detection (LOD), limit of quantification (LOQ), dynamic range, and coefficient of variation (CV) are reported for the μ MD's and Simoa's measurement of GM-CSF in FBS. **e.** The duplex assay is tested by measuring various concentrations of GM-CSF and IL6 spiked into FBS. **f.** Varying concentrations of GM-CSF into FBS resulted in insignificant cross-talk with the measurement of IL6 and did not significantly change the LOD for GM-CSF. **g.** Conversely, varying concentrations of IL6 into FBS resulted in insignificant cross-talk with the measurement of GM-CSF and did not significantly change the LOD for IL6. **h.** 22 various concentrations of GM-CSF and IL6

were spiked into FBS and measured. Good agreement was found between the spiked and measured results, for both GM-CSF ($R^2 = 0.99$) and IL6 ($R^2 = 0.99$).

Ultrasensitive, duplex protein detection in complex media

To evaluate our integrated μ MD's capability for sensitively detecting proteins, we first measured IL6 and GM-CSF in PBS, complex media (FBS), and human serum, and compared the results with those from a commercial dELISA device (Quanterix Simoa). Non-human serums provides a good model to simulate human serum^{168,197,198}, because it has the convenient property that it does not include any human IL6 or GM-CSF allowing titration experiments to be performed down to our device's LOD. In these initial experiments, we performed bead processing off-chip, such that the droplet generator, incubator, and detector could be evaluated. In PBS, we first performed separate single-plex measurements on GM-CSF (**Fig. 5a**) and IL6 (**Fig. 5b**) by measuring serial dilutions from 10^{-4} - 10^2 pg/ml. We achieved a limit of detection $LOD = 0.0045$ pg/mL (320 aM) and $LOD = 0.0070$ pg/mL (350 aM) for GM-CSF and IL6, respectively. We next performed the same titration measurement for GM-CSF in 1:4 FBS solution. In this experiment we split the sample between our μ MD platform and Simoa (GM-CSF 2.0 kit) to perform a head-to-head comparison. We found excellent agreement between the output of our chip and that of Simoa ($R^2 = 0.95$). (**Fig. 5c**) The LOD, limit of quantification (LOQ), dynamic range, and average CV were tabulated for the μ MD and Simoa, (**Fig. 5d**) and showed similar performance.

Next, we evaluated the μ MD chip's capability to simultaneously measure two protein levels in a duplex measurement of GM-CSF and IL6 in complex media. To this end, we first spiked various quantities of GM-CSF into FBS, keeping IL6 concentrations

at 0 pg/ml. In these samples, we measure both GM-CSF and IL6 using our duplex microbead assay and evaluate cross-talk and compare to our single-plex results. (**Fig. 5f,g**) We also performed the same experiment, but instead spiked various levels of IL6 and kept GM-CSF concentrations at 0 pg/ml. In both cases the LOD, for GM-CSF or IL6, did not change significantly from the singleplex measurement ($p > 0.88$ for GM-CSF, $p > 0.90$ for IL6) To further verify our capability to simultaneously measure both GM-CSF and IL6, we evaluated our chip's accuracy in measuring $N = 22$ separate titrations of various quantities of GM-CSF and IL6 spiked into FBS. (**Fig. 5h**) We found excellent agreement between the expected spiked concentrations and the measured concentrations ($R^2 > 0.99$) for GM-CSF and ($R^2 > 0.99$) for IL6.

We next validated that the μ MD can measure endogenous protein in human serum. We collected serum from $N = 14$ healthy subjects, and for each subject measured an aliquot using our mobile μ MD platform's IL6 and GM-CSF duplex assay and we measured an aliquot using Quanterix's commercial assay (**Fig. 6a**), allowing us to compare our results to the commercial gold standard. We saw excellent agreement between measurements on our mobile platform and that performed on Quanterix's Simoa ($R^2 = 0.96$) (**Fig. 6b**), demonstrating that our microfluidic device can perform on human serum.

3.5 Conclusion

Our μ MD platform, with its integrated and miniaturized implementation, its high sensitivity, and its high droplet throughput, allows digital assays containing millions of droplets to be performed rapidly on a mobile platform. By integrating and miniaturizing digital assays, the μ MD can translate the benefits of dELISA assays to a mobile diagnostic platform. While in this paper we performed a duplex assay, we can further

leverage improvement in droplet throughput} and multicolor detection to increase multiplexing to 100s of markers. Multiplexing can be increased by both 1. running M assays in parallel by leveraging our chip's high droplet throughput and dividing the sample to be mixed with different reagents in either individual channels or sets of channels of the $N = 120$ detection channels. This approach comes at the expense of device throughput and a reduction in sensitivity that comes from splitting the sample volume for each additional assay. 2. Microbeads with varying concentrations of multiple dyes can be used to barcode the microbeads for M assays in a single pot, as has been done by groups such as Luminex.¹⁹⁹ Moreover, these two approaches can be combined on the same chip to achieve $M > 100$ multiplexed assays. Similarly, multiple samples can be processed by either running them serially through the μ MD or in parallel by dividing up the $N = 120$ detection channels. In either approach, the samples would be incubated with beads, labeled, and washed in separate wells to avoid cross-contamination. In serial operation, the incubation time would remain the same (currently three hours), and the total processing time would increase linearly with the number of samples (5 additional minutes per sample, given a droplet throughput of 100k droplets/sec and a four minute droplet incubation time). The additional processing time per sample could be reduced by parallelizing the droplet incubation stage. Our miniaturized technology matches the limit of detection to existing dELISA, however, it is important to highlight that the μ MD does not currently have the ability to sequentially load samples in an automated fashion that the Simoa HD-1 has demonstrated for up to 384 samples⁸⁶ By making use of recent developments of applying dELISA to miRNA detection,¹⁷⁹ multiplexed detection of miRNA and protein can be measured on the same chip for multi-modal characterization of complex disease states.^{200,201} By automating and incorporating dELISA onto a mobile platform, the μ MD allows ultrasensitive, multiplexed

biomarker detection to be brought directly to the point-of-use, where digital assays can have the greatest impact.

3.6 Methods and Materials

Device Fabrication

The μ MD is composed primarily of four components, all integrated into a monolithic chip (**Fig. 2a**): 1. a bead processor where beads are incubated and washed in successive steps, 2. droplet generators, 3. a delay line for the enzymatic amplification reaction, and 4. the fluorescence detection region. The bead filtration unit consists of a 3 μ m polycarbonate filter (Sterlitech) sandwiched between laser-cut layers of adhesive coated mylar (7602A54, McMaster Carr). The top PDMS piece contains the droplet generators, and is fabricated using multi-layer soft lithography, consisting of a layer that contains the nozzles and the spine ($h = 10 \mu$ m), a second layer that contains only the spine delivery channels ($h = 120 \mu$ m), and a third layer that contains herringbone structures for enhanced mixing ($h = 30 \mu$ m). The bottom PDMS piece was also fabricated using soft lithography, and consist of the spiral delay line ($h = 1.5$ mm) and the detector channels ($h = 40 \mu$ m). The three pieces are assembled by bonding the droplet generators PDMS piece to the top of a glass slide and the delay line PDMS piece to the bottom, using plasma bonding. The glass slide (Corning® Glass Slides, ID: 26005) is etched with a through-hole $d = 200 \mu$ m using a CO₂ laser, to serve as a via between the top and bottom pieces of PDMS microfluidics. (**Fig. 2a**) The bead processing unit is adhered to the top PDMS piece using adhesive coated mylar (7602A54, McMaster Carr). The PDMS portion of the chip was made hydrophobic by running 1% silane (Trichloro(1H,1H,2H,2H-perfluorooctyl)silane, Sigma) in Novec 7500 (Oakwood Chemical) and flushed with Novec7500 alone. The filter portion of the μ MD was soaked

in 1% F127 in PBS, flushed with PBS, and then soaked in T20 buffer to reduce adhesion with antibodies and labeling enzyme.

Measurement of Endogenous Protein in Human Serum

We collected blood from N = 14 healthy subjects (age = 20-43, 71% male, 29% female), in which all experiments involving human subjects were approved by University of Pennsylvania Institutional Review Board protocols (Protocol 828435). Informed consent was obtained from the eligible subject directly. A written document was provided to the subject detailing the procedure involved and the rational for the study. The risks and benefits of study participation were explained. After a consent document was signed, an 8 mL blood draw was acquired along with information regarding gender and age. Blood was collected in yellow cap tubes which contain Acid Citrate Dextrose Solution (ACD) and serum separating gels (BD Vacutainer™ Venous Blood Collection Tubes: SST™ Serum Separation Tubes: Hemogard, BD 368013). Blood was allowed to sit for 15 minutes after collection, and then centrifuged at 1500 rcf for 15 minutes to isolate the serum. After centrifugation, serum was frozen at -80°C. Samples were thawed immediately before use, ensuring that all samples experienced the same freeze-thaw cycling. For Simoa measurements, we followed Quanterix's protocol for the singleplex GM-CSF 2.0 and IL-6 2.0 kits, using the standard protocol. (SimoaIL6, SimoaGMCSF)

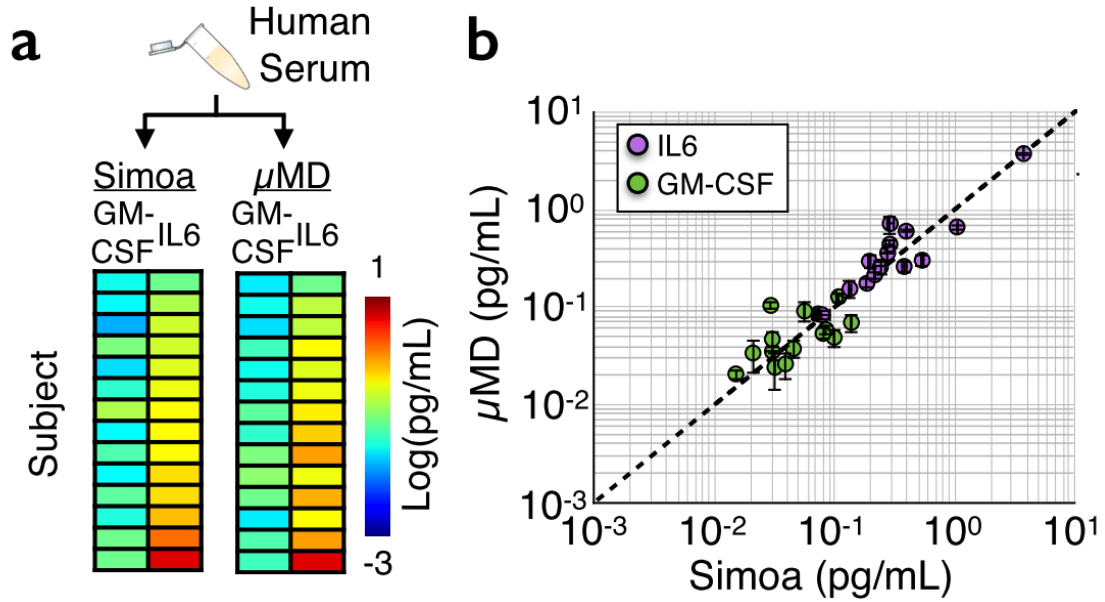


Figure 6. The measurement of endogenous protein in human serum. **a.** Human serum was collected from N = 14 healthy controls, and an aliquot was measured using our μMD's duplex IL6, GM-CSF assay and measured on Quanterix's commercial assay. **b.** Good agreement between Simoa and the μMD was found for measurements of both IL6 and GM-CSF ($R^2 = 0.96$).

Acknowledgements

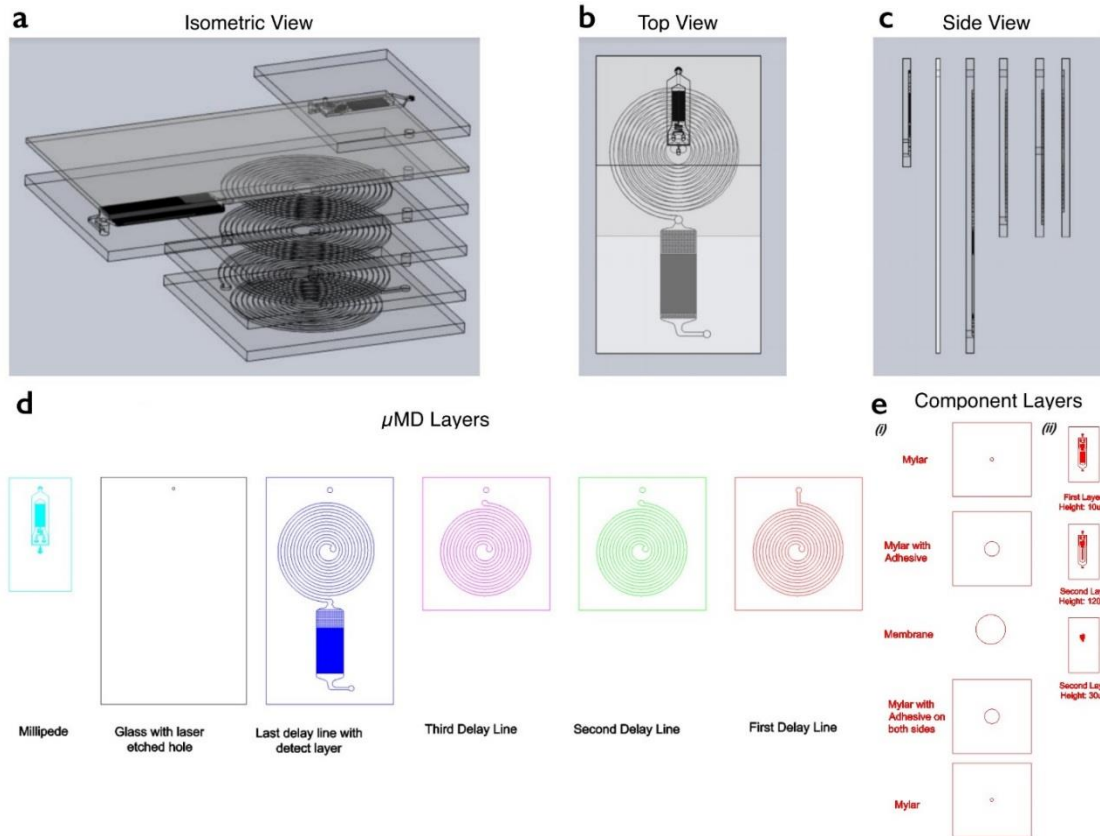
This work was supported by the Department of Bioengineering, University of Pennsylvania. Funding was provided by the National Institute of Health: 1R33CA206907, 5R21CA182336. Funding was also provided by The Hartwell Foundation. Funding was also provided by the Pennsylvania Consortium on Traumatic Brain Injury. David Issadore was supported by an American Cancer Society - CEOs Against Cancer - CA Division Research Scholar Grant, (RSG-15-227-01-CSM). We would like to thank Erika

Silverman and Nimay Kulkarni for helping with blood draws for human subject experiments. Venkata Yelleswarapu is generously supported by the Microsoft Graduate Fellowship. We would also like to thank Margalit Haber on experimental setup with the Simoa and Brian Chow for advice on our manuscript.

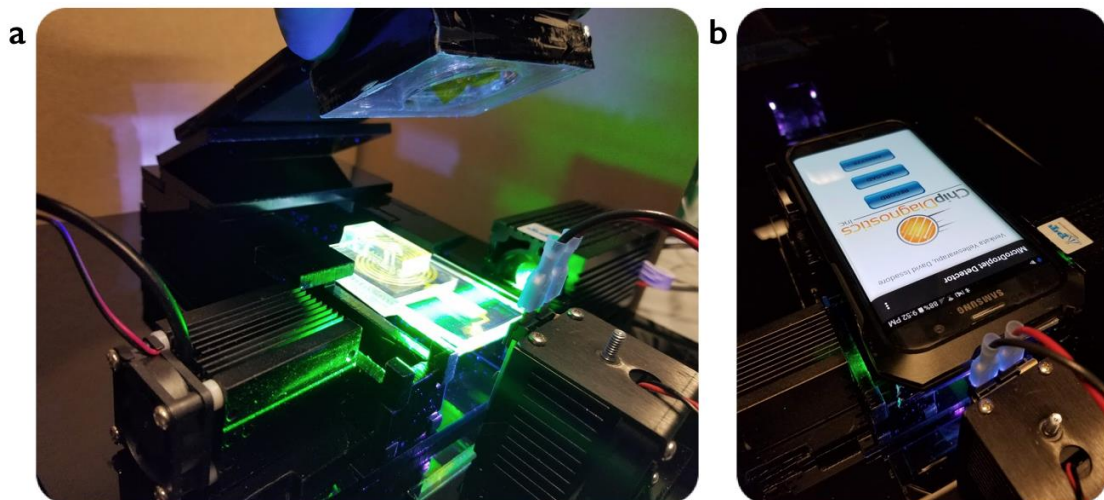
3.7 Supplementary Material

Table S1. Technologies to perform digital ELISA assays

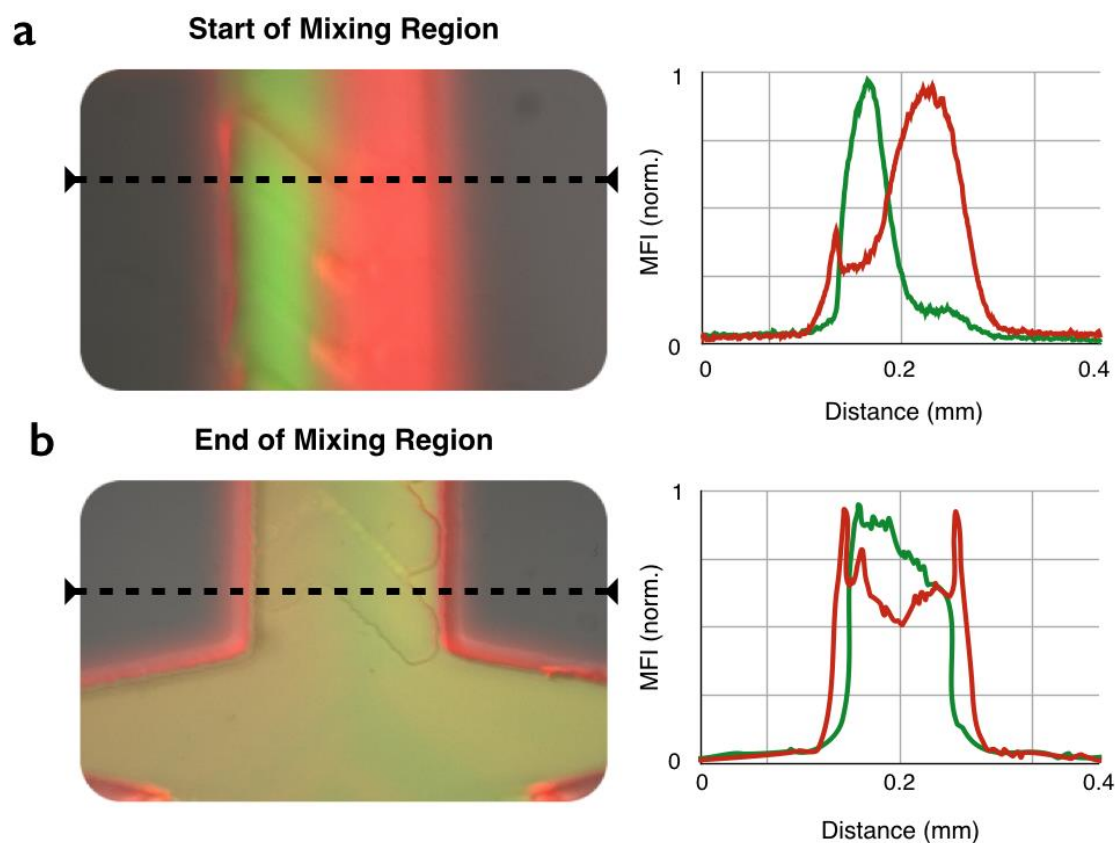
| Ref. | Target | LOD | Volume | Compartmentments | Device material | Multiplex Capability | Readout Equipment | Method of Detection |
|------------------------------|-----------------------|--|---------|----------------------------|--|-------------------------------------|-------------------------|---|
| Single Enzyme Studies | | | | | | | | |
| (1) | β -Gal | 0.88 μ M | 4.2 pL | 200k | PDMS | Green only | Fluorescence Microscope | -Single β -Gal in droplets;
-Measured rate of fluorescence production |
| (2) | ALP/
β -Gal | 7.0 fM | 44 fL | 7600*120 chamber | CYTOP on glass coverslip | Green Orange | Fluorescence Microscope | -Noted only 2.5% of the substrate was consumed in 20 min |
| Biological Targets | | | | | | | | |
| (3) | TNF- α and PSA | 6 fg/mL (200aM) | 50 fL | 50k well | Glass wells
Silicone gasket/oil | Singleplex | Fluorescence Microscope | Microarray with bead-based dELISA |
| (4) | P24 | 100 vir/mL | 50 fL | comp | Simoa array | Multiplex Capability | Fluorescence Microscope | Measured number of p24 proteins
-Converted to virion count by dividing 2000 p24 proteins/virion
Verified with RNA extracted |
| (5) | PSA | 1.2 pg/mL (43 fM) | 32 fL | 20k drops | PDMS Glass | Demonstrated Singleplex | Fluorescence Microscope | -Static array with around 20k droplets analyzed
-Low dynamic range
-No false positives reported |
| (6) | Flu | 4 fM in buffer | 38 fL | 62.5k wells | Patterned Teflon-Af on glass slides | Multiplex Capability | Fluorescence Microscope | -Detected nucleoprotein from flu virus in nasopharyngeal swabs to show dELISA in clinical sample. |
| (7-9) | Commercial assays | 3.8 fg/mL (200 aM)
IL-10 | 40 fL | 216k wells
25-50k beads | Cyclic Olefin Polymer
Bluray Printing | Multiplex (6-plex
66 samples/h) | Fluorescence Microscope | -Fully automated commercial digital ELISA from Quanterix Simoa HD-1 Analyzer |
| This | GM-CSF
IL6 | 3.7 fg/mL (300 aM)
7.0 fg/mL (350 aM) | 22.5 pL | 10M droplets
1M beads | PDMS and Glass
3D stack | Multiplex (Duplex
Samples/5 min) | Cell Phone Camera | -Integrated mobile platform with parallelized droplet generation and detection with cloud computing |



Supplementary Figure 1. 3D design of chip. a-c. Isometric and side views of the μ MD display the how the modular components are stacked in a 3d case. **d.** Draftsight drawings of each layer of μ MD, followed by component layers for the bead processor **(e,i)** and the droplet generator **(e,ii)**.



Supplementary Figure 2. Design of μ MD casing. a,b. The μ MD consists of a disposable microfluidic chip, a cell phone, and an acrylic casing that we designed. The acrylic casing comes in two parts: one that is attached to the cell phone to fix the distance between the imaging plane and the macro lens, and the second which houses the LEDs and locks the cell phone into position when the disposable chip is inserted.



Supplementary Figure 3. Mixing of aqueous phases. A channel length of 14 mm is used to ensure proper mixing of the beads and the substrate, while minimizing background signal that comes from enzymes generating fluorescence signal before they are encapsulated into droplets.

The [video](#) demonstrates the workflow of the droplet digital assay, as well as features of the robust droplet generation and detection.

dELISA Assay

On our chip, the bead processing, droplet generation, droplet incubation, and detection are integrated. By avoiding manual processing steps, loss, contamination, and unreliable reinjection of droplets after incubation, as has been observed in similar systems²⁰², can be avoided. To functionalize the microbeads used in our assay, we first washed both the 5.4 μm Carboxyl Green Particles (Spherotech, CFH-5052-2) and 4.5 μm Carboxyl UV beads (CFP-4041-2) 6 times each, using centrifugation at 15k rcf for 5 min to remove the sodium azide, which inhibits HRP, from the supernatant. Subsequently, we used the PolyLink Protein Coupling Kit (PolySciences, 24350-1) to attach anti-human GM-CSF (R&D, MAB2172) and anti-human IL-6 (MAB206) antibodies onto the beads, respectively. To evaluate our device, we created serial dilutions of the protein targets (R&D #215-GM-010, R&D #206-IL-010) in low protein binding tubes to reduce protein binding to the surface.

The on-chip bead processing steps were carried out as follows. The input to the device is 1:4 diluted serum, diluted in T20 buffer. Incubation with the beads is performed in a total volume of 100 μL T20 buffer and protein sample. Reagents are stored off-chip in this study, but can be preloaded on-chip in future device generations. The reagents for the HRP substrate are prepared immediately before the assay to reduce the background of the fluorescence substrate. The reagents can be loaded into a pre-loaded tubing and dispensed using a peristaltic pump. On the on-chip membrane, which captures the beads for processing, the following steps are carried out. Following the initial incubation, the beads are washed and then incubated with 0.7 nM concentration of detection antibody in T20 buffer. After an hour of incubation, the sample is washed and replaced with 12.5 pM concentration of HsHRP in T20 Buffer (Life Technologies), and washed

again. Subsequently, the flow is reversed so that beads are released and the output is encapsulated into droplets for analysis. For droplet generation, the continuous phase is Biorad Oil. Droplets of diameter $d = 40 \mu\text{m}$ ($\text{CV} = 5.3\%$) are generated with the total dispersed phase fixed at $\Phi_d = 12 \text{ ml/hr}$ with a fixed continuous phase of $\Phi_c = 55 \text{ ml/hr}$. QuantaRed™ Enhanced Chemifluorescent HRP Substrate Kit was mixed with the microbeads in the on-chip vortex mixer (**Fig. 2a, SI Appendix, Fig. S3**) immediately upstream of the droplet generator. The substrate is introduced at a flow rate of 6 ml/hr . We selected QX200 Droplet Generation Oil for EvaGreen (Biorad) to encapsulate the beads in stable droplets with minimal dye leakage. The μMD uses high fluorescence intensity dye beads, and HRP substrate compared to the low intensity dyes and the β -gal enzyme and RGP substrate found in Simoa's technology.^{49,168}

When performing the bead-processing off-chip, we used the following protocol. Capture beads are added into sample in low protein binding tubes, and incubated for an hour. The sample is diluted into 1mL with T20 Buffer and centrifuged at 12k rcf to remove background cell debris and nontarget molecules in the supernatant. The beads are resuspended into 0.7 nM concentration of detection antibody in T20 buffer and incubated for an hour. This solution is diluted into 1mL T20 Buffer and centrifuged at 12k rcf to remove unbound detection antibody, and 12.5 pM concentration of HsHRP in T20 Buffer. This sample is washed 4 times using a centrifuge and resuspended in T20 Buffer, to remove any HsHRP that could result in a false positive. The resulting sample is then introduced as the aqueous inlet for the droplet generating device.

To calculate the limit of detection (LOD) and limit of quantification (LOQ), we measured the number of false positives in replicate ($N = 3$) "blank" samples that included FBS but contained no spiked protein. The LOD and LOQ was converted to units pg/mL

using the known molecular weights of the target molecules. The LOD was defined as $\text{LOD} = \langle \text{FP} \rangle + 2.5 \sigma(\text{FP})$, where $\langle \text{FP} \rangle$ was the mean number of false positives and $\sigma(\text{FP})$ was the standard deviation of the false positives. The LOQ was defined as $\text{LOQ} = \langle \text{FP} \rangle + 10\sigma(\text{FP})$. We defined these values so that they agree with what is used to describe the gold standard technology, Quanterix's Simoa. (SimoaLL6, SimoaGMCSF)

Design of the Non-Disposable Components of the μMD and its Software

The μMD consists of a disposable microfluidic chip, a cell phone, and an acrylic casing that we designed. (**SI Appendix, Fig. S1,S2**) The acrylic casing comes in two parts. The first part is attached to the cell phone and fixes the distance between the imaging plane and the macro lens. The second part houses the LEDs and the cell phone, and sets the position of the disposable chip relative to the excitation sources and the camera (**SI Appendix, Vid S1**). This casing contains a low cost commercial plastic lens (<\$4), a bandpass filter ($\lambda_{\text{cw}} = 512 \pm 11.5 \text{ nm}$, $630 \pm 45.5 \text{ nm}$, Edmund Optics, #87-241), and a slot to automatically align the microfluidic chip. The disposable microfluidic chip is constructed of only PDMS, glass and mylar, and is prototyped using soft lithography at The University of Pennsylvania's Singh Center for Nanotechnology. The low cost plastic macro lens (15x magnification, Carson HookUpz, ML-515) is used to image the device. Field of View $\text{FOV} = 7 \times 12 \text{ (mm}^2\text{)}$. (**Fig. 3b**) There are three excitation sources, each mounted in the acrylic casing: an ultra-bright UV LED ($\lambda_{\text{ex}} = 400 \text{ nm}$, Luminus, CBT-90-UV-C31-M400-22), a fat beam (laser diameter > 10mm) blue laser diode (450nm, 400mW Laser Diode Module, APT Lighting), and a fat beam green laser (532nm, 300mW Laser Diode Module, APT Lighting). The light sources are driven using external electronics consisting of an LED driver circuit (Luminus Development Kit, DK-114N-3) for the LEDs, TTL modules for the laser diodes, and a microcontroller (Arduino

Mega2560) programmed with unique MLS patterns for each light source. To illuminate the droplets in the microfluidic channels we make use of antiresonant side coupling to achieve uniform illumination ¹⁵². The non-disposable cost, excluding the cell phone, of the μ MD prototype is < \$1000.

The software used in this study implements the data analysis shown in **Fig. 3**. This software detects multiple fluorescent colors in each individual droplet, rather than just one, as was done in previous work. ¹⁹⁰ A custom App is written that is installed on a Galaxy S8 phone. This App controls, and coordinates, the multiple components in this experiment, including the cloud computing, and the cell phone camera. A commercially available App Open Camera is used to interface with the cell phone's camera, and allows manual control of the camera's settings. Video collected on the phone is uploaded to a Matlab cloud server (MathWorks Cloud). Optical aberrations in the video are fixed by the software based on a calibration used to calculate the distortion from the macro lens. Small errors in the position and angle of the chip relative to the camera are also corrected. The software then parses the frames into 120 individual channels, and carries out the algorithm described in **Fig. 3**. The data analysis currently takes 10 minutes to analyze 10 million droplets. Data analysis can further be sped up using a GPU or cloud server, but we currently run the process locally on a Using an Ubuntu OS with an Intel Core i7-7700HQ @ 2.80 GHz x 8 and 16 GB RAM. All source code for the software used in this study is included in the **SI Appendix, SI Text**.

3.8 Supplementary Code

Source code can be found in the following

<https://sites.google.com/site/issadorelab/Issadore-Lab/protocols-and-software>

to the lab website contains all of the software with a readme file to explain how to use

each of the components. All code is commented thoroughly for ease of use. Source code is shared for: (i) Matlab software for image analysis, (ii) Arduino code that modulates the LED excitation, and (iii) an Android App that connects the software to cloud.

~~~~~

## **MATLAB\_uMD\_Video\_Analysis-code**

### **uMD\_Initialize\_Code.m**

```
%initializes all variables such as expected signals, camera parameters,
etc.
%sets the frames to view within the video to start analysis
%calls Frame_Undistortion to start a chain to .m files that creates a
matrix where correlations are stored
%once the vector is saved into a .mat file that can also be accessed
later as done typically...
%calls Corr_Hough_matrix_script to begin a chain for peak finding
analysis

close all force
clear all
% parpool
%uncommenting the above can start the parallel computing toolbox if
%available in matlab. Doing so increases computational speed
significantly

%initialize variables
x1 = 0 ;
x2 = 0;
y1 = 0;
y2 = 0;
inc = 0;

%load the MLS that was used in the Arduino Code
MLS_seq = [-1, 1, -1, 1, -1, 1, 1, -1, -1, 1, 1, -1, 1, 1, 1, -1,
1, 1, -1, 1, -1, -1, 1, -1, -1, 1, 1, 1, -1, -1, -1, 1, -1, 1,
1, 1, 1, -1, -1, 1, -1, 1, -1, -1, -1, 1, 1, -1, -1, -1, -1,
1, -1, -1, -1, -1, -1, 1, 1, 1, 1, 1, 1];

MLS_seqR = [-1, 1, -1, 1, -1, 1, 1, -1, -1, 1, 1, -1, 1, 1, 1, -1,
1, 1, -1, 1, -1, -1, 1, -1, -1, 1, 1, 1, -1, -1, -1, 1, -1, 1,
1, 1, 1, -1, -1, 1, -1, 1, -1, -1, -1, 1, 1, -1, -1, -1, -1,
1, -1, -1, -1, -1, -1, 1, 1, 1, 1, 1, 1];
```

```

MLS_seqG = [-1, 1, -1, 1, 1, 1, 1, -1, -1, 1, -1, -1, 1, -1, 1,
1, 1, -1, -1, 1, 1, 1, -1, -1, -1, -1, -1, 1, 1, 1, -1, 1,
1, 1, -1, 1, -1, -1, 1, 1, 1, 1, -1, 1, -1, 1, -1, -1, 1, -1,
1, -1, -1, -1, -1, -1, -1, 1, -1, 1, -1, 1];
MLS_seqB = [-1, -1, 1, 1, 1, 1, 1, 1, -1, -1, 1, -1, 1, -1, 1, -
1, 1, -1, -1, 1, 1, -1, -1, 1, 1, -1, -1, 1, -1, 1, -1, -1,
1, 1, 1, 1, 1, -1, 1, -1, -1, 1, 1, 1, -1, -1, -1, 1, -1, -
1, -1, 1, 1, -1, 1, 1, -1, -1, 1, -1, -1, -1];

%load camera params once to fix image distortion
%The main variables that affect spherical distortion is
'RadialDistortion'
load('cameraParams1.mat')
cameraParams2 = cameraParameters('IntrinsicMatrix',
[716,0,0;0,716,0;1920/2,1080/2,1],...
'RadialDistortion',[.06,0.0,.00],...
'TangentialDistortion',[0,0],...
'RotationVectors',[0 0 0],...
'TranslationVectors',[0 0 0],...
'ReprojectionErrors',[0 0],...
'WorldPoints',cameraParams1.WorldPoints,...
'WorldUnits',cameraParams1.WorldUnits,...
'EstimateSkew',cameraParams1.EstimateSkew,...

'NumRadialDistortionCoefficients',cameraParams1.NumRadialDistortionCoef
ficients,...

'EstimateTangentialDistortion',cameraParams1.EstimateTangentialDistorti
on);

%select amount of channels and segment based on the pixels per channel
segmented_ch_num = 120;
pixels_per_ch = floor(1080/segmented_ch_num);

%load the interpolated masks. these represent the expected signal
%NOTE: the interpolated masks can change to fit the velocity range
required
%and can be increased or shortened to improve computation. In this
%particular case, the range was chosen to match the data, and
obviously,
%larger ranges with finer resolution will always work but the tradeoff
is
%computation time.
load('All_Interpolated_Masks.mat')
load('All_Interpolated_MasksB.mat')
load('All_Interpolated_MasksG.mat')

%the table below has several values, but the main ones that are
relevant
%are the first entry which is the filename of a video to be analyzed,
and

```

```

%the last term (flip) which represents the direction the droplets are
going
%in.

%Droplets can either go left to right or right to left based on how the
%chpi is attached; the flip vector properly selects the option

%The remaining variables can be ignored for this code.
data_table = {'20160927_165111.mp4' 27 7 624 800 1142 800 0 624
392 1142 377 624 1142 1};
load('cmap2.mat')

filename = data_table{1}; frame = data_table{2};
flip = data_table{15}; inc = data_table{8};
x1 = data_table{4}; y1 = data_table{5}-inc; x2 = data_table{6}; y2 =
data_table{7} -inc;
%bead two start and end
x3 = data_table{9}; y3 = data_table{10}; x4 = data_table{11}; y4 =
data_table{12};
dropletstart = data_table{13}; dropletend = data_table{14};

startframe = 450; endframe = 455; %select frames in video to analyze
%a portion of the video is analyzed since there may be a lag time for
%droplets to reach the proper velocity initially, saving computation
time.

%select the background frame to subtract out background signal in the
%algorithm
background_frame = 1;
v_file = VideoReader(filename);
video_frame = read(v_file,background_frame);
R_channel = video_frame(:,:,1);
R_background = R_channel;
G_channel = video_frame(:,:,2);
G_background = G_channel;
B_channel = video_frame(:,:,3);
B_background = B_channel;

%begin loop through each frame
for framestoprocess = 1:endframe-startframe+1
    framenum=framestoprocess ;
    frame = startframe+framestoprocess-1;
    fprintf(num2str(framestoprocess))
    %%%%%%%%%%%%%%%%%%%%%%%%%%%%%%%%% Workflow Chain Begins
    %%%%%%%%%%%%%%%%%%%%%%%%%%%%%%%%%
    Frame_Undistortion

end

```

```

%save the correlation results in a matrix for analysis later if
necessary
save('FramesAnalyzed.mat','-
v7.3','corr_matrix_final','corr_matrix_final_G','corr_matrix_final_B')
%begin analysis on the correlation matrix
Corr_Hough_matrix_script

```

## Frame\_Undistortion.m

```

%uses camera parameters to undistort spherical aberrations and rotates
any offsets
%calls Frame_segmentation

```

```

close all

```

```

%load frame and subtract background
video_frame = read(v_file,frame);
img = video_frame;
red = img(:,:,1)-R_background; % Red channel
blue = img(:,:,2)-R_background; % Red channel
green = img(:,:,3)-R_background; % Red channel

```

```

%undistort with camera parameters chosen
[J1] = undistortImage(red, cameraParams2);
[J2] = undistortImage(blue, cameraParams2);
[J3] = undistortImage(green, cameraParams2);

```

```

%define angle to rotate image
x_ang_1 = 607; y_ang_1 = 669;
x_ang_2 = 1435; y_ang_2 = 655 ;

J1 = imrotate(J1,rad2deg(atan((y_ang_2-y_ang_1)/(x_ang_2-x_ang_1))));
J2 = imrotate(J2,rad2deg(atan((y_ang_2-y_ang_1)/(x_ang_2-x_ang_1))));
J3 = imrotate(J3,rad2deg(atan((y_ang_2-y_ang_1)/(x_ang_2-x_ang_1))));
%resize properly. during this portion, we lose several channels that
can be
%imaged but are too distorted at the edges on the top and bottom.
J1 = J1(57:1026,119:1835,:);
J2 = J2(57:1026,119:1835,:);
J3 = J3(57:1026,119:1835,:);

```

```

red = imresize(J1,[1080 1920]);
green = imresize(J1,[1080 1920]);
blue = imresize(J1,[1080 1920]);

```

```

%begin segmenting each channel to create 1D line vectors
Frame_segmentation

```

## Frame\_segmentation.m

```
%segments the frame into N channels and stores the vector into a 1d
line vector
%sends 1d line vector to Segmented_1D_CrossCorr_PhaseVel

x = [1:1920];
for segmented_channel= 1:segmented_ch_num
    %take line average for channel
    %If fluorescent signal is leeching onto the edge of the channels,
    the
        %segmented channels, Sn, can be made narrower to prevent the
        leakage.
        droplet_line = mean(red(1+(0+pixels_per_ch)*(segmented_channel-
1):(0+pixels_per_ch)*(segmented_channel),:));
        droplet_line_g = mean(green(1+(0+pixels_per_ch)*(segmented_channel-
1):(0+pixels_per_ch)*(segmented_channel),:));
        droplet_line_b = mean(blue(1+(0+pixels_per_ch)*(segmented_channel-
1):(0+pixels_per_ch)*(segmented_channel),:));
        %send each segmented vector for correlation analysis
        Segmented_1D_CrossCorr_PhaseVel

    %store the results in a matrix based on frame, channel, and
    position
    %where peak occurs (mapped to CMOS pixel location)
    corr_matrix_final(framenum, segmented_channel,:) =
max_corr_Vec_phase(1:1920);
    corr_matrix_final_G(framenum, segmented_channel,:) =
max_corr_Vec_phase_G(1:1920);
    corr_matrix_final_B(framenum, segmented_channel,:) =
max_corr_Vec_phase_B(1:1920);
end
```

## Segmented\_1D\_CrossCorr\_PhaseVel.m

```
%loops through phase and for each phase, begins proper correlation
initiation
%after calling Cross_Corr_no_graphs.m, it finds the optimal phase and
velocity

%store the 1d vector in a variable
Patterned_droplet = droplet_line;
whatbead = 1;

sig = Patterned_droplet;

%if droplets flow in reverse direction, we can flip the 1d line vector
for
%correlation here
if flip ==1
    sig = fliplr(sig);
```

```

end

%begin looping through phase. phase is defined as when the MLS starts,
so
%since the MLS is cyclical, we simply begin at the next cycle of the
MLS to
%loop through the phase
for phase = 1:4:length(MLS_seq)
    %for each phase, store the output into a 2d matrix
    Cross_Corr_no_graphs

    Final_vec_before_phase(phase,1:mat_b) = FINAL_CORR_VECTOR;
    Final_vec_before_phase_G(phase,1:mat_b) = FINAL_CORR_VECTOR_G;
    Final_vec_before_phase_B(phase,1:mat_b) = FINAL_CORR_VECTOR_B;

end

%find the optimal fit for all the phases;
[I,J] = find(Final_vec_before_phase==max(max(Final_vec_before_phase)));
max_corr_Vec_phase = fliplr(Final_vec_before_phase(I(1),:));
[I,J] =
find(Final_vec_before_phase_G==max(max(Final_vec_before_phase_G)));
max_corr_Vec_phase_G = fliplr(Final_vec_before_phase_G(I(1),:));
[I,J] =
find(Final_vec_before_phase_B==max(max(Final_vec_before_phase_B)));
max_corr_Vec_phase_B = fliplr(Final_vec_before_phase_B(I(1),:));

```

### **Cross\_Corr\_no\_graphs.m**

```

%begins a 2d correlation for the input signal and the selected expected
signal based on the phase
%finds the best matching velocity for the given phase after searching
through the 2d map

%To vary the range of velocities to scan, this variable can be altered.
%Preallocating the expected signal improves computational time.
Signal_Mat(:, :) = All_Interpolated_Masks(phase, :, :);
ma = Signal_Mat;
out8=xcorr2(sig,ma);
[mat_a mat_b] = size(out8);
%store the length of each MLS for different velocities to normalize
later
flipped_vec = fliplr(lengths_vector);
out8_new = zeros(mat_a,mat_b);

%take correlatoins and normalize by length of the mask
for i = 1:mat_a
    out8_new(i,1:mat_b) = out8(i,:)/flipped_vec(i);
end

%select the velocity that generates the largest peak.

```

```

[M,N] = find(out8_new==max(max(out8_new)));
Max_out = out8_new(M(1),:);

%Filter to get rid of DC effects
Fs = 1920;
half_freq = Fs/2;
notch_freq_filter =1;
low_freq_filt = 1;
smoothing_factor = 1;
w0=notch_freq_filter/half_freq;
[num,den]=iirnotch(w0,w0/35,-45);
[a,b]=butter(2,low_freq_filt/half_freq,'high'); %remove low frequency
components

y=filter(num,den,Max_out);
yfil=filtfilt(a,b,y);
ysm=smooth(yfil,smoothing_factor);

FINAL_CORR_VECTOR = (ysm);

%%%%%%%%%%%% Repeat for G channel %%%%%%%%%%%%%
%To vary the range of velocities to scan, this variable can be altered.
%Preallocating the expected signal improves computational time.
Signal_Mat(:, :) = All_Interpolated_MasksG(phase, :, :);
ma = Signal_Mat;
out8=xcorr2(sig,ma);
[mat_a mat_b] = size(out8);
%store the length of each MLS for different velocities to normalize
later
flipped_vec = fliplr(lengths_vector);
out8_new = zeros(mat_a,mat_b);

%take correlatoins and normalize by length of the mask
for i = 1:mat_a
    out8_new(i,1:mat_b) = out8(i,:)/flipped_vec(i);
end

%select the velocity that generates the largest peak.
[M,N] = find(out8_new==max(max(out8_new)));
Max_out = out8_new(M(1),:);

%Filter to get rid of DC effects
Fs = 1920;
half_freq = Fs/2;
notch_freq_filter =1;
low_freq_filt = 1;
smoothing_factor = 1;
w0=notch_freq_filter/half_freq;
[num,den]=iirnotch(w0,w0/35,-45);
[a,b]=butter(2,low_freq_filt/half_freq,'high'); %remove low frequency
components

y=filter(num,den,Max_out);

```



```

yfil=filtfilt(a,b,y);
ysm=smooth(yfil,smoothing_factor);

FINAL_CORR_VECTOR_G = (ysm);

%%%%%%%%%%%%%%%%%%%%%%%%%%%%%%%%%%%%%%%%%%%%%%%%%%%%%%%%%%%%%%%%%%%%%%%%% Repeat for B channel %%%%%%%%%%%%%%%
%To vary the range of velocities to scan, this variable can be altered.
%Preallocating the expected signal improves computational time.
Signal_Mat(:, :) = All_Interpolated_MasksB(phase, :, :);
ma = Signal_Mat;
out8=xcorr2(sig,ma);
[mat_a mat_b] = size(out8);
%store the length of each MLS for different velocities to normalize
later
flipped_vec = fliplr(lengths_vector);
out8_new = zeros(mat_a,mat_b);

%take correlatoins and normalize by length of the mask
for i = 1:mat_a
    out8_new(i,1:mat_b) = out8(i,:)/flipped_vec(i);
end

%select the velocity that generates the largest peak.
[M,N] = find(out8_new==max(max(out8_new)));
Max_out = out8_new(M(1),:);

%Filter to get rid of DC effects
Fs = 1920;
half_freq = Fs/2;
notch_freq_filter = 1;
low_freq_filt = 1;
smoothing_factor = 1;
w0=notch_freq_filter/half_freq;
[num,den]=iirnotch(w0,w0/35,-45);
[a,b]=butter(2,low_freq_filt/half_freq,'high'); %remove low frequency
components

y=filter(num,den,Max_out);
yfil=filtfilt(a,b,y);
ysm=smooth(yfil,smoothing_factor);

FINAL_CORR_VECTOR_B = (ysm);

```

### Corr\_Hough\_matrix\_script.m

```

%loads the correlation matrix and begins to search for each segmented
channel, how droplets travel through sequentially
%calls detect_real_droplets
clear all
load('FramesAnalyzed.mat')
clear loc_info_all
load('cmap2.mat')

```

```

%it may be useful to segment the vector into smaller pieces to analyze
%we now allocate the number of frames, the 1D line segments, and the
pixel
%length of each of the correlations we took earlier
[frames_total, numberofchannels ,framelengtha] =
size(corr_matrix_final);
% (100,19200)

% frames_total*numberofchannels, framelengtha
%We look through and find the local peaks for each of them based on a
%threshold found experimentally

%if the droplet was going in the reverse direction, the direction the
%droplet peaks move can be reversed if the proper flip variable was not
%set; rearranging the correlations can correct this
% for i = 1:numberofchannels-1
%     corr_matrix_final(:,i,:) = flipud(corr_matrix_final(:,i,:));
% end

%plot everything frame by frame
warning('off','all')
%convert the 3d matrix into a 1d for each channel

%count all the peaks in a certain channel
%one way to set the threshold is to find the max correlation value in
all
%the correlations found; and set the threshold to be 40% of that;
%assuming there was at least one positive in the entire analysis done

%Another method is to take an average of the entire correlation
vector
%matrix and use this as the background noise if the events are
sparse,
%and add 3*standadd deviation of the noise to the mean to separate
the
%peaks from the background

%A final way to set threshold is to manually verify in several peaks
that
%can be visually inspected and verified, and then setting the
threshold
%based on what was experimeentally observed in cases of misalignment
of
%the chip and excitation sources.
max_entire_vector = max(max(max(corr_matrix_final)));
max_entire_vector_G = max(max(max(corr_matrix_final_G)));
max_entire_vector_B = max(max(max(corr_matrix_final_B)));
numberofdroplets = zeros(numberofchannels);
allchannelsvectors =
zeros(numberofchannels,frames_total*framelengtha);
threshold2 = max_entire_vector*.4; %set threshold; threshold was
determined experimentally for each particle and varies for dye, and
bead color based on the intensity of background and particle intensity

```

```

threshold2_G = max_entire_vector_G*.4;
threshold2_B = max_entire_vector_B*.4;

%for each channel, loop through all the frames and begin counting
for chan_loop_2 = 1:numberofchannels
    for chan_loop_2_2 = 1:frames_total
        corr_mat_R(chan_loop_2,(chan_loop_2_2-
1)*framelengtha+1:chan_loop_2_2*framelengtha) =
corr_matrix_final(chan_loop_2_2,chan_loop_2,:);
        corr_mat_G(chan_loop_2,(chan_loop_2_2-
1)*framelengtha+1:chan_loop_2_2*framelengtha) =
corr_matrix_final_G(chan_loop_2_2,chan_loop_2,:);
        corr_mat_B(chan_loop_2,(chan_loop_2_2-
1)*framelengtha+1:chan_loop_2_2*framelengtha) =
corr_matrix_final_B(chan_loop_2_2,chan_loop_2,:);
    end
end

counter_R_G = 0;
counter_R_B = 0;
counter_G = 0;
counter_B = 0;

[indexR_a, indexR_b] = size(corr_mat_R);
[indexG_a, indexG_b] = size(corr_mat_G);
[indexB_a, indexB_b] = size(corr_mat_B);

for chan_loop_2 = 1:numberofchannels
    [pks,locs] =
findpeaks(corr_mat_R(chan_loop_2,:), 'MinPeakDistance',30, 'MinPeakHeight
',threshold2);
    [pks,locs_G] =
findpeaks(corr_mat_G(chan_loop_2,:), 'MinPeakDistance',30, 'MinPeakHeight
',threshold2);
    [pks,locs_B] =
findpeaks(corr_mat_B(chan_loop_2,:), 'MinPeakDistance',30, 'MinPeakHeight
',threshold2);

    peaks_R(chan_loop_2,1:length(locs)) = locs;
    peaks_G(chan_loop_2,1:length(locs_G)) = locs_G;
    peaks_B(chan_loop_2,1:length(locs_B)) = locs_B;
end

%find where both colors peak together to count true positives
for chan_loop_2 = 1:numberofchannels
    %go through each 1d line vector segment
    for index_track = 1:nnz(peaks_R(chan_loop_2,:))
        %for each nonzero number for the 1d vector; check if there is a
value
        %that is close to the peak location in G or B

```

```

        for index_track_G = 1:nnz(peaks_G(chan_loop_2,:))
            if (peaks_R(chan_loop_2,index_track)-10) <
peaks_G(chan_loop_2,index_track_G) &&
(peaks_R(chan_loop_2,index_track)+10) >
peaks_G(chan_loop_2,index_track_G)
                counter_R_G=counter_R_G+1;
            end
        end

        for index_track_B = 1:nnz(peaks_B(chan_loop_2,:))
            if (peaks_R(chan_loop_2,index_track)-10) <
peaks_B(chan_loop_2,index_track_B) &&
(peaks_R(chan_loop_2,index_track)+10) >
peaks_B(chan_loop_2,index_track_B)
                counter_R_B=counter_R_B+1;
            end
        end

end
end

%count the number of beads based on the total nonzero elements in the
%matrix containing peaks for g and b correlation peaks
counter_G = nnz(peaks_G);
counter_B = nnz(peaks_B);

%Active enzyme for beads is defined as fraction of total beads that
%caputred a protein
AEB_G = counter_R_G/counter_G;
AEB_B = counter_R_B/counter_B;
~~~~~

```

## uMD\_ThreeColor\_Arduino\_Code

### ThreeColorArduino

```

int fps = 25;
int bits = 63;
//int delay_time = 0;
long delay_time = 1000000L/(fps*bits); //delaytime is in us based on
fps
//int MLS_Seq[63];
int MLS_Seq[] = {-1, 1, -1, 1, -1, 1, 1, -1, -1, 1, 1, -1, 1, 1,
1, -1, 1, 1, -1, 1, -1, -1, 1, -1, -1, 1, 1, 1, -1, -1, -1, 1,
-1, 1, 1, 1, 1, -1, -1, 1, -1, 1, -1, -1, -1, 1, 1, -1, -1, -
1, -1, 1, -1, -1, -1, -1, -1, 1, 1, 1, 1, 1, 1};
int MLS_SeqTwo[] = {-1, 1, -1, 1, 1, 1, 1, -1, -1, 1, -1, -1, 1,
-1, 1, 1, 1, -1, -1, 1, 1, 1, -1, -1, -1, -1, -1, -1, 1, 1,
1, -1, 1, 1, 1, -1, 1, -1, -1, 1, 1, 1, 1, -1, 1, -1, 1, -1, -
1, 1, -1, 1, -1, -1, -1, -1, -1, -1, 1, -1, 1, -1, 1};

```

```

int MLS_Seq3[] = {-1, -1, 1, 1, 1, 1, 1, 1, -1, -1, 1, -1, 1, -1,
1, -1, 1, -1, -1, 1, 1, -1, -1, 1, 1, -1, -1, 1, -1, 1, -1, -
1, 1, 1, 1, 1, 1, -1, 1, -1, -1, 1, 1, 1, -1, -1, -1, -1, 1, -
1, -1, -1, 1, 1, -1, 1, 1, -1, -1, 1, -1, -1, -1};

// the setup function runs once when you press reset or power the board
void setup() {

 // initialize digital pin 13 as an output.
 pinMode(24, OUTPUT);pinMode(25, OUTPUT);pinMode(26, OUTPUT);
 Serial.begin(9600);

}

// the loop function runs over and over again forever
void loop() {
 //Serial.print(delay_time);
 Serial.print('\n');
 //Largest number for delayMicroseconds function is 16383

 for (int i=0; i<bits; i=i+1){
 if (MLS_Seq[i]>0){
 digitalWrite(24, LOW); //LOW leads ot LED being on from the Driver
 }
 else {
 digitalWrite(24, HIGH);
 }

 if (MLS_SeqTwo[i]>0){
 digitalWrite(25, LOW); //LOW leads ot LED being on from the Driver
 }
 else {
 digitalWrite(25, HIGH);
 }

 if (MLS_Seq3[i]>0){
 digitalWrite(26, LOW); //LOW leads ot LED being on from the Driver
 }
 else {
 digitalWrite(26, HIGH);
 }

 delayMicroseconds(delay_time);
 }
 //Serial.print(micros()) ;

}

~~~~~

```

## ddELISA\_App\_Final\_Package\_COMPLETE

### MainActivity.java

```
package vraviy.exosomedetection;

import android.app.Notification;
import android.app.NotificationManager;
import android.app.PendingIntent;
import android.content.ComponentName;
import android.content.Context;
import android.content.pm.PackageManager;
import android.graphics.Bitmap;
import android.media.MediaMetadataRetriever;
import android.support.v4.app.NotificationCompat;
import android.support.v7.app.AppCompatActivity;
import android.os.Bundle;
import android.view.Menu;
import android.view.MenuItem;
import java.io.File;
import java.io.FilenameFilter;
import java.util.Arrays;
import android.app.Activity;
import android.app.AlertDialog;
import android.app.AlertDialog.Builder;
import android.app.Dialog;
import android.content.DialogInterface;
import android.content.Intent;
import android.content.SharedPreferences;
import android.database.Cursor;
import android.graphics.Color;
import android.net.Uri;
import android.os.Bundle;
import android.os.Environment;
import android.preference.PreferenceManager;
import android.provider.MediaStore;
import android.provider.MediaStore.MediaColumns;
import android.util.Log;
import android.view.Menu;
import android.view.MenuInflater;
import android.view.MenuItem;
import android.view.MotionEvent;
import android.view.View;
import android.view.View.OnClickListener;
import android.widget.Button;
import android.widget.ImageView;
import android.widget.TextView;
import android.widget.Toast;
import android.widget.VideoView;
import java.util.HashMap;
import java.lang.Object;
```

```

public class MainActivity extends AppCompatActivity implements
OnTouchListener{

    private static final int SELECT_VIDEO = 1;
    private static final int RECORD_VIDEO = 2;
    // private static final int SELECT_GIF = 3;
    private static final String TAG = "MainActivity";
    private NotificationManager notificationManager;
    MediaMetadataRetriever retriever = new MediaMetadataRetriever();
    //FFmpegMediaMetadataRetriever retriever = new
    FFmpegMediaMetadataRetriever();

    private VideoView selected_video;

    //Getting video dimensions for pixels
    private int vid_width = 0;
    private int vid_height = 0;

    //Frames from video

    ImageView img, img2, img3, img4, img5, img6, img7, img8, img9,
    img10;
    ImageView imageView;
    TextView textview_ratio, t0,t1,time0_text,time5_text,time10_text;
    TextView rotatedYLabel;
    @Override
    protected void onCreate(Bundle savedInstanceState) {

        super.onCreate(savedInstanceState);
        if(savedInstanceState != null){
            Log.d("STATE",savedInstanceState.toString());
        }

        setContentView(R.layout.activity_main);

        setupButtonClickListeners();

        notificationManager = (NotificationManager)
            getSystemService(Context.NOTIFICATION_SERVICE);

        CharSequence tickerText = "Hello";
        long when = System.currentTimeMillis();
        NotificationCompat.Builder mBuilder = new
        NotificationCompat.Builder(this)

```

```

        .setSmallIcon(R.mipmap.ic_launcher)
        .setContentTitle("Microdroplet Detector");
Intent resultIntent = new Intent(this, MainActivity.class);
PendingIntent resultPendingIntent = PendingIntent.getActivity(
    this,
    0,
    resultIntent,
    PendingIntent.FLAG_UPDATE_CURRENT);
mBuilder.setContentIntent(resultPendingIntent);
Notification notification = mBuilder.build();
notification.flags |= Notification.FLAG_NO_CLEAR |
Notification.FLAG_ONGOING_EVENT;

    NotificationManager mNotifyMgr = (NotificationManager)
getSystemService(NOTIFICATION_SERVICE);
    mNotifyMgr.notify(1, notification);

}

private void setupButtonClickListeners()
{
    //Button exitButton = (Button)findViewById(R.id.exit);
    //exitButton.setOnClickListener(this);

    ((Button)findViewById(R.id.GalleryButton)).setOnTouchListener(this);
    ((Button)findViewById(R.id.RecordButton)).setOnTouchListener(this);
    ((Button)findViewById(R.id.Matlabbutton)).setOnTouchListener(this);
}

@Override
public void onActivityResult(int requestCode, int resultCode,
Intent data)
{
    Log.d("CREATION", "Clicked button");

    //        Intent browserIntent = new Intent(Intent.ACTION_VIEW,
Uri.parse("https://drive.matlab.com"));
    //        startActivity(browserIntent);

}

```



```

private void VideoAnalysis(String path) {

    retriever.setDataSource(path);

    imageView.setImageBitmap(retriever.getFrameAtTime(1000000,
MediaMetadataRetriever.OPTION_CLOSEST));

}

private String getPath(Uri uri)
{
    //file:///mnt/sdcard/DCIM/Camera/VID_20111217_233451.mp4

    if(uri.toString().contains("content"))
    {
        try
        {
            String[] projection = {MediaColumns.DATA};
            Cursor cursor =
managedQuery(uri,projection,null,null,null);
            int column_index =
cursor.getColumnIndex(MediaColumns.DATA);
            cursor.moveToFirst();
            return cursor.getString(column_index);
        }
        catch(Exception ex)
        {
            return null;
        }
    }
    else
    {
        return uri.toString();
    }
}

private void handleClickEvent(View v)
{
    switch(v.getId())
    {
        case R.id.GalleryButton:
            Intent browserIntent = new Intent(Intent.ACTION_VIEW,
Uri.parse("https://drive.matlab.com"));
            startActivity(browserIntent);
            //            Intent intent = new Intent();
            //            intent.setType("video/*");
            //            intent.setAction(Intent.ACTION_GET_CONTENT);
            //
            startActivityForResult(Intent.createChooser(intent,"Select
Video"),SELECT_VIDEO);

```

```

        //image/*
        break;
    case R.id.RecordButton:
        Intent recordIntent = new Intent();

recordIntent.setAction(MediaStore.ACTION_VIDEO_CAPTURE);
        recordIntent.putExtra(MediaStore.EXTRA_VIDEO_QUALITY,
1);
        //recordIntent.putExtra(MediaStore.EXTRA_OUTPUT,
Uri.fromFile(file));
        startActivityForResult(recordIntent, RECORD_VIDEO);
        break;
    case R.id.Matlabbutton:
        //
        Intent intent = new Intent(Intent.ACTION_MAIN);
        //
        intent.setComponent(ComponentName.unflattenFromString("com.mathworks.ma
tlabmobile"));
        //
        intent.addCategory(Intent.CATEGORY_LAUNCHER);
        //
        startActivity(intent);

        PackageManager pm = this.getPackageManager();
        Intent appStartIntent =
pm.getLaunchIntentForPackage("com.mathworks.matlabmobile");
        if (null != appStartIntent)
        {
            this.startActivity(appStartIntent);
        }

        break;
    }
}

// #FFA500
@Override
public boolean onTouch(View v, MotionEvent event) {
    switch(event.getAction())
    {
        case MotionEvent.ACTION_DOWN:
            switch(v.getId())
            {
                case R.id.GalleryButton:

// ((Button) findViewById(R.id.GalleryButton)).setBackgroundColor(0xFFFFFA
500);

                break;
                case R.id.RecordButton:
                    //
                    ((Button) findViewById(R.id.RecordButton)).setBackgroundColor(0xFFFFFA500
);

                break;
            }
        }
    }
}

```

```

    }
    return true;
case MotionEvent.ACTION_UP:
    switch(v.getId())
    {
        case R.id.GalleryButton:
            //
            ((Button)findViewById(R.id.GalleryButton)).setBackgroundColor(Color.BLA
CK);
            handleClickEvent(v);
            break;
        case R.id.RecordButton:
            //
            ((Button)findViewById(R.id.RecordButton)).setBackgroundColor(Color.BLAC
K);
            handleClickEvent(v);
            break;
        case R.id.Matlabbutton:
            //
            ((Button)findViewById(R.id.RecordButton)).setBackgroundColor(Color.BLAC
K);
            handleClickEvent(v);
            break;
    }

default:
    return true;
}
}

//In an Activity
private String[] mFileList;
private File mPath;
private String mChosenFile;
private static final String FTYPE = ".gif";
private static final int DIALOG_LOAD_FILE = 1000;

private void loadFileList(){

    try
    {
        mPath = new
File(getApplicationContext().getExternalFilesDir(null).getAbsolutePath(
) + "/");
        Log.i(TAG,"loadFileList() path: " + mPath.getAbsolutePath()
+ "/");
    }
    catch(Exception ex)
    {
        mPath = null;
        return;
    }
    try{
        mPath.mkdirs();

```

```

    }
    catch (SecurityException e) {
        Log.e(TAG, "unable to write on the sd card " +
e.toString());
    }
    if (mPath.exists()) {
        FilenameFilter filter = new FilenameFilter() {
            @Override
            public boolean accept(File dir, String filename) {
                File sel = new File(dir, filename);
                return filename.contains(FTYPE) ||
sel.isDirectory();
            }
        };
        mFileList = mPath.list(filter);
    }
    else {
        mFileList = new String[0];
    }
}

@Override
public boolean onCreateOptionsMenu(Menu menu) {
    // Inflate the menu; this adds items to the action bar if it is
present.
    getMenuInflater().inflate(R.menu.menu_main, menu);
    return true;
}

@Override
public boolean onOptionsItemSelected(MenuItem item) {
    // Handle action bar item clicks here. The action bar will
    // automatically handle clicks on the Home/Up button, so long
    // as you specify a parent activity in AndroidManifest.xml.
    int id = item.getItemId();

    //noinspection SimplifiableIfStatement
    if (id == R.id.action_settings) {
        return true;
    }

    return super.onOptionsItemSelected(item);
}
}

```

## **CHAPTER 4: MAGNETIC NICKEL IRON ELECTROFORMED TRAP (MAGNET): A MASTER / REPLICA FABRICATION STRATEGY FOR ULTRA-HIGH THROUGHPUT (> 100 ML/HR) IMMUNOMAGNETIC SORTING**

This chapter is a slightly modified version of a manuscript published in Lab on a Chip:

J Ko\*, **VR Yelleswarapu\***, A Singh, N Shah, D Issadore. Magnetic Nickel iron Electroformed Trap (MagNET): A master / replica fabrication strategy for ultra-high throughput (> 100 mL/hr) immunomagnetic sorting, Lab on a Chip, 2016. (\*Equal Contribution)

V. Y. conceived and performed experiments in this study, coded the Comsol and Matlab software, as well as prepared the manuscript and figures.

### **4.1 Abstract**

Microfluidic devices can sort immunomagnetically labeled cells with sensitivity and specificity much greater than that of conventional methods, primarily because the size of microfluidic channels and micro-scale magnets can be matched to that of individual cells. However, these small feature-sizes come at the expense of limited throughput  $\phi < 5$  mL/hr and susceptibility to clogging, which have hindered current microfluidic technology from processing relevant volumes of clinical samples, e.g.  $V > 10$  mL whole blood. Here, we report a new approach to micromagnetic sorting that can achieve highly specific cell separation in unprocessed complex samples at a throughput ( $\phi > 100$  mL/hr) 100x greater than that of conventional microfluidics. To achieve this goal, we have devised a new approach to micromagnetic sorting, the Magnetic Nickel iron Electroformed Trap (MagNET), which enables high flow rates by having millions of micromagnetic traps operate in parallel. Our design rotates the conventional microfluidic approach by 90° to form magnetic traps at the edges of pores instead of in channels, enabling millions of the magnetic traps to be incorporated into a centimeter sized device. Unlike previous work, where magnetic structures were defined using conventional

microfabrication, we take inspiration from soft lithography and create a master from which many replica electroformed magnetic micropore devices can be economically manufactured. These free-standing 12  $\mu\text{m}$  thick permalloy ( $\text{Ni}_{80}\text{Fe}_{20}$ ) films contain micropores of arbitrary shape and position, allowing the device to be tailored for maximal capture efficiency and throughput. We demonstrate MagNET's capabilities by fabricating devices with both circular and rectangular pores and use these devices to rapidly ( $\phi = 180 \text{ mL/hr}$ ) and specifically sort rare tumor cells from white blood cells.

## 4.2 Introduction

The isolation of specific populations of cells, such as stem cells, pathogens, or circulating tumor cells (CTCs), from complex biological fluids is an emerging methodology that holds enormous potential for detecting, monitoring, and studying a wide variety of diseases.<sup>203–206</sup> The use of magnetic fields to separate cells labeled with magnetic nanoparticles (MNPs) has shown particular promise because it can achieve highly selective sorting even in complex biological media, due to the inherently negligible magnetism of biological samples compared to MNP labeled cells.<sup>207–211</sup> Moreover, platforms that use micro-scale structures, where the dimensions of the microfluidic channels and the micrometer-scale magnets can be designed to match those of the targeted cells, have been harnessed for highly selective sorting of rare cells. However, conventional microfluidic geometries where immunomagnetically labelled cells travel through microfluidic channels and are captured with patterned microstructures have limited throughput ( $\phi < 5 \text{ mL/hr}$ ) and are susceptible to clogging, due to their microscale channels. The limited throughput ( $\phi < 5 \text{ mL/hr}$ ) and susceptibility to clogging of microscale devices have kept these approaches from being translated from the laboratory to many medical applications, where large volume samples, e.g.  $V > 10 \text{ mL}$  of whole blood, must be processed rapidly ( $< 15 \text{ minutes}$ ) to provide relevant point-of-care

information. In particular, applications where extremely rare cells (e.g. CTCs, pathogens, stem cells) must be sorted from complex biological fluids (e.g. blood, sputum, environmental samples) require large volumes of unprocessed clinical samples to be sorted with the precision of microfluidics within timescales relevant to providing real-time information ( $T < 30$  minutes). For example, using CTCs for the diagnosis of cancer requires the detection of extremely sparse cells ( $< 1$  CTC / mL) in volumes of blood  $> 10$  mL.<sup>212</sup>

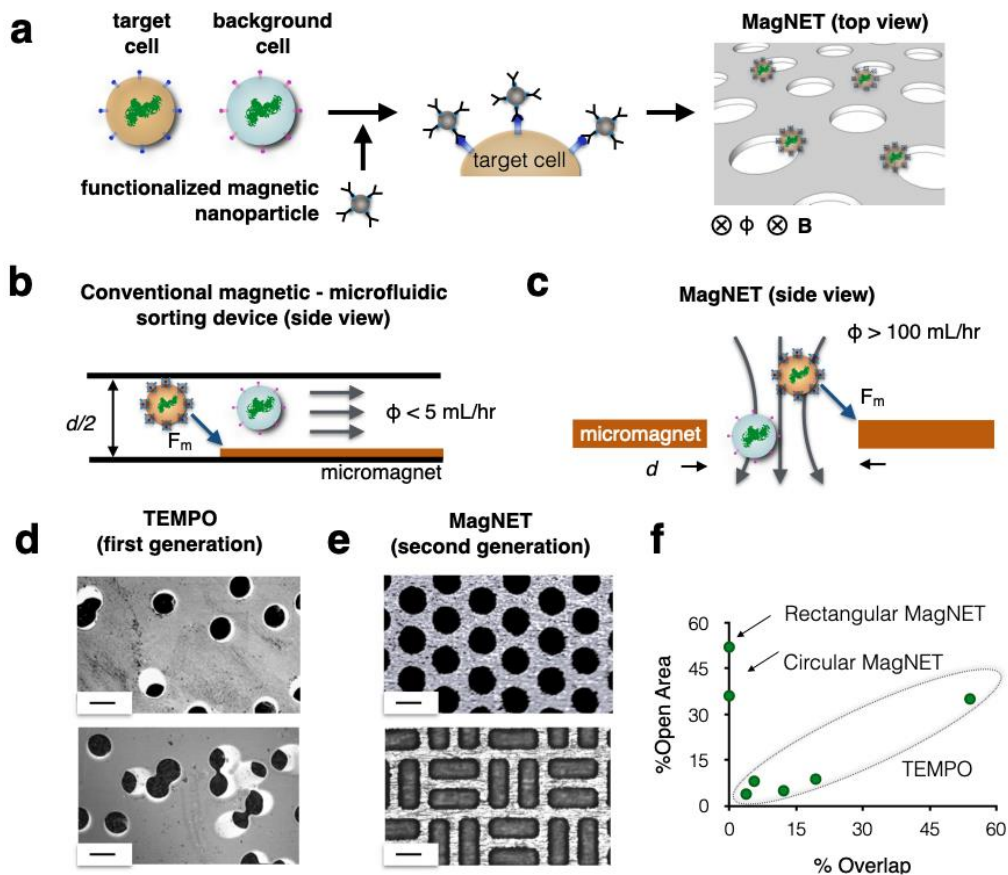


**Figure 4.1. High throughput immunomagnetic sorting with the Magnetic Nickel iron Electroformed Trap (MagNET).** **a.** MagNET uses magnetophoretic traps to isolate cells specifically targeted with functionalized magnetic nanoparticles. This design enables high flow rates by having millions of micromagnetic traps operate in parallel. **b.**

MagNET rotates the conventional microfluidic geometry by 90° to form magnetic traps at the edges of pores instead of in microfluidic channels (**c**). **d**. Micrographs of Track Etched Magnetic microPOre (TEMPO) devices. In this approach as the density of micropores is increased so did the number of overlapped pores, which limited performance. Scale bar 30  $\mu\text{m}$ . **e**. Micrographs of MagNET devices. In this approach density and the shape of the micropores could be tailored to maximize performance. Scale bar 30  $\mu\text{m}$ . **f**. A graph summarizing the trade-off relationship between % open area and % overlap for both TEMPO and MagNET.

To address these challenges, we have developed a new approach to the micromagnetic separation of cells, the Magnetic Nickel iron Electroformed Trap (MagNET).(**Fig. 1a**) In contrast to lateral flow devices<sup>208–210,212213</sup>, our vertical flow design enables high flow rates ( $\phi > 100 \text{ mL/hr}$ ) by having millions of micromagnetic traps operate in parallel. This improved throughput allows typical clinical samples ( $V > 10 \text{ mL}$  of blood) to be processed in less than fifteen minutes, allowing precise microfluidic cell sorting to be used for rapid point-of-care diagnostics. Our design achieves this performance by rotating the conventional microfluidic geometry (**Fig. 1b**) by 90° to form magnetic traps at the edges of pores instead of in microfluidic channels. (**Fig. 1c**) An external static field, provided by an inexpensive NdFeB magnet, magnetizes both the MNP labeled cells and the MagNET filter. This geometry allows millions of magnetic traps to be incorporated into a single centimeter sized device. Furthermore, the large density of micropores ( $\rho = 5 \times 10^4 \text{ pores/cm}^2$ ) reduces clogging from clinical samples, as the blockage of a few pores does not significantly change the device's behavior.<sup>214</sup> The trapping of a cell in MagNET is based on a competition between the individual cell's drag force and its magnetic force as it passes through a magnetic micropore. Thus, the contrast in the magnetic trapping



of targeted cells *versus* non-targeted cells is not affected by the concentration of cells. Unlike previous work, where magnetic micropores were defined using conventional microfabrication,<sup>215,216</sup> we instead take inspiration from soft lithography<sup>217</sup> and create a master that can be used repeatedly to economically produce replica permalloy membranes with lithographically defined micropores. The micropores on these 12  $\mu\text{m}$  thick electroformed membranes can have arbitrary shape and position, allowing the device to be tailored for maximal capture efficiency and throughput. We demonstrate MagNET's capabilities by fabricating devices with both circular and rectangular pores and use these devices to rapidly ( $\phi = 180 \text{ mL/hr}$ ) and specifically sort rare tumor cells ( $\text{LOD} = 3 \text{ cells/mL}$ ) from white blood cells.

Our MagNET approach builds upon previous work from our lab, where track etching was used to fabricate magnetic micropores.<sup>214,216</sup> The MagNET approach offers several important advantages over our previous approach, which we called Track Etched Magnetic microPOre (TEMPO). The TEMPO consists of an ion track-etched polycarbonate membrane coated with soft magnetic film, permalloy ( $\text{Ni}_{80}\text{Fe}_{20}$ ). The main advantage of track etching is the ability to fabricate microscale pores over large areas ( $A > 1 \text{ cm}^2$ ) at a cost  $< 5\text{¢}/\text{cm}^2$ , much less than conventional microfabrication.<sup>214</sup> MagNET conserves the advantages of TEMPO, and also addresses its two key weaknesses:

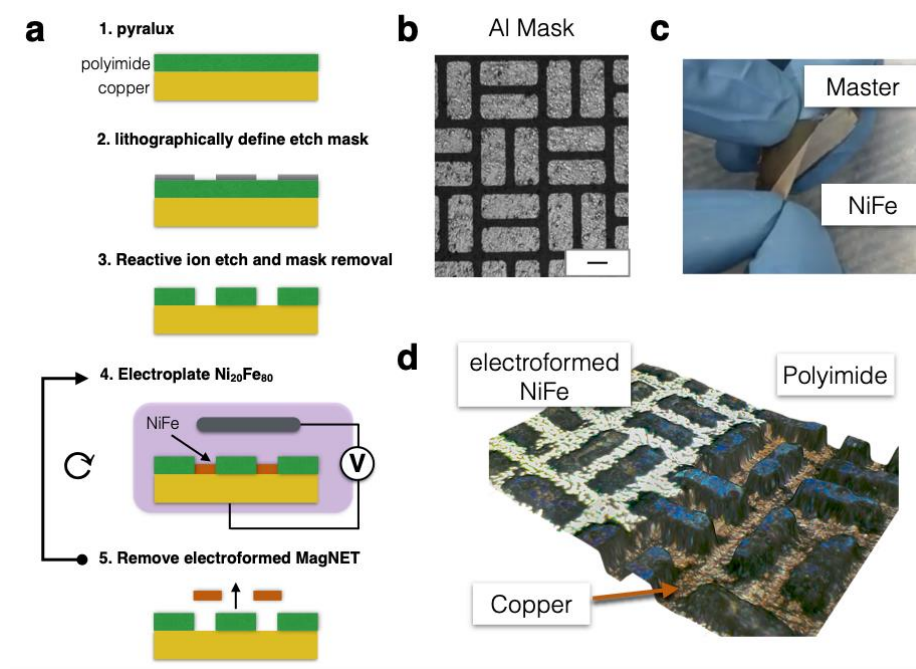
1. TEMPO's low cost fabrication comes at the expense of its inability to control the position or shape of the pores. **(Fig. 1d)** The MagNET strategy solves this challenge, allowing pores to be created with arbitrary shape and position. **(Fig. 1e)** The inability of TEMPO to control the position of the pores creates a tradeoff relationship between the density of the micropores and the fraction of pores that overlap with one another **(Fig. 1f)**, which results in a tradeoff between the device's throughput  $\phi$  and the

capture efficiency of magnetically labeled cells  $\zeta$ . The reason for this tradeoff is that as the fraction of open area is increased by increasing the density of micropores, the flow velocity through each pore decreases. As the flow rate decreases, the capture efficiency of each magnetic micropore increases, increasing the overall capture rate  $\zeta$ . However, for TEMPO, as the density of track etched micropores increases, so does the fraction of pores that overlap. (**Fig. 1d**) For pores that overlap, the effective pore diameter is increased and so fewer cells come in close proximity to the pore's edge to be trapped, and thus the overall capture efficiency  $\zeta$  is reduced. MagNET's ability to control the position and shape of the pores allows this tradeoff relationship to be broken (**Fig. 1f**) and extremely high flow rates to be achieved  $\phi > 100$  mL/hr without having to sacrifice capture rate  $\zeta > 10^4$ .

2. While track etching allows the polycarbonate membranes in TEMPO to be fabricated at low-cost, the deposition of the magnetic film is expensive, slow, and requires specialized facilities.<sup>12</sup> The MagNET strategy solves this challenge. Once the master is made, which requires a cleanroom and lithography equipment, subsequent replicas only require electroplating, which can be performed at high throughput and without specialized laboratory facilities.<sup>218</sup> Moreover, the MagNET method allows thick permalloy films (12  $\mu\text{m}$ ) compared to thermal evaporation, which is practically limited to  $< 1$   $\mu\text{m}$ , while also achieving consistent reproducibility of film thickness ( $\pm 0.5$   $\mu\text{m}$ ). The increased thickness of MagNET leads to an increased capture rate, due to both increased magnetic field gradients (**Fig. 3b**) and the formation of two traps in series for each pore: one on the top surface of the filter and one on the bottom (**Fig. S2**).

### 4.3 Methods

**Fabrication of the MagNET master.** We take inspiration from soft lithography<sup>217</sup> and create a master from which many replica MagNET devices can be produced using electroformation. Electroformation is a well-known process to form metal parts by electroplating onto a master (i.e. a mandrel), and subsequently removing the electroplated piece from the master to form a free-standing metal piece. Much work has been done to use this technique to form free-standing metal pieces with microscale features,<sup>219–221</sup> but to our knowledge this work represents the first such work that creates a reusable microscale master to generate many replica devices. The creation of a reusable micro-scale master for electroformation comes with the following challenges: **1.** A thin metal piece (i.e. 12  $\mu\text{m}$ ) must be removed from the master without tearing. **2.** The master must be mechanically robust, such that the removal of the electroformed metal piece from the master does not cause the microscale features of the master to be destroyed.



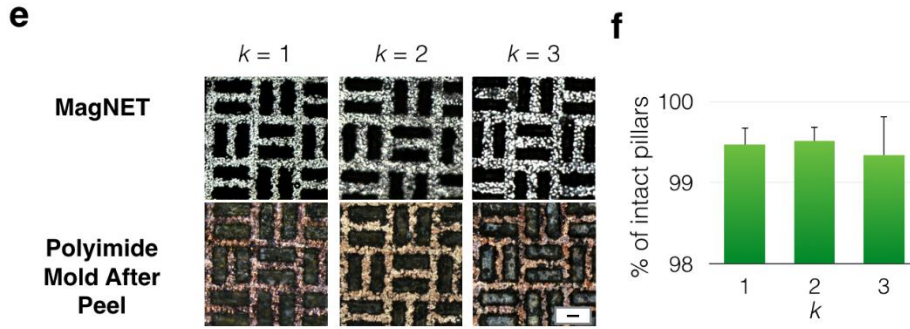


**Figure 4.2. Master / replica fabrication of MagNET.** **a.** Step by step fabrication of the master and subsequent replicas of MagNET. **b.** A micrograph of the lithographically defined aluminum mask. Scale bar 30  $\mu\text{m}$ . **c.** Photograph of a replica MagNET being mechanically removed from its Master. **d.** Three dimensional optical micrograph of MagNET. In the region to the left, a MagNET has been electroformed. In the region to the right, the MagNET has been removed and the polyimide and copper master can be seen. **e.** Micrographs of the master and replica MagNETs after  $k$  replications. Scale bar: 30  $\mu\text{m}$ . **f.** The fraction of damaged pillars was quantified after each replication, and there was no statistically significant change observed. ( $P \gg 0.05$ ). Error bars indicate standard error from the ratio of intact pores to total number of pores of different regions from the same device.

To address these challenges, we made the following design choices. To remove the electroformed permalloy piece without tearing, we needed to find a metal substrate that has minimum adhesion to the electroformed material. We chose copper as a substrate because it is known to have low adhesion to permalloy.<sup>222</sup> To allow the electroformed permalloy to be removed without destroying the master, we patterned the microscale features of the master in polyimide, which was adhered to a roll annealed copper substrate. The roll annealed copper on polyimide is more strongly adhered than is possible with spun-on photo-activated polymers (e.g. SU8),<sup>219–221</sup> and so does not

delaminate when the electroformed permalloy is removed. We used conventional microfabrication techniques to etch the polyimide to create the micropore pattern through which MagNET was electroformed.

To fabricate the master for MagNET, we perform the following procedure. **(Fig. 2a)** We begin with Pyralux AC181200R (Dupont), a substrate typically used for flexible electronics, where an 18  $\mu\text{m}$  copper layer is roll annealed onto a 12  $\mu\text{m}$  polyimide film. We adhere the Pyralux to a glass slide to prevent the film from wrinkling during processing. Next, a hard mask of aluminum (Al) is thermally evaporated (PVD75 E-beam/Thermal evaporator) and patterned using conventional planar UV photolithography (Singh Center for Nanotechnology). **(Fig. 2b)** We use the same Tetramethylammonium hydroxide (TMAH) solution (MF319, Microposit) to both develop the S1805 (Microchem) photoresist and chemically etch the Al mask. Finally, the unexposed photoresist is stripped in acetone. After patterning the Al hard mask, the polyimide is etched using Inductively Coupled Plasma (ICP) etching.<sup>223–225</sup> Whereas a pure plasma etch would result in isotropic etching, a combination of a plasma etch with ion bombardment provided an etch with a sufficiently anisotropic etch profile. Exposed regions of the copper without the polyimide pillars are used as zones for electroplating permalloy. Once the permalloy filter is  $> 10\ \mu\text{m}$ , the filter can be peeled off mechanically due to poor adhesion between the copper and electroplated permalloy<sup>222</sup> **(Fig. 2c)**. The Pyralux substrate facilitates the easy removal of the permalloy film. By gently flexing the substrate, the permalloy delaminates from the copper.

We optimized RIE conditions for the MagNET master using The Trion Phantom at University of Pennsylvania's Singh Center for Nanotechnology. After exploring a variety of combinations of pressures, RIE powers, RF powers, and gas flow rates, we found that

O<sub>2</sub>/CF<sub>4</sub> resulted in large undercuts in the polyimide and made etching 12µm polyimide impractical since the undercut resulted in the erosion of the hardmask. O<sub>2</sub>/SF<sub>6</sub> etching resulted in less undercut, as well as slower etch rates. The optimal recipe for the etching of the polyimide was with 40 sccm O<sub>2</sub>/ 10 sccm SF<sub>6</sub>/ 40mT Pressure/ 300W ICP/ 50W RIE for 50 minutes. The etch profile was characterized using profilometry and 3D imaging (Zeiss Smartzoom5 2D/3D).

**Electroformation of MagNET.** Permalloy was electroplated onto the MagNET master using nickel foil (1 mm thick, 99.5%, Alfa Aesar) as the anode in an electroplating solution containing 200 g/l NiSO<sub>4</sub>·6H<sub>2</sub>O, 8 g/l FeSO<sub>4</sub>·7H<sub>2</sub>O, 5 g/l NiCl<sub>2</sub>·6H<sub>2</sub>O, 25 g/l H<sub>3</sub>BO<sub>3</sub>, and 3 g/l saccharin (pH=2.5-3).<sup>218</sup> 12 µm thick permalloy layer was deposited on the 3.8 cm [W] × 4.3 cm [L] master at 0.2A for 45 min. The master was firmly attached to a flexible mylar support for plating. To peel off the filter, the mylar/Pyralux combination was flexed until the permalloy started to lift off at the corner. The permalloy was separated mechanically as shown in **Fig. 2c**. Once removed from the master, the free standing electroformed MagNET was then plated (Bright Electroless Gold, Transene) with approximately 100 nm of gold to passivate the surface.

Electroformation allows precise and repeatable control over film thickness. In prior work, permalloy has been electroplated with film thickness ranging from 500 nm to 5 µm in uniform, smooth layers (surface roughness < 100 nm)<sup>226,227</sup>. To control the thickness of our electroformed film, we fixed the device area exposed to the electroplating solution, and then calibrated the deposition current and the deposition time to produce specific film thicknesses. We measured film thickness using a profilometer (KLA Tencor P7 2D profilometer). The variation of film thickness across individual devices was determined by measuring film thickness at  $N = 10$  locations across the 3.8 × 4.3 cm<sup>2</sup> film, resulting in

a coefficient of variation of  $CV = 3.6\%$ . The variation of film thickness across various devices was determined by measuring the average film thickness of  $N = 8$  independently fabricated devices, resulting in a coefficient of variation between devices of  $CV = 3.3\%$ . These measurements indicate that MagNETs can be fabricated with accurate and reproducible film thickness.

**Device fabrication.** The MagNET filter was incorporated into the device using a moisture-resistant polyester film (McMaster-Carr, 0.004" thick) and a solvent-resistant tape (McMaster-Carr, adhesive on both sides). Multiple layers of the polyester film and the solvent-resistant tape were cut by a laser cutter (Universal Laser VLS 3.50) and assembled. For the device with multiple filters stacked in series, the filters were separated by the height of the polyester film (0.004") and the tape (0.004"). An optically clear cast acrylic sheet (McMaster-Carr) was used as a reservoir, and the output was made using a blunt syringe tip (McMaster-Carr) epoxy-bonded to the device to pull the fluid from the reservoir. The design of each of the device layers, as well as a three dimensional rendering of the device, are shown in detail in **Fig. S3**.

## 4.4 Results

**Robustness of MagNET fabrication over multiple replications.** One design challenge that we overcame in developing MagNET was to find a material that we could use to pattern the microscale features of our master that is not damaged during the removal of each electroformed MagNET replica. We found that spin-on polymers such as photoresists (SU8, S1818, SPR220) delaminated during mechanical peel off even after surface treatment to improve adhesion. Dupont's Pyralux – a material used for flexible circuit PCBs – consisting of 18  $\mu\text{m}$  copper film roll annealed onto a 12  $\mu\text{m}$  polyimide film proved to be perfect due to the polyimide layer's strong adherence to copper. To

demonstrate the robustness of the MagNET master for reusability, we performed multiple cycles of plating and peeling, and for each cycle checked for any damaged pillars (**Fig. 2e**). Profilometer (KLA Tencor P7 2D profilometer) and 3d images (Zeiss Smartzoom5 2D/3D Optical Microscope) of the master confirmed that there was no structural damage during mechanical peel off, and that the electroformed filters were identical after multiple rounds of fabrication. The percent of damaged pores after rounds one, two, and three were 0.5%, and did not show a statistically significant increase after repeated use. ( $P \gg 0.05$ ) To visually demonstrate the functionality of our fabrication process, we mechanically removed a MagNET such that a portion of the electroformed permalloy remained on the polyimide pillars, and subsequently imaged it (**Fig. 2d, Fig. S1**)(Zeiss Smartzoom5 2D/3D Optical Microscope). In this image, the electroformed permalloy has been plated to the height of the pillars. Adjacent to this film, there is a region where the film has been peeled away and the copper and polyimide pillars are visible. The image demonstrates that the pillars are still intact, and at the same height as the permalloy, and thus the master is robust for multiple rounds of reuse.

**Magnetic Field Finite Element Simulation.** To aid in the design and characterization of the MagNET filter, we performed finite element simulations. We modeled MagNET as a circular  $d = 30 \mu\text{m}$  pore in a  $12 \mu\text{m}$  thick permalloy film using a finite element simulation package (Comsol). We created a 2D axisymmetric model, containing one circular pore at the center of the permalloy film. The film is magnetized by a  $B = 0.4 \text{ T}$  field in the cylindrical direction provided by centimeter-sized NdFeB magnet placed below MagNET. In addition to MagNET, we also modeled a TEMPO filter for comparison. The TEMPO model was identical to MagNET's except the thickness of the permalloy film was  $200 \text{ nm}$ .



In these simulations, we used as our boundary conditions that at distances far from MagNET or TEMPO, the magnetic field dropped to zero.

To calculate the magnetophoretic force  $F_m = (m \cdot \nabla) B$  on a cell as it passes through MagNET, we combined the finite element field simulations described above with a simplified model for a cell. The total magnetic moment of the cell was calculated to be proportional to the number of magnetic nanoparticles  $n$ , each with a magnetic moment  $m_p = 10^6$  Bohr magnetons, with the assumption that the external magnetic field was sufficient to fully magnetize the beads.<sup>225</sup> Due to the low Reynold's number regime of flow through the micropore, the mass of the cell does not play a role in determining the cell's behavior. The total number of particles per cell was assumed to be  $10^4$  particles. There are a total of  $>10^5$  CD45 receptors on a leukocyte<sup>208</sup>. The assumed number of particles ( $10^4$ ) corresponds to 6.2% coverage of the surface of the cell, and thus would not result in significant steric hinderance. We assumed the cell to have a diameter  $d = 10 \mu\text{m}$  and the particles to have a diameter  $d = 50 \text{ nm}$ . We calculated the magnetic force experienced by the cell,  $F_m = ([m_p * n] \cdot \nabla) B$ , as the sum of the magnetic force experienced by all of the beads bound to the cell.

We calculated and plotted the radial force  $F_r$  experienced by the cell at one cell radius  $r = 5 \mu\text{m}$  above the filter. Additionally, the force in the cylindrical direction  $F_z$  on the cell was calculated and plotted along a line one cell radius  $r = 5 \mu\text{m}$  away the filter edge. The magnetophoretic force is opposed by a drag force, which can be calculated using Stokes equation  $F_d = 6\pi\eta rv$ , where  $\eta_{\text{water}} = 0.8 \text{ mPa/s}$ ,  $r = 5 \mu\text{m}$  for a cell. The average flow velocity in the pore  $v_{\text{avg}} = \phi / (n_{\text{pore}} A_{\text{pore}})$ , where  $n_{\text{pore}}$  is the total number of pores and  $A_{\text{pore}}$  is the cross sectional area of the pore. We calculated the maximum flow rate  $\phi$  at which

the magnetic trapping force  $F_m$  would still be greater than the drag force  $F_d$ , and the cell would remain trapped on the edge.

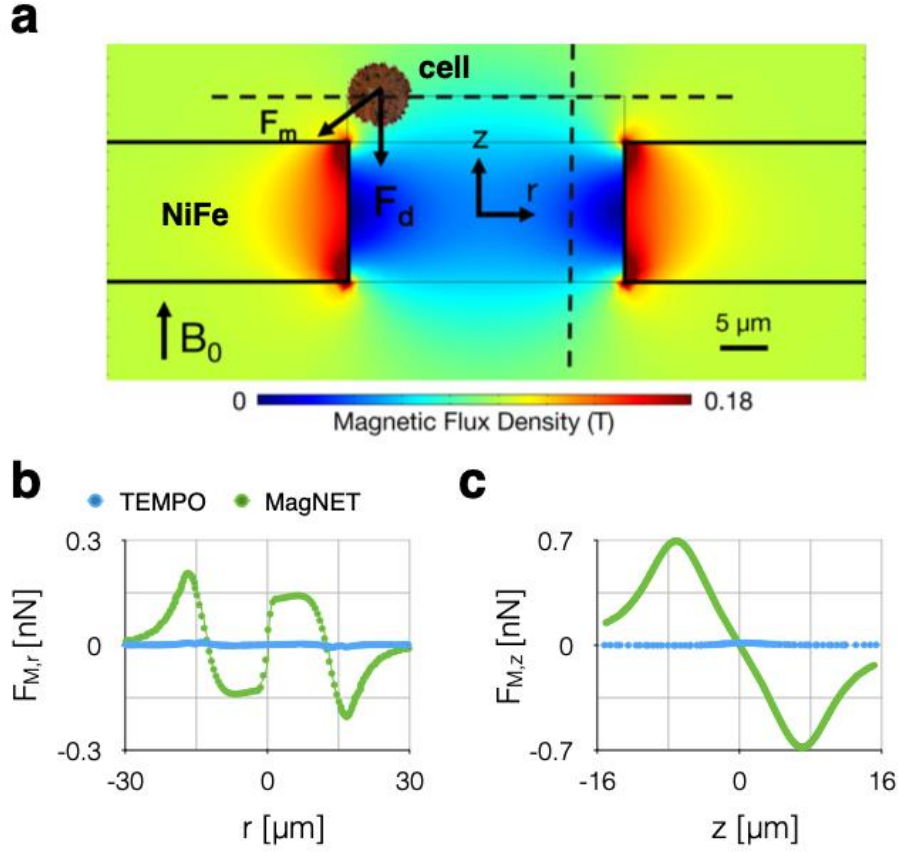


**Figure 4.3. Finite element simulations of MagNET.** **a.** The field strength  $|B|$  is plotted on the cross-section of an individual 30 μm pore. The magnetophoretic force  $F_m$  competes with drag force  $F_d$  to trap cells at the edge of the pore. **b.** The magnetophoretic force in the radial direction  $F_{M,r}$  is plotted along  $r$ , one cell radius  $d = 5$  μm above the MagNET's surface. **c.** The magnetophoretic force in the cylindrical direction  $F_{M,z}$  is plotted along  $z$ , one cell radius  $d = 5$  μm away the MagNET's edge.

The results of the finite element simulations were used to choose design parameters, such as the pore diameter, and to guide us in approaches to further improve the

throughput and enrichment of our device. **Fig. 3a** shows the simulated magnetic flux density around the edge of the pore. The magnetic flux density drops rapidly away from the edge of the pore, leading to strong gradients and magnetic forces at this region. Based on this simulated field, we calculated the radial and vertical forces experienced by a cell as it moves through the pore. The radial force, which pulls cells to the edge of the pore, was plotted 5  $\mu\text{m}$  above the MagNET's surface. (**Fig. 3b**) The force has a maximum magnitude of  $F_r = 266$  pN at the edge of the pore and drops rapidly in distance  $r$  from the pore's edge. Thus, we can improve the device's performance by making the pore as small as possible, as that will force cells to come into close proximity of the regions where the magnetic force is the strongest. However, the pores must be large enough that we do not capture off-target cells based on their size. The max  $F_r$  and  $F_z$  are  $\sim 10\times$  and  $\sim 50\times$ , respectively, larger for MagNET than TEMPO, demonstrating that the thicker metal film allows stronger trapping forces. Once a cell is translated to the pore's edge, the magnetic force  $F_z$  opposes the drag force  $F_d$ , and determines whether the cell will stay in the trap or not. The magnetophoretic force (**Fig. 3c**), at one cell radius  $r = 5$   $\mu\text{m}$  away from the filter, is  $F_z = 707$  pN. For the device described above ( $A = 6.2$   $\text{cm}^2$ ), the magnetic force will exceed the drag force up to extremely large flow rates  $\phi > 1000$  mL/hr. Thus, the performance of the device will be limited solely on what fraction of cells make it to the pore's edge. And, based on this fact, we predict that device performance can be improved, even at flow rates  $\phi \gg 100$  mL/hr, by stacking multiple filters in series to give cells multiple chances to be trapped.

**Characterization of MagNET's using a suspension of microbeads as a model sample.** Before testing the MagNET's capability to sort cells, we first tested it with magnetic and non-magnetic polystyrene beads that have well

characterized, homogenous properties. We used 1  $\mu\text{m}$  pink fluorescent magnetic beads (FCM-1058-2, Spherotech) and 1  $\mu\text{m}$  yellow fluorescent polystyrene beads (F13081, Invitrogen). We first compared the performance of MagNET to TEMPO, where both filters had an area of  $A = 6.2 \text{ cm}^2$ . The input to each device contained a 100:1 ratio of magnetic to non-magnetic beads. To characterize the capability of these devices to selectively sort magnetic beads, we calculated an enrichment factor  $\zeta = (C_{1p}/C_{1m})/(C_{0p}/C_{0m})$ , at different flow rates  $\Phi$ , where  $C_{0p}$  and  $C_{1p}$  are the numbers of non-targeted beads before and after sorting respectively, and  $C_{0m}$  and  $C_{1m}$  are the numbers of targeted beads before and after sorting respectively. We found that as flow rate increased, the enrichment dropped as a power law. **(Fig. 4a)** At all flow rates the enrichment of MagNET was  $> 30\times$  the enrichment of TEMPO. One of the reasons for MagNET's enhanced performance is that, in contrast to TEMPO where beads are captured on only one side of the filter (NiFe deposited), on MagNET the beads were captured both on the front and back side of the 12  $\mu\text{m}$  thick MagNET layer. By forming two traps, on the top and bottom surface of MagNET, the capture efficiency is increased by providing a second chance for cells missed by the trap on the top surface of MagNET to be captured. **(Fig. S2)** Moreover, we demonstrated that enrichment could be further improved by stacking multiple MagNET filters in series. **(Fig. 4b)** By increasing from  $N = 1$  to  $N = 5$  at  $\Phi = 150 \text{ ml/hr}$ , enrichment was improved  $\sim 1,000\times$ , allowing high enrichment ( $\zeta > 5,000$ ) to be achieved even at exceedingly high flow rates  $\Phi = 150 \text{ mL/hr}$ . As the filters are vertically stacked, the subset of the cells missed by the previous filter can be captured on the next filter, which leads

to an exponential increase in the enrichment  $\zeta \propto \zeta_0^N$ , where  $\zeta_0$  is the enrichment of one filter. (**Fig. 4b - inset**)

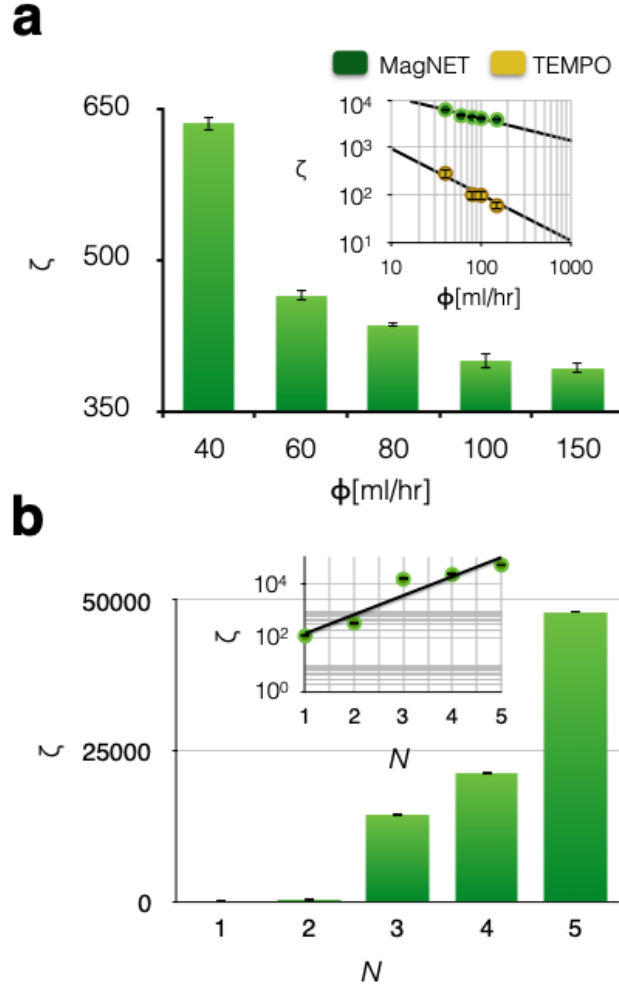


**Figure 4.4. Characterization of the MagNET using microbeads.** a. 1  $\mu\text{m}$  diameter magnetic polystyrene microbeads were sorted from non-magnetic 1  $\mu\text{m}$  polystyrene microbeads using MagNET. The enrichment of the non-magnetic beads  $\zeta$  is plotted vs. flow rate. Inset: Enrichment vs. flow rate on a log-log plot for both MagNET and TEMPO. At all flow rates the enrichment of MagNET was  $\zeta > 30\times$  the enrichment of TEMPO. The error bars indicate standard error from

replicates from flow cytometry measurement. **b.** As  $N$  filters are vertically stacked the enrichment at  $\Phi = 150$  ml/hr was improved  $\sim 1,000\times$ . Inset: Enrichment  $\zeta$  vs.  $\Phi$  on a log-linear plot, shows that enrichment  $\zeta$  scales exponentially with the number of filters  $N$ . The error bars indicate standard error from replicates from flow cytometry measurement.

**Reusability of the electroformed device.** In addition to the reusability of the master, MagNET can also be reused since it consists of only metal (NiFe passivated with gold) and can be cleaned with aggressive mechanical agitation. Unlike conventional micro-magnetic sorting devices, where a magnetic film is adhered to a substrate, in MagNET there is no risk of delamination of the metal layer from the substrate during cleaning. Additionally, aggressive solvents can be used that would not be compatible with a polymer-based device (e.g. acetone with PDMS). To test the reusability of MagNET, we compared the performance of a previously used MagNET to a newly fabricated device. At 6 different flow rates, the enrichment of the used MagNET was not statistically significantly different from the newly fabricated device. ( $P \gg 0.05$ )

**Characterizing MagNET's ability to sort tumor cells from leukocytes.** To demonstrate the utility of our chip to perform highly specific cell sorting, we used MagNET to isolate spiked tumor cells from a large background of leukocytes. The detection of rare circulating tumor cells (CTCs) ( $< 100$  cells/mL) has demonstrated great potential to diagnose and monitor cancer and has gained enormous attention in the field of microfluidics.<sup>209,210,212,213,228</sup>

MagNET's highly specific capture of cells at ultra-high flow rates offers an important new tool for the study of CTC biomarkers as well as their translation to the clinics. While many ingenious microfluidic devices have been used with great success to sort CTCs,<sup>204,209,211</sup> there is currently a mismatch between the throughput of microfluidic devices ( $\phi \cong 1$  mL/hr) and the large sample volume of blood ( $V \sim 20$  mL) necessary for ultra-rare cell detection. This mismatch leads to run times unsuitable for practical use ( $T > 10$  hrs). MagNET, with its  $\phi = 100$  mL/hr flow rates, can process 20 mL of whole blood in only twelve minutes. In this demonstration, rather than using MagNET to trap tumor cells based on one of their heterogeneous properties, we instead use negative selection, wherein the cells that are easily identified as not being tumor cells are removed from suspension (*i.e.* white blood cells) to create a concentrated population enriched for potential CTCs.<sup>209,229</sup> Because CTCs are present in clinical samples at a ratio of approximately 1 tumor cell for every 1 million leukocytes, the high enrichment of MagNET ( $\zeta \sim 10^6$ ) is necessary to create enriched populations (1 tumor cell for every 100 leukocytes) that can be practically analyzed. And, MagNET is capable of even greater enrichment  $\zeta$  for applications that require high purity, *e.g.* molecular analyses, by either decreasing the flow rate  $\phi$  or increasing the number of filters  $N$ .

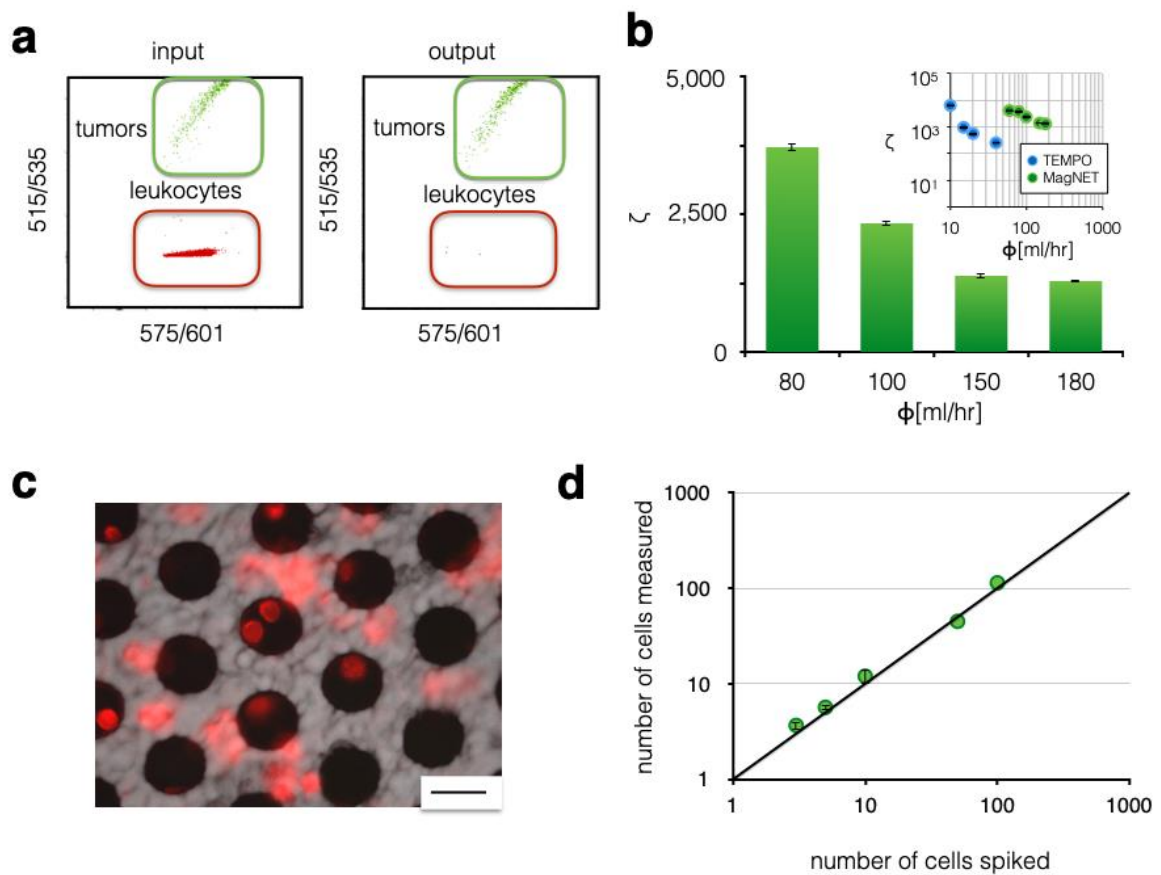


**Figure 4.5. Characterizing MagNET's ability to sort tumor cells from leukocytes. a.**

Cytometry quantified cell populations before and after filtration. **b.** Very high enrichment  $\zeta$  was achieved at flow rates  $\Phi > 80$  mL h<sup>-1</sup> using  $N = 4$  filters. Inset: Enrichment vs. flow rate on a log-log scale for the sorting of leukocytes from tumor cells using both MagNET and TEMPO. The error bars indicate standard error from replicates from flow cytometry measurement. **c.** A fluorescence micrograph showing leukocytes, stained red, trapped on the MagNET filter. Scale bar: 30  $\mu$ m. **d.** Titration of cultured cells into whole blood measured using MagNET, for negative selection of leukocytes, combined with a sized-based filter that concentrated the tumor cells into a small field of view (3x3 mm<sup>2</sup>) were enumerated using microscopy. A limit of detection LOD < 3 cells in a 1 mL suspension was achieved at a flow rate of  $\Phi = 80$  mL/hr.



To test our chip's ability to sort rare CTCs from leukocytes, a known number of cells from pancreatic cancer cell line (PD7591) were spiked into a background of leukocytes (Jurkat), and the enrichment of CTCs relative to leukocytes was quantified. Cancer cells and leukocytes were stained with different fluorescent dyes, green (CellTracker Green, Invitrogen) and red (CellTracker Red, Invitrogen) respectively, and a suspension of 100:1 of leukocytes to cancer cells was fed into the device. The leukocytes were labeled with CD45 functionalized MNPs (Miltenyi) to be captured on MagNET. Both the input and output were measured using flow cytometry, and the enrichment  $\zeta$  quantified. **(Fig. 5a)** The magnetically labeled leukocytes were captured on MagNET and only a very small fraction ( $< 0.04\%$ ) were missed, even at extremely high flow rates  $\phi = 100$  mL/hr using  $N = 4$  MagNET filters in series. **(Fig. 5b)** MagNET's performance sorting tumor cells from leukocytes was directly compared to TEMPO's **(Fig. 5b - inset)**, which showed that MagNET matched TEMPO's enrichment at 5x the flow rate of TEMPO. A fluorescence micrograph of MagNET after sorting shows leukocytes, stained in red, captured at the edge of the pores of where the magnetic field gradients are the largest, confirming that the cells were captured due to magnetic forces **(Fig. 5c)**.

To test the sensitivity of our chip to rare cells, we challenged our device with an in-vitro model for CTCs, wherein we spiked a known number of cultured pancreatic cancer cells (PD7591) into a background of leukocytes (Jurkat) and enumerated the number of recovered tumor cells. To quantify the number of

CTCs, a size-based filter that consisted of a nucleopore track-etched polycarbonate membrane was incorporated into our device downstream of MagNET. The size-based filter had a size of only 3x3 mm<sup>2</sup>, allowing rapid enumeration with microscopy. On this filter, captured potential CTCs could be imaged using an inverted fluorescence microscope (Leica DM750M). This device used  $N = 4$  MagNET filters in series, with an area of 6.2 cm<sup>2</sup>. A titration of varying numbers of tumor cells spiked into a background of Jurkat cells was prepared using serial dilution and then ran through our device (**Fig. 5d**). The enumeration of these spiked cells agreed with expected cell numbers ( $R^2 = 0.99$ ) over a dynamic range of 3 to >100 cells. A limit of detection (LOD) of <3 cells in a 1 mL suspension was achieved at a flow rate of 80 mL/hr.

#### 4.5 Discussion

MagNET offers a new approach to immunomagnetic separation that can be performed at extremely high flow rates ( $\phi > 100$  ml/hr) without sacrificing the high sorting efficiency ( $\zeta > 10^4$ ) typical of microfluidics. Additionally, we have developed a fabrication strategy for MagNET that can produce these high performance, microfabricated devices without specialized facilities, enabling MagNET to be manufacturable for applications such as low-cost medical diagnostics.<sup>230</sup> In this paper we demonstrated the utility of MagNET to sort rare tumor cells from blood cells for CTC detection. However, the approach is broadly applicable to any application that requires highly specific sorting of rare cells from large volume unprocessed samples, such as the diagnosis of infectious disease, environmental sensing, cancer biology, and stem cell research.<sup>211,231</sup>

Our MagNET approach to rapidly sort immunomagnetically labeled cells from unprocessed samples is well suited for incorporation into integrated microfluidic systems. For example, MagNET can be used to perform negative selection upstream of ultrasensitive, low throughput single cell measurements.<sup>230,231</sup> By removing the vast majority of background cells, it can improve the effective throughput of these single cell detection modalities by orders of magnitude. Additionally, due to the high enrichment  $\zeta$  of MagNET, it can isolate rare cells with the purity necessary for downstream molecular analysis, such as quantitative polymerase chain reaction (qPCR), sequencing, or nanodevice (e.g. nanowire, graphene, etc...) sensing.<sup>194,212,232</sup> In addition to negative selection, MagNET can also be used for positive selection. The MagNET filter has the advantage that when the external NdFeB magnet is removed, the magnetic force disappears, and the trapped cells can be released for downstream analysis. The viability of trapped cells in the MagNET has not yet been evaluated, but traps with similar forces have been demonstrated to keep trapped cells viable.<sup>233,234</sup>

The master / replica electroformation fabrication strategy developed in this paper has uses beyond the cell sorting highlighted in this manuscript. It also has broad applications for the manufacturing of electroformed microscale devices. There have been many previous approaches to electroform metal pieces with microscale features for a variety of applications,<sup>219–221,235,236</sup> but our MagNET technology represents the first such work that creates a reusable microscale master to generate many replica devices. There have been several recent,

particularly exciting, applications that use electroformed micromagnets. One publication combined electroformation with a novel process to transfer NiFe micro-scale structures to flexible PDMS membranes to confer magnetic properties to substrates such as coverslips and eppendorf tubes.<sup>235</sup> In another example, electroformed NiFe microstructures were created to generate large magnetic ratcheting forces to trap and translate cells in a microfluidic channel labeled with magnetic nanomaterials.<sup>236</sup> Our reusable master / mold technique can reduce the cost of fabrication of such technologies by eliminating the need to do costly lithography to create each device, and thus aid in the translation of these emerging technologies to commercial use. Our MagNET fabrication strategy offers a general approach to produce low-cost devices at high production rates for a wide range of microchemical systems (MEMS), including microsensors, microactuators, and microswitchers<sup>219</sup>.

### **Acknowledgements**

This work would not have been possible without the help of Dupont, which provided the Pyralux substrate for research purposes. We would like to thank the Stanger Lab, in particular Neha Bhagwat for the pancreatic and Jurkat cell lines. We would like to thank the Mark Allen Lab, in particular Minsoo Kim, for advice in creating the electroplating formulations. We would like to thank the Singh Center Staff, in particular Eric Johnston, Meredith Metzler, Gerald Lopez, and Noah Clay, for their advice in fabricating the master.

## 4.6 Supplementary Information

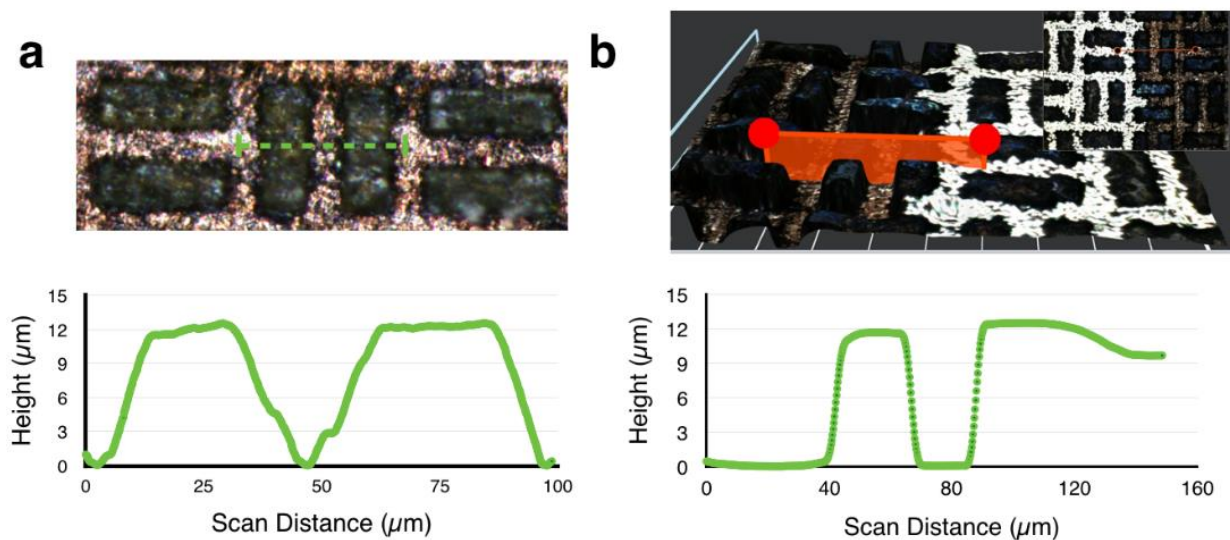


**Figure 4.S1. Characterization of polyimide pillars on the master and during electroformation.** **a.** Profilometer measurement along two rectangle pillars in the master shows the RIE process etched 12  $\mu\text{m}$  deep. The profilometer tip was not able to fit in between the gaps of the two pillars so we used the Zeiss Smartzoom5 2D/3D Optical Microscope to verify the pillar profiles. **b.** 3D optical profile of the pillars shows the copper surface at the bottom, and a boundary between where permalloy was plated and peeled. The depth profile is plotted here to show that the permalloy can be plated to the height of the pillars and successfully peeled at a thickness of 10  $\mu\text{m}$ .

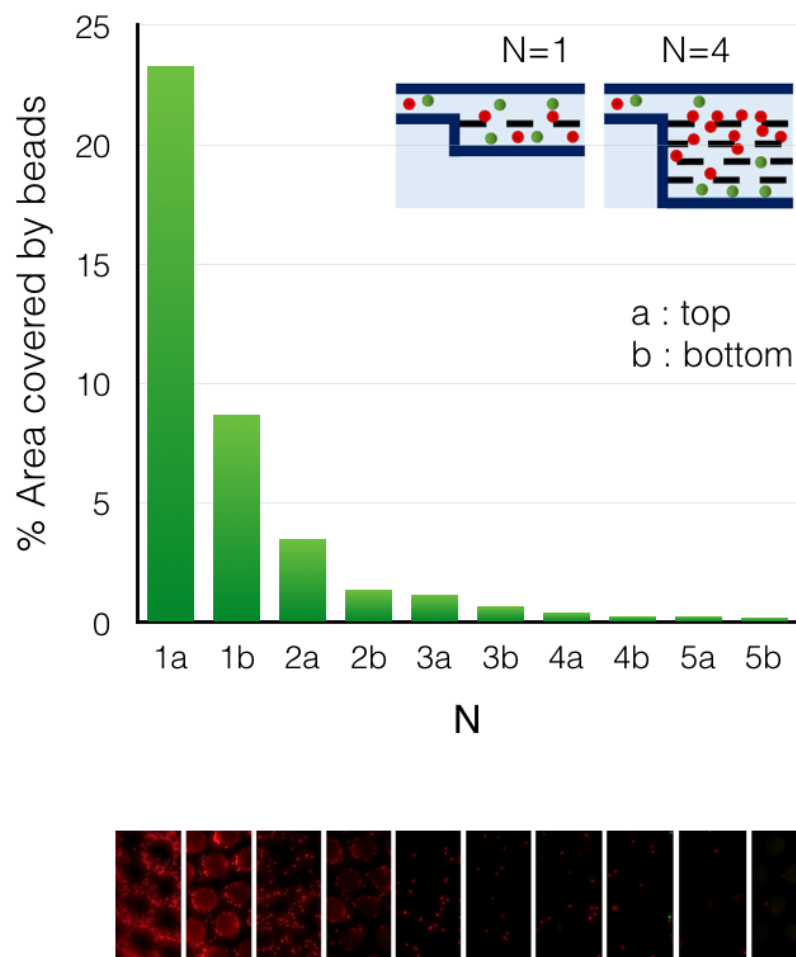


**Figure 4.S2. Bead distribution capture rate on the top and bottom surface of each filter in stacked devices.** Since MagNET is formed completely of permalloy, this leads to the formation of two traps at the top and bottom surface of each filter (a = top, b = bottom). To demonstrate that each surface does capture beads, the capture rate of each surface for N=5 filters stacked in series was calculated. The capture rate was defined as the area of the microscope image (shown below for each surface) that was covered with beads since individual 1 $\mu$ m beads could not be counted individually. We also

demonstrate that by stacking filters in series with two surfaces, we give magnetically labelled particles multiple chances to become trapped on MagNET to exponentially increase capture rate.

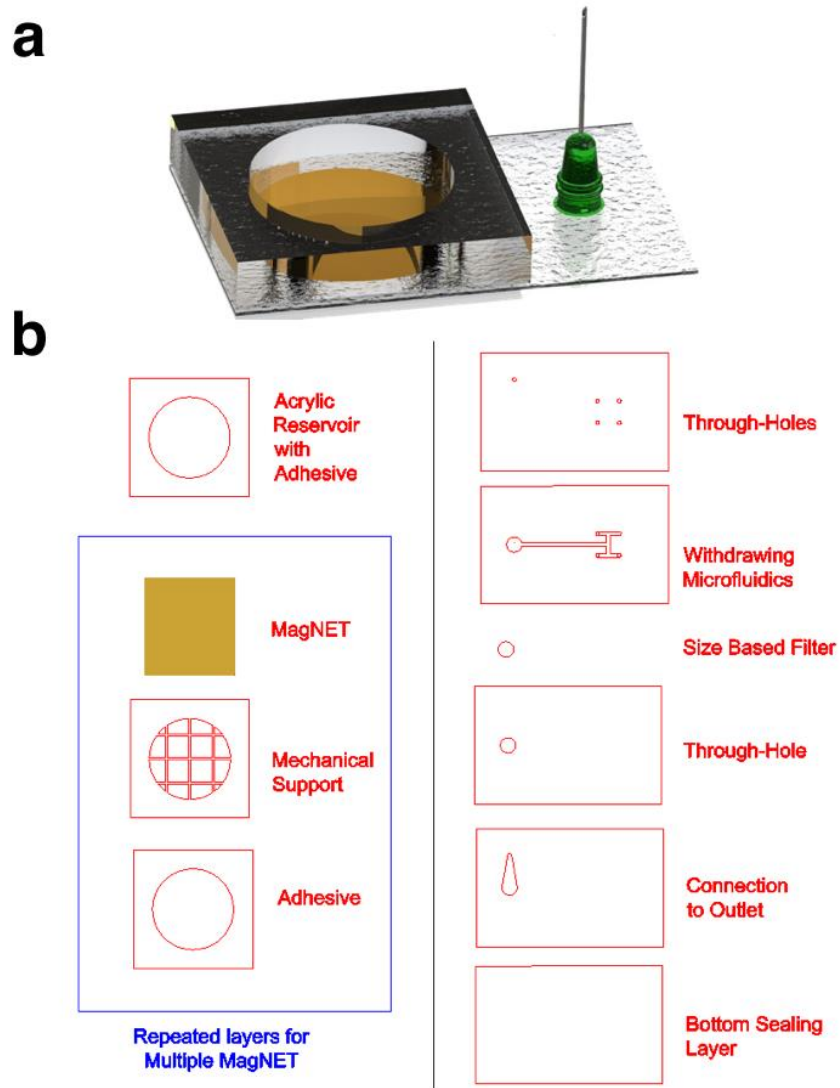


**Figure 4.S3. Device Fabrication.** **a.** A three dimensional rendering of the device. The sample is loaded into the acrylic reservoir that sits on top of MagNET. A negative pressure is applied at the blunt tip, which draws sample through the MagNET to isolate immunomagnetically labeled cells. **b.** The design of each of the

device layers. The boxed in area to the left are the layers associated with each layer of MagNET. The layers shown on the right are the microfluidics that are used to withdraw sample from the reservoir. In this particular device, a size based filter is attached near the output for viewing target cells in a fluorescence microscope after the negative enrichment of the background cells.



## CHAPTER 5: MULTICOLOR DETECTION OF FLUORESCENT DROPLETS ON A CELL PHONE USING TIME DOMAIN ENCODED OPTOFLUIDICS

This chapter is a slightly modified version of a manuscript published in IEEE:

**VR. Yelleswarapu**, D. Issadore. Multicolor detection of fluorescent droplets on a cell phone using time domain encoded optofluidics. Healthcare Innovations and Point of Care Technologies (HI-POCT), 2017 IEEE, 245-248.

V. Y. conceived and performed all experiments in this study, coded the Matlab software, created the Android app, as well as prepared the manuscript and figures.

### 5.1 Abstract

Digital droplet assays – in which biological samples are compartmentalized into millions of femtoliter volume droplets and interrogated individually – have generated enormous enthusiasm for their ability to robustly detect nucleic acids and proteins with single molecule sensitivity. A key challenge in the field however has been the cumbersome instrumentation necessary to generate, process, and detect millions of individual droplets. We have demonstrated the miniaturization of droplet diagnostics into a portable platform that can process millions of droplets per second by combining the parallelization of thousands of microfluidic droplet generators onto a single chip and a strategy to rapidly detect droplets using time-domain encoded cell phone imaging. Building on our work in this area, we show that multiple fluorescent dyes can be detected in each individual droplet by encoding the excitation light from multiple LEDs with unique maximum length sequences that are decoded using cloud-based computation. By developing a strategy to carry out multiplexed digital droplet assays in a portable platform at a rate ( $10^6$  droplets / sec), 1000x faster than conventional approaches on a cell phone based device, we have demonstrated a key step towards translating the

sensitivity of digital assays from research laboratories to portable molecular diagnostics.

## 5.2 Introduction

Digital droplet-based assays use femtoliter volume emulsions as isolated compartments to run massively parallel biochemical reactions. These digital assays have demonstrated enormous utility as a platform for the ultrasensitive, single molecule detection of nucleic acids and proteins. However, although these assays are robust to reaction conditions and thus have enormous potential for point of care diagnostics, translating these assays into portable devices has proven challenging due to the expensive, semi-automated machinery necessary to generate, process, and readout each of the millions of droplets in every assay. We developed a new approach to miniaturize droplet based assays that achieves a throughput ( $10^6$  droplets/sec) 1000x faster than conventional methods, using a smartphone camera and disposable plastic microfluidic chips<sup>237</sup>. The key innovation of this approach is the modulation of the excitation light in time with a pseudorandom sequence that enables individual droplets to be resolved that would otherwise overlap due to the limited frame rate of digital cameras. This approach combines ultra-bright LEDs, the sensitivity and computing power of smartphone based imaging, and the ubiquity and computational power of cloud-based computing to implement our platform as a self-contained mobile device. A limitation of our previous work in this area has been that it can only interrogate a single fluorescent dye in each droplet, severely limiting the use of the chip for the multiplexed molecular detection necessary for most clinical applications<sup>238,239</sup>. Building on prior work, we show that multiple fluorescent dyes can be detected in each individual droplet by using multiple LEDs, each encoded with a unique maximum length sequence (MLS) that can be specifically readout using a correlation based detection, borrowing techniques from the telecommunications industry. (**Fig. 1a**) In this paper, we experimentally demonstrate

a two-color system wherein we can detect up to three separate molecular targets in each droplet. (**Fig. 1b,c**) Our microdroplet Megascale Detector ( $\mu$ MD) detects droplets on a low frame rate camera by using modulated fluorescent emission from a modulated light source to resolve overlapping fluorescent droplets and improve signal to noise ratio (SNR) by 100x compared to conventional optical detection. Moreover, our  $\mu$ MD achieves flow-rate invariant detection at rates as high as 160 mL/hr ( $10^6$  droplets/sec) and a dynamic range of  $1:10^7$  to  $1:40$  fluorescent: non-fluorescent droplets.

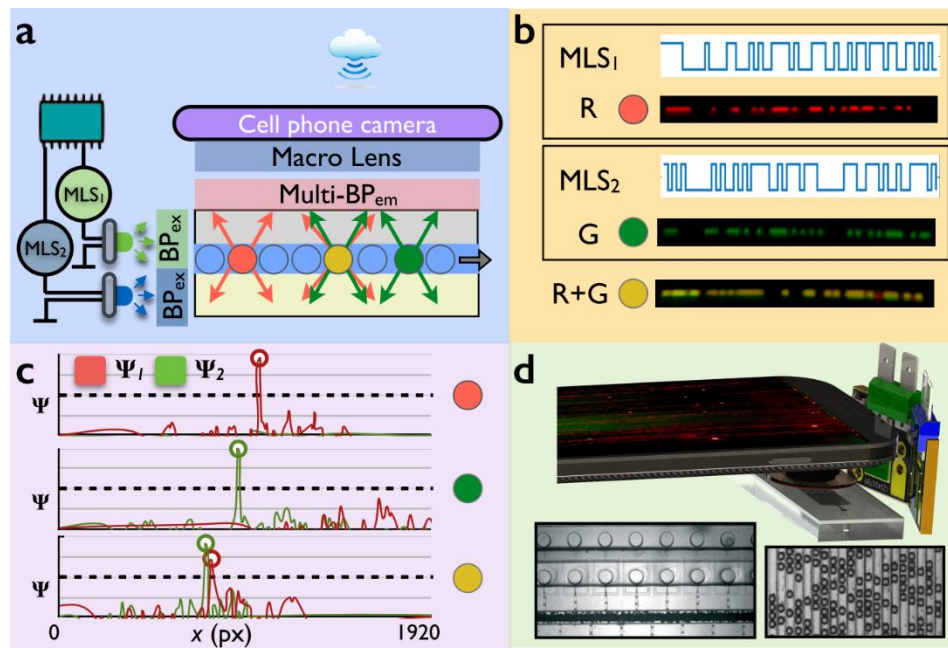


**Fig. 5.1. Design Strategy of our Multiplexed Microdroplet Megascale Detector ( $\mu$ MD).** (a) Cross section schematic; a microcontroller strobes LED excitation to modulate the fluorescent emission. (b) Each dye has its own MLS pattern. Droplets with a mix of dyes emit both patterns. (c) We can resolve the presence of each MLS pattern in low SNR, and when MLS overlap – to achieve high dynamic range and to identify mixed dye droplets. (d) Phone based implementation that monitors 120 microfluidic channels simultaneously.

### 5.3 Background

Digital assays have met the demand for ultrasensitive detection, but their utility can be greatly expanded by incorporating multiplexed detection of multiple biomarkers. Multiplexed assays have demonstrated higher sensitivity and specificity for the detection of cancers, genetic diseases, and infectious diseases than is possible using any single biomarker<sup>238,239</sup>. To expand digital droplet based assays to multiplexed detection, there are two main options: 1. Samples can be run one after another in series, which adds additional labor costs, time and requires sample to be aliquoted, or 2. By expanding to multiple color detection, it is possible to simultaneously monitor multiple biomarkers in individual droplets, preserving precious sample, reducing assay time, and simplifying use. Droplet assays can measure  $N > 2$  biomarkers, using only two colors, by using endpoint fluorescence measurements in droplets where ratiometric combinations of two reporter dyes at specific combinations signify a target. Multicolor digital assays have proven useful in detecting, nucleic acids in digital PCR<sup>180</sup>, proteins in digital ELISA using barcoded fluorescent beads<sup>86</sup>, cell surface markers in droplets<sup>240</sup>, and in the Luminex system, wherein barcoded beads are used to detect multiple proteins<sup>241</sup>. However, current commercially available multicolor panels for digital assays, such as Quanterix's Simoa technology for single protein detection<sup>49,86</sup>, and Biorad's multiplexed digital PCR assay<sup>180</sup>, require complex optics and bulky machinery. Various microfluidic approaches to miniaturize and increase the throughput of digital assays have been proposed, including spatial modulation of fluorescent particles in flow to increase the SNR as well as resolve multiple fluorescent families<sup>129,141</sup>, a highly parallel microfluidic chip that sits directly on a CMOS which monitor droplets<sup>139</sup>, using a microlens array to monitor multiple droplet channels<sup>133</sup>, a miniaturized confocal microscope observing a cuvette of droplets<sup>135</sup>, and optical fibers integrated into a microfluidic chip<sup>242</sup>. However, these

approaches require complex fabrication processes, do not achieve a throughput sufficient for ultrasensitive, multiplexed assays (<10k drops / sec), or use difficult to miniaturize microscopy to readout the fluorescence.

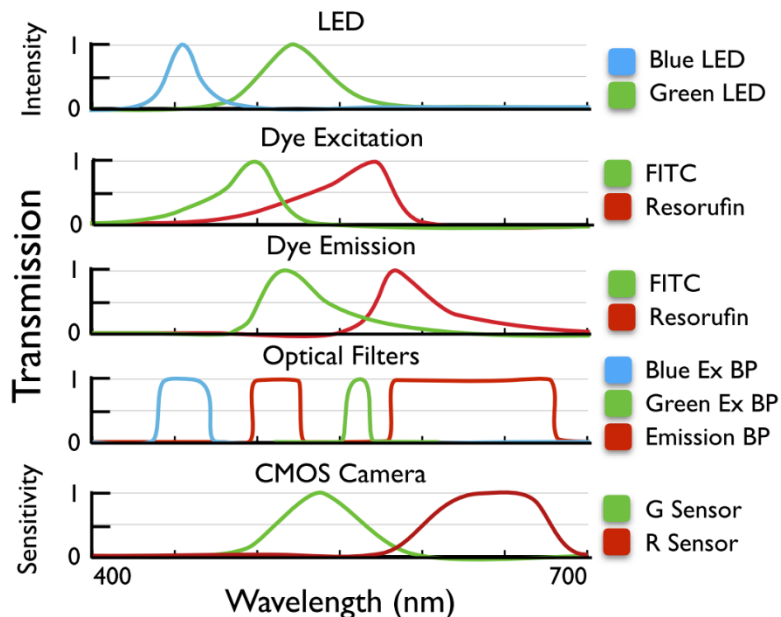


**Fig. 5.2. Optical and dye spectra.** Components and dyes were selected to separate the excitation and emission spectra for each of the LED/dye combinations to prevent crosstalk.

## 5.4 Methods

### Imaging Implementation

We have previously published on our cell phone based approach that addressed the challenges of portability, high dynamic range, and high throughput required for droplet assays<sup>237</sup>. Briefly, the microfluidic chip is made using standard photolithography to create PDMS devices that are plasma bonded to glass. The PDMS chip contains  $n = 120$  channels, through which droplets flow in parallel and are monitored by a cell phone camera to achieve high flow rates.

In our next generation device, which we herein report, we measure droplets using a cell phone camera on the Galaxy S7 Edge using pro mode to fix the focus and settings<sup>144</sup>. The optics consist of a hobbyist-grade macro lens (Carlson Hookupz), followed by a dual band emission filter (512 & 630nm, Edmund). The chip is illuminated from the side by a green and blue LED (Luminus) that are coupled to maximize total internal reflection. Each LED has its own bandpass filter (Green: 560DF15; Blue: 450BP50, Omega). **(Fig. 2)** To test the device, we used Dextran-FITC 10kDa (Sigma) and QuantaRed Enhanced HRP substrate (Life) – a red Resorufin based dye used for immunoassays such as ELISA. We combined the dyes at different ratios to generate three populations of fluorescent droplets. Droplets were generated off-chip using a parallelized droplet generator<sup>130</sup>, to ensure monodispersity, and then added to a suspension, which includes droplets that contain fluorescent dye and those that contain only water. For the oil phase, we used Biorad Oil and for aqueous we added dye in the concentrations specified into a 1% PBS solution. For the Resorufin spiked droplets, we mixed the substrate as specified by the manufacturer and added HRP until the product was saturated.

### **Droplet Patterning and Detection**

The key innovation to achieve multicolor droplet detection is the modulation of each dye with its own excitation LED. Each LED-dye set uses a unique pseudorandom sequence. The modulated excitation light in time patterns the droplet streak in space **(Fig. 1b)**, which allows multiple overlapping droplets to be resolved. To extract the individual droplets, we correlate the image streak with the expected modulation pattern  $m$ , to generate the correlation vector  $\Psi(X) = \int S_n(x)m(x+X)dx = S_n \otimes m$ . We chose to pattern the droplets using MLS sequences with  $|m| = 63$  bits, where each bit

corresponds to 10 pixels. Thus, 63 bits would correspond to 630px, or 1/3 of a 1920px wide video frame. To create a set of MLS with minimal auto-correlation and cross correlation from each other, we followed the process in MacWilliams and Sloane<sup>151</sup> to create a pseudorandom vector with  $2^{12}-1=4095$  elements, that was folded into a 63\*65 matrix, and chose the first two rows to select the two MLS patterns.

The workflow (**Fig. 3**) to detect droplets is as follows: *(i)* The video is broken up into images and each image is separated into two frames, based on the camera's red (CMOS-R) and green (CMOS-G) sensors. *(ii)* Each frame is segmented along the x-axis to generate 1D signal vectors  $S_n^{R,G}(x)$  that correspond to the  $n = 120$  microfluidic channels. *(iii)* To simplify the hardware of the system, we do not control the droplet velocity  $v$  or phase  $\theta$ , relative to the MLS excitation, of the passing droplets, and instead use cloud computing to computationally detect droplets with unknown phase and velocity. We generate a 3d matrix by correlating each of the modulated signals with expected emission patterns that scans the range of velocities and phase at which the LED strobes  $[m_1(x/v - \theta) \otimes S_n^R \text{ and } m_2(x/v - \theta) \otimes S_n^G]$ . *(iv)* By selecting the optimal phase  $\theta_c$  and velocity  $v_c$  of every  $k^{th}$  droplet, we pick out the maximum correlation peaks  $[R(x_k, v_c, \theta_c), G(x_k, v_c, \theta_c)]$  and record the locations of the peaks  $x_k$  that cross a defined threshold from  $\Psi_n^R$  and  $\Psi_n^G$ , respectively. By comparing the intensities R,G at each of the peak locations,  $x_k$ , we identify which family of dye combinations the droplet contains and report the results back to the smartphone via a custom app. *(v)* The software is available as an Android App to make the system truly portable by allowing the user to record the video, send the data to Matlab Mobile with predefined code that remotely analyzes the data, and receive the results on the smartphone.

In the case of a droplet that contains both FITC and QuantaRed dye, we observe peaks in both  $\Psi^R$  and  $\Psi^G$ . As expected, R and G match in droplet velocity ( $v_c$ ) and location ( $x_k$ ), as seen in the 3D/2D plots of  $\Psi$ . (Fig 3c, *iii-iv*). For droplets that contain only QuantaRed, we observed peaks only in  $\Psi^R$  and for droplets that contain only FITC, we detected peaks in  $\Psi^G$  only.

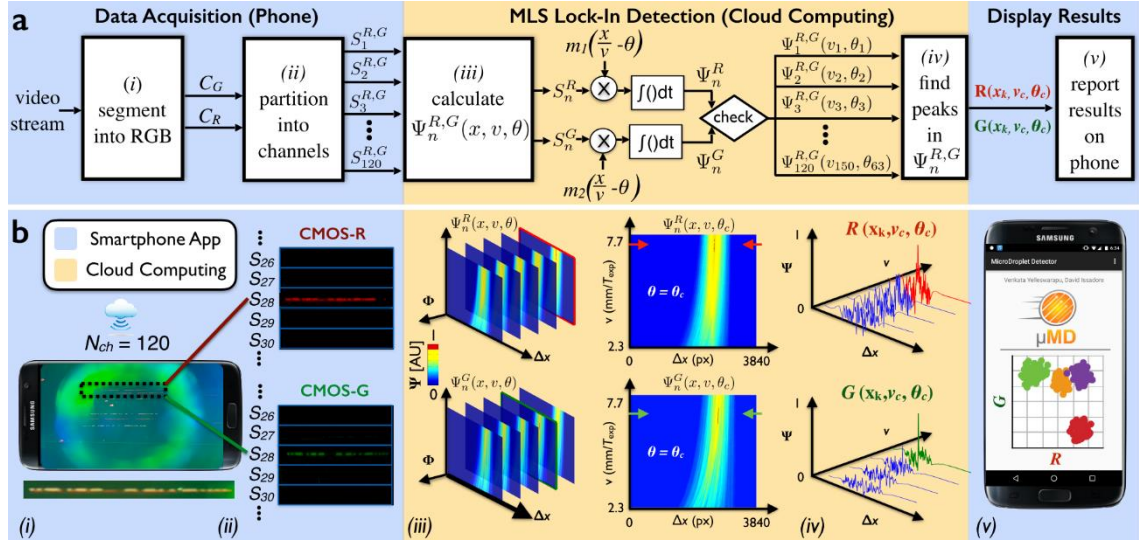


**Fig. 5.3. Software Workflow for Phase and Velocity Invariant Detection of fluorescent droplets.** (a) Workflow for detecting droplets, with lock-in detection that scans for the emitted fluorescence as a function of droplet velocity and phase at which the LED pattern starts. (b) Sample workflow for a single droplet that contains Resorufin and FITC. Images from the video are filtered into CMOS-R & -G frames, and are partitioned into 1d vectors (ii). We generate a 3d correlation matrix with all phases and velocities for a droplet (ii), and select the optimal correlation for each MLS (iv). From these results, we use the location of the correlation peaks to determine which population a droplet belongs to. The cell phone records the video, while the data is processed using cloud computing, and returns the results on the Android using Matlab Mobile and a custom app.



## 5.5 Results and Discussion

### Simulation for Multicolor Detection

Ideally, each of the dye emission MLS patterns would only show up in the respective CMOS channel, where the emission from Resorufin would only show up in the CMOS-R and emission from the FITC would only show up in CMOS-G. However, we observed non-zero cross talk between the channels, where a droplet that contained only FITC had some signal in the CMOS-R channel and a droplet that contained only QuantaRed had some signal in CMOS-G, due to the broad tail of the emission from both dyes (**Fig. 2**).

To measure the impact of crosstalk on the ability to resolve droplets, we simulated the total signal in a given 1D vector  $S_{total}^R = \alpha S_G + (1 - \alpha) S_R$ , where  $\alpha$  represents the amount of  $S_G$  that leeches into the  $S_R$  channel. We scanned the length of the MLS,  $|m|$ , and the crosstalk intensity,  $\alpha$ , affect the peaks R and G for a mixed droplet. When  $\alpha = 0$ , there is no crosstalk and depicts an ideal scenario. In **Fig. 4a**, we demonstrate that the ability to resolve droplets decreases with crosstalk and increases with the number of bits. In **Fig. 4b**, we observe the impact of MLS length, crosstalk, and noise on the ability to group multicolor droplets. Increasing  $|m|$  results in a tighter grouping of droplets, while increasing  $\alpha$  causes a shift towards the channel where the crosstalk originates from. Decreasing the SNR causes the scatter to increase. A combination of poor SNR with substantial crosstalk can shift and spread out the populations of droplets to a point where the resolved droplets cannot be grouped. However, this occurs at -30dB SNR which is much lower than the typical >0dB SNR levels observed for droplet assays[4].

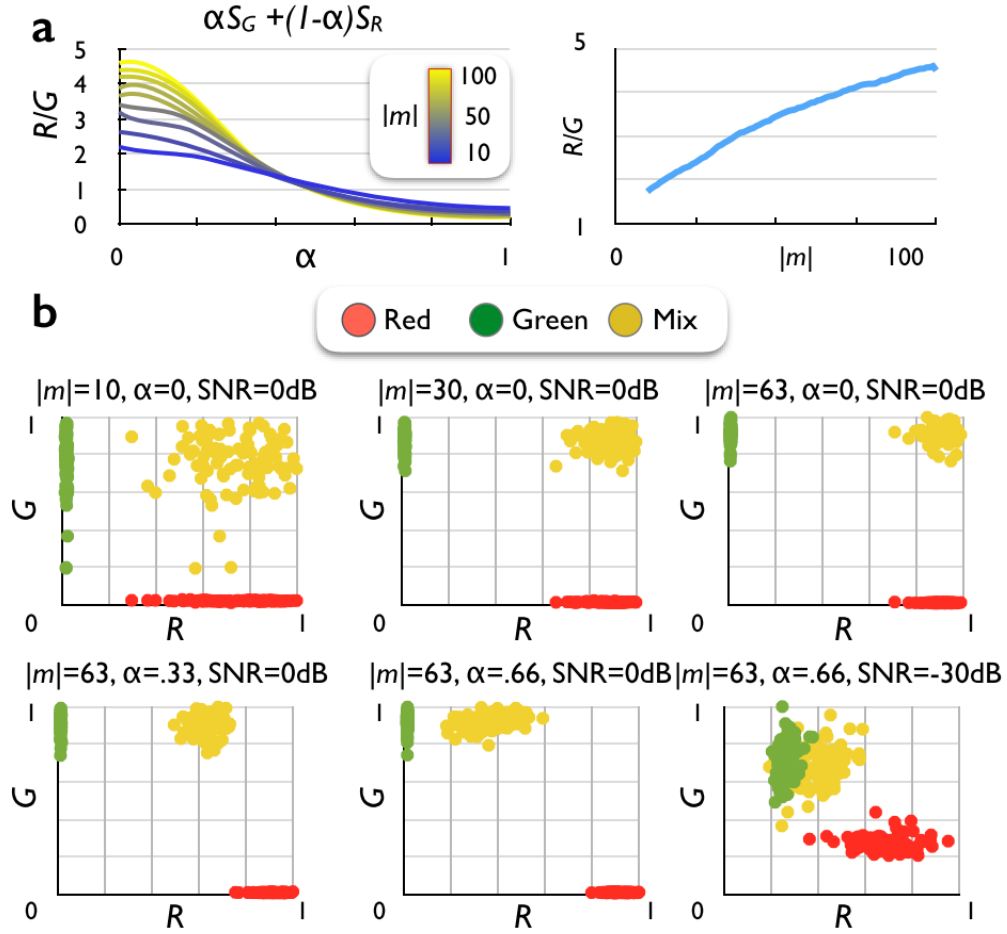


**Fig. 5.4. Simulation for Multicolor Detection.** (a) We scan the impact of crosstalk ( $\alpha$ ) and the number of bits ( $|m|$ ) on the ability to resolve droplets ( $R/G$ ). As crosstalk increases from the green channel into the red, the ability to resolve the green droplet weakens. *Right:* As  $|m|$  increases, scatter reduces and droplets separate better. (b) Increasing crosstalk results in a shift, while decreasing SNR increases scatter.

#### Multiplexed detection of droplets with two dyes at various ratios

To experimentally evaluate our approach, we generated three populations of monodisperse 40  $\mu\text{m}$  diameter droplets: 500 $\mu\text{M}$  FITC droplets, saturated Resorufin droplets, and one that contains both dyes. We spiked 10  $\mu\text{L}$  of these droplets into 10mL of an emulsion with empty droplets, and thoroughly mixed the droplets to create a

homogenous population. We ran this suspension through the  $\mu$ MD at a flow rate  $\phi = 70$  mL/hr while recording in Samsung 7 Edge's Pro mode with the following settings: a frame rate of 1920x1080p resolution at 30 fps, ISO = 2000, Exposure = 0, aperture = 1/30, metering mode set to Matrix, and a fixed focus determined by the macro lens. The field of view was  $\sim 12\text{mm} \times 7\text{ mm}$ , and spherical aberrations from the lens were corrected with Matlab's computer vision toolbox.

We analyzed the computed R and G spread of the scatter for each population and showed a sample of  $N = 50$  droplets (**Fig. 5a**). The scatterplot shows that we can separate all three populations. The centroids for Resorufin, FITC, and mixed populations with scatter,  $r$ , defined as the average distance from the centroid were:  $[x_R=0.58, y_R=0.08, r_R=0.09]; [x_F=0.35, y_F=0.64, r_F=0.22]; [x_{RF}=0.73, y_{RF}=0.40, r_{RF}=0.14]$ . We also calculated the crosstalk defined as the total intensity in the "incorrect" channel divided by the intensity in the "correct" channel. For Resorufin, the crosstalk was  $17 \pm 3\%$ , while for FITC the crosstalk was  $49 \pm 17\%$ . We used this measurement to correct for crosstalk by a linear transformation where the coefficient of correction matched the calculated crosstalk (**Fig. 5b**). As expected from simulation, scatter was larger in populations that had more noise and crosstalk. Interestingly, when we add the centroids based on the concentrations for a theoretical mixed droplet centroid:  $(x_R+0.5*x_F, y_R+0.5*y_F)$ , or (0.69, 0.40), we find that it nearly matches the calculated  $(x_{RF}, y_{RF})$  at (0.72, 0.40). The scatter resulted from nonuniform excitation as the LED intensity decreased further away from the source, which can be corrected in software. Crosstalk between fluorescence signals can be further reduced by redesigning the filters, at the expense of a decrease in signal to noise (**Fig. 2**).

Using our platform, we demonstrate that we could detect three distinct groups of droplets, defined by their unique combination of the two dyes. Moreover, using a

computational model, we showed that it is possible to further expand to a linear combination of droplets with dye concentrations  $\beta_c R + \gamma_c G$ , where  $\beta_c$  and  $\gamma_c$  represent the concentration of each dye within a droplet – as has been previously demonstrated in commercial N-plex assays[4]. In addition, we can expand our platform to include additional LEDs, beyond the two demonstrated in this manuscript, each patterned with its distinct MLS patterns. Using this approach, the highly multiplexed molecular diagnostics that are emerging to diagnose cancer, infectious disease, and trauma can be miniaturized and made accessible for clinical use.

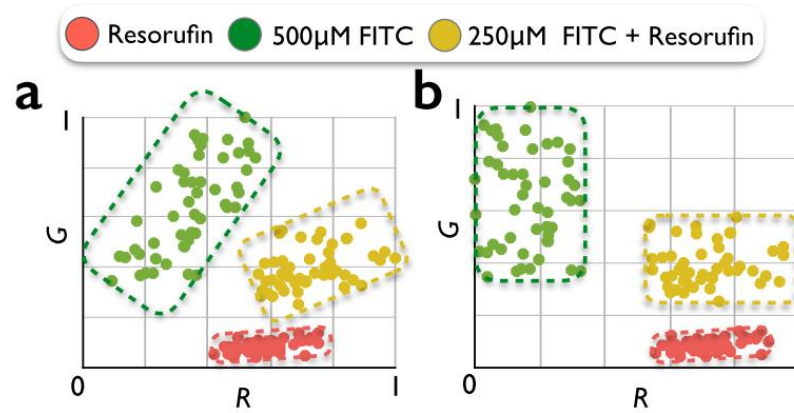


**Fig. 5.5. Experimental Verification of  $\mu$ MD.** (a) Classification of Resorfuin, FITC, and mixed droplet populations. (b) Linear transformation correcting for the crosstalk of the FITC droplets results in tighter scatter groups.

### Acknowledgement

This work was supported by the Department of Bioengineering, University of Pennsylvania. Funding was provided by the National Institute of Health: 1R21CA182336-01A1. David Issadore owns shares in Chip Diagnostics. Venkata Yelleswarapu is supported by the Microsoft Graduate Fellowship.

## CHAPTER 6: FUTURE WORK

While the  $\mu$ MD is currently functional for a duplex biomarker detection with digital ELISA, there are several applications that could be expanded including with minimal hardware change including: Digital PCR, multiplexed detection of biomarkers, washless ELISA, and nanoparticle enhanced ddELISA.

### 6.1 Digital PCR

#### Introduction:

Droplet-based assays have been used extensively for nucleic acids due to their sensitivity for amplifying single molecules of DNA, RNA; and their robustness to reaction conditions since only endpoint measurements are necessary<sup>16569</sup>. Similar to ddELISA, ddPCR has enormous potential for early detection, and differentiating small fold changes compared to traditional PCR; yet the equipment is often limited due to cost or bulkiness or suffers from poor dynamic range in static array-based digital PCR devices.

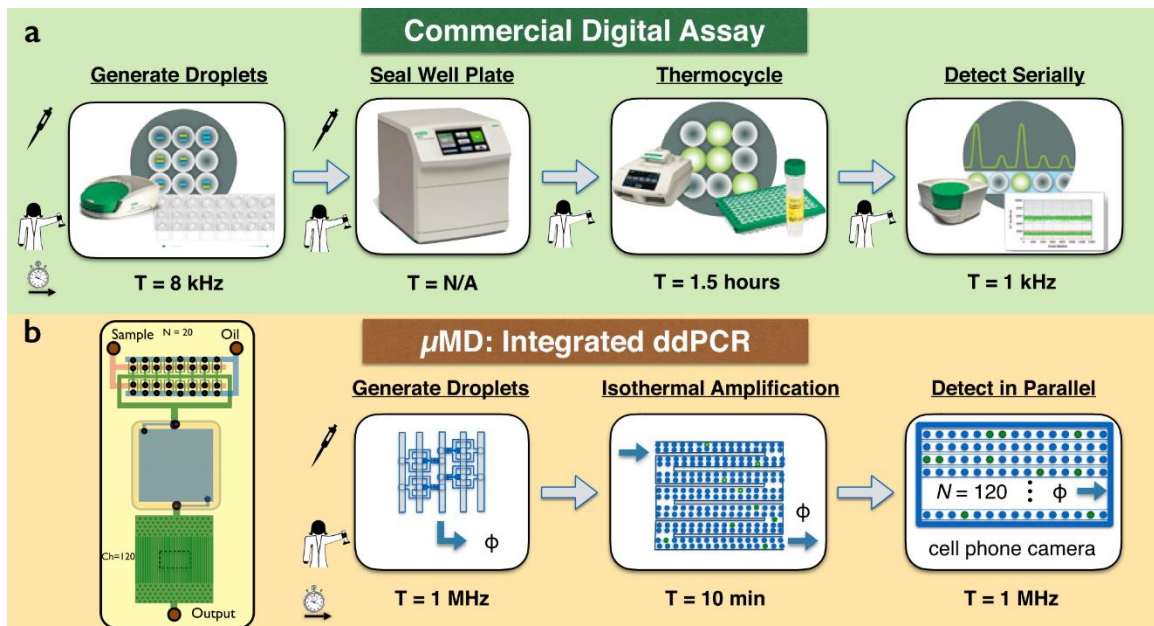


**Figure 6.1. a. Comparison of traditional and digital PCR.** Typical commercial digital PCR assays such as Biorad's system come in several parts for each function of the workflow. Manual intervention is necessary for steps, and the slow throughput requires overnight runs or suffers from low dynamic range. **b.** The  $\mu$ MD integrates all of this onto one chip, where droplets are rapidly generated in parallel, thermocycled, and imaged after. The parallel approach speeds up the process, while minimizing manual labor and any steps that could cause contamination.

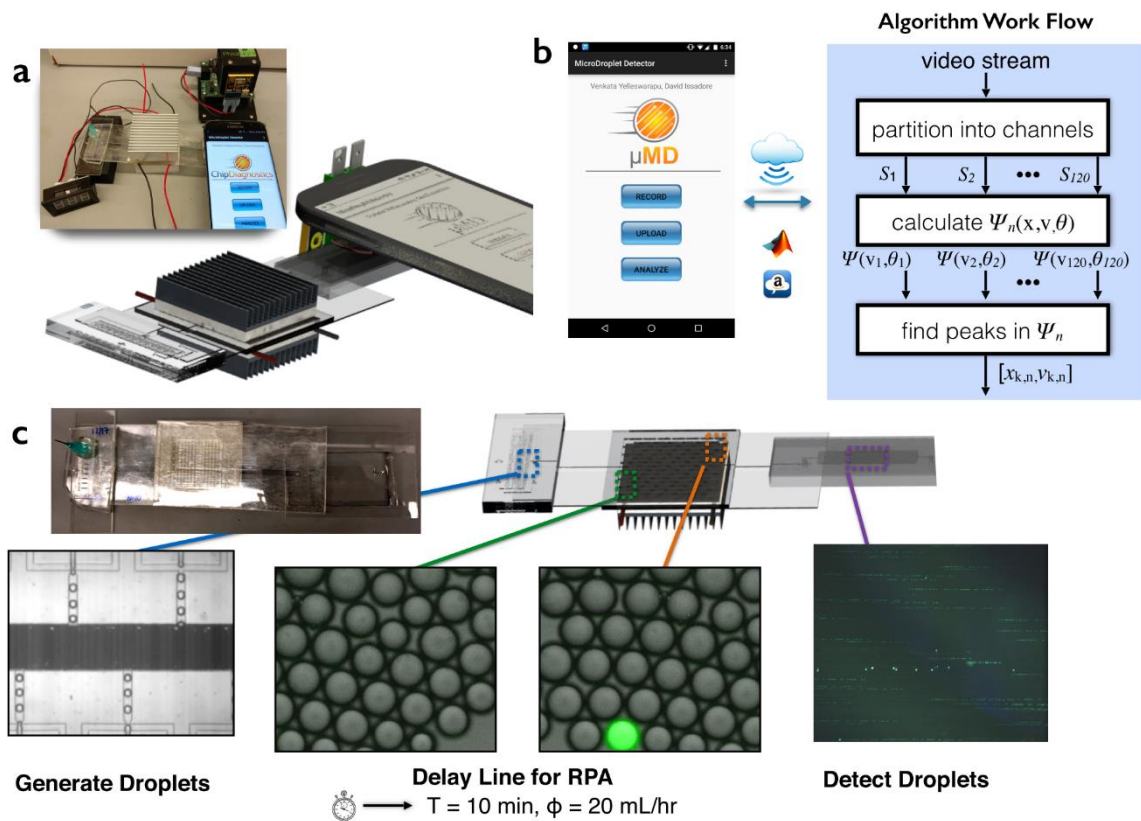


**Figure 6.2 Components and workflow for integrated digital PCR.** **a.** The major components are the droplet generators followed by a compact 3d chip for thermocycling. The 3d component is sandwiched by two peltiers on either side for rapid heating and cooling, while an app detects droplets (inset: setup in lab). **b.** App analyzes the video on the cloud by finding signatures that identify positive droplets. **c.** Integrated workflow

shows droplet generation, a droplet fluorescent through RPA, and finally what the droplets would potentially look like under the cell phone detection system.

To address this challenge, we began developing the integrated microscale mobile droplet detector ( $\mu$ MD) – an integrated sample to answer to droplet based platform that generates droplets in parallel, incubates them in a delay line for 10 minutes to amplify target nucleic acids via recombinase polymerase amplification (RPA)<sup>243</sup>, and detects droplets on a cell phone camera that is linked to cloud computing. The key innovation of our platform that enables high-throughput is the parallelization of both the generators and detectors, as well a rapid and robust isothermal amplification scheme that obviates the need for bulky thermal cyclers. Using this approach, the  $\mu$ MD demonstrated that isothermal amplification using Recombinase Polymerase Amplification (RPA) could be possible by amplifying targeted strands and measuring their fluorescence after a delay line. The device footprint was less than 100 cm<sup>2</sup>. In addition, thermocycling approaches were also tested for traditional digital PCR since this technique could measure a wider range of RNA and DNA targets that are not possible by isothermal amplification. By miniaturizing and integrating droplet-based diagnostics into a handheld format, the  $\mu$ MD platform can translate ultra-sensitive droplet-based assays into a self-contained platform for practical use in clinical and industrial settings.

**Table 6.1 – Digital PCR Technologies**

Ref.	Throughput	Droplet Volume	Method of Thermal	Material	Method of Detection
<b>Continuous</b>					
Hatch <sup>51</sup>	125 to 250 k/s based on 4-8s exposure	50 pL	Thermoelectric Cooler, Copper, Si wafer, PDMS	PDMS	Wide field 21 MP DSLR camera

Schaerli <sup>65</sup>	Flow rates ~ <b>160</b> ul/h; 4.7*10 <sup>6</sup> /mL	40um to 150um; 33.5 pL to 1.76nL	Peltier module with copper rod at center; spatial	SU8 embedded in PMMA	Droplets were collected, opened for gel electrophoresis
Beer et al <sup>66</sup>	Generate 1k/s and then stop while it cycles.	10 pL	Peltier temporal heating	.5 mm thick silicon wafer a anodic bonded to .5mm coverslip	Nikon microscope w/ 5k fps camera.
Kiss <sup>67</sup>	500/s	65 pL; observed 14k droplets per cycle at 11 points	Spatial heating; two heaters at 95 and 65c zone; 55 s cycles/ 35 min	PDMS; incubation channels 260um	Droplets flash frozen and analyzed on gel and fluorescence microscope
Terazono <sup>68</sup>	2.2k/3.5 min	20-30um droplets made with micro- pipetting 10- 30uL at a time	Single monolayer of droplets heated w/ IR laser; 3.5min for 50 cycles	Droplets were covered w/ mineral oil and heated on glass base dish	Inverted microscope, laser,
<b>Off Chip</b>					
Biorad	1.92 mL can be loaded on thermocycler at once...	1 nL; 1 k/s	Off chip thermocycler	Well plate with collected droplets	Dual laser
Raindance	400 uL sets	5 pL; 1 k/s			Dual laser
<b>Isothermal</b>					
Rane <sup>69</sup>	1M/110 min; 10uL per 110min	8 pL; 1-2 ms/droplet	Peltier heater with water cooling	glass, pdms, coverslip	Custom built optical dual fluorescence
Li <sup>70</sup>	27,000	314 pL  Static array	Peltier heater with copper chamber, PWA chip, and glass; 10 min... 30 min for entire procedure at 39C		Wide field image microscopy
SlipChip <sup>48</sup>	1550 reaction	9 nL each;	39C on flat metal adapter;	Glass	Leica DMI 6000 B epi-



	wells	1550 wells/hr	plate reader with temperature controlled at 25°C. 1 hr at 39C, 30 min at 42C		fluorescence microscope (Leica Microsystems, Germany) with a 5X / 0.15 NA objective and L5 filter
Schuler <sup>71</sup>	Volume calculated from given dimensions: ~30000 120um dia droplets;	0.9048 nL; volume of chamber where droplets form is 27 µL	Labdisk player with built in heater; 30 min for entire thing	Lab disks were micro milled in PMMA – at foundry service	Stroboscopic setup for droplet dia only; fluorescence imaging with Lavion bioanalyzer
Kang <sup>72</sup>	100 kHz	10 kHz	Red/Green colors;	8 pL	Rotating cuvette with mini confocal detector for DNAzyme detection

Several digital PCR commercial platforms already exist that demonstrated several advantages of digital PCR when compared to standard qPCR. These advantages include robustness to background, absolute quantification where every single nucleic acid target is counted rather than compared to standards, and endpoint measurements that do not require as much optimization when compared to tracking PCR fluorescence in traditional qPCR systems. While these commercial assays such as Biorad and Raindance demonstrated great strides in digital PCR, they were limited to lab facilities that could afford the equipment and were low throughput – relying on overnight runs for their droplet generation to analysis workflow.

Several techniques to miniaturize the platform using microfluidics are described in **Table 6.1**. Continuous flow digital PCR was first demonstrated in several chip materials including glass, silicon, and PDMS. Continuous flow heating consists of two major methods: cycle the chip through the temperatures required using rapid heating/cooling<sup>6667</sup> or using spatial heating<sup>65</sup> that control the temperature of the surface at different regions of the chip and as droplets flow between regions, the droplets also go

through various temperatures. Beer et al<sup>66</sup> and Kiss et al<sup>67</sup> first demonstrated that by rapidly heating and cooling a chip, and monitoring several locations for droplet fluorescence, digital PCR could be done in continuous flow. However rapid heating and cooling of large chips often require bulky equipment since the thermal load does not only consist of the channels where the droplets travel through, but also the entire thermal mass of the glass, silicon or PDMS chip. With insulated materials, this can become problematic and thus low throughput. A different strategy was employed by Schaerli with spatial modulation, where a Silicon and SU8 chip hybrid had different regions of cool and hot regions for amplification.

### **Design and Methods**

In order to address the problem of the large thermal mass that is often cycled in many of these setups and the inherent low throughput nature of these devices, we built a thermocycler with a copper chip that was less than 200um in height. In addition, we wanted the chip to be as thermally conductive as possible, which meant materials like PDMS or thick glass would pose obstacles in rapid thermal cycling. We used COMSOL to simulate several materials with different thicknesses to find out how long it would take for droplets and the carrier oil to heat up from room temperature to the targeted temperature. These simulations showed that PDMS and thick glass would be poor choices for the design. We also tried using PDMS experimentally and found that problems with evaporation and gas bubbles was a major issue despite papers demonstrating success with degassing or using thin glass slides to prevent evaporation. Silicon was also explored but the expensive manufacturing with deep reactive ion etching, and the eventual need to have a compact footprint by stacking in 3D made this not practical since the bonding between several layer would get complex and have a

high risk of failure. **Figure 6.3** shows the final design choice with a copper-based chip that was stacked in 3d to have a compact yet large volume where droplets could cycle rapidly.

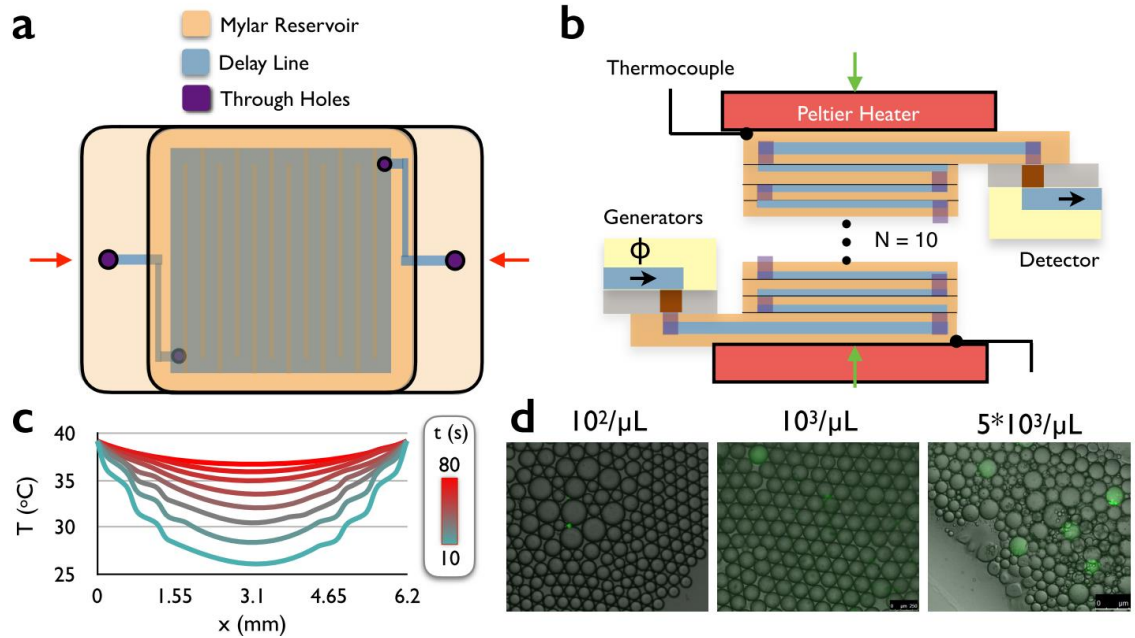


**Figure 6.3 Heating component for on chip isothermal amplification.** **a.** The chip was fabricated using both copper and thin mylar sheets that acted as a 3d reservoir for droplets to travel through. **b.** Ten of these were stacked on top of each other, with peltiers sandwiching both sides to keep the temperature at 37C. As room temperature liquid entered, it spent several minutes inside the delay line where the 37C for isothermal amplification was reached. **c.** COMSOL simulation shows how long it takes for room temperature liquid to reach the intended temperature, while **(d)** shows the results of spiking in varying concentrations of target templates. Droplet homogeneity was an issue due to heating, but surface treatment and degassing of the devices should fix these issues.

In order to regulate the temperature, we used peltiers designed for high temperatures and used an Arduino that measured the surface using thermocouples and an H-bridge to reverse the current and cool the system. Heatsinks were added so the peltiers did not lose efficiency over time; yet one issue was where the thermocouple probe would be placed. Surface temperatures overestimated the liquid interface, so to measure the effect of the surface temperature and the actual temperature of the liquid, we used a Rhodamine calibration curve to relate the surface temperature to the liquid temperature. We first measured the Rhodamine and its fluorescence at various temperatures at steady state and then measured how the surface temperature changed with the Rhodamine and optimized by thickness and channel height until the Rhodamine followed the surface temperature quickly, covering about 4 cycles in 2 minutes.

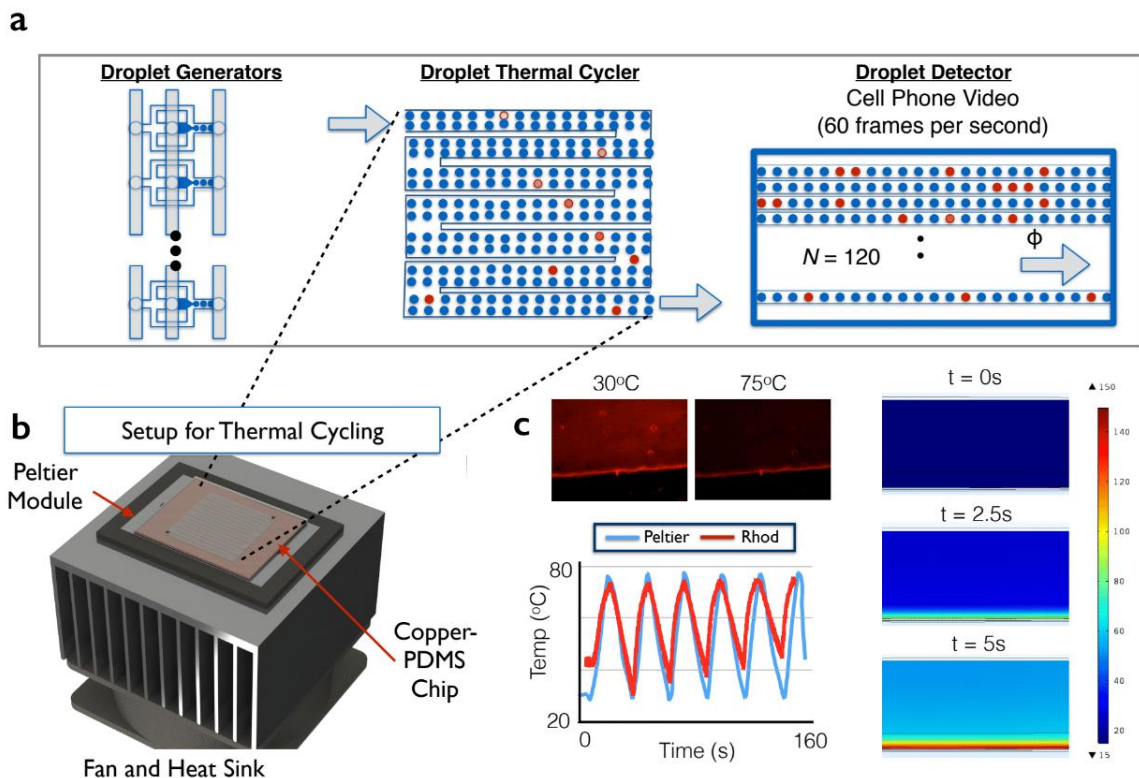


**Figure 6.4. Rapid on chip thermal cycling.** **a.** A similar approach can also be applied for digital PCR rather than just isothermal applications. **b.** A larger heatsink with a

copper chip is used for rapid thermal cycling. **c.** Rhodamine dye was used to first calibrate the surface temperatures at 30C and 75C. These fluorescent measurements were associated with surface temperatures, and then probe surface temperature was compared with the fluorescent signal from the Rhodamine. The graph shows that the liquid closely follows the surface temperature, but over time can begin to lag and not cool as effectively. COMSOL simulations also demonstrate how fast temperature should change in the liquid as a function of surface temperature.

However, even with the thermal cycling, this did not seem fast enough, so we looked at alternatives that would simplify the heating but still enable ultrasensitive detection. RPA<sup>244</sup> was previously demonstrated to be a robust isothermal amplification that only requires 37C to amplify fluorescent signal in the presence of target DNA. While existing commercial kits focused on bacterial nucleic acid targets, several labs have developed RPA for digital assays covering a wider range by carefully designing primers<sup>702432457148246</sup>. While RPA also was harder to control due to primer design and nonobvious correlations between the speed and efficiency of the amplification<sup>247</sup>, we demonstrated that RPA could be done in a continuous flow system.

Biorad Oil for Evagreen was used as the continuous phase, a rehydrated pellet from the RPA kit was used for the dispersed phase. A serial dilution of the target DNA was mixed in with each of the rehydrated pellet solution, which was then formed into droplets through a parallelized droplet generator. Since the droplets only had to be held at 37C for a few minutes, the reaction could be observed immediately after in a microscope setup. **Figure 6.3d** shows the results of the onchip amplification when observed on a microscope, with higher concentrations leading to a higher fraction of fluorescent droplets. While this assay was not optimized for the loss of target molecules

due to the sticky surfaces, improvements in the non-stick surface treatments from ELISA would significantly improve the existing problems. Furthermore, multiplexing of isothermal amplification has already been demonstrated and could be implemented to cover a wider range of targets once primers have been verified<sup>248–250</sup>.

## **6.2 Higher order multiplexing for ddELISA**

In order to detect multiple biomarkers simultaneously based on the ddELISA approach, there were several options for the design. The first is to have separate microfluidic channels each with its own inlet so that biomarkers are separated spatially. Here one bead color can be used, and each inlet would identify which biomarker was present based on the number of fluorescent droplets counted. While the approach is simpler, the drawbacks are that the sample has to be split into as many biomarkers to be measured. If the sample is limited or precious, this can be an issue. Next, from an engineering perspective, having 100 inlets with tubing for each would also make this impractical even if the oil and substrate inlets could be shared; limiting the amount of inlets to about 10 bead samples practically if we wanted to avoid connection complexity.

The second approach uses multiple excitation and emission filters for each bead color. While this requires more complex hardware, the limitations here stem from the trade off between the amount of narrowband excitation and emission sources that can be purchased. In addition, as the bands become more narrow, the amount of light for each color will also be decreased, reducing the electrical signal generated by the pixels. If the narrowbands are not tight, cross talk will severely reduce the ability to classify each bead population.

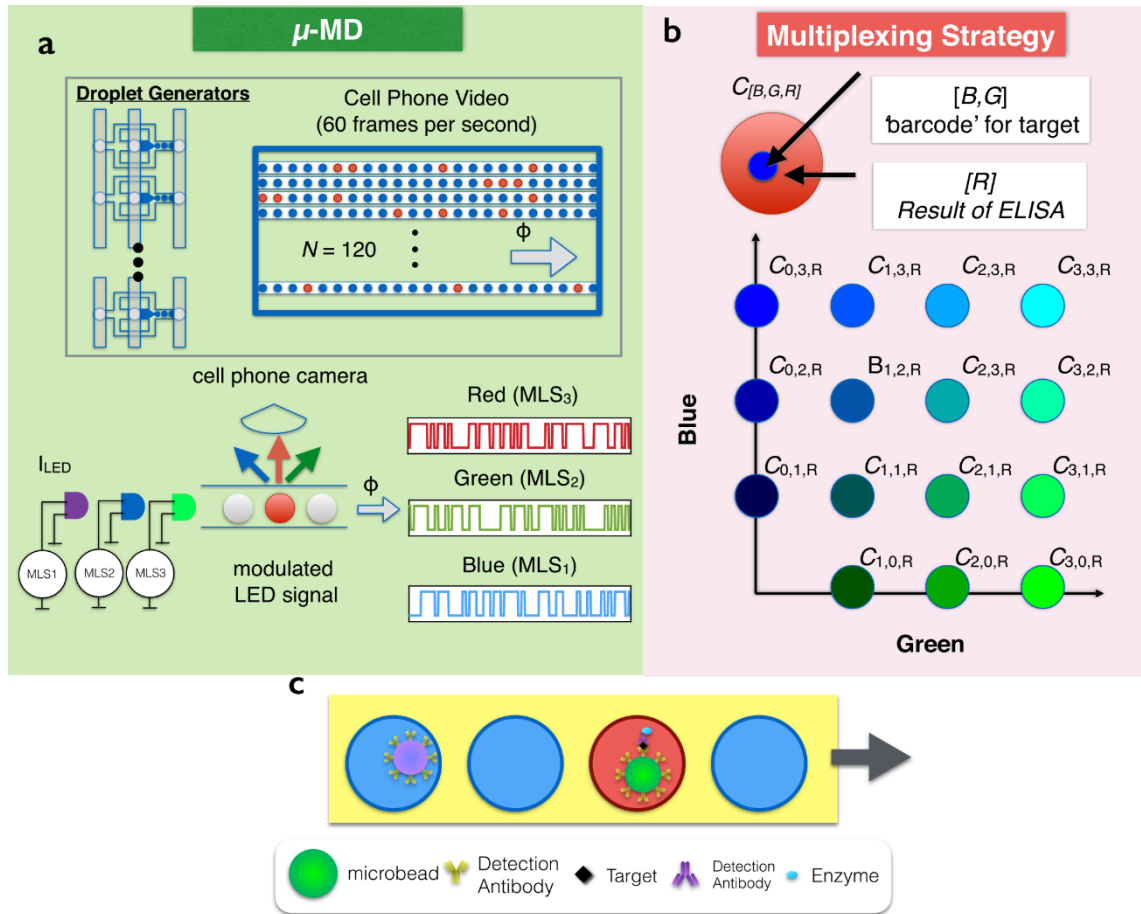


**Figure 6.5 Higher order multiplexing strategy for color coded-beads.** **a.** A similar strategy from the duplex ddELISA is employed, except this time there are three excitation sources each with a unique MLS. **b.** A color coded bead array is generated based on various combinations of dye concentrations. One color indicates the presence of a protein, whereas each color-coded bead is uniquely coated with capture antibody for a single protein target. **c.** Droplets that contain a protein will fluoresce, while those that do not remain blank.

Therefore, since we began with a cell phone-based approach and wanted to limit hardware complexity, we chose a higher order multiplexing method that only relies on three excitation sources, and a bandpass filter that fits the given ranges of emission

sources. In order to do this, we had to select beads that emitted in two colors at different intensities, where each combination of intensity would map out to a different target protein, and a final color that would identify if a target protein was present or not inside a droplet. This three-color system would be able to resolve as many populations of biomarkers as long as the bead populations separated into tight clusters in 2d map. While Luminex beads are the dominant player in this multiplexing bead approach, their red and infrared emission wavelengths were not compatible with our setup.

Therefore, we choose to use PolyAn beads that were fluorescent with blue and green lasers and had to shift to a UV fluorescent dye. These beads come in 12 distinct populations, with 6 sets of fluorescent beads at various combinations of dye. Therefore, each bead color would produce one MLS peak, and the third color would detect the presence of a protein. The first iteration was running beads through at high flow rate and measuring their MLS peaks for each wavelength of the bead dye. We observed that there were several causes for large scatter in the correlation 2d indexing plot: (1) phase variation from where the MLS starts, (2) excitation variation since the laser diodes have nonuniform excitation, (3) beads travel at different velocities, (4) high pass filters in the code, (5) software for normalizing the peak, and (6) crosstalk between signals.

In order to address the phase variation and get better sensitivity, we switched from a cell phone-based detector to the FLIR machine vision camera (Grasshopper 3). The FLIR 3 camera was swapped in, and this had several advantages: (1) higher sensitivity, (2) control of parameters that were automated in the cell phone, (3) a smaller angle of incidence which allows optical filters to work more effectively in narrow bands, (4) removal of any optical aberrations that required software correction previously, and (5) triggering of the recording frame in phase with the modulation of excitation light. Higher



sensitivity allowed dimmer droplets and substrates to be resolved in a dynamic range that covered the dimmest bead component to the brightest while flowing, without saturating the pixels. In order to address excitation variation, a background frame with the light intensities were used to first subtract and divide a real frame analyzed to normalize each frame for nonuniform intensity. Bead velocities, high pass filters, and bead length normalization were all related and in order to fix this, we first measured how the correlation peaks changed for different streaks of the MLS after passing it through the correlation analysis. The data was then used to correct for variations by multiplying by the inverse and reduce a theoretical scatter from  $\pm 10\%$  to  $\pm 1\%$ . Finally, the crosstalk was limited as much as possible by choosing the sharpest optical filters and notch filters for the excitation, yet the fluorescent emissions of the dyes overlapped in the same CMOS segment. Therefore, the MLS patterns were used to distinguish which dye was present in the beads. The results of the correlation analysis and rectangles representing the centroid with widths of two standard deviations are shown. While the beads are currently still clustered, there are some obvious steps to improve this process.

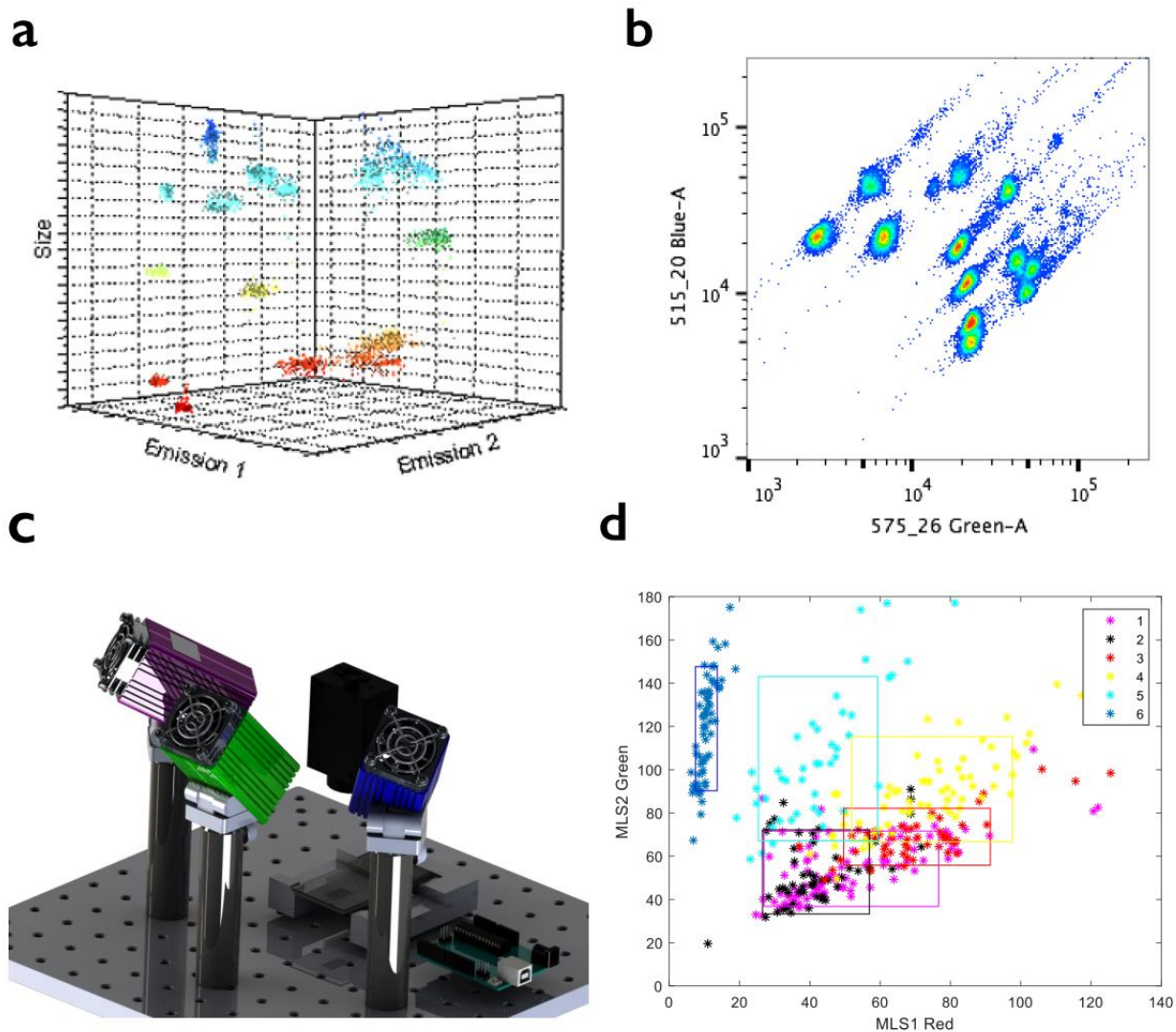


**Figure 6.6 Color-coded beads resolved in  $\mu$ MD.** **a.** Spectra from the company showing two sets of six color coded beads, that are also separated by size. **b.** Beads were run in flow cytometry. **c.** Setup with the FLIR camera, and three excitation sources controlled by an Arduino that triggers the excitation and detection. **d.** Resulting correlations of the beads in the  $\mu$ MD, with rectangles representing centroids and two standard deviations in width and length.

### 6.3 Washless ddELISA

One weakness in digital ELISA techniques, is that aggressive wash steps can cause dissociation between proteins and antibodies that are bound. Additionally, even with a fast workflow from when the sandwich is completely formed to detection, the incubation times and wash steps needed for each prior step of the sandwich can be lengthy. While doing these in parallel can reduce time, bead-based approaches require wash steps that often include centrifuges, magnetic washes, or more inexpensive size based membrane filters. Each of these systems has loss from beads or proteins from sticking to surfaces or not resuspending back properly after each wash step.

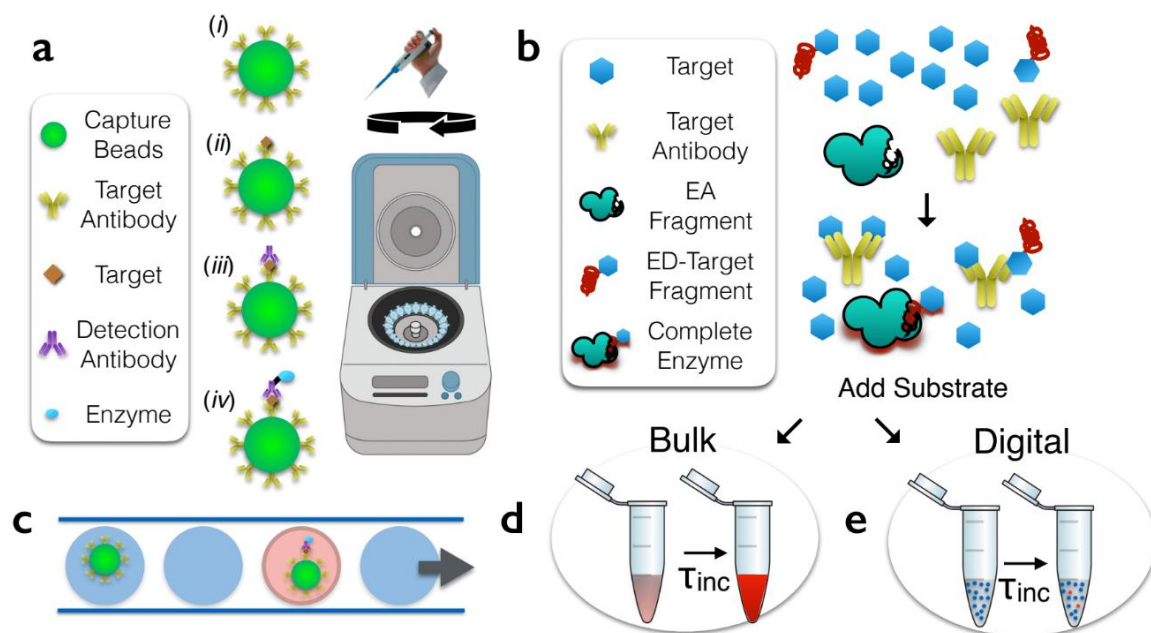


**Figure 6.7 Schematic of washless ELISA.** **a.** Typical bead based digital ELISA often requires (ii) capture beads to capture target proteins, (iii) bind detection antibody, and (iv) label with an enzyme. Each step requires multiple wash steps that often use a centrifuge or magnetic washer before they can be compartmentalized into droplets (**c**). **b.** In washless ELISA, active enzyme is only completed in the presence of excess

targets. Target protein compete with target attached to an enzyme fragment. When excess target is added, the ED-target fragment can dissociate from the antibody and complement with the EA fragment. Competition assays show lower sensitivity in bulk (**d**) than the digital assay where single complemented enzyme can be measured (**e**).

A one step reaction process that removes the needs for beads or wash steps could overcome this challenge. There are several enzymes that use complementation in the presence of a target to turn active, and cause fluorescence. This was demonstrated with Luciferase, HRP, and B-Gal; however there was no commercial kit that allowed us to test this. The principle of such an assay would require no washing since the two halves would only join and turn active in the presence of a target, and could directly be loaded into droplets after incubation. In order to test this with a similar technology called the HitHunter cAMP assay that uses enzyme fragmentation technology for cAMP (**Figure 6.7**). We tested this kit in bulk first, and then in droplets and measured fluorescence when enzymes complemented successfully. There were some issues in terms of running the kit completely with target proteins and inhibitors, so there was significant loss. An additional issue is that the kit is only available for cAMP which may not have potential as a significant diagnostic marker and is rather used for cell based studies. Several labs have been developing fragmentation technology that could be created for any target and are hopeful that this technology would enable a bead-free washless digital ELISA.

## 6.4 Nanoparticle enhanced ddELISA

Digital ELISA is currently severely limited by the antibodies that are available to form a strong sandwich complex that can withstand various wash steps. Digital ELISA is only possible when both the capture antibody and detection antibodies have low  $K_d$ s, allowing a single protein molecule to bind and stick to the bead surface. For the capture antibody, this problem is not as severe since the entire capture bead is coated with antibodies, and if a protein molecule dissociates, it has a chance to attach to a neighboring antibody, termed avidity effects. However, when this happens with the detection antibody, the problem is that there is only one detection antibody per protein molecule. If the detection antibody dissociates either due to kinetics or from aggressive wash steps, this will result in a lower sensitivity. Additionally, finding a sandwich pair that has effective antibodies for digital ELISA is a limiting step in establishing assays that can detect single proteins, where a low  $K_d$  antibody might not even be available.

**Table 6.2 Bulk Nanoparticle enhanced ELISA**

Ref.	Method of Verification and Improvement in Results
Zhan <sup>251</sup>	<ul style="list-style-type: none"> <li>• Five anti-RSV–HRP molecules for each AuNPs.</li> <li>• Improved LOD of conventional ELISA probe by 50 times.</li> <li>• 6x improvement in color signal development from 15-30 min to 5 min</li> </ul>
Bill <sup>252</sup>	<ul style="list-style-type: none"> <li>• Two-step detection assay that utilizes HRP-conjugated secondary IgG;</li> <li>• 150 nm diameter nanoshells (NS) composed of 120 nm silica cores and 15 nm thick gold shells</li> <li>• 13 fold increase in sensitivity</li> <li>• 40x more conjugated antibodies were required to detect EGFR</li> </ul>
Bang <sup>253</sup>	<ul style="list-style-type: none"> <li>• Binding affinity of affibody functionalized gold nanoparticles of ~500 pM, exceeded that of the anti-NS1 affibody dimer (<math>K_d = 5</math> mM) by 10000 times.</li> <li>• 14.2 fold improvement in sensitivity</li> <li>• Average of 150 affibodies per gold nanoparticle</li> </ul>

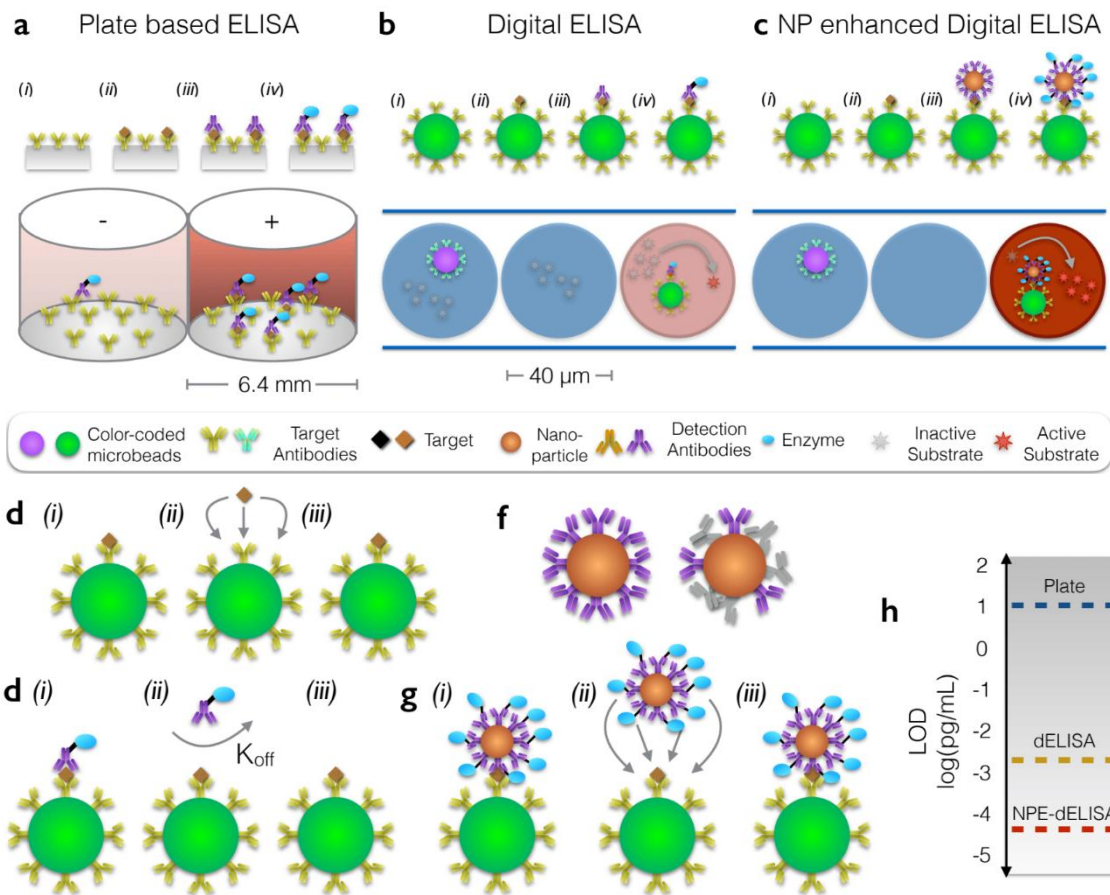


**Figure 6.8 Enhancement from nanoparticle based digital ELISA.** **a.** Traditional plate based ELISA suffer from poor sensitivity. **b.** Digital ELISA measures the end point reactions of single protein molecules in millions of tiny compartments where the amplified dye can be concentrated for a strong signal. **c.** When the detection antibody is replaced with a nanoparticle containing multiple detection antibodies, the higher number of enzymes will speed up the reaction for a stronger signal compared to digital ELISA. **d,e.** In digital ELISA, the protein has multiple chances to bind to neighboring capture antibody, but only one detection antibody per captured protein. If the antibody weakly binds, washing or dissociation will reduce total protein counted. **f,g,h.** In nanoparticle enhanced ELISA, there are multiple chances for detection antibody to bind to the protein, allowing a higher rate of proteins to be counted.

We propose that nanoparticles covered with detection antibody can overcome this limitation by enabling the avidity effects to the detection antibody. A nanoparticle covered with detection antibody has the following advantages: (1) if the nanoparticle dissociates, neighboring antibodies could rebind to the protein and (2) additional biotin groups from multiple detection antibodies would capture more HRP/single protein molecule. Additional HRP enzymes would result in faster signal generation, and avidity would enable more sensitive measurements. Several groups have shown that this enhancement has improved bulk ELISA by several orders of magnitude, allowed lower levels of reagents, and lower false positive signals.

## REFERENCES

1. Arneth, B. Update on the types and usage of liquid biopsies in the clinical setting: a systematic review. *BMC Cancer* **18**, 527 (2018).
2. Heitzer, E., Haque, I. S., Roberts, C. E. S. & Speicher, M. R. Current and future perspectives of liquid biopsies in genomics-driven oncology. *Nat. Rev. Genet.* **20**, 71–88 (2019).
3. IJzerman, M. J., Berghuis, A. M. S., de Bono, J. S. & Terstappen, L. W. M. M. Health economic impact of liquid biopsies in cancer management. *Expert Rev. Pharmacoecon. Outcomes Res.* **18**, 593–599 (2018).
4. Posti, J. P. *et al.* Correlation of blood biomarkers and biomarker panels with traumatic findings on computed tomography after traumatic brain injury. *J. Neurotrauma* neu.2018.6254 (2019). doi:10.1089/neu.2018.6254
5. Su, Y. S., Schuster, J. M., Smith, D. H. & Stein, S. C. Cost Effectiveness of Biomarker Screening for Traumatic Brain Injury. *J. Neurotrauma* neu.2018.6020 (2018). doi:10.1089/neu.2018.6020
6. Domínguez-Vigil, I. G., Moreno-Martínez, A. K., Wang, J. Y., Roehrl, M. H. A. & Barrera-Saldaña, H. A. The dawn of the liquid biopsy in the fight against cancer. *Oncotarget* **9**, 2912–2922 (2018).
7. Heitzer, E., Haque, I. S., Roberts, C. E. S. & Speicher, M. R. Current and future perspectives of liquid biopsies in genomics-driven oncology. *Nat. Rev. Genet.* **20**, 71–88 (2019).
8. Cabrera, C., Chang, L., Stone, M., Busch, M. & Wilson, D. H. Rapid, Fully Automated Digital Immunoassay for p24 Protein with the Sensitivity of Nucleic Acid Amplification for Detecting Acute HIV Infection. *Clin. Chem.* **61**, 1372–1380 (2015).
9. Passaes, C. P. B. *et al.* Ultrasensitive HIV-1 p24 Assay Detects Single Infected Cells and Differences in Reservoir Induction by Latency Reversal Agents. *J. Virol.* **91**, e02296-16 (2017).
10. Pekin, D. & Taly, V. in 143–164 (Humana Press, New York, NY, 2017). doi:10.1007/978-1-4939-6734-6\_12
11. Bosman, K. J. *et al.* Comparison of digital PCR platforms and semi-nested qPCR as a tool to determine the size of the HIV reservoir. (2015). doi:10.1038/srep13811
12. Chaipan, C. *et al.* Single-Virus Droplet Microfluidics for High-Throughput Screening of Neutralizing Epitopes on HIV Particles. *Cell Chem. Biol.* **24**, 751–757 (2017).
13. Loosen, S. H., Neumann, U. P., Trautwein, C., Roderburg, C. & Luedde, T.



Current and future biomarkers for pancreatic adenocarcinoma. *Tumor Biol.* **39**, 101042831769223 (2017).

14. Papa, L., Edwards, D. & Ramia, M. *Exploring Serum Biomarkers for Mild Traumatic Brain Injury. Brain Neurotrauma: Molecular, Neuropsychological, and Rehabilitation Aspects* (CRC Press/Taylor & Francis, 2015). at <<http://www.ncbi.nlm.nih.gov/pubmed/26269900>>
15. Duffy, M. J., Diamandis, E. P. & Blasutig, I. M. Biochemical markers as prognostic indices in breast cancer. *Clin. Chem.* **36**, 188–91 (1990).
16. Preische, O. *et al.* Serum neurofilament dynamics predicts neurodegeneration and clinical progression in presymptomatic Alzheimer's disease. *Nat. Med.* **25**, 277–283 (2019).
17. Wilson, D. H. *et al.* Fifth-generation digital immunoassay for prostate-specific antigen by single molecule array technology. *Clin. Chem.* **57**, 1712–21 (2011).
18. Stone, M. *et al.* Comparison of Detection Limits of Fourth- and Fifth-Generation Combination HIV Antigen-Antibody, p24 Antigen, and Viral Load Assays on Diverse HIV Isolates. *J. Clin. Microbiol.* **56**, (2018).
19. O'Bryant, S. E. *et al.* Blood-based biomarkers in Alzheimer disease: Current state of the science and a novel collaborative paradigm for advancing from discovery to clinic. *Alzheimer's Dement.* **13**, 45–58 (2017).
20. Rivnak, A. J. *et al.* A fully-automated, six-plex single molecule immunoassay for measuring cytokines in blood. *J. Immunol. Methods* **424**, 20–27 (2015).
21. Ahmad, R. *et al.* *Rapid Point-Of-Care Diagnosis Of Tuberculosis In Patients With Persistent Cough.* at <[www.atsjournals.org](http://www.atsjournals.org)>
22. Altschuler, S. J. & Wu, L. F. Cellular heterogeneity: do differences make a difference? *Cell* **141**, 559–63 (2010).
23. Ko, J. *et al.* miRNA Profiling of Magnetic Nanopore-Isolated Extracellular Vesicles for the Diagnosis of Pancreatic Cancer. *Cancer Res.* **78**, 3688–3697 (2018).
24. Ko, J. *et al.* Diagnosis of traumatic brain injury using miRNA signatures in nanomagnetically isolated brain-derived extracellular vesicles. *Lab Chip* **18**, 3617–3630 (2018).
25. Korley, F. K. *et al.* Performance Evaluation of a Multiplex Assay for Simultaneous Detection of Four Clinically Relevant Traumatic Brain Injury Biomarkers. *J. Neurotrauma* **36**, 182–187 (2019).
26. Ko, J. *et al.* Machine learning to detect signatures of disease in liquid biopsies – a user's guide. *Lab Chip* **18**, 395–405 (2018).
27. Drain, P. K. *et al.* Diagnostic point-of-care tests in resource-limited settings. *Lancet. Infect. Dis.* **14**, 239–49 (2014).

28. Datta, S., Shah, L., Gilman, R. H. & Evans, C. A. Comparison of sputum collection methods for tuberculosis diagnosis: a systematic review and pairwise and network meta-analysis. *Lancet. Glob. Heal.* **5**, e760–e771 (2017).
29. Lee, E. S. & Lee, J. M. Imaging diagnosis of pancreatic cancer: a state-of-the-art review. *World J. Gastroenterol.* **20**, 7864–77 (2014).
30. Banerjee, R. & Jaiswal, A. Recent advances in nanoparticle-based lateral flow immunoassay as a point-of-care diagnostic tool for infectious agents and diseases. *Analyst* **143**, 1970–1996 (2018).
31. Sajid, M., Kawde, A.-N. & Daud, M. Designs, formats and applications of lateral flow assay: A literature review. *J. Saudi Chem. Soc.* **19**, 689–705 (2015).
32. Koczula, K. M. & Gallotta, A. Lateral flow assays. *Essays Biochem.* **60**, 111–20 (2016).
33. Connelly, J. T., Rolland, J. P. & Whitesides, G. M. “Paper Machine” for Molecular Diagnostics. *Anal. Chem.* **87**, 7595–7601 (2015).
34. Chin, C. D., Linder, V. & Sia, S. K. Commercialization of microfluidic point-of-care diagnostic devices. *Lab Chip* **12**, 2118 (2012).
35. and, A. B. & Catherine M. Klapperich†, \*. Thermoplastic Microfluidic Device for On-Chip Purification of Nucleic Acids for Disposable Diagnostics. (2005). doi:10.1021/AC051449J
36. Betters, D. M. Use of Flow Cytometry in Clinical Practice. *J. Adv. Pract. Oncol.* **6**, 435–40 (2015).
37. Adan, A., Alizada, G., Kiraz, Y., Baran, Y. & Nalbant, A. Flow cytometry: basic principles and applications. *Crit. Rev. Biotechnol.* **37**, 163–176 (2017).
38. Doan, M. *et al.* Diagnostic Potential of Imaging Flow Cytometry. *Trends Biotechnol.* **36**, 649–652 (2018).
39. Suvarnaphaet, P. & Pechprasarn, S. Graphene-Based Materials for Biosensors: A Review. *Sensors* **17**, 2161 (2017).
40. Hill, R. T. Plasmonic biosensors. *WIREs Nanomed Nanobiotechnol* **7**, 152–168 (2015).
41. Haun, J. B. *et al.* Micro-NMR for Rapid Molecular Analysis of Human Tumor Samples. *Sci. Transl. Med.* **3**, 71ra16–71ra16 (2012).
42. Jain, M., Olsen, H. E., Paten, B. & Akeson, M. The Oxford Nanopore MinION: delivery of nanopore sequencing to the genomics community. *Genome Biol.* **17**, 239 (2016).
43. Cohen, L. & Walt, D. R. Single-Molecule Arrays for Protein and Nucleic Acid Analysis. *Annu. Rev. Anal. Chem.* **10**, 345–363 (2017).

44. Chang, L. *et al.* Single molecule enzyme-linked immunosorbent assays: Theoretical considerations. *J. Immunol. Methods* **378**, 102–115 (2012).
45. Tang, H., Cai, Q., Li, H. & Hu, P. Comparison of droplet digital PCR to real-time PCR for quantification of hepatitis B virus DNA. *Biosci. Biotechnol. Biochem.* **80**, 2159–2164 (2016).
46. Basu, A. S. Digital Assays Part I: Partitioning Statistics and Digital PCR. *SLAS Technol. Transl. Life Sci. Innov.* **22**, 369–386 (2017).
47. Zhu, Q. *et al.* Digital PCR on an integrated self-priming compartmentalization chip. *Lab Chip* **14**, 1176–85 (2014).
48. Shen, F. *et al.* Digital Isothermal Quantification of Nucleic Acids via Simultaneous Chemical Initiation of Recombinase Polymerase Amplification Reactions on SlipChip. *Anal. Chem.* **83**, 3533–3540 (2011).
49. McGuigan, W. *et al.* The optics inside an automated single molecule array analyzer. in (eds. Vo-Dinh, T., Mahadevan-Jansen, A. & Grundfest, W. S.) 89350X (2014). doi:10.1117/12.2041706
50. Kan, C. W. *et al.* Isolation and detection of single molecules on paramagnetic beads using sequential fluid flows in microfabricated polymer array assemblies †. doi:10.1039/c2lc20744c
51. Hatch, A. C. *et al.* 1-Million droplet array with wide-field fluorescence imaging for digital PCR. *Lab Chip* **11**, 3838 (2011).
52. Lievens, A., Jacchia, S., Kagkli, D., Savini, C. & Querci, M. Measuring Digital PCR Quality: Performance Parameters and Their Optimization. *PLoS One* **11**, e0153317 (2016).
53. Macosko, E. Z. *et al.* Highly Parallel Genome-wide Expression Profiling of Individual Cells Using Nanoliter Droplets. *Cell* **161**, 1202–1214 (2015).
54. Kaminski, T. S. & Garstecki, P. Controlled droplet microfluidic systems for multistep chemical and biological assays. *Chem. Soc. Rev.* **46**, 6210–6226 (2017).
55. Baret, J.-C. *et al.* Fluorescence-activated droplet sorting (FADS): efficient microfluidic cell sorting based on enzymatic activity. *Lab Chip* **9**, 1850–8 (2009).
56. Zhu, P. & Wang, L. Passive and active droplet generation with microfluidics: a review. *Lab Chip* **17**, 34–75 (2017).
57. Rosenfeld, L., Lin, T., Derda, R. & Tang, S. K. Y. Review and analysis of performance metrics of droplet microfluidics systems. *Microfluid. Nanofluidics* **16**, 921–939 (2014).
58. Debski, P. R., Gewartowski, K., Sulima, M., Kaminski, T. S. & Garstecki, P. Rational Design of Digital Assays. *Anal. Chem.* **87**, 8203–8209 (2015).

59. Kaminski, T. S., Scheler, O. & Garstecki, P. Droplet microfluidics for microbiology: techniques, applications and challenges. *Lab Chip* **16**, 2168–2187 (2016).
60. Leong, C. M., Gai, Y. & Tang, S. K. Y. Internal flow in droplets within a concentrated emulsion flowing in a microchannel. *Phys. Fluids* **28**, 112001 (2016).
61. Shang, L., Cheng, Y. & Zhao, Y. Emerging Droplet Microfluidics. *Chem. Rev.* **117**, 7964–8040 (2017).
62. Liebherr, R. B. & Gorris, H. H. molecules Enzyme Molecules in Solitary Confinement. *Molecules* **19**, 14417–14445 (2014).
63. Ahrberg, C. D., Manz, A., Geun Chung, B., Bong Geun Chung, S. & Manz bc, A. Featuring work from the BioNano Technology Lab As featured in: Polymerase chain reaction in microfluidic devices. *Lab Chip* **16**, 3866 (2016).
64. Polini, A. *et al.* Reduction of water evaporation in polymerase chain reaction microfluidic devices based on oscillating-flow. *Biomicrofluidics* **4**, (2010).
65. Schaerli, Y. *et al.* Continuous-Flow Polymerase Chain Reaction of Single-Copy DNA in Microfluidic Microdroplets. *Anal. Chem.* **81**, 302–306 (2009).
66. Beer, N. R. *et al.* On-Chip, Real-Time, Single-Copy Polymerase Chain Reaction in Picoliter Droplets. doi:10.1021/ac701809w
67. Kiss, M. M. *et al.* High-Throughput Quantitative Polymerase Chain Reaction in Picoliter Droplets. *Anal. Chem.* **80**, 8975–8981 (2008).
68. Terazono, H. *et al.* Development of 1480 nm Photothermal High-Speed Real-Time Polymerase Chain Reaction System for Rapid Nucleotide Recognition. *Jpn. J. Appl. Phys.* **47**, 5212–5216 (2008).
69. Rane, T. D. *et al.* Microfluidic continuous flow digital loop-mediated isothermal amplification (LAMP). *Lab Chip* **15**, 776–782 (2015).
70. Li, Z. *et al.* Picoliter Well Array Chip-Based Digital Recombinase Polymerase Amplification for Absolute Quantification of Nucleic Acids. *PLoS One* **11**, e0153359 (2016).
71. Schuler, F. *et al.* Centrifugal step emulsification applied for absolute quantification of nucleic acids by digital droplet RPA. *Lab Chip* **15**, 2759–2766 (2015).
72. Kang, D.-K. *et al.* Rapid detection of single bacteria in unprocessed blood using Integrated Comprehensive Droplet Digital Detection. *Nat. Commun.* **5**, 5427 (2014).
73. Sanders, R., Mason, D. J., Foy, C. A. & Huggett, J. F. Evaluation of Digital PCR for Absolute RNA Quantification. *PLoS One* **8**, e75296 (2013).
74. Stein, E. V. *et al.* Steps to achieve quantitative measurements of microRNA using two step droplet digital PCR. *PLoS One* **12**, e0188085 (2017).

75. Postel, M., Roosen, A., Laurent-Puig, P., Taly, V. & Wang-Renault, S.-F. Droplet-based digital PCR and next generation sequencing for monitoring circulating tumor DNA: a cancer diagnostic perspective. *Expert Rev. Mol. Diagn.* **18**, 7–17 (2018).
76. Perkins, G., Lu, H., Garlan, F. & Taly, V. in *Advances in clinical chemistry* **79**, 43–91 (2017).
77. Taylor, S. C., Laperriere, G. & Germain, H. Droplet Digital PCR versus qPCR for gene expression analysis with low abundant targets: from variable nonsense to publication quality data. *Sci. Rep.* **7**, 2409 (2017).
78. Basu, A. S. Digital Assays Part I: Partitioning Statistics and Digital PCR. *SLAS Technol. Transl. Life Sci. Innov.* **22**, 369–386 (2017).
79. Whale, A. S., Huggett, J. F. & Tzonev, S. Fundamentals of multiplexing with digital PCR. *Biomol. Detect. Quantif.* **10**, 15–23 (2016).
80. Dobnik, D., Štebih, D., Blejec, A., Morisset, D. & Žel, J. Multiplex quantification of four DNA targets in one reaction with Bio-Rad droplet digital PCR system for GMO detection. *Sci. Rep.* **6**, 35451 (2016).
81. Guan, Z. *et al.* A highly parallel microfluidic droplet method enabling single-molecule counting for digital enzyme detection. *Biomicrofluidics* **8**, 014110 (2014).
82. Obayashi, Y. *et al.* A single-molecule digital enzyme assay using alkaline phosphatase with a coumarin-based fluorogenic substrate. *Analyst* **140**, 5065–5073 (2015).
83. Chang, L. *et al.* Simple diffusion-constrained immunoassay for p24 protein with the sensitivity of nucleic acid amplification for detecting acute HIV infection. *J. Virol. Methods* **188**, 153–160 (2013).
84. Shim, J. *et al.* Ultrarapid Generation of Femtoliter Microfluidic Droplets for Single-Molecule-Counting Immunoassays. *ACS Nano* **7**, 5955–5964 (2013).
85. Leirs, K. *et al.* Bioassay Development for Ultrasensitive Detection of Influenza A Nucleoprotein Using Digital ELISA. *Anal. Chem.* **88**, 8450–8458 (2016).
86. Wilson, D. H. *et al.* The Simoa HD-1 Analyzer. *J. Lab. Autom.* **21**, 533–547 (2016).
87. Kan, C. W. *et al.* Isolation and detection of single molecules on paramagnetic beads using sequential fluid flows in microfabricated polymer array assemblies. doi:10.1039/c2lc20744c
88. Yelleswarapu, V. *et al.* Mobile platform for rapid sub-picogram-per-milliliter, multiplexed, digital droplet detection of proteins. *Proc. Natl. Acad. Sci. U. S. A.* **116**, 4489–4495 (2019).
89. Cohen, L., Hartman, M. R., Amardey-Wellington, A. & Walt, D. R. Digital direct detection of microRNAs using single molecule arrays. *Nucleic Acids Res.* **45**,

e137–e137 (2017).

90. Guan, W., Chen, L., Rane, T. D. & Wang, T.-H. Droplet Digital Enzyme-Linked Oligonucleotide Hybridization Assay for Absolute RNA Quantification. *Sci. Rep.* **5**, 13795 (2015).
91. Guan, W., Chen, L., Rane, T., Kaushik, A. & Wang, J. T.-H. Digital droplet ELOHA for nucleic acid molecule counting and analysis. in *2015 Transducers - 2015 18th International Conference on Solid-State Sensors, Actuators and Microsystems (TRANSDUCERS)* 460–463 (IEEE, 2015). doi:10.1109/TRANSDUCERS.2015.7180960
92. Rivnak, A. J. *et al.* A fully-automated, six-plex single molecule immunoassay for measuring cytokines in blood. *J. Immunol. Methods* **424**, 20–27 (2015).
93. Schaum, N. *et al.* Single-cell transcriptomics of 20 mouse organs creates a Tabula Muris the tabula Muris consortium\*. *Nature* (2018). doi:10.1038/s41586-018-0590-4
94. Zhang, X., Lowe, S. B. & Gooding, J. J. Brief review of monitoring methods for loop-mediated isothermal amplification (LAMP). *Biosens. Bioelectron.* **61**, 491–499 (2014).
95. Camplisson, C. K., Schilling, K. M., Pedrotti, W. L., Stone, H. A. & Martinez, A. W. Two-ply channels for faster wicking in paper-based microfluidic devices. *Lab Chip* **15**, 4461–4466 (2015).
96. Koczula, K. M. & Gallotta, A. Lateral flow assays. *Essays Biochem.* **60**, 111–20 (2016).
97. Figueroa, C. *et al.* Reliability of HIV rapid diagnostic tests for self-testing compared with testing by health-care workers: a systematic review and meta-analysis. *Lancet HIV* **5**, e277–e290 (2018).
98. García-Basteiro, A. L. *et al.* Point of care diagnostics for tuberculosis. *Pulmonology* **24**, 73–85 (2018).
99. Chan, H. N., Tan, M. J. A. & Wu, H. Point-of-care testing: applications of 3D printing. *Lab Chip* **17**, 2713–2739 (2017).
100. Vashist, S. K., Lippa, P. B., Yeo, L. Y., Ozcan, A. & Luong, J. H. T. Emerging Technologies for Next-Generation Point-of-Care Testing. *Trends Biotechnol.* **33**, 692–705 (2015).
101. Nayak, S., Blumenfeld, N. R., Laksanasopin, T. & Sia, S. K. Point-of-Care Diagnostics: Recent Developments in a Connected Age. *Anal. Chem.* **89**, 102–123 (2017).
102. Song, J. *et al.* Instrument-Free Point-of-Care Molecular Detection of Zika Virus. *Anal. Chem.* **88**, 7289–7294 (2016).
103. Rivenson, Y. *et al.* Deep Learning Enhanced Mobile-Phone Microscopy. *ACS*

*Photonics* **5**, 2354–2364 (2018).

104. Hernández-Neuta, I. *et al.* Smartphone-based clinical diagnostics: towards democratization of evidence-based health care. *J. Intern. Med.* **285**, 19–39 (2019).
105. Zhang, K. *et al.* Digital quantification of miRNA directly in plasma using integrated comprehensive droplet digital detection. *Lab Chip* **15**, 4217–26 (2015).
106. Kang, D.-K. *et al.* Rapid detection of single bacteria in unprocessed blood using Integrated Comprehensive Droplet Digital Detection. *Nat. Commun.* **5**, 5427 (2014).
107. Ko, J. *et al.* miRNA Profiling of Magnetic Nanopore-Isolated Extracellular Vesicles for the Diagnosis of Pancreatic Cancer. *Cancer Res.* **78**, 3688–3697 (2018).
108. Ko, J. *et al.* A magnetic micropore chip for rapid (. *Lab Chip* **17**, 3086–3096 (2017).
109. Baret, J.-C. *et al.* Fluorescence-activated droplet sorting (FADS): efficient microfluidic cell sorting based on enzymatic activity. *Lab Chip* **9**, 1850 (2009).
110. Milbury, C. A. *et al.* Determining lower limits of detection of digital PCR assays for cancer-related gene mutations. *Biomol. Detect. Quantif.* **1**, 8–22 (2014).
111. Perkins, G., Lu, H., Garlan, F. & Taly, V. Droplet-Based Digital PCR: Application in Cancer Research. *Adv. Clin. Chem.* **79**, 43–91 (2017).
112. Chiu, M. L. *et al.* Matrix EffectsdA Challenge Toward Automation of Molecular Analysis. *J. Assoc. Lab. Autom.* **15**, 233–242 (2010).
113. Debski, P. R. & Garstecki, P. Designing and interpretation of digital assays: Concentration of target in the sample and in the source of sample. *Biomol. Detect. Quantif.* **10**, 24–30 (2016).
114. Shahi, P., Kim, S. C., Haliburton, J. R., Gartner, Z. J. & Abate, A. R. Abseq: Ultrahigh-throughput single cell protein profiling with droplet microfluidic barcoding. *Sci. Rep.* **7**, 44447 (2017).
115. Yager, P., Domingo, G. J. & Gerdes, J. Point-of-care diagnostics for global health. *Annu. Rev. Biomed. Eng.* **10**, 107–44 (2008).
116. Guo, M. T. *et al.* Droplet microfluidics for high-throughput biological assays. *Lab Chip* **12**, 2146 (2012).
117. Joensson, H. N. & Andersson Svahn, H. Droplet Microfluidics-A Tool for Single-Cell Analysis. *Angew. Chemie Int. Ed.* **51**, 12176–12192 (2012).
118. Hindson, B. J. *et al.* High-throughput droplet digital PCR system for absolute quantitation of DNA copy number. *Anal. Chem.* **83**, 8604–10 (2011).
119. Pekin, D. *et al.* Quantitative and sensitive detection of rare mutations using

- droplet-based microfluidics. *Lab Chip* **11**, 2156–66 (2011).
120. Shembekar, N. *et al.* Droplet-based microfluidics in drug discovery, transcriptomics and high-throughput molecular genetics. *Lab Chip* **16**, 1314–1331 (2016).
  121. Wen, N. *et al.* Development of Droplet Microfluidics Enabling High-Throughput Single-Cell Analysis. *Molecules* **21**, 881 (2016).
  122. Cao, L. *et al.* Advances in digital polymerase chain reaction (dPCR) and its emerging biomedical applications. *Biosens. Bioelectron.* **90**, 459–474 (2017).
  123. Pinheiro, L. B. *et al.* Evaluation of a droplet digital polymerase chain reaction format for DNA copy number quantification. *Anal. Chem.* **84**, 1003–11 (2012).
  124. Rosenfeld, L., Lin, T., Derda, R. & Tang, S. K. Y. Review and analysis of performance metrics of droplet microfluidics systems. *Microfluid. Nanofluidics* **16**, 921–939 (2014).
  125. Leman, M., Abouakil, F., Griffiths, A. D. & Tabeling, P. Droplet-based microfluidics at the femtolitre scale. *Lab Chip* **15**, 753–765 (2015).
  126. Jeffries, G. D. M., Lorenz, R. M. & Chiu, D. T. Ultrasensitive and high-throughput fluorescence analysis of droplet contents with orthogonal line confocal excitation. *Anal. Chem.* **82**, 9948–54 (2010).
  127. Romanowsky, M. B., Abate, A. R., Rotem, A., Holtze, C. & Weitz, D. A. High throughput production of single core double emulsions in a parallelized microfluidic device. *Lab Chip* **12**, 802–7 (2012).
  128. Nisisako, T. & Torii, T. Microfluidic large-scale integration on a chip for mass production of monodisperse droplets and particles. *Lab Chip* **8**, 287–93 (2008).
  129. Muluneh, M., Kim, B., Buchsbaum, G. & Issadore, D. Miniaturized, multiplexed readout of droplet-based microfluidic assays using time-domain modulation. *Lab Chip* **14**, 4638–46 (2014).
  130. Jeong, H.-H., Yelleswarapu, V. R., Yadavali, S., Issadore, D. & Lee, D. Kilo-scale droplet generation in three-dimensional monolithic elastomer device (3D MED). *Lab Chip* **15**, 4387–92 (2015).
  131. Amstad, E. *et al.* Robust scalable high throughput production of monodisperse drops. *Lab Chip* **16**, 4163–4172 (2016).
  132. Hatch, A. C. *et al.* 1-Million droplet array with wide-field fluorescence imaging for digital PCR. *Lab Chip* **11**, 3838–45 (2011).
  133. Lim, J. *et al.* Ultra-high throughput detection of single cell  $\beta$ -galactosidase activity in droplets using micro-optical lens array. *Appl. Phys. Lett.* **103**, 203704 (2013).
  134. Coskun, A. F. & Ozcan, A. Computational imaging, sensing and diagnostics for global health applications. *Curr. Opin. Biotechnol.* **25**, 8–16 (2014).



135. Kang, D.-K. *et al.* Rapid detection of single bacteria in unprocessed blood using Integrated Comprehensive Droplet Digital Detection. *Nat. Commun.* **5**, 5427 (2014).
136. Schonbrun, E., Abate, A. R., Steinvurzel, P. E., Weitz, D. A. & Crozier, K. B. High-throughput fluorescence detection using an integrated zone-plate array. *Lab Chip* **10**, 852–6 (2010).
137. Agresti, J. J. *et al.* Ultrahigh-throughput screening in drop-based microfluidics for directed evolution. *Proc. Natl. Acad. Sci.* **107**, 4004–4009 (2010).
138. Clausell-Tormos, J. *et al.* Droplet-Based Microfluidic Platforms for the Encapsulation and Screening of Mammalian Cells and Multicellular Organisms. *Chem. Biol.* **15**, 427–437 (2008).
139. Kim, M. *et al.* Optofluidic ultrahigh-throughput detection of fluorescent drops. *Lab Chip* **15**, 1417–1423 (2015).
140. McKenna, B. K., Evans, J. G., Cheung, M. C. & Ehrlich, D. J. A parallel microfluidic flow cytometer for high-content screening. *Nat. Methods* **8**, 401–403 (2011).
141. Martini, J. *et al.* Time encoded multicolor fluorescence detection in a microfluidic flow cytometer. *Lab Chip* **12**, 5057–62 (2012).
142. Kiesel, P., Bassler, M., Beck, M. & Johnson, N. Spatially modulated fluorescence emission from moving particles. *Appl. Phys. Lett.* **94**, 041107 (2009).
143. Zheng, G. *et al.* Sub-pixel resolving optofluidic microscope for on-chip cell imaging. *Lab Chip* **10**, 3125 (2010).
144. Skandarajah, A. *et al.* Quantitative Imaging with a Mobile Phone Microscope. *PLoS One* **9**, e96906 (2014).
145. Balsam, J., Bruck, H. A. & Rasooly, A. Cell streak imaging cytometry for rare cell detection. *Biosens. Bioelectron.* **64**, 154–160 (2015).
146. Chin, C. D., Linder, V. & Sia, S. K. Lab-on-a-chip devices for global health: past studies and future opportunities. *Lab Chip* **7**, 41–57 (2007).
147. Zhu, H., Yaglidere, O., Su, T.-W., Tseng, D. & Ozcan, A. Cost-effective and compact wide-field fluorescent imaging on a cell-phone. *Lab Chip* **11**, 315–22 (2011).
148. Switz, N. A. *et al.* Low-Cost Mobile Phone Microscopy with a Reversed Mobile Phone Camera Lens. *PLoS One* **9**, e95330 (2014).
149. Xie, H. *et al.* Rapid point-of-care detection of the tuberculosis pathogen using a BlaC-specific fluorogenic probe. *Nat. Chem.* **4**, 802–9 (2012).
150. Lim, J., Gruner, P., Konrad, M. & Baret, J.-C. Micro-optical lens array for fluorescence detection in droplet-based microfluidics. *Lab Chip* **13**, 1472 (2013).

151. MacWilliams, F. J. & Sloane, N. J. A. Pseudo-random sequences and arrays. *Proc. IEEE* **64**, 1715–1729 (1976).
152. Schmidt, O., Bassler, M., Kiesel, P., Knollenberg, C. & Johnson, N. Fluorescence spectrometer-on-a-fluidic-chip. *Lab Chip* **7**, 626–9 (2007).
153. Kaminaga, M. *et al.* Uniform Cell Distribution Achieved by Using Cell Deformation in a Micropillar Array. *Micromachines* **6**, 409–422 (2015).
154. Xia, Y. & Whitesides, G. M. SOFT LITHOGRAPHY. *Annu. Rev. Mater. Sci* **28**, 153–84 (1998).
155. Emi Dangla, R., Gallaire, F. & Baroud, C. N. Microchannel deformations due to solvent-induced PDMS swelling. doi:10.1039/c003504a
156. Sandoz, P. A. *et al.* DIGITAL READOUT PLATFORM FOR WATER-IN-OIL DROPLET IMMUNOASSAYS RUNNING ON A CELL-PHONE FOR POINT OF CARE VIRAL LOAD SENSING. at <http://www.rsc.org/images/loc/2012/pdf/M.1.18.pdf>
157. Jones, G. M. *et al.* Digital PCR dynamic range is approaching that of real-time quantitative PCR. *Biomol. Detect. Quantif.* (2016). doi:10.1016/j.bdq.2016.10.001
158. Frenz, L., Blank, K., Brouzes, E. & Griffiths, A. D. Reliable microfluidic on-chip incubation of droplets in delay-lines. *Lab Chip* **9**, 1344–8 (2009).
159. Strain, M. C. *et al.* Highly Precise Measurement of HIV DNA by Droplet Digital PCR. *PLoS One* **8**, e55943 (2013).
160. Zborowski, M. & Chalmers, J. J. Rare Cell Separation and Analysis by Magnetic Sorting. *Anal. Chem.* **83**, 8050–8056 (2011).
161. Chen, D. *et al.* An integrated, self-contained microfluidic cassette for isolation, amplification, and detection of nucleic acids. *Biomed. Microdevices* **12**, 705–719 (2010).
162. Ko, J., Carpenter, E. & Issadore, D. Detection and isolation of circulating exosomes and microvesicles for cancer monitoring and diagnostics using micro-/nano-based devices. *Analyst* **141**, 450–460 (2016).
163. Rao, M. V. G., Kumar, P. R. & Prasad, A. M. Implementation of real time image processing system with FPGA and DSP. in *2016 International Conference on Microelectronics, Computing and Communications (MicroCom)* 1–4 (IEEE, 2016). doi:10.1109/MicroCom.2016.7522496
164. Prakadan, S. M., Shalek, A. K. & Weitz, D. A. Scaling by shrinking: empowering single-cell ‘omics’ with microfluidic devices. *Nat. Rev. Genet.* **18**, 345–361 (2017).
165. Pekin, D. *et al.* Quantitative and sensitive detection of rare mutations using droplet-based microfluidics. *Lab Chip* **11**, 2156 (2011).
166. Hindson, C. M. *et al.* Absolute quantification by droplet digital PCR versus analog

real-time PCR. *Nat. Methods* **10**, 1003–1005 (2013).

167. Hindson, B. J. *et al.* High-Throughput Droplet Digital PCR System for Absolute Quantitation of DNA Copy Number. *Anal. Chem.* **83**, 8604–8610 (2011).
168. Rissin, D. M. *et al.* Single-molecule enzyme-linked immunosorbent assay detects serum proteins at subfemtomolar concentrations. *Nat. Biotechnol.* **28**, 595–599 (2010).
169. and, D. M. R. & Walt\*, D. R. Digital Concentration Readout of Single Enzyme Molecules Using Femtoliter Arrays and Poisson Statistics. (2006). doi:10.1021/NL060227D
170. Chang, L. *et al.* Simple diffusion-constrained immunoassay for p24 protein with the sensitivity of nucleic acid amplification for detecting acute HIV infection. *J. Virol. Methods* **188**, 153–160 (2013).
171. Guan, Z. *et al.* A highly parallel microfluidic droplet method enabling single-molecule counting for digital enzyme detection. *Biomicrofluidics* **8**, 014110 (2014).
172. Obayashi, Y. *et al.* A single-molecule digital enzyme assay using alkaline phosphatase with a coumarin-based fluorogenic substrate. *Analyst* **140**, 5065–5073 (2015).
173. Shembekar, N., Hu, H., Eustace, D. & Merten, C. A. Single-Cell Droplet Microfluidic Screening for Antibodies Specifically Binding to Target Cells. *Cell Rep.* **22**, 2206–2215 (2018).
174. Li, M., van Zee, M., Goda, K. & Di Carlo, D. Size-based sorting of hydrogel droplets using inertial microfluidics. *Lab Chip* (2018). doi:10.1039/C8LC00568K
175. Eastburn, D. J., Sciambi, A. & Abate, A. R. Ultrahigh-Throughput Mammalian Single-Cell Reverse-Transcriptase Polymerase Chain Reaction in Microfluidic Drops. *Anal. Chem.* **85**, 8016–8021 (2013).
176. Eastburn, D. J., Sciambi, A. & Abate, A. R. Identification and genetic analysis of cancer cells with PCR-activated cell sorting. *Nucleic Acids Res.* **42**, e128–e128 (2014).
177. Liu, C. *et al.* Single-Exosome-Counting Immunoassays for Cancer Diagnostics. *Nano Lett.* **18**, 4226–4232 (2018).
178. Korley, F. K. *et al.* Performance Evaluation of a Multiplex Assay for Simultaneous Detection of Four Clinically Relevant Traumatic Brain Injury Biomarkers. *J. Neurotrauma* **36**, 182–187 (2019).
179. Rissin, D. M. *et al.* Polymerase-free measurement of microRNA-122 with single base specificity using single molecule arrays: Detection of drug-induced liver injury. *PLoS One* **12**, e0179669 (2017).
180. McDermott, G. P. *et al.* Multiplexed Target Detection Using DNA-Binding Dye Chemistry in Droplet Digital PCR. *Anal. Chem.* **85**, 11619–11627 (2013).

181. Albayrak, C. *et al.* Digital Quantification of Proteins and mRNA in Single Mammalian Cells. *Mol. Cell* **61**, 914–924 (2016).
182. Passaes, C. P. B. *et al.* Ultrasensitive HIV-1 p24 Assay Detects Single Infected Cells and Differences in Reservoir Induction by Latency Reversal Agents. *J. Virol.* **91**, e02296-16 (2017).
183. Olivera, A. *et al.* Peripheral Total Tau in Military Personnel Who Sustain Traumatic Brain Injuries During Deployment. *JAMA Neurol.* **72**, 1109 (2015).
184. Schubert, S. M. *et al.* Ultra-sensitive protein detection via Single Molecule Arrays towards early stage cancer monitoring. *Sci. Rep.* **5**, 11034 (2015).
185. Descours, B. *et al.* CD32a is a marker of a CD4 T-cell HIV reservoir harbouring replication-competent proviruses. *Nature* **543**, 564–567 (2017).
186. Du, W., Li, L., Nichols, K. P. & Ismagilov, R. F. SlipChip. *Lab Chip* **9**, 2286 (2009).
187. Shen, F., Du, W., Kreutz, J. E., Fok, A. & Ismagilov, R. F. Digital PCR on a SlipChip. *Lab Chip* **10**, 2666 (2010).
188. Zhu, Q. *et al.* Digital PCR on an integrated self-priming compartmentalization chip. *Lab Chip* **14**, 1176–85 (2014).
189. Yadavali, S., Jeong, H.-H., Lee, D. & Issadore, D. Silicon and glass very large scale microfluidic droplet integration for terascale generation of polymer microparticles. *Nat. Commun.* **9**, 1222 (2018).
190. Yelleswarapu, V. R. *et al.* Ultra-high throughput detection (1 million droplets per second) of fluorescent droplets using a cell phone camera and time domain encoded optofluidics. *Lab Chip* **17**, 1083–1094 (2017).
191. Jeong, H.-H. *et al.* Kilo-scale droplet generation in three-dimensional monolithic elastomer device (3D MED). *Lab Chip* **15**, 4387–4392 (2015).
192. Ward, T., Faivre, M., Abkarian, M. & Stone, H. A. Microfluidic flow focusing: Drop size and scaling in pressure versus flow-rate-driven pumping. *Electrophoresis* **26**, 3716–3724 (2005).
193. Weigl, B. H., Bardell, R., Schulte, T., Battrell, F. & Hayenga, J. Design and Rapid Prototyping of Thin-Film Laminate-Based Microfluidic Devices. *Biomed. Microdevices* **3**, 267–274 (2001).
194. Shaffer, S. M. *et al.* Multiplexed detection of viral infections using rapid in situ RNA analysis on a chip. *Lab Chip* **15**, 3170–82 (2015).
195. Lee, W., Walker, L. M. & Anna, S. L. Competition Between Viscoelasticity and Surfactant Dynamics in Flow Focusing Microfluidics. *Macromol. Mater. Eng.* **296**, 203–213 (2011).
196. Stroock, A. D. *et al.* Chaotic Mixer for Microchannels. *Science (80-. )*. **295**, 647–651 (2002).

197. Gaster, R. S. *et al.* Matrix-insensitive protein assays push the limits of biosensors in medicine. *Nat. Med.* **15**, 1327–1332 (2009).
198. Wu, D., Milutinovic, M. D. & Walt, D. R. Single molecule array (Simoa) assay with optimal antibody pairs for cytokine detection in human serum samples. *Analyst* **140**, 6277–82 (2015).
199. Dunbar, S. A., Vander Zee, C. A., Oliver, K. G., Karem, K. L. & Jacobson, J. W. Quantitative, multiplexed detection of bacterial pathogens: DNA and protein applications of the Luminex LabMAP system. *J. Microbiol. Methods* **53**, 245–52 (2003).
200. Ko, J. *et al.* Combining Machine Learning and Nanofluidic Technology To Diagnose Pancreatic Cancer Using Exosomes. *ACS Nano* **11**, 11182–11193 (2017).
201. Ko, J. *et al.* Machine learning to detect signatures of disease in liquid biopsies – a user's guide. *Lab Chip* **18**, 395–405 (2018).
202. Zhang, Y. & Jiang, H.-R. A review on continuous-flow microfluidic PCR in droplets: Advances, challenges and future. *Anal. Chim. Acta* **914**, 7–16 (2016).
203. Chen, Y. *et al.* Rare cell isolation and analysis in microfluidics. *Lab Chip* **14**, 626 (2014).
204. Nagrath, S. *et al.* Isolation of rare circulating tumour cells in cancer patients by microchip technology. *Nature* **450**, 1235–1239 (2007).
205. Gallacher, L. *et al.* Isolation and characterization of human CD34(-)Lin(-) and CD34(+)Lin(-) hematopoietic stem cells using cell surface markers AC133 and CD7. *Blood* **95**, 2813–20 (2000).
206. Ardehali, R. *et al.* Prospective isolation of human embryonic stem cell-derived cardiovascular progenitors that integrate into human fetal heart tissue. *Proc. Natl. Acad. Sci. U. S. A.* **110**, 3405–10 (2013).
207. Miltenyi, S., Müller, W., Weichel, W. & Radbruch, A. High gradient magnetic cell separation with MACS. *Cytometry* **11**, 231–238 (1990).
208. Pamme, N. On-chip bioanalysis with magnetic particles. *Curr. Opin. Chem. Biol.* **16**, 436–443 (2012).
209. Ozkumur, E. *et al.* Inertial Focusing for Tumor Antigen-Dependent and -Independent Sorting of Rare Circulating Tumor Cells. *Sci. Transl. Med.* **5**, 179ra47-179ra47 (2013).
210. Issadore, D. *et al.* Ultrasensitive Clinical Enumeration of Rare Cells ex Vivo Using a Micro-Hall Detector. *Sci. Transl. Med.* **4**, 141ra92-141ra92 (2012).
211. Muluneh, M. & Issadore, D. Microchip-based detection of magnetically labeled cancer biomarkers. *Adv. Drug Deliv. Rev.* **66**, 101–9 (2014).

212. Lang, J. M., Casavant, B. P. & Beebe, D. J. Circulating Tumor Cells: Getting More from Less. *Sci. Transl. Med.* **4**, 141ps13-141ps13 (2012).
213. Chen, P., Huang, Y.-Y., Hoshino, K. & Zhang, J. X. J. Microscale Magnetic Field Modulation for Enhanced Capture and Distribution of Rare Circulating Tumor Cells. *Sci. Rep.* **5**, 8745 (2015).
214. Muluneh, M., Shang, W. & Issadore, D. Track-etched magnetic micropores for immunomagnetic isolation of pathogens. *Adv. Healthc. Mater.* **3**, 1078–85 (2014).
215. Earhart, C. M. *et al.* Isolation and mutational analysis of circulating tumor cells from lung cancer patients with magnetic sifters and biochips. *Lab Chip* **14**, 78–88 (2014).
216. Earhart, C. M., Wilson, R. J., White, R. L., Pourmand, N. & Wang, S. X. Microfabricated magnetic sifter for high-throughput and high-gradient magnetic separation. *J. Magn. Magn. Mater.* **321**, 1436–1439 (2009).
217. Whitesides, G. M., Ostuni, E., Takayama, S., Jiang, X. & Ingber, D. E. Soft Lithography in Biology and Biochemistry. *Annu. Rev. Biomed. Eng.* **3**, 335–373 (2001).
218. Park, J.-W., Park, J. Y., Joung, Y.-H. & Allen, M. G. *Fabrication of High Current and Low Profile Micromachined Inductor With Laminated Ni/Fe Core.* *IEEE TRANSACTIONS ON COMPONENTS AND PACKAGING TECHNOLOGIES* **25**, (2002).
219. McGeough, J. A., Leu, M. C., Rajurkar, K. P., De Silva, A. K. M. & Liu, Q. Electroforming Process and Application to Micro/Macro Manufacturing. *CIRP Ann.* **50**, 499–514 (2001).
220. Makarova, O. V *et al.* *Microfabrication of freestanding metal structures using graphite substrate* \$. at <<https://pdfs.semanticscholar.org/ea1a/2f32b3c6bec41c8dc73d2b90c0b793b99bf7.pdf>>
221. Hosokawa, M. *et al.* Size-Selective Microcavity Array for Rapid and Efficient Detection of Circulating Tumor Cells. *Anal. Chem.* **82**, 6629–6635 (2010).
222. Okamoto, N., Wang, F. & Watanabe, T. *Adhesion of Electrodeposited Copper, Nickel and Silver Films on Copper, Nickel and Silver Substrates \* 1.* at <<https://www.jim.or.jp/journal/e/pdf3/45/12/3330.pdf>>
223. Turban, G. & Rapeaux, M. Dry Etching of Polyimide in O<sub>2</sub>-CF<sub>4</sub> and O<sub>2</sub>-SF<sub>6</sub> Plasmas. *J. Electrochem. Soc.* **130**, 2231 (1983).
224. Mimoun, B., Pham, H. T. M., Henneken, V. & Dekker, R. Residue-free plasma etching of polyimide coatings for small pitch vias with improved step coverage. *J. Vac. Sci. Technol. B, Nanotechnol. Microelectron. Mater. Process. Meas. Phenom.* **31**, 021201 (2013).

225. Buder, U., von Klitzing, J.-P. & Obermeier, E. Reactive ion etching for bulk structuring of polyimide. *Sensors Actuators A Phys.* **132**, 393–399 (2006).
226. Kim, M., Kim, J., Herrault, F., Schafer, R. & Allen, M. G. A MEMS lamination technology based on sequential multilayer electrodeposition. *J. Micromechanics Microengineering* **23**, 095011 (2013).
227. Taylor, W. P., Brand, O. & Allen, M. G. *Fully Integrated Magnetically Actuated Micromachined Relays*. *JOURNAL OF MICROELECTROMECHANICAL SYSTEMS* **7**, (1998).
228. Parkinson, D. R. *et al.* Considerations in the development of circulating tumor cell technology for clinical use. *J. Transl. Med.* **10**, 138 (2012).
229. Chung, J. *et al.* Rare cell isolation and profiling on a hybrid magnetic/size-sorting chip. *Biomicrofluidics* **7**, 54107 (2013).
230. *Point-of-Care Diagnostics on a Chip*. (Springer Berlin Heidelberg, 2013). doi:10.1007/978-3-642-29268-2
231. Dharmasiri, U., Witek, M. A., Adams, A. A. & Soper, S. A. Microsystems for the Capture of Low-Abundance Cells. *Annu. Rev. Anal. Chem.* **3**, 409–431 (2010).
232. Aaron R. Wheeler, †,‡ *et al.* Microfluidic Device for Single-Cell Analysis. (2003). doi:10.1021/AC0340758
233. Vieira, G. *et al.* Magnetic Wire Traps and Programmable Manipulation of Biological Cells. *Phys. Rev. Lett.* **103**, 128101 (2009).
234. Nilsson, J., Evander, M., Hammarström, B. & Laurell, T. Review of cell and particle trapping in microfluidic systems. *Anal. Chim. Acta* **649**, 141–157 (2009).
235. Tseng, P. *et al.* Flexible and Stretchable Micromagnet Arrays for Tunable Biointerfacing. *Adv. Mater.* **27**, 1083–1089 (2015).
236. Murray, C. *et al.* Quantitative Magnetic Separation of Particles and Cells Using Gradient Magnetic Ratcheting. *Small* **12**, 1891–9 (2016).
237. Yelleswarapu, V. R., Jeong, H.-H., Yadavali, S. & Issadore, D. Ultra-high throughput detection (1 million droplets per second) of fluorescent droplets using a cell phone camera and time domain encoded optofluidics. *Lab Chip* **17**, 1083–1094 (2017).
238. Ren, G. & Krawetz, R. Applying computation biology and “big data” to develop multiplex diagnostics for complex chronic diseases such as osteoarthritis. *Biomarkers* **20**, 533–539 (2015).
239. Dixon, A. R. *et al.* Recent developments in multiplexing techniques for immunohistochemistry HHS Public Access. *Expert Rev Mol Diagn* **15**, 1171–1186 (2015).
240. Joensson, H. N. *et al.* Detection and Analysis of Low-Abundance Cell-Surface

Biomarkers Using Enzymatic Amplification in Microfluidic Droplets. *Angew. Chemie Int. Ed.* **48**, 2518–2521 (2009).

241. Periyannan Rajeswari, P. K. *et al.* Multiple pathogen biomarker detection using an encoded bead array in droplet PCR. *J. Microbiol. Methods* **139**, 22–28 (2017).
242. Cole, R. H. *et al.* Compact and modular multicolour fluorescence detector for droplet microfluidics. *Lab Chip* **15**, 2754–2758 (2015).
243. Daher, R. K., Stewart, G., Boissinot, M. & Bergeron, M. G. Recombinase Polymerase Amplification for Diagnostic Applications. *Clin. Chem.* **62**, (2016).
244. Piepenburg, O., Williams, C. H., Stemple, D. L. & Armes, N. A. DNA Detection Using Recombination Proteins. doi:10.1371/journal.pbio.0040204
245. DeJournette, C. J. *et al.* Creating Biocompatible Oil–Water Interfaces without Synthesis: Direct Interactions between Primary Amines and Carboxylated Perfluorocarbon Surfactants. *Anal. Chem.* **85**, 10556–10564 (2013).
246. Kong, J. E. *et al.* Highly Stable and Sensitive Nucleic Acid Amplification and Cell-Phone-Based Readout. *ACS Nano* **11**, 2934–2943 (2017).
247. Khorosheva, E. M., Karymov, M. A., Selck, D. A. & Ismagilov, R. F. Lack of correlation between reaction speed and analytical sensitivity in isothermal amplification reveals the value of digital methods for optimization: validation using digital real-time RT-LAMP. *Nucleic Acids Res.* **44**, e10 (2016).
248. Crannell, Z. *et al.* Multiplexed Recombinase Polymerase Amplification Assay To Detect Intestinal Protozoa. *Anal. Chem.* **88**, 1610–1616 (2016).
249. Kim, J. Y. & Lee, J.-L. Development of a multiplex real-time recombinase polymerase amplification (RPA) assay for rapid quantitative detection of *Campylobacter coli* and *jejuni* from eggs and chicken products. *Food Control* **73**, 1247–1255 (2017).
250. Rohrman, B. & Richards-Kortum, R. Inhibition of Recombinase Polymerase Amplification by Background DNA: A Lateral Flow-Based Method for Enriching Target DNA. *Anal. Chem.* **87**, 1963–1967 (2015).
251. Zhan, L., Wu, W. B., Yang, X. X. & Huang, C. Z. Gold nanoparticle-based enhanced ELISA for respiratory syncytial virus. *New J. Chem.* **38**, 2935–2940 (2014).
252. Billingsley, M. M., Riley, R. S. & Day, E. S. Antibody-nanoparticle conjugates to enhance the sensitivity of ELISA-based detection methods. *PLoS One* **12**, e0177592 (2017).
253. Bang, J. *et al.* Sensitive detection of dengue virus NS1 by highly stable affibody-functionalized gold nanoparticles. *New J. Chem.* **42**, 12607–12614 (2018).